UNIVERSITAT ROVIRA I VIRGILI
DEVELOPMENT OF TECHNOLOGY AND APPLICATIONS BASED ON POROUS ALUMINA NANOSTRUCTURES
Lukas Vojkuvka
DL: T-1536-2009/ISBN: 978-84-692-4555-2

**Lukáš Vojkůvka**

# DEVELOPMENT OF TECHNOLOGY AND APPLICATIONS BASED ON POROUS ALUMINA NANOSTRUCTURES

**DOCTORAL THESIS**

*Supervised by*

Dr. Lluís Francesc Marsal Garví

Departament d'Enginyeria Electrónica, Eléctrica i Automática

UNIVERSITAT ROVIRA I VIRGILI

**Tarragona**

**2009**

UNIVERSITAT ROVIRA I VIRGILI
DEVELOPMENT OF TECHNOLOGY AND APPLICATIONS BASED ON POROUS ALUMINA NANOSTRUCTURES
Lukas Vojkuvka
DL: T-1536-2009/ISBN: 978-84-692-4555-2

UNIVERSITAT ROVIRA I VIRGILI
DEVELOPMENT OF TECHNOLOGY AND APPLICATIONS BASED ON POROUS ALUMINA NANOSTRUCTURES
Lukas Vojkuvka
DL: T-1536-2009/ISBN: 978-84-692-4555-2

UNIVERSITAT ROVIRA I VIRGILI

Departament d'Enginyeria Electrónica, Eléctrica i Automática
Av. Paisos Catalans 26
43007 Tarragona

Lluís Francesc Marsal Garví, professor titular del Departament d'Enginyeria Electrònica, Elèctrica i Automàtica de la Universitat Rovira i Virgili,

CERTIFICO:

Que aquest treball, titulat "Development of technology and applications based on porous alumina nanostructures", que presenta Lukas Vojkuvka per a l´obtenció del títol de Doctor, ha estat realitzat sota la meva direcció al Departament d'Enginyeria Electrònica, Elèctrica i Automàtica d´aquesta universitat i que acompleix els requeriments per poder optar a Menció Europea.

Tarragona, 2 de febrer de 2009

UNIVERSITAT ROVIRA I VIRGILI
DEVELOPMENT OF TECHNOLOGY AND APPLICATIONS BASED ON POROUS ALUMINA NANOSTRUCTURES
Lukas Vojkuvka
DL: T-1536-2009/ISBN: 978-84-692-4555-2

UNIVERSITAT ROVIRA I VIRGILI
DEVELOPMENT OF TECHNOLOGY AND APPLICATIONS BASED ON POROUS ALUMINA NANOSTRUCTURES
Lukas Vojkuvka
DL: T-1536-2009/ISBN: 978-84-692-4555-2

# Abstract

This thesis discusses the fabrication and characterization of self-ordered porous alumina structures. Two anodizing techniques—'two step anodization' and 'hard anodization'— were used to prepare porous alumina structures. Morphological observation with scanning electron microscopy (SEM) showed that the geometrical properties of the porous alumina structures were diverse: the pore diameter varied between 20 nm and 250 nm, and the interpore distance was 50 nm, 100 nm, 300 nm or 450 nm. By combining both anodizing techniques, novel porous structures such as double- and multi-layered porous alumina were developed.

The physical properties of several porous alumina structures were studied using various characterization techniques: namely, X-ray diffraction, optical spectroscopy in the visible-ultraviolet (UV-Vis) and infrared range (FT-IR), photoluminescence spectroscopy (PL), nanoindentation and friction measurements. The results of UV-Vis spectroscopy revealed the presence of the bandgap centred at a wavelength of 380 nm. This bandgap was observed to be blue-shifted for the porous alumina samples thermally treated at high temperatures. The divergences in the optical properties are related to the crystallization process that takes place in the heat-treated porous alumina. The temperature-dependent band was also similar in FT-IR and PL spectra indicating the presence of impurities in the porous alumina. In this case, the variation of the band is attributed to the actual structural state and impurity concentration within the porous alumina structure. Mechanical properties expressed by hardness and Young's modulus of porous alumina with different porosities were extracted from the nanoindentation measurements. The decrease observed in both mechanical constants is ascribed to the increase in alumina porosity. The friction coefficients were calculated from the scratch tests performed on the porous alumina samples with different porosities. A closer SEM examination of the scratched areas revealed the interesting fact that some types of porous alumina behave rather plastically at the nanometric scale. This may be caused by contamination of the water and the presence of metal in the porous alumina studied.

DL: T-1536-2009/ISBN: 978-84-692-4555-2

Derived applications such as metal nanowire arrays and polymer nanopillar arrays were prepared using porous alumina templates. The re-anodization technique was directly applied after the anodization process in order to open pore bottoms. In this way, the porous alumina templates were continuously attached to the aluminium substrate serving as an electrical contact for consequent metal electro-deposition. Another application of porous alumina was based on the periodical nanometric geometry with air holes distributed within the alumina in the triangular lattice. The optical properties were simulated using an ideal photonic crystal with the same geometrical parameters as the porous alumina prepared in laboratory. The results obtained from the simulations were in a good agreement with the previous optical measurements in the UV-Vis range.

The preliminary results from the novel and promising anodization approach of discontinuous anodization showed that the pore diameter in porous alumina could be modulated. A three-dimensional porous alumina structure makes novel applications possible in the fields of nanostructured materials and optical nanodevices.

UNIVERSITAT ROVIRA I VIRGILI
DEVELOPMENT OF TECHNOLOGY AND APPLICATIONS BASED ON POROUS ALUMINA NANOSTRUCTURES
Lukas Vojkuvka
DL: T-1536-2009/ISBN: 978-84-692-4555-2

# Acknowledgements

Foremost, I would like to thank my supervisor Dr. Lluís Marsal for the opportunity to accomplish my Ph.D. thesis at University Rovira i Virgili in Tarragona, and for his guidance during past four years. I deeply appreciate Josep Ferré-Borrull and his professional advices and comments on my work. I also thank Josep Pallarés for his support, especially at the beginning of my Ph.D. period. The scholarship from the University Rovira i Virigili is highly acknowledged.

I sincerely acknowledge all my committee members and dissertation reviewers for their precious time and valuable comments.

I also wish to thank an expert in macroporous silicon Trifon Trifonov for introducing me the work with clean room facilities, for his willing help with my work, and for a good friendship. Similarly, I was very glad to be a student of Jaromir Hubalek, the first person who has opened for me a gate to nanoworld.
Special thanks goes to Nephos group members for their collaboration and "buen rollo". Particularly, I appreciate Abel Santos for his willingness to help me with the experimental work as well as to discuss about stimulating alumina topics. Many thanks to my best pal Zdenek Kral for his long company since we have started our studies in Spain and for our unforgettable social and leisure activities outside the university. Funny memories not only from the lab will remain in my mind thanks to my lab mates such as Julio, Edgar, Mariona, Mariana, Alex, Fer, Mauricio and many others.

I deeply acknowledge Mercé Moncusí, Mariana Stankova and Francesc Giraldo for their professional help with the characterization techniques. I also thank to ICIQ in Tarragona for the photoluminescence measurements. Special thanks belong to Prof. Jean-Pierre Celis from MTM department in Katholieke University Leuven for the acceptance and later supervision of my research stay in his working group.

I dedicate this thesis to the three most important persons in my life, to my Mum, to my sister Lenka and to my beloved Stella. Without them and all they did for me, this work would never come to light.

UNIVERSITAT ROVIRA I VIRGILI
DEVELOPMENT OF TECHNOLOGY AND APPLICATIONS BASED ON POROUS ALUMINA NANOSTRUCTURES
Lukas Vojkuvka
DL: T-1536-2009/ISBN: 978-84-692-4555-2

UNIVERSITAT ROVIRA I VIRGILI
DEVELOPMENT OF TECHNOLOGY AND APPLICATIONS BASED ON POROUS ALUMINA NANOSTRUCTURES
Lukas Vojkuvka
DL: T-1536-2009/ISBN: 978-84-692-4555-2

# Contents

UNIVERSITAT ROVIRA I VIRGILI
DEVELOPMENT OF TECHNOLOGY AND APPLICATIONS BASED ON POROUS ALUMINA NANOSTRUCTURES
Lukas Vojkuvka
DL: T-1536-2009/ISBN: 978-84-692-4555-2

UNIVERSITAT ROVIRA I VIRGILI
DEVELOPMENT OF TECHNOLOGY AND APPLICATIONS BASED ON POROUS ALUMINA NANOSTRUCTURES
Lukas Vojkuvka
DL: T-1536-2009/ISBN: 978-84-692-4555-2

# Introduction

DL: T-1536-2009/ISBN: 978-84-692-4555-2

**History of porous alumina science**

The anodizing of metals in the industrial area has its origins back in early 1920's. Thanks to Bengough-Stuart anodizing process patented in 1923 and lately in 1927 Gower and O'Brien process, the industrial anodizing can still be widely used for many commercial purposes such as metal passivation or decorativeness.

The most common anodized metal is aluminium and we can notice its presence everywhere in many things. The anodized aluminium has high corrosion resistance, surface hardness and good ability for colouring [1]. Besides this usage of anodized aluminium, the first deeper studies focused on basics of porous alumina have been realized since 1950. Keller et al. have reported structural features of porous alumina using electron microscope for the first time based on porous and barrier oxide layer [2]. This pioneering work was an initial springboard for later investigation of porous alumina.

First detailed state of the art for anodic films on aluminium has been composed by Diggle et al in 1968 [3]. In this profound review, the authors have described in detail the porous alumina chemical composition, the formation theories and basic properties of barrier-type and porous-type anodic oxide films.

The knowledge of oxide growth mechanism and relationship between pore morphology and anodizing conditions has been significantly broadened by research of Thompson and Wood [4-6]. The implement of new characterization techniques such as transmission microscopy and marker methods have resulted in novel discoveries of porous alumina. The first application of porous alumina have started to appear in 1980`s. The fabrication of porous alumina membranes for filtration or gas separation have been reported by Itaya et al [7]. Later Furneaux et al. have presented an approach for barrier layer removal by lowering anodizing voltage resulting in separation of free-standing porous alumina membrane [8].

A breakthrough in porous alumina science has become in 1995. That time, Masuda and Fukuda have discovered two-step replication process for fabrication of self-ordered porous alumina structure with highly ordered pores [9]. This essential work has served as fundamental recipe for the following

DL: T-1536-2009/ISBN: 978-84-692-4555-2

investigation in this field. In addition, it is also one the most cited reference between porous alumina scientific communities.

During last two decades, porous alumina has attracted much interest in the investigation and application fields due to its unique nanometric properties which are highly required in the nanotechnology. Figure 1 reflects an increasing number of scientific contributions from different countries related to porous alumina. Many of them could not be referenced in this work; however there are a few significant reviews and book chapters that are worth to start with [3, 10, 11].

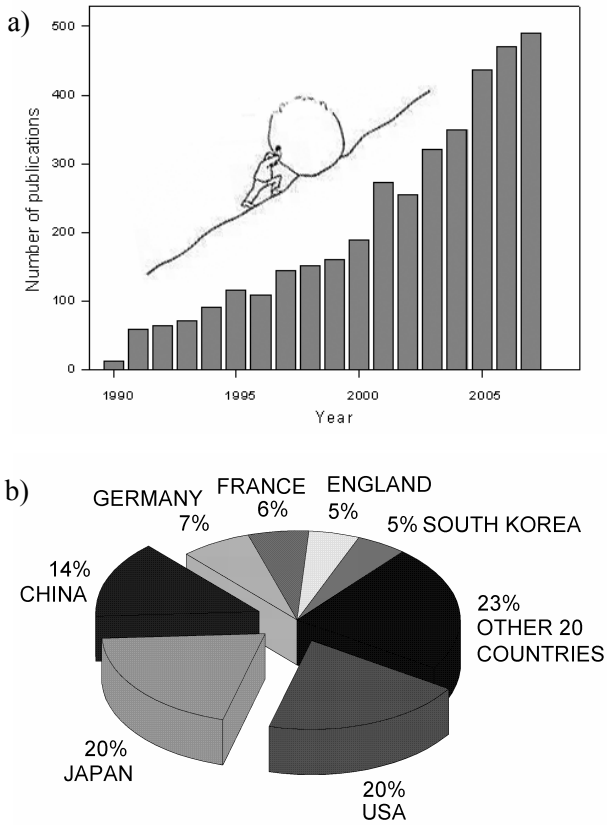


**Figure 1.** a) Increasing number of publications per year related to porous alumina in the last two decades and b) country proportions in the gross scientific contribution focused on porous alumina investigation since 1990. (presented data were taken from Web of knowledge database in October 2008).

DL: T-1536-2009/ISBN: 978-84-692-4555-2

**Objectives**

The general purpose of this dissertation is to develop the technology of self-ordered porous alumina and its applications. In this context, the specific objectives are defined as follows:

i) To develop and control the fabrication processes of self-ordered porous alumina by means of two-step anodization and hard anodization. At the same time, to examine the morphology of the porous alumina structures produced using scanning electron microscopy (SEM) and atomic force microscopy (AFM) characterization techniques.

ii) To study the physical properties of self-ordered porous alumina using such characterization techniques as X-ray diffraction spectroscopy, optical spectroscopy, infrared spectroscopy, photoluminescence spectroscopy, nanoindentation and friction tests.

iii) To propose and produce the applications based on the self-ordered porous alumina.

**Thesis structure**

The thesis has the following structure. Chapter one deals with the state of the art of porous alumina and includes basic concepts of aluminium electrochemistry, the growth phases of pores and their self-ordering behaviour, the two-step anodization process and a review of the most common porous alumina structures. Particular attention is given to an overview of the studies that report novel fabrication approaches for porous alumina structures and their applications. Chapter two discusses the fabrication process and morphological features of porous alumina that is experimentally prepared using the two step anodization process. Chapter three focuses on preparing porous alumina with the hard anodization process. A comparative study of porous alumina produced by two-step and hard anodization is also made. At the end of this chapter, the attempts at fabricating novel porous alumina structures using a combined two-step/hard anodization process are described. Chapter four presents the structural, optical and mechanical properties of porous alumina determined with such characterization techniques as X-ray diffraction, optical, infrared and photoluminescence spectroscopy, nanoindentation and friction tests. Chapter five summarizes the applications derived from the as-produced porous alumina and describes the synthesis of metal nanowire arrays and polymer nanopillar

DL: T-1536-2009/ISBN: 978-84-692-4555-2

arrays from porous alumina templates. Ideal photonic crystal simulations based on the porous alumina geometry and the preliminary results from a new anodizing technique for pore modulation are also included. Finally, the last chapter gives the conclusions.

UNIVERSITAT ROVIRA I VIRGILI
DEVELOPMENT OF TECHNOLOGY AND APPLICATIONS BASED ON POROUS ALUMINA NANOSTRUCTURES
Lukas Vojkuvka
DL: T-1536-2009/ISBN: 978-84-692-4555-2

UNIVERSITAT ROVIRA I VIRGILI
DEVELOPMENT OF TECHNOLOGY AND APPLICATIONS BASED ON POROUS ALUMINA NANOSTRUCTURES
Lukas Vojkuvka
DL: T-1536-2009/ISBN: 978-84-692-4555-2

# 1

# State of the Art

UNIVERSITAT ROVIRA I VIRGILI
DEVELOPMENT OF TECHNOLOGY AND APPLICATIONS BASED ON POROUS ALUMINA NANOSTRUCTURES
Lukas Vojkuvka
DL: T-1536-2009/ISBN: 978-84-692-4555-2

*Chapter 1*

## 1.1

## Anodizing of Aluminium

When a valve metal such as tantalum, zirconium or aluminium is exposed to ambient conditions, the metal surface is covered with a very thin natural oxide film called barrier oxide. Similar reaction occurs also when the metal is employed as anode in the electrochemical system for electrolysis. Compared to the environment, the oxidizing conditions in this case are highly enhanced by means of electrical current and electrolyte. Particularly, the oxidizing process that takes place on the anode surface is called anodizing. The sketch of such a system for anodizing is illustrated in Figure 2. The oxidized metal anode (A) and inert cathode made of carbon or platinum (C) are immersed in electrolyte (acid or salt solution). Both electrodes are connected to power supply, positive pole to anode and negative pole to cathode. During the electrolysis, the redox (reduction/oxidation) reactions are simultaneously in progress on the electrodes. The anode is oxidized by negative electrolyte substances (anions) resulting in the formation of anodic oxide layer on the metal surface. On the other side, the negative cathode supplied with electrons serves to reduce positive substances (cations). Therefore, the redox reactions are characterized by a balance of electron production and consumption.

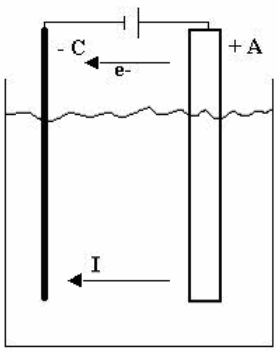


**Figure 2.** Schematic of electrochemical system for anodizing.

DL: T-1536-2009/ISBN: 978-84-692-4555-2

The electrolyte is an important medium in the anodizing process and it has an essential influence on the property of the final anodic oxide layer. Basically, there two types of electrolytes that can be used for the metal anodizing. The first type is neutral, completely insoluble electrolyte prepared for example from citric acid, maleic acid or mixture of boric acid with sodium borate. The resulting thin, compact and non-porous anodic oxide is called barrier-type film [3, 12]. Porous-type film is produced in slightly soluble, acidic aqueous electrolytes such as sulphuric, oxalic, phosphoric or chromic acid [3, 13]. This porous anodic film in contrary to barrier-type has very distinct geometry and consistency that strongly depends on the anodizing conditions such as electrolyte, pH, time, temperature or power supply.

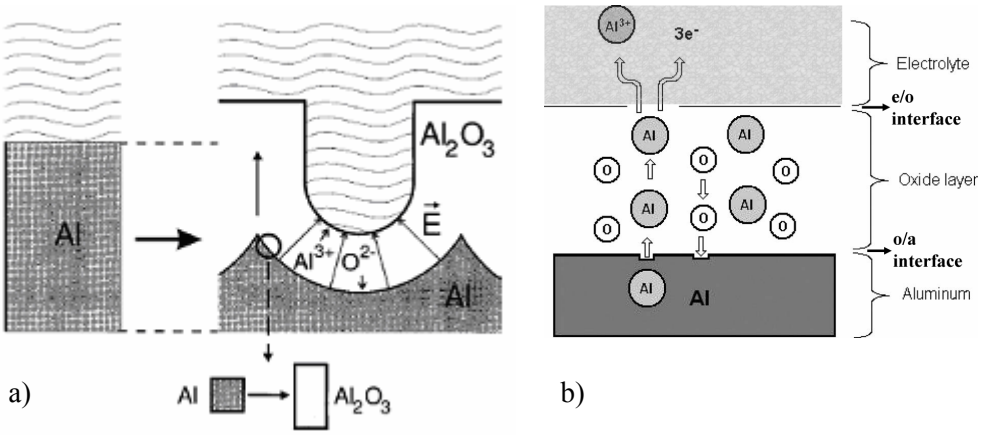


**Figure 3.** a) Model for porous alumina formation [14] and b) anodizing interfaces [15].

From now on, the given description will be referred to anodization of aluminium in acidic aqueous electrolyte. Figure 3(a) shows an idealised model of formation of porous-type aluminium oxide so-called porous alumina [14]. As illustrated in Figure 3(b), the complex of chemical reactions occurring during aluminium anodization proceeds in the electrolyte/oxide (e/o) and oxide/aluminium (o/a) interfaces at the pore tip [15]. The pore growth in the oxide layer is assigned to the equilibrium between the alumina formation at o/a interface and alumina dissolution at e/o interface. Written in the terms of their chemical reactions the oxide formation process can be formulated as follows:

$$2Al(s) + 3O^{-2} = Al_2O_3(s) + 6e^- \quad (1)$$

UNIVERSITAT ROVIRA I VIRGILI
DEVELOPMENT OF TECHNOLOGY AND APPLICATIONS BASED ON POROUS ALUMINA NANOSTRUCTURES
Lukas Vojkuvka
DL: T-1536-2009/ISBN: 978-84-692-4555-2


According to (1) and Figure 3(b), the oxygen anions penetrate through the e/o interface to the o/a interface, where they react with aluminium forming oxide layer and some free electrons. Conversely, the cations of aluminium that are withdrawn from the metal bulk under electric field move towards the e/o interface where they are either injected directly to the electrolyte or they also contribute to the oxide formation in the reaction with water. This reaction can be described as follows:

$$2Al^{+3}(aq) + 3H_2O \leftrightarrow Al_2O_3(s) + 6H^+(aq) \quad (2)$$

Reversibly, the oxide dissolution continuously takes place at the e/o interface, where protons of H+ cause alumina decomposition loosing Al cations and forming water. Accordingly to (2), it can be assumed that the e/o and o/a interfaces at the pore tips are in constant motion during the anodization process. The result of (2) is enhancement of oxide layer and production of hydrogen cations that starts to migrate towards the negative electrode. Simultaneously, on the cathode there is continuous reduction of these hydrogen cations in the reaction with free electrons carried through the electrical circuit from the anode. This process can be described with following equation:

$$6H^+(aq)+6e^- = 3H_2(g) \quad (3)$$

The formed hydrogen molecules in (3) are led away from the electrolyte in the form of bubbles.

The previous description of aluminium anodization was intentionally simplified and only basic explanation with principal chemical equations was given. In fact there is a complex of electrochemical processes and reactions involved in the formation process of porous alumina which can be find with description in more detail elsewhere [12, 15, 16].

### 1.1.1 Pore Growth in Stages

The pore formation can be explained using Figure 4 that shows typical current density-time transient from aluminium anodization under constant voltage. The four parts marked in Figure 4 correspond to different regimes of pore formation. In regime 1, the formation process begins with sharp decrease of the current characterized by uniform creation of insulating compact barrier oxide layer all over the metal surface. The thickness of such layer is determined

by applied voltage and it reaches the maximum when the current drops to the lowest value. Then in regime 2, the pores start to nucleate randomly on the surface followed by increasing the current until regime 3, where it slightly decreases again to reach the stable value. This slow current reduction is caused by the pore dying due to the in-between competition. The final stage in regime 4 can be described as steady – state pore growth with balanced current value and the pores uniformly grow during the remaining anodization time [3, 12, 17]. However, practically the current density moderately decreases as the anodization progress because of the diffusion limits in the very deep pores.

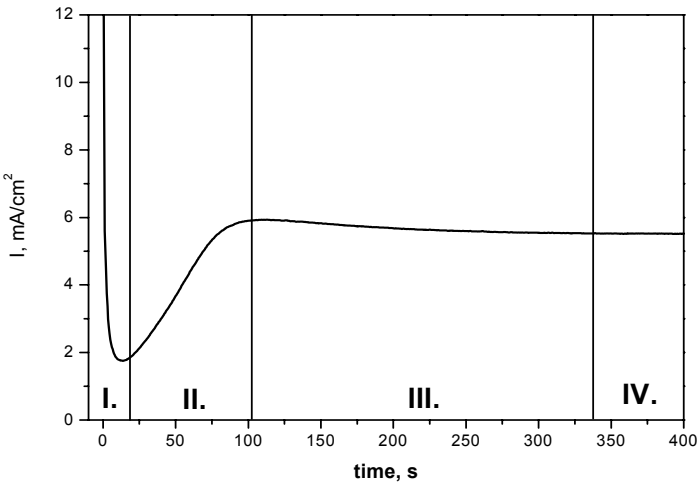


**Figure 4.** Typical current density transient with four different regimes of pore growth.

### 1.1.2 Theories of Pore Formation

The ranges for porous alumina geometry are much larger than any crystallographic periodicity of Al and its oxides. Therefore, it is clear that the porous alumina formation is not a crystal growth phenomenon. Several mechanism and theories of pore growth during aluminium anodizing have been proposed [3, 4, 18, 19]. Thompson et al suggested that the pore nucleation is due to a cracking and self-healing of the oxide layer at the surface ridges on the aluminium substrate [4]. Li et al supposed that the pores are initiated when the electric field is increased into a shallow pore bottom and initiates local acid

corrosion. The hexagonal ordering occurs either: (i) by an evolutionary selection of those pore bottoms that have the correct spacing for the acid and voltage used or (ii) by a diffusion of the pore bottoms, aided by lateral mobility of the ions that constitute the barrier layer [12].

In 1998 Jessensky et al. have proposed the explanation of self-organizing effect of the pores based on mechanical stress produced during pore formation [14, 20]. When aluminium is anodized to form porous alumina, the metal bulk is continuously consumed during the anodizing process. The atomic density of aluminium in the final porous alumina is much lower than in aluminium. Therefore, the possible origin of interactive forces between the neighbouring pores at the o/a interface can be associated to the mechanical stress due to the material expansion during the alumina formation. Since the oxidation takes place at the entire metal surface, the repulsed pores can grow only in vertical direction [14, 20, 21]. In addition, the study of the effect of an applied external tensile stress on the self-ordering process was reported by Sulka et al. [22]. They showed that the formation of self-organized pores is permitted up to a certain maximum of applied stress.

In previous interpretations of Jessensky et al., it has been stated that origins of porous self-ordering processes are stresses in o/a interface due to volume expansion. In order to study these stresses, an examination of the relative ratio of volume expansion factor thickness of alumina layer grown to an aluminium layer consumed during the process, i.e. was investigated by the same group [21]. The value of this factor varies largely from 0.8 up to 1.7 according to different conditions of anodization. There is a unique observation, that although anodization parameters of examined samples differ for the each of the three types of acid, the volume expansion factors are about 1.4 in the all cases of ordered pore arrangements. Therefore, in order to obtain an ordered structure, a moderate factor about 1.4 is required, independent of any type of solution. The volume expansion rate is closely related to the applied voltage, therefore very low or excessively high voltage will cause a variation in volume expansion. All, which has been described above, indicates that an applied voltage and the volume expansion of aluminium during anodization play an important role and there are specific optimums most suitable for self-organized pore formation [6, 12, 14, 20, 21, 23].

Also mathematical model of pore formation was proposed by Parkhutik and Shershulsky [18]. Their theoretical dependence of pore radius on applied voltage and pH of electrolyte reproduced previous experimental observation of [24].

### 1.1.3 Porous Anodic Alumina – State of the Art

Porous anodic alumina (PAA) structures, which are produced by the anodization of aluminium under specific conditions, have been used as starting material for fabrication of various nanodevices in many fields. Figure 5 represents a model of PAA that consists of close-packed arrays of cells with regular pores in the centre [25]. The porous cells grow perpendicularly to the Al substrate with hexagonal ordering over the entire surface. The geometrical properties of PAA such as cell size, pore diameter, interpore distance or pore depth are dependent on the anodizing conditions. The interpore distance is determined by the applied voltage used in the anodization. The pore diameter depends on many anodizing parameters such are electrolyte, temperature, anodizing time and voltage. The interpore distance can vary between 10 – 500 nm and the pores have diameter in the range of 5 to 400 nm depending on anodizing parameters. The pore depth can reach several hundreds microns after the long anodizing period [11].

The ordering degree of the pores in the PAA is essential for the derived applications. Basically, the self-ordering effect takes place on the bottom side of the PAA during the long anodizing period under appropriate conditions. The key parameters for successful ordering degree are applied voltage and type of electrolyte [11].

UNIVERSITAT ROVIRA I VIRGILI
DEVELOPMENT OF TECHNOLOGY AND APPLICATIONS BASED ON POROUS ALUMINA NANOSTRUCTURES
Lukas Vojkuvka
DL: T-1536-2009/ISBN: 978-84-692-4555-2


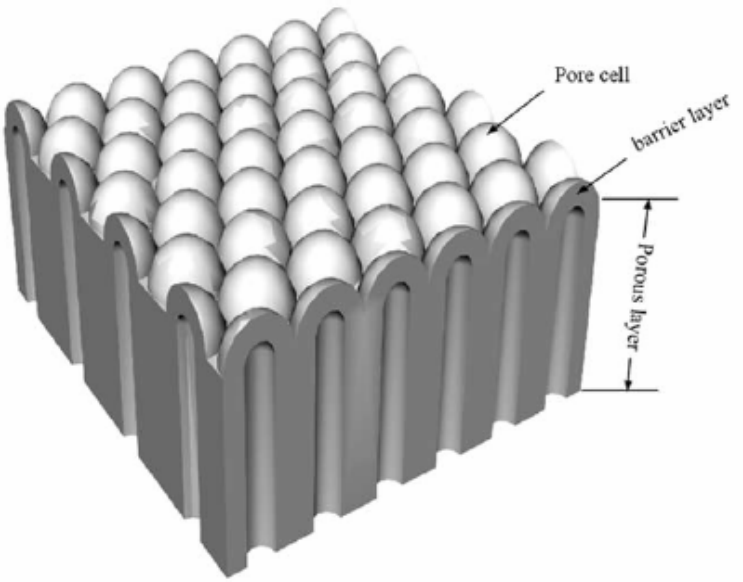


**Figure 5.** Idealised model of self-ordered porous alumina structure.

In 1995 Masuda and Fukuda have taken advantage of self-ordering effect that occurs during PAA formation and they have discovered a legendary two step anodizing process [9]. This simple fabrication approach relies on natural patterning of aluminium substrate in order to obtain perfectly self-ordered PAA structures. This method is successful only with use of specific anodizing conditions so-called self-ordering regimes. The main parameters and key factors of this two step process will be discussed later.

Porous anodic alumina has self-organized hexagonal pore arrays obtained by the anodization in aqueous electrolyte of the most commonly used acids: sulphuric, oxalic and phosphoric. The properties of the electrolyte solution together with the value of an applied voltage have substantial effect on the final geometry of the porous structure. As it is shown in Figure 6, PAA structures obtained from each type of acid have different pore diameters and interpore distances, whereas the hexagonal ordering is observable in all mentioned instances [14, 20, 21, 26-29].

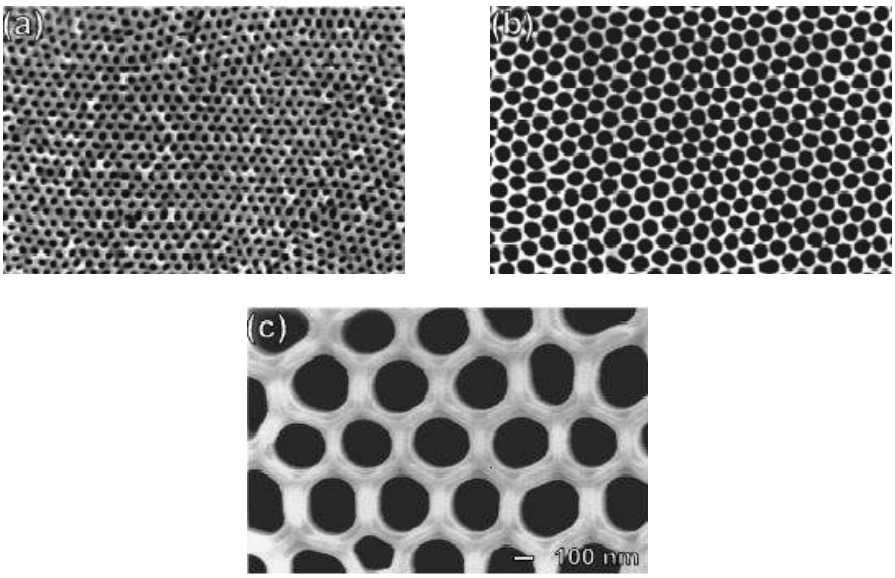


**Figure 6.** SEM images of porous alumina nanostructures produced in three major electrolytes: a) sulphuric acid, b) oxalic acid and c) phosphoric acid [21].

In the interesting study of Nielsch et al., they found the dependence of the PAA porosity on the anodizing conditions [30]. The formula for porosity *P* of ideal hexagonal porous structure is given by:

$$P \approx \frac{2\pi}{\sqrt{3}}\left(\frac{r}{D_{\text{int}}}\right)^2 \tag{4}$$

, where r is pore radius and $D_{\text{int}}$ interpore. It was found that the ratio $r/D_{\text{int}}$ is constant for self-ordered porous alumina produced using self-ordering regimes of most typical acids. Based on this, the porosity of the resultant porous alumina should always be around 10 %. Since the interpore distance is voltage-dependent and pore radius is dependent on pH value of electrolyte, the applied voltage and electrolyte conditions should match to fulfil the 10 % porosity rule. These findings helped to explain the deviations of ordered growth after long time anodization in terms of a change of the pH value the pore bottoms. The fundamental results presented in mentioned study are shown in Figure 7, where the table summaries experimental data (a) extracted from high-resolution TEM images (b).

a)

| electrolyte | interpore distance $D_{int}$ | inner wall thickness $D_{inner}$ | pore diameter $D_p$ (= 2r) | porosity P | p$K_s$ |
|---|---|---|---|---|---|
| $H_2SO_4$ 25 V, 0.3 M | 66.3 nm | 7.2 nm | 24 nm | 12% | 0.1 |
| $(COOH)_2$ 40 V, 0.3 M | 105 nm | 9.1 nm | 31 nm | 8% | 1.125 |
| $H_3PO_4$ 195 V, 0.1 M | 501 nm | 54 nm | 158.4 nm | 9% | 2.1 |

b)

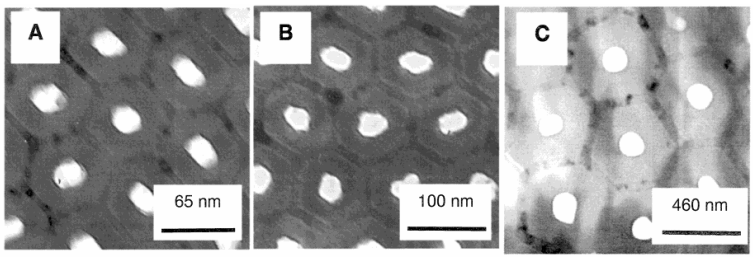


**Figure 7.** a) Summary table with geometrical properties of porous alumina analyzed from b) high-resolution TEM micrographs [30].

### 1.1.4 Anodizing Parameters Influencing Self-ordering

One of the key factors of Al anodization required for self-ordering formation of porous alumina is applied voltage. In Figure 8, it is shown that the interpore distance $D_{int}$ has a linear dependence on the applied voltage $U_a$ with proportionality constant $k$ = 2.5 – 2.8 nm/V, which can be described with following equation [2, 17, 21, 28, 29, 31]:

$$D_{int} = k \cdot U_a \tag{5}$$

The thickness of the barrier layer can be approximately estimated as the half of the interpore distance.

The electrolyte conditions including acid type, temperature, concentration and pH are all together important parameter that has to be controlled in order to ensure the formation of well-ordered PAA. The use of acid type with a given concentration is somewhat restricted by means of applied voltages values. For example, if the anodization is carried out in the high-conductive sulphuric acid solution (10 wt. %), then the low voltages (below 25 V) must be applied. For oxalic acid and phosphoric acid solutions usually moderate voltages in the range of 40 V to 60 V and high voltages up to 195 V are applied, respectively. It is useful to mention that pH value of the electrolyte determines also the final pore

diameter so that the lower pH (high acidity) solution together with lower voltages, the smaller pore will be and vice versa. Once the permitted voltage for given solution type is exceeded, the breakdown of the system occurs accompanied by excessively high current densities (~A/cm$^2$). Then, the irreversible damage of the porous structure as well as aluminium substrate in the form of locally burned areas and spots is expected. Generally, for most anodizing electrolytes, relationships between current density and bulk electrolyte pH exist, delineating porous and barrier film growth as shown in Figure 9.

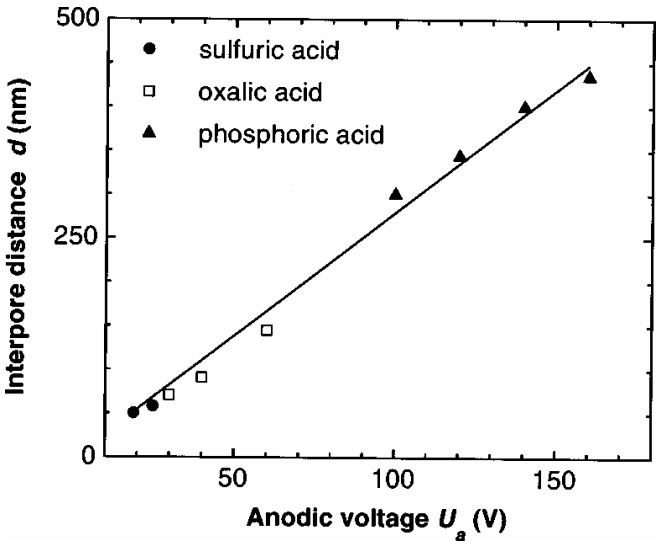


**Figure 8.** Linear relationship between the interpore distance and applied voltage for three common acids.

The temperature stability during the anodization can be provided by vigorous stirring of the electrolyte with external unit for temperature control. If the reaction heat produced at pore bottoms can not be dispersed, then locally enhanced temperature could accelerate either chemical dissolution or oxide formation. A large local heating due to Joule heating and local oxide dissolution could also rise the temperature accompanied by a large thermal stress in the barrier layer and o/a interface. This can lead to generation of cracks and bursts within the pore structure and in the worst case the breakdown of the system can occurred. Notice that Joule heating, due to electrical power dissipation within the high-resistance barrier oxide layer, is much larger than the exothermicity of

UNIVERSITAT ROVIRA I VIRGILI
DEVELOPMENT OF TECHNOLOGY AND APPLICATIONS BASED ON POROUS ALUMINA NANOSTRUCTURES
Lukas Vojkuvka
DL: T-1536-2009/ISBN: 978-84-692-4555-2


the chemical reactions. In addition, the growth speed of porous alumina oxide is also affected by the temperature fluctuation. Figure 10 shows the current density dependence on the temperature. It is known that with the increasing temperature, the higher current density will accelerate the speed of pore growth [12].

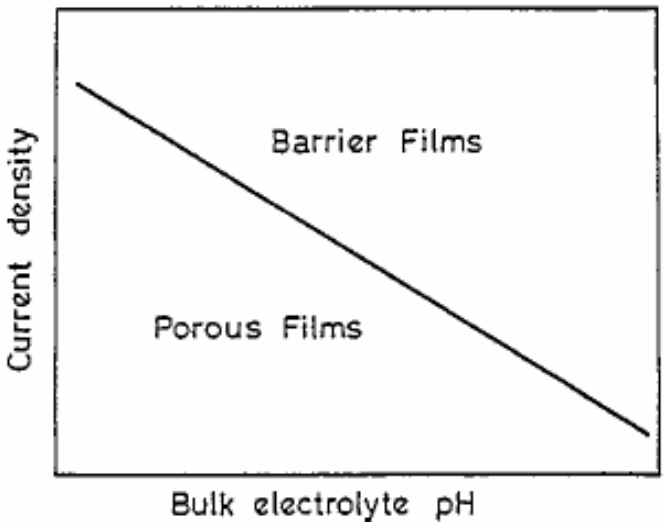


**Figure 9.** Current density dependence on the pH of electrolyte forming either barrier-type or porous type alumina films [6].

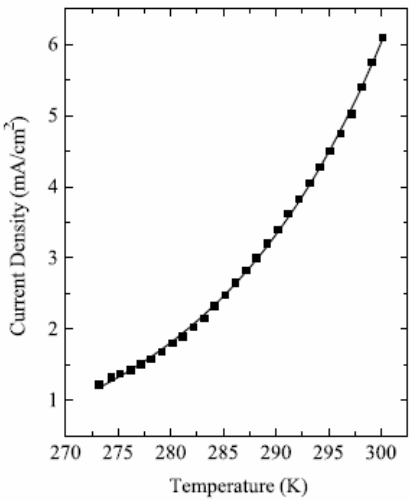


**Figure 10.** Effect of temperature on the current density during anodizing.

DL: T-1536-2009/ISBN: 978-84-692-4555-2

Another necessary condition for the formation of ordered pore arrays is the annealing of the aluminium foils prior to anodizing in order to enhance the grain size and remove the mechanical stress in the metal substrate and. The self-ordering process in the non-annealed Al substrates can be disturbed by a large number of grain boundaries [14, 20].

Since the well-ordered PAA structure can be obtained only when the pores start to grow from very a smooth and clean aluminium surface, the electrochemical polishing is necessary before anodizing. The high surface roughness leads to a local faster formation of barrier oxide and pores develop at different rates leading to suppression the self-ordering process. The non-polished aluminium surfaces are characterized by high roughness of several microns, mainly due to the parallel trenches, which arose during the industrial rolling of the aluminium foils. Usually, to successful polishing of rough surfaces, it is necessary to dissolve preferentially the protuberant parts on the metal surface profile. This can be achieved by applying of sufficiently high current densities (~few hundreds $mA/cm^2$) and specific mixture of electrolyte (in this case ethanol solution of perchloric acid).

UNIVERSITAT ROVIRA I VIRGILI
DEVELOPMENT OF TECHNOLOGY AND APPLICATIONS BASED ON POROUS ALUMINA NANOSTRUCTURES
Lukas Vojkuvka
DL: T-1536-2009/ISBN: 978-84-692-4555-2


## 1.2

## Extraordinary Porous Anodic Alumina: Fabrication and Applications

### 1.2.1 Anodization of Pre-patterned Aluminium

In the case of the self-ordered porous anodic alumina (PAA), the pores are closed to the defect-free groups called domains. The borders of these domains are defined by the dislocations in the crystalline lattice and the usual area of such domain is several microns. PAA has then a kind of poly-domain structure which is a certain limitation from the application viewpoint. To overcome this problem, several methods have been developed by different groups in order to produce long-range ordered mono-domain porous anodic alumina (MPAA). One possibility is pre-patterning of aluminium (Al) substrate prior to anodizing. The goal is to create a perfectly ordered pattern of indentations over the aluminium surface. Similarly to 2 step anodization process, when the textured aluminium is anodized in the second step, the pores nucleate and grow from the indented sites at the initial stage of anodization. The resume of the most common techniques for obtaining an ideally ordered MPAA from the patterned Al will be given in the following section. Most of the mentioned techniques are summarized together with the brief experimental details and basic results in Table I in the Appendix.

The primary idea for fabrication of a MPAA using pre-patterning of Al was proposed by Masuda et al. [32] only two years after the discovery of 2 step anodization in 1995 [9]. They have used conventional electron beam (EB) lithography to fabricate SiC mould with pattern of hexagonally ordered dots on the surface. The usual dimension of SiC mould was 5 x 5 mm with 3 x 3 mm of patterned area. The indentation of aluminium was done by a pressing of mould to the polished metal surface (approximately 5 tons/cm$^2$). The anodization of textured Al was carried out under appropriate conditions and the applied voltage $U_a$ was calculated from the relation $D_{int} = 2.5 \cdot U_a$ established by Keller et al. [2]: The interpore distance $D_{int}$ corresponds to the lattice constant of the dot pattern on the master SiC mould. In the particular case of Masuda and Asoh, they have produced MPAA with $D_{int}$ = 100 – 200 nm and aspect ratio (AR = pore depth/pore diameter) of 150 – 500 using oxalic acid ($(COOH)_2$) [33-35]. Moreover, they also reported on triangular and square cell shape [36, 37] and

DL: T-1536-2009/ISBN: 978-84-692-4555-2

self-healing effect [38] of the PAA using specific master mould intentionally created dot-free areas. Very recently, Nishio et al. have produced MPAA with large surface area (2.5 $cm^2$), $D_{int}$ = 100 nm and AR ~ 20 using direct deposition of Al onto Ni mould [39].

Later on, Choi et al. have developed a novel imprint stamp using structured Si wafer with $Si_3N_4$ pyramids [40, 41]. Due to the pyramidal shape, the pressure necessary for indentation of Al substrate was much lower (50 times) than that of Masuda used in his work. They have fabricated large-area MPAA with $D_{int}$ = 500 nm and AR ~ 800 using imprinting process with pyramidal stamp. Based on the self-healing effect reported by Masuda [38] and choosing the correct applied voltage, they were able to reduce $D_{int}$ to 300 nm which is 60% of the lattice constant of the master stamp. As they finally concluded, only three imprinted points are sufficient to guide a new pore in the centre. In the same group, Lee et al. have proposed two inexpensive approaches for pre-patterning of Al using Ni imprint stamp with triangular as well as square lattice. In comparison with SiC and $Si_3N_4$ stamps, the Ni one requires less fabrication steps and during the use, any cracks on the stamp were observed, thus allowing multiple uses [42]. Also Yasui et al. have used electro-planting for preparation of Ni stamp for fabrication of ideally ordered MPAA with $D_{int}$ less than 50 nm [43].

Instead of costly SiC mould or imprint stamps, Mikulskas et al. used commercially available optical diffraction grating with groove distance of 833 nm [44]. The texturing of Al substrate was formed by a mechanical impressing of grating in the first step and then rotating the same grating by 60 º in the second impress. The rhomb-like indentations with periodicity of 962 nm were obtained on the aluminium surface. The proper anodizing voltage was just adjusted on purpose only for the half of the indentation periodicity. Finally as expected, the resulting MPAA had $D_{int}$ = 480 nm and AR ~ 100. However, this quite simple technique has also a certain limitation related to the commercial availability of the optical gratings with fixed groove dimensions.

The different approach of patterning of Al surface without master stamp is direct writing on the substrate using advanced lithographic techniques. In 2000, Li et al. have fabricated a mono-domain pore array with $D_{int}$ = 200 nm and AR ~ 500 based on conventional EB lithography [29]. Liu et al. have found the appropriate conditions of focus-ion-beam (FIB) lithography for the preparation

of ordered MPAA with $D_{int}$ = 100 nm and AR ~ 100 [45, 46]. The ordered MPAA with $D_{int}$ = 300 - 400 nm and AR ~ 1, grown on a thin Al film deposited onto the holographically patterned Si substrate, was presented by Sun et al in 2002 [47]. The advantage of this technique compared to EB and FIB lithography is large patterned area (~$cm^2$ or grater) and easy on-chip integration. Recently, Krishnan et al. have showed the fabrication of three-dimensional (3D) MPAA structures named nanofunnels [48]. They have directly patterned the deposited Al film using interference lithography followed by the two anodization processes using different electrolytes but the same applied voltage. The PAA nanofunnels with $D_{int}$ = 200 nm, variable pore diameter ($d_p$) of 85 nm and 55 nm and AR ~ 50 were achieved. Although all the mentioned approaches for MPAA based on the lithographic techniques has a very high accuracy and reproducibility, they are time-consuming and more expensive compared to imprinting techniques.

Relatively new, non-lithographic and cost-effective technique for nano-patterning of Al substrate is imprinting by nanoparticle arrays. In 2004, Fournier-Bidoz et al. have introduced the imprinting technique based on pressing (10 ton/ $cm^2$) of colloidal nanosphere layers on the aluminium films [49]. The large MPAA with broad $D_{int}$ = 150 – 500 nm but low AR have been successfully obtained by this technique. Two years later, Matsui et al. have produced the MPAA with extremely small interpore distance ($D_{int}$ = 13 nm) using anodization under voltage as low as 3 V. The MPAA structures have been grown from thick (6 μm) Al film deposited onto a template of $Fe_2O_3$ nanoparticle arrays [50]. The colloidal crystal templating and subsequent anodization have also used Asoh et al. in order to produce 2D/3D composite PAA structures [51]. First, the polystyrene (PS) beads were templated on the Al surface followed by anodization in neutral solution in order to create 3D porous structure. Afterwards, the traditional anodizing conditions were used to form PAA underneath.

The selection of the fundamental results adopted form the mentioned reports can be found in the summary tables placed at the appendix section (Table I-a, b, c).

DL: T-1536-2009/ISBN: 978-84-692-4555-2

### 1.2.2 Novel Anodization Techniques: New Self-ordering Regimes

*Hard anodization of Al*

It is state-of-the-art, that PAA with fixed geometrical properties formed during self-organized process can only be prepared within narrow processing conditions. Since 1995 when Masuda and Fukuda have discovered 2 step anodization [9], many efforts have been done in order to find different approaches for production of extraordinary self-ordered PAA with novel structural properties. One of such a new approach so-called hard anodization (HA) was introduced by Lee et al. few years ago [52]. Originally, this process was invented in early 1960s [53] in the industry field for surface finishing of aluminium. Lee et al. have also adopted this process to research level in the terms of a novel oxalic-acid-based anodization for preparation of PAA with new dimensions and properties. Based on this HA process, a new self-ordering regime with so far unexplored interpore distances was established. Compared to the conventional PAA, the hard anodized PAA structures have: i) very fast nonlinear film growth rate (50-70 μm/h), lower porosity (~3%) and larger interpore distance ($D_{int}$ = 220 – 300 nm). In addition, Lee et al. have prepared long-range ordered MPAA membranes with modulated pore diameters using imprinting technique followed by multi-step anodization process with alternative conventional or HA conditions [52].

The Lee's idea was later extended by the study focused on the HA of aluminium in the sulphuric acid presented by Schwirn et al. [54]. Once again, the self-ordered thick PAA with novel interpore distances $D_{int}$ = 70 – 140 V were achieved in this work. Recently, Lee et al. have completed the topic of HA with ultimate publication dedicated to structural engineering of PAA by means of novel fabrication approach termed pulsed anodization [55]. They were able to produce a new type of PAA with periodically modulated pore diameter by applying a proper voltage profile that consists of a sequence of long low-voltage pulses and short HA pulses. Two-step HA in sulphuric acid mixture was already reported by Li et al. giving the detailed view on the pore distribution during the anodizing process [56].

*High-voltage anodization at critical conditions*

Except for the Al pre-patterning methods, highly ordered PAA is suggested to be obtained in three common types of electrolytes at specific self-

ordering voltages: sulphuric acid at 25 V, oxalic acid at 40 V and phosphoric acid at 195 V, giving interpore distances of $D_{int}$ = 63 nm, 100 nm and 500 nm, respectively. To expand the application field of PAA, the fabrication of porous alumina with arbitrary interpore distances is highly required. Various approaches have been proposed to broaden the geometrical properties of novel PAA and among others the following points were considered as key factors: i) electrolyte conditions such as type, ii) concentration and temperature, iii) high anodizing voltages and current densities.

There is a strong relationship between the applied voltage and interpore distance, but once the applied voltage exceeds a certain maximum that is closely related to the electrolyte type, it will lead to the extremely high current flow followed by electrical breakdown so-called burning phenomena. This extreme case is accompanied by a high heat emission, large gas evolution and cracking of the oxide structure due to the excessive mechanical stress. Ono et al. have found that the self-ordering of the pores in PAA can be obtained at appropriate electrolyte conditions and maximum voltage required to sufficient high current density while preventing the burning phenomena [57-59]. They suggested that the condition for PAA film growth under high electric field is the key factor for the self-ordering effect. Based on these findings, they have successfully produced PAA with new interpore distances of $D_{int}$ = 300, 500 and 600 nm obtained in low-acidity organic electrolytes such as malonic, tartaric and citric acid. A detailed study about self-ordering behaviour of PAA in malonic acid was presented by Lee el al. [60]. Similar to Ono`s suggestions, the main conclusion was that the key factor of self-ordering is sufficiently high current density during anodization.

Recently, Katsuta et al. have obtained PAA with extra-large cell (1 μm) on the Al/glass substrate anodized in citric acid at 420 V [61]. In the same work, they also reported on fabrication of double-layer PAA structure with two cell sizes of 340 nm and 640 nm produced separately in two steps using phosphoric and citric acid. The PAA with interpore distance $D_{int}$ = 73 nm produced in 1:1 mixture of $H_2SO_4$ : $(COOH)_2$ at 36 V was reported by Shingubara et al. [23]. The extensive report on anodizing at critical-high potentials in various inorganic as well as organic acids was published by Chu et al. [62, 63]. The produced PAA have arbitrary interpore distance ranging form 130 nm to 980 nm anodized at potentials from 8 V to 450 V depending on the electrolyte. In contrary to the

DL: T-1536-2009/ISBN: 978-84-692-4555-2

common two step anodization, this high field anodization approach is performed in a single step.

The PAA with extra short interpore distance less than 30 nm was recently reported by Masuda et al. [64, 65]. The key of this process lies in a modified two step anodization with the use of highly concentrated electrolyte at high temperature in the first step, and after oxide removal, the second step is performed with low concentration and temperature. An interesting approach based on the stable high-field anodization was proposed by Li et al. [66-68]. They added ethanol in the electrolyte in order to avoid burning phenomena due to the heat evolution during high voltage anodization. The mixture ethanol/acid/water permits to lower the temperature down to – 10 ºC. The fast production (4 - 10 μm/min) of PAA with $D_{int}$ = 70 - 140 nm and 225 - 450 nm was successfully achieved.

The selection of the fundamental results adopted form the mentioned reports can be found in the summary tables placed at the appendix section (Table II-a, b, c).

### 1.2.3 Miscellaneous and Complex-shaped Porous Alumina

*Horizontal alumina*

The ordered PAA as a template grown on the Si substrate have been successfully used for fabrication of several nanoelectronic devices such as data storage [69-71], field emitters [72, 73] or sensors [74]. However, it is still difficult to utilize PAA in the application fields which require main-stream planar processing technology. It is due to the vertical direction of the pore growth in two dimensions (2D) on the substrate. Therefore, also one-dimensional (1D) PAA arrays horizontally aligned on a substrate would be highly desirable to broaden application possibilities for instance in electro-mechanical systems.

The initial work on this topic was given by Chen et al. in 2005 [75]. Their simple theoretical model of 1D formation mechanism corresponds to the experimental results from modified 2 step anodization of sandwich $SiO_2$/Al/$SiO_2$/Si structure. Finally, a well-ordered 1D PAA array was obtained when the anodized Al thickness approaches a size of a single pore cell. The fabrication of microstructured horizontal PAA for multi- and single- nanowire

devices was demonstrated by Xiang et al. [76]. The finger PAA arrays in the $SiO_2$/Al/$SiO_2$/Si structure were prepared with diverse interpore distances $D_{int}$ = 10 – 130 nm and 30 – 275 nm using various anodizing parameters. Due to the anisotropy of the system, the change from hexagonal to quadratic pore arrangement was observed with increasing interpore distance. A similar work was performed by Gowtham et al. resulting in confined PAA horizontally ordered in the single row up to 30 rows with $D_{int}$ = 50 – 200 nm [77].

*Anodization of complex-shaped Al substrates*

Generally, the PAA is grown on planar Al surface in the form of foil or thin film deposited on the Si substrate. Nowadays, it is needed to control the production of PAA on more complex-shaped substrates for further advance in the nanotechnology fields, especially nanosynthesis of materials. Zakeri et al. have shown synthesis and characterization of nonlinear PAA anodized from various geometric (rectangular, cylindrical or square) Al substrates [78]. The pores tend to curve, merge and branch during the film growth due to the stress produced on the substrate edges. They also proposed a simple model that predicts the shape and orientation of nonlinear pores grow on non-planar substrates. Recently, Sanz et al. have presented fabrication and functionalization of cylindrical PAA anodized from Al wire [79].

*Branched PAA*

It is well-known that the constant applied voltage is an essential parameter to obtain a uniform pore distribution in the PAA. Once the voltage is reduced during the anodizing, the pores starts to branch in different directions. Based on this branching effect, in 1999 Li et al. have already synthesized Y-shaped carbon nanotubes by applying the voltage reduction by a factor of 0.71 [80]. More recent work of Wang et al. has shown the preparation of netlike meso-porous PAA membranes with a saw-like voltage profile during anodization [81, 82]. The following chemical etching of PAA caused the interconnections of neighbouring pores in the different levels along the pore. Finally, the resultant structure showed out interesting optical properties useful in photonic crystals. A different approach based on non-steady-state anodizing conditions by means of exponentially stepping down the applied voltage was proposed by Cheng et al [83]. The produced PAA named tree-like alumina was then employed as a template for synthesis of gold nanotrees. Last but not least it is worth to mention very recent report on fabrication of multi-tiered 3D PAA

DL: T-1536-2009/ISBN: 978-84-692-4555-2

presented by Ho et al. [84]. The tiered PAA structure was realized in various steps by sequentially stepping down the applied potential while etching of the barrier layer at the pore bottom is performed after each step.

*Stepped and coned pores in PAA*

A simple way how to modulate pore diameter in PAA is the combination of multi-step anodization with pore widening process (wet etching in diluted $H_3PO_4$). The idea is to widen the pore diameter after each anodizing step. Lee et al. [85] and Im et al. [86] have similarly synthesized complex-shaped carbon nanotubes from PAA template with stepped pores. The coned pore shape produced by a repetition of very short (seconds) anodizing steps followed by pore widening were concurrently reported by Yanagishita et al. [87, 88] and lately by Nagaura and Yamauchi et al. [89-91]. Although this modulation technique is very suitable for nano-structuring of various materials such polymers, metals or semiconductors, the multi-step approach makes it rather time-consuming and in addition, only modulated PAA with very low aspect ratio (AR ~ 1-5) can be obtained.

*Miscellaneous PAA*

A novel PAA structure with a six-member ring symmetry co-exiting with usual hexagonal ordering was recently reported by Zhao et al. [92]. They have implemented constant current method over the entire anodizing period with consecutive etching step. These PAA with ring ordering has particular application potential in the mosaic nanowire arrays. Tip-like anodic alumina with array of ordered nanotips on the top surface was fabricated by Sun et al [93]. This one step electrochemical approach consists of anodization at 180 V in a mixture of various acids at room temperature. The highly dense and ordered arrays of nanoscaled tips are promising material for sensors. The porous alumina with ultra thick barrier layer on the bottom was grown in the ethylene glycol solutions under specific anodizing conditions such as galvanostatic anodization and high electrolyte temperatures [94]. The pore ordering degree of produced alumina is rather poor, but the barrier layer as thick as 0.5 μm is a promising material for electrolytic capacitors.

The selection of the fundamental results adopted form the mentioned reports can be found in the summary tables placed at the appendix section (Table III-a, b, c).

## 1.3

## Summary

This chapter presents a general overview of self-ordered porous alumina starting with some basic concepts of aluminium anodizing. It is generally accepted that pores are self-organized in the triangular lattice only if specific anodizing parameters—so called self-ordering regimes—are maintained throughout the anodization process. Several mechanisms have been suggested to explain the self-organizing phenomenon: i) cracking and self-healing of the oxide layer; ii) local corrosion at the pore bottoms; or iii) mechanical stress. However, there is still no clear evidence of the real origin of the self-organized formation of pores. Since 1995, three major types of self-ordered porous alumina with ideally formed pore distribution have been reported based on two step anodization. Besides these well-known porous alumina structures, a great deal of research and development has recently focused on fabricating novel alumina structures. In particular, anodizing techniques based on aluminium pre-patterning enable perfectly ordered porous alumina with large areas to be fabricated. The studies on novel anodizing approaches are summarized in the tables in the Appendix.

UNIVERSITAT ROVIRA I VIRGILI
DEVELOPMENT OF TECHNOLOGY AND APPLICATIONS BASED ON POROUS ALUMINA NANOSTRUCTURES
Lukas Vojkuvka
DL: T-1536-2009/ISBN: 978-84-692-4555-2

# 2

# Porous Alumina Fabrication

UNIVERSITAT ROVIRA I VIRGILI
DEVELOPMENT OF TECHNOLOGY AND APPLICATIONS BASED ON POROUS ALUMINA NANOSTRUCTURES
Lukas Vojkuvka
DL: T-1536-2009/ISBN: 978-84-692-4555-2

# *Chapter 2*

This chapter describes the experimental preparation of self-ordered porous alumina using two-step anodization. First, a detailed description is given of the laboratory setup with a specially designed anodizing cell that is used for the electrochemical etching of aluminium. The impact of annealing and electropolishing on the aluminium substrate is studied. Much of the chapter is devoted to describing two-step anodization and making a detailed morphological examination of the porous alumina samples prepared. The model of pore formation based on current characteristics is proposed. Finally an overview of the techniques for detaching porous alumina film from the aluminium substrate is given.

## 2.1

## Experimental Setup

Basically, two types of experimental setup designed for the anodization of aluminium foils were developed and tested in this work. The utility and main features of the first preliminary system with individual anodizing device and the second more advanced system for anodizing will be described and compared in the following section.

### 2.1.1 Preliminary Anodizing Setup

Figure 11(a) illustrates a simple schematic of the first experimental setup that consists of a computer-controlled power supply for constant voltage or constant current, i.e. potenciostatic and galvanostatic modes, an anodizing cell, a stirrer and a cooling machine. The electronic control unit is directly connected to the anodizing cell shown in the Figure 11(b). The anode device (3) with fixed sample (inset of Figure 11(b)) is immersed into the coolant double-wall cell (2) filled with the electrolyte. The cell makes a part of external temperature-controlled circuit provided by powerful cooling machine (Landa). The continuous stirring of the electrolyte is ensured by a magnetic stirrer (4) placed just below the anodizing cell. During the process, the actual current or voltage values are simultaneously recorded to PC via the same power supply. Although various porous alumina samples were produced using this experimental setup, several problems such as electrolyte leakage to the anode device, temperature instability and non-uniform electrolyte flow over the sample surface were encountered.

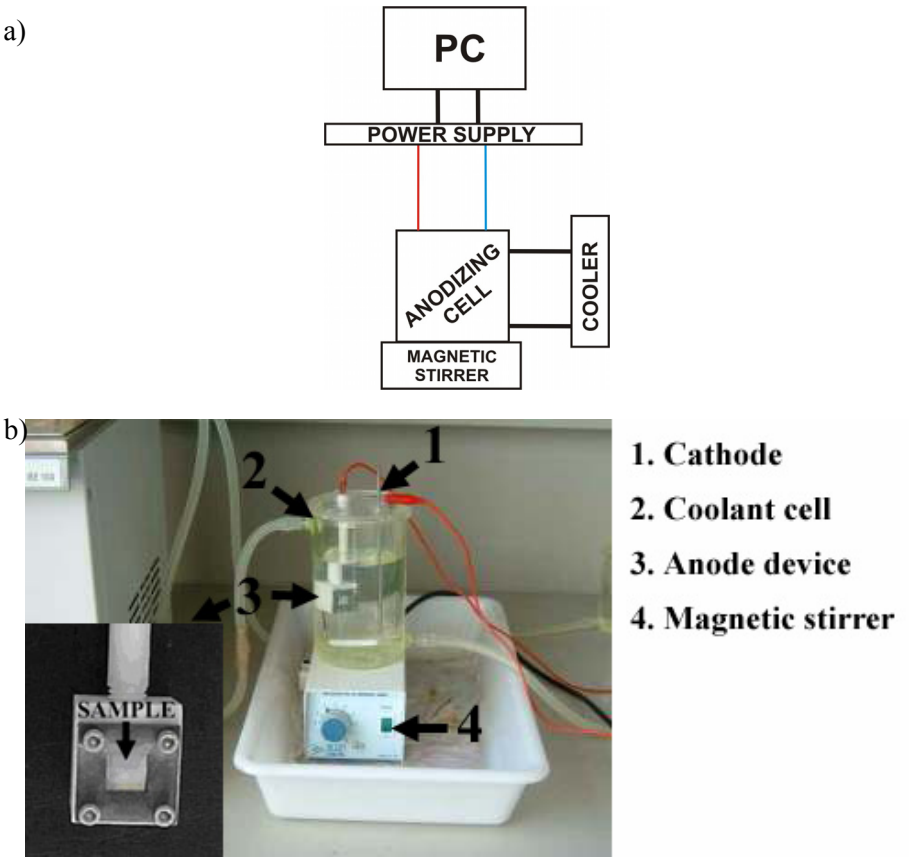


**Figure 11.** a) Scheme of the complete preliminary setup for anodizing and b) detailed photograph of anodizing cell with anode.

### 2.1.2 Improved Setup with all-in-one Anodizing Cell

In order to dispose of the faced difficulties of the preliminary setup, an improved setup for anodizing was designed. In the Figure 12(a) is a schematic of the newly developed anodizing system with several substantial modifications. First upgrade is noticeable in the electronic part, where two multimeter units for measuring the actual value of current and voltage variables were implemented. Also the anodizing system passed through a general modification. Basically, the novel electrochemical cell illustrated in Figure 12(b) has two main parts. First one is the plastic cell cover (5) that has several implemented subparts such as Teflon propeller driven by a motor (1) to provide the electrolyte stirring, a platinum wire wounded to a Teflon bar which serves as

a cathode (2), coolant stainless coil ensuring the internal temperature control of electrolyte (3) and a metal probe for in-situ temperature monitoring (4). The bottom part of the anodizing cell is a cylindrical Teflon tank (6) with the sample holder at the bottom. The tank is screwed down to the copper plate (7) and in this way the sample is always sealed with O-ring between the tank and plate. The complete cell stands on the Peltier coolant plate which makes a refrigerating circuit together with stainless coil.

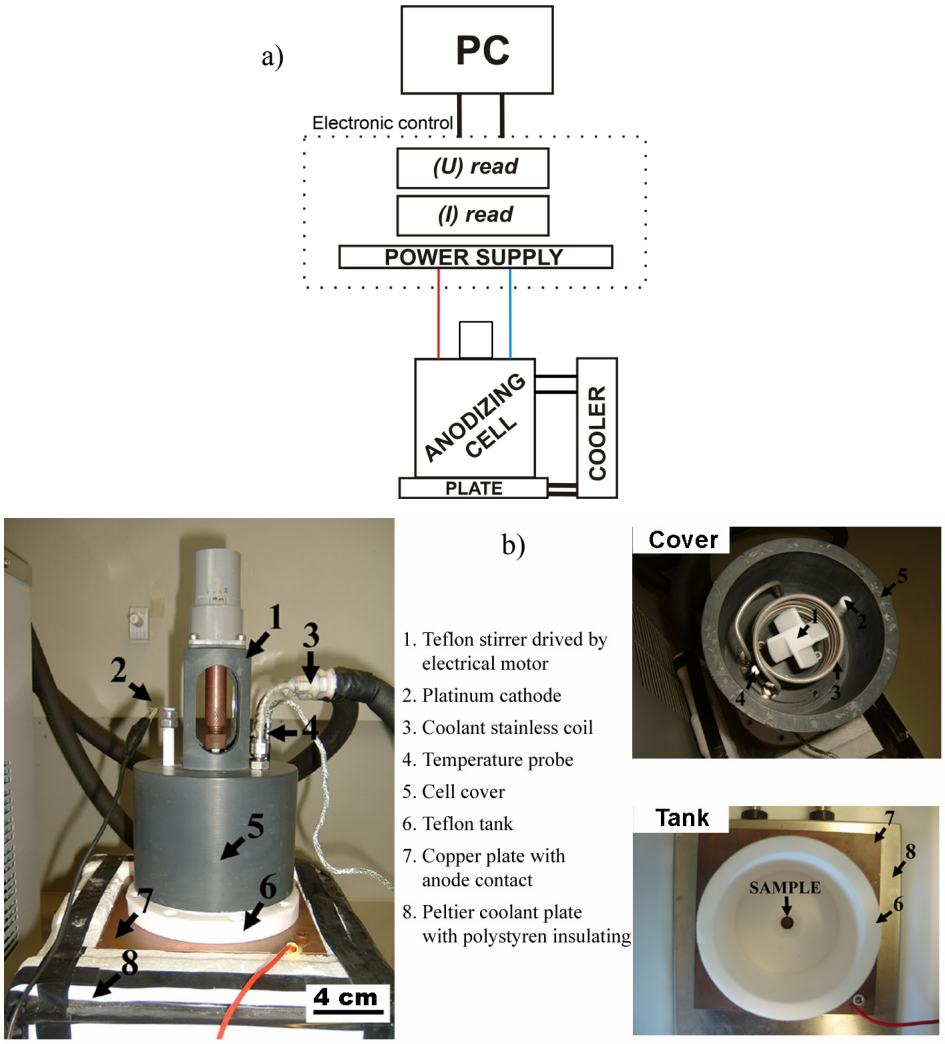


**Figure 12.** a) Scheme of the improved experimental setup and b) described photographs of the anodizing cell with elements for temperature and stirring control.

The experimental trials performed on the new anodizing system revealed many advantages in comparison with the preliminary system. Firstly, both of the current and voltage variables can be precisely read with the multimeters employed in the electronic part of the new system. Secondly, the temperature control and uniform electrical contact of the sample is provided by a large copper plate. The actual electrolyte temperature given by the coolant coil is directly monitored using a Pt probe during the anodizing process. Next advantage is more effective stirring of the electrolyte provided by the horizontal position of the sample surface with the propeller head closely placed just above the sample. Finally, the important point is the tight O-ring sealing on the sample that effectively avoids the electrolyte leakage. It is also worth to mention, that also a few drawbacks of the second anodizing setup should be remarked: i) impossible visual observation of the sample state during the anodizing process and ii) the robustness of the electrochemical cell which can cause handling difficulties during the inter-operations.

UNIVERSITAT ROVIRA I VIRGILI
DEVELOPMENT OF TECHNOLOGY AND APPLICATIONS BASED ON POROUS ALUMINA NANOSTRUCTURES
Lukas Vojkuvka
DL: T-1536-2009/ISBN: 978-84-692-4555-2

## 2.2

## Preparation of Aluminium Substrates

As stated in the first chapter, the annealing and electro-polishing processes are inherent pre-anodizing treatments of aluminium foils in order to obtain porous alumina with satisfactory geometrical properties. In this section both experimental procedures will be described and the principal results will be discussed with SEM, AFM and XRD analysis.

### 2.2.1 Annealing of As-purchased Al Foils

First, an ultra-pure (99.999 %) Al foils (Goodfellow) with thickness of 250 μm were thoroughly cleaned in the ultrasonic bath with acetone and then rinsed in deionised water. Then, the dried foils were put in the annealing furnace with a nitrogen inlet to avoid the oxidation process at high temperatures. The annealing temperature was controlled by a programmable profile such as shown in Figure 13(a), where the final annealing temperature was usually preset just below the Al melting point ($T_a$ = 660 ºC) in the range of 400 - 500 ºC with slowly increasing initial ramp of 10 ºC/min. Once the heat-treatment was completed, the 5 $cm^2$ foils were equally cut into desired dimensions.

### 2.2.2 Electro-polishing of Annealed Al Foils

The annealed Al sheets were employed as anode in the electro-polishing system with 0.5 l double-wall coolant vessel filled ethanol mixture of perchloric acid (4:1) [14, 20, 21, 28, 29, 95]. The mixture temperature must be kept below 5 ºC and one has to follow working precautions due to the explosiveness of perchloric acid. In order to achieve a good electro-polishing effect on the Al surface, the current density should be over 100 mA/ $cm^2$ during the process [19, 96, 97]. In this work, the applied constant voltage of 20 V turned out to be sufficient for obtaining a proper polishing current. Also a vigorous electrolyte stirring is necessary to remove bubbles and heat formation on the Al surface produced by a high rate of electrochemical reactions. A typical current transient

UNIVERSITAT ROVIRA I VIRGILI
DEVELOPMENT OF TECHNOLOGY AND APPLICATIONS BASED ON POROUS ALUMINA NANOSTRUCTURES
Lukas Vojkuvka
DL: T-1536-2009/ISBN: 978-84-692-4555-2


from the electro-polishing process is illustrated in Figure 13(b) showing a constant behaviour with initial fast slope caused by a reducing of total sample area during the polishing process. Notice, that presented experimental data for the current divided by a complete sample area gives approximately the current density of 130 mA/ $cm^2$. After electro-polishing period of 2 minutes, the Al foils were rinsed in DI water and dried with air flow.

a)

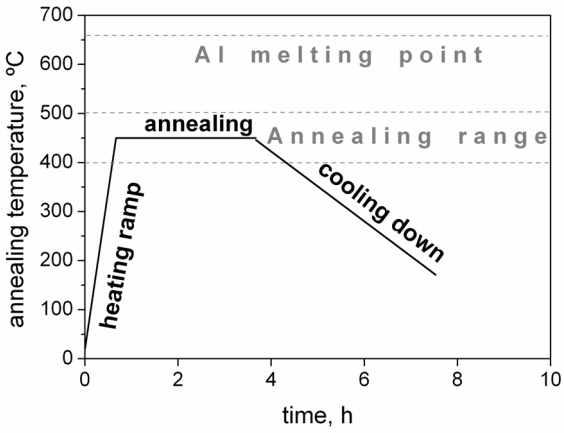


b)

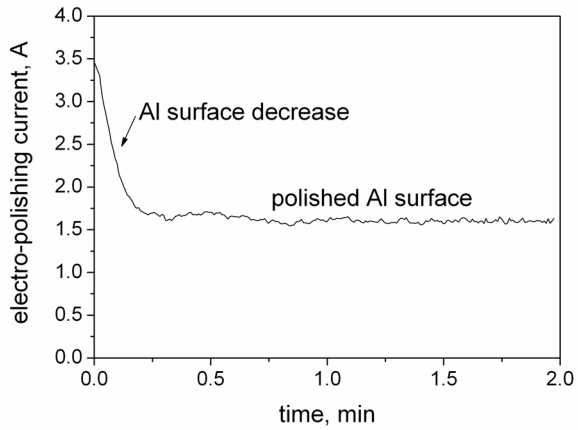


**Figure 13.** a) Temperature profile for annealing process of Al foils and b) typical current transient from electro-polishing of Al sample at constant applied voltage of 20 V.

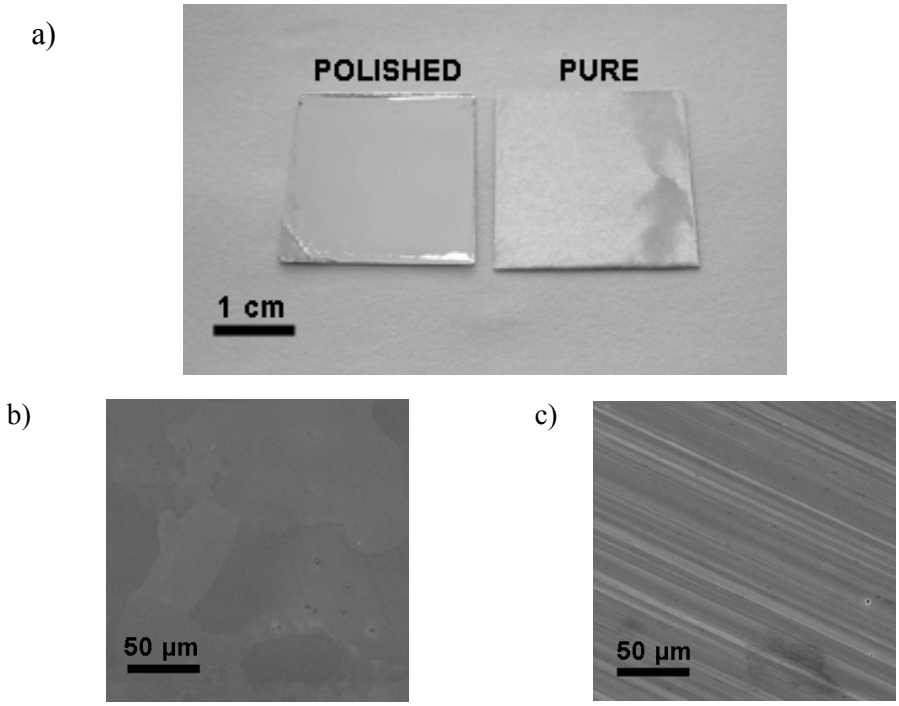


**Figure 14.** a) Digital photograph shows a comparison of polished and pure Al surface and SEM top surface images of the same Al samples b) with and c) without electro-polishing treatment.

The difference between polished and non-treated aluminium foil is shown in Figure 14, where a) represents a photograph taken with a digital camera showing the Al foil with and without electro-polishing treatment. The polished Al has a very bright, mirror-like surface compared to non-treated foil. Also, the scanning electron microscope (SEM) top surface images placed in Figure 14 illustrates b) very smooth polished Al and c) a high roughness observed on non-polished Al with parallel grooves formed probably during the manufacturing process using rolling procedure [14, 20]. Figure 15 compares the surface profiles of polished (solid line) and non-polished (dashed line) Al foil measured by the atomic force microscope (AFM) analysis of approximately 90 $\mu m^2$ (see inserted 3D AFM scans). The Al surface without electro-polishing shows a high roughness with regular sharp corrugations compared to the flattened surface profile of polished foil [21, 28, 29, 97].

UNIVERSITAT ROVIRA I VIRGILI
DEVELOPMENT OF TECHNOLOGY AND APPLICATIONS BASED ON POROUS ALUMINA NANOSTRUCTURES
Lukas Vojkuvka
DL: T-1536-2009/ISBN: 978-84-692-4555-2


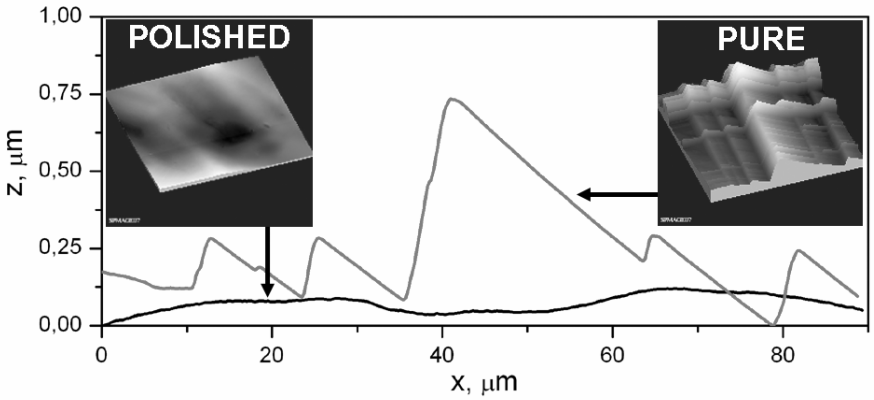


**Figure 15.** AFM topography images of the polished and pure Al sample together with corresponding surface profiles.

The annealing effect on the Al crystalline growth is evident from Figure 16, where are SEM top surface images of two electro-polished samples without (a) and with (b) previous heat treatment. The non-annealed Al metal structure in the Figure 16(a) is formed by many small crystallites with size of few tens of microns whereas the annealed foil consist of several large-area crystals depictured in Figure 16(b). The results revealed the fact that the Al crystallites are significantly enlarged during the high-temperature treatment [20, 21]. These large crystals within the annealed Al after anodization can be clearly seen in Figure 16(c) taken by an optical microscope with polarized filter.

The pole figures with (220) plane from X-ray diffraction analysis representing the crystallographic structure and orientation are shown together with corresponding 3D views in Figure 17. Similarly to previous observation from SEM analysis, the pole figure of the non-annealed Al foil in Figure 17(a) demonstrates four major groups of accumulated diffraction peaks indicating a high number of small crystallites detected in the particular X-ray diffraction analysis. Notice also the tendency of interconnection of the two neighbouring groups caused probably due to forced Al texture as a result of previously mentioned rolling process. In comparison, the pole figure of annealed Al foil in Figure 17(b) is represented only by a few narrow and high peaks corresponding to a low number of large crystallites included the analysed area. Moreover, all the diffraction peaks are also arranged in distinct way confirming that the Al

DL: T-1536-2009/ISBN: 978-84-692-4555-2

texture is somehow modified during the annealing process. Apparently, the high temperature removes the mechanical stress formed within the Al bulk during the rolling process.

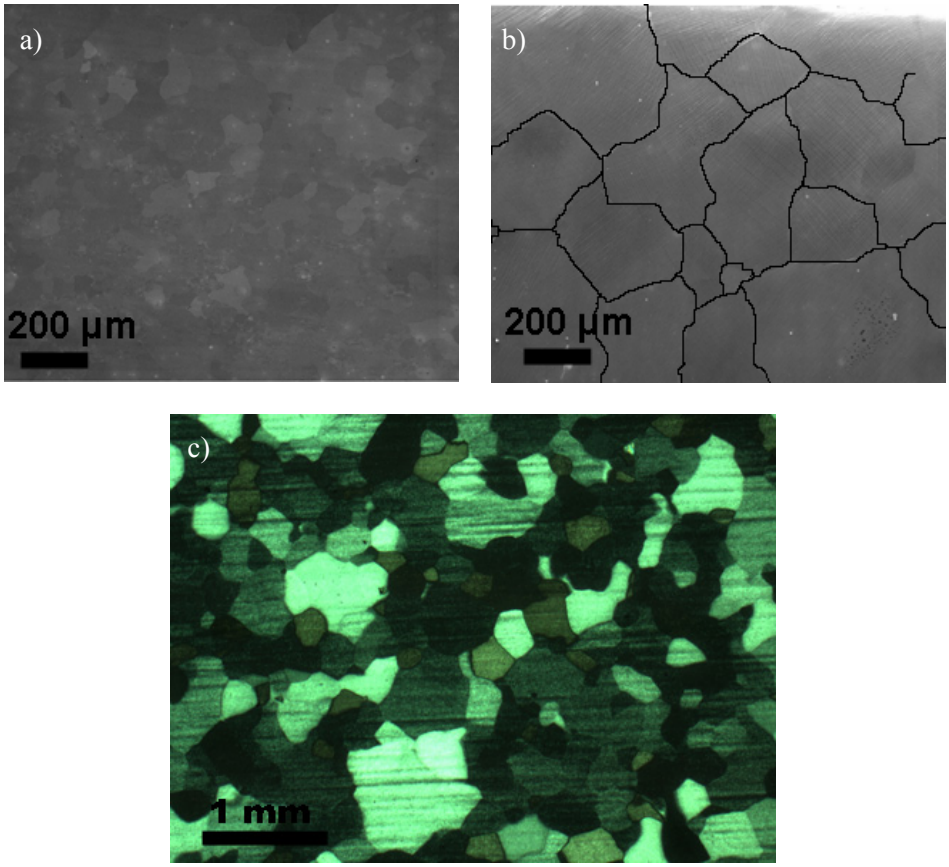


**Figure 16.** a) Top surface images from SEM analysis of electro-polished Al samples a) without and b) with previous annealing treatment, c) top surface image of anodized Al substrate from optical microscope with polarized filter.

UNIVERSITAT ROVIRA I VIRGILI
DEVELOPMENT OF TECHNOLOGY AND APPLICATIONS BASED ON POROUS ALUMINA NANOSTRUCTURES
Lukas Vojkuvka
DL: T-1536-2009/ISBN: 978-84-692-4555-2


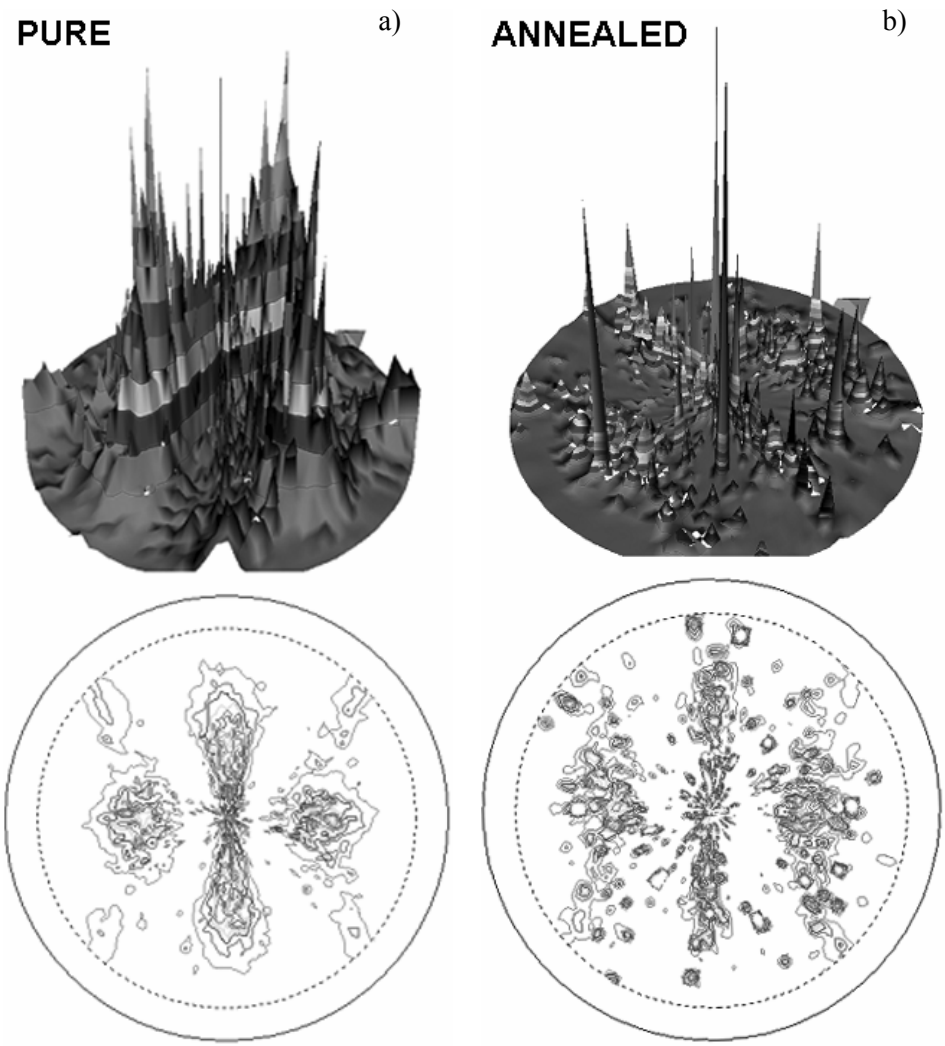


**Figure 17.** Comparison of pole figures (220) from X-ray diffraction analysis of a) pure and b) annealed Al sample.

UNIVERSITAT ROVIRA I VIRGILI
DEVELOPMENT OF TECHNOLOGY AND APPLICATIONS BASED ON POROUS ALUMINA NANOSTRUCTURES
Lukas Vojkuvka
DL: T-1536-2009/ISBN: 978-84-692-4555-2

## 2.3

## Fabrication and Characterization of Porous Alumina

In the following section, the experimental fabrication process and the detailed characterization of porous alumina structures will be described. First part is devoted to a two step anodization process that takes an advantage of self-ordering phenomenon. The second part of this section deals with the analysis of the as-produced samples using SEM, ESEM; FEG-SEM and AFM techniques.

### 2.3.1 Two Step Anodization Process

In 1995, Masuda and Fukuda have reported on a novel technique for aluminium anodization in two steps that is based on naturally occurring phenomenon of pore self-ordering [9]. Since then, the self-ordered nanoporous alumina has attracted a great interest among the scientists all over the world.

In this work, the step-by-step experimental preparation of porous alumina (PA) films based on 2 step anodization is illustrated in Figure 18. Each fabrication step (1-5) is represented by a schematic drawing with attached SEM top surface image from particular result [98-100]. The starting procedures of annealing and electro-polishing of as-purchased Al substrates (1) were already described in the previous section. In the next phase, the ready polished Al samples were mounted in the electrochemical cell that is filled with one of the electrolyte types prepared from sulphuric ($H_2SO_4$), oxalic ($(COOH)_2$) or phosphoric ($H_3PO_4$) acid. The first anodization step (2) was conducted under an appropriate voltage in the potenciostatic mode. The exact value of applied voltage is highly electrolyte-dependent and usually low voltages in the range of 20 – 25 V are used with high conductive 10 wt.% $H_2SO_4$, medium voltages between 40 V and 60 V are applied for 0.3M $(COOH)_2$, high voltages of 160 V – 180 V are used for 0.3M $H_3PO_4$ electrolyte [21]. After the first step, the PA oxide layer grown on the Al surface was removed by a wet chemical etching (3) in a hot mixture (~ 60 - 80 ºC) of 0.4 M phosphoric acid and 0.2 M chromic acid (1:1 volume ratio) [97] [101, 102]. The second anodization step (4) was repeated under the same experimental conditions as they were used in the first step. Finally, if it is

necessary the PA film can be detached (5) from the Al substrate using one of the techniques which will be commented later. The complete fabrication process including all the procedures from (1) to (5) can take between 4 – 12 hours depending particularly on the time-consuming anodizing periods.

### 2.3.2 Disordered Porous Alumina

The preliminary results from the SEM analysis of PA sample after the first anodization step carried out in the oxalic electrolyte at 40V are shown in the Figure 19. The SEM top surface image in Figure 19(a) shows a random ordering of the pores which have very irregular shapes and disordered distribution over the surface. Interestingly, two distinct forms of pore disordering were observed on the PA surface. Figure 19(b) shows a "worm-like" part that has disordered pore distribution compared to parallel form, where the pores seem to be aligned in rows. This is probably due to the different orientations of Al grains observed before on the Al foil with annealing and electro-polishing treatments (see Figure 16) [20, 96]. Figure 19(c) represents the SEM cross-section image of the PA fracture that was detached from the Al substrate. In contrast to the top surface, at the bottom surface of the sample all the pore tips are uniformly covered by so-called barrier layer. It can be noticed that the pore tips have a form of hemispherical shapes uniformly ordered over the bottom surface.

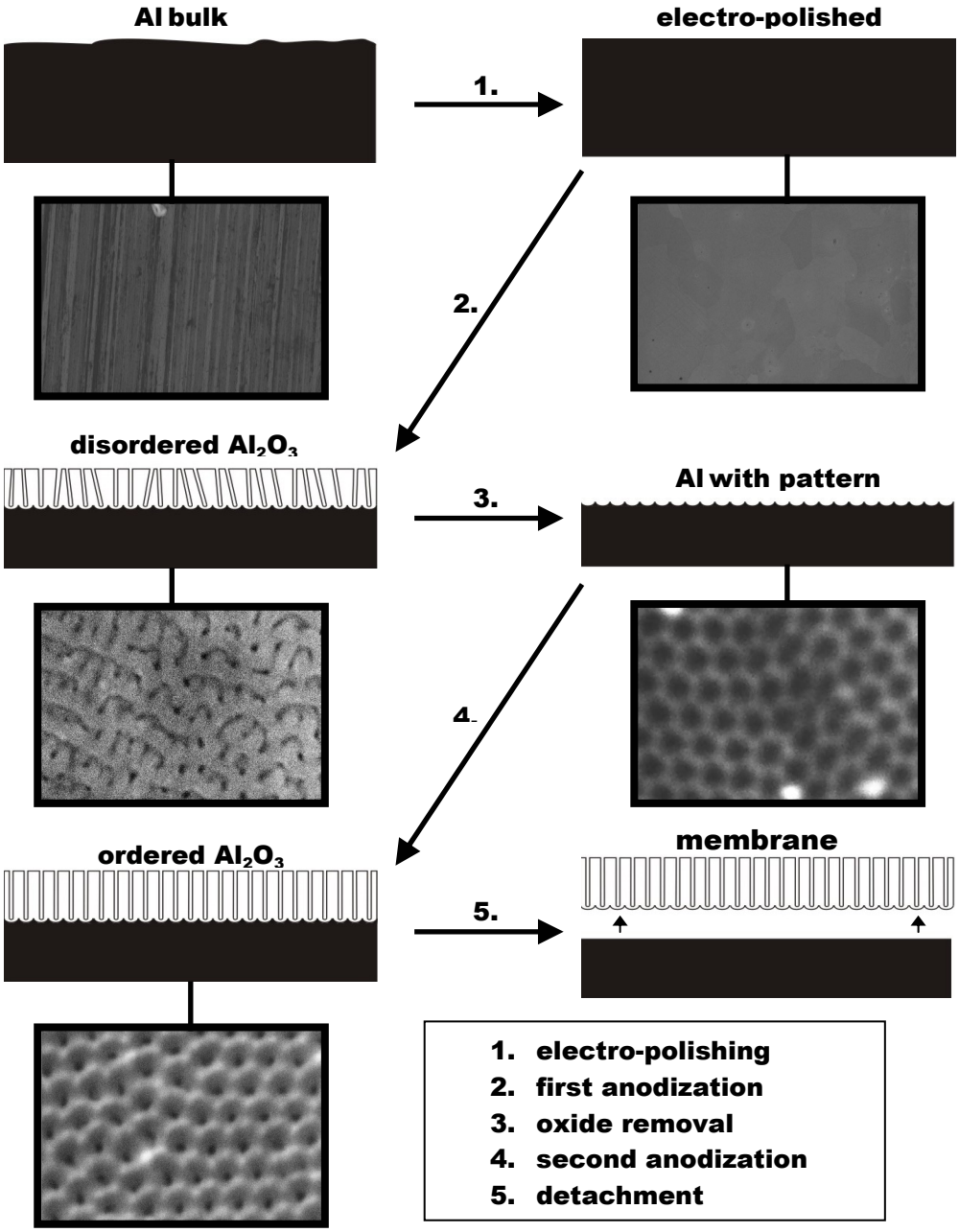


**Figure 18.** Scheme of step-by-step fabrication process of porous alumina based on two step anodization. Each step is represented by a drawing with embed top surface SEM image corresponding to the particular result.

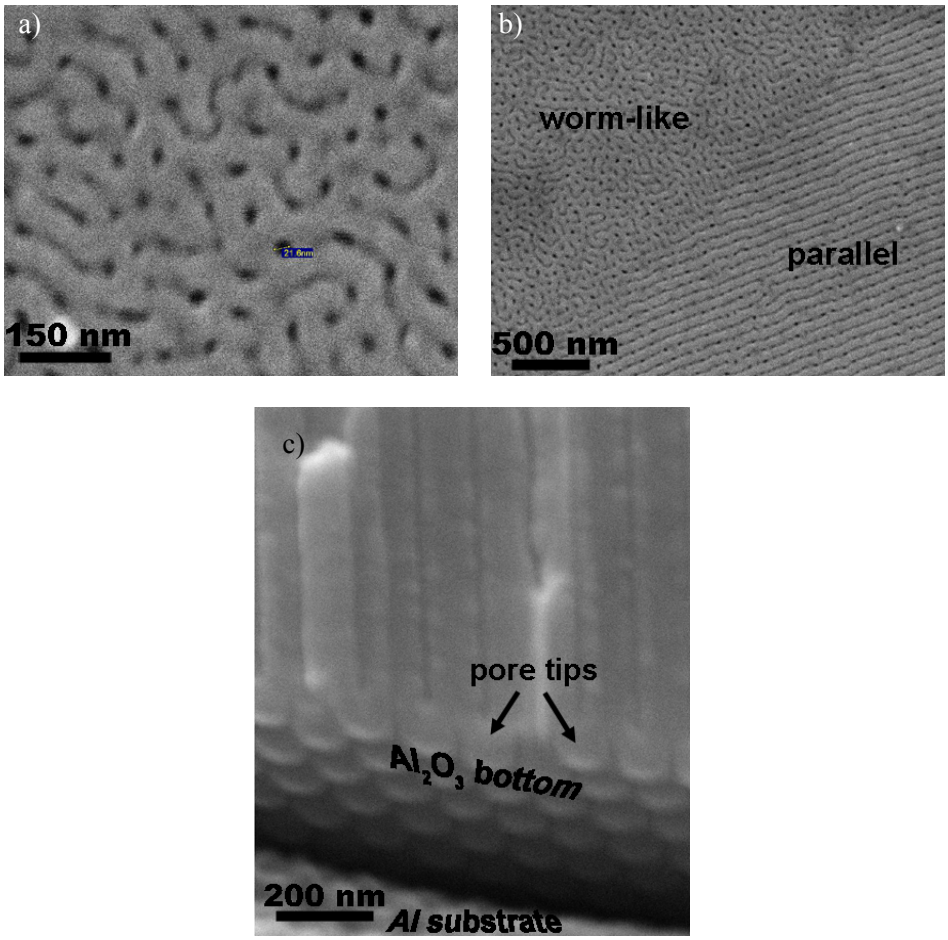


**Figure 19.** a) and b) SEM top surface images of porous alumina sample obtained after first anodizing step in oxalic acid solution, c) cross-section SEM image of the fractured sample.

This ordered arrangement of the pore tips is more evident also from Figure 20, where is a comparison of the SEM images from the top (a) and bottom (b) surface of the PA sample analysed after the first anodization step in the phosphoric electrolyte. The top surface of PA contains the pores randomly distributed over the surface with some big and tiny spots indicating different pore diameter and depth. The smaller pores probably died due to the competition between the neighbouring pores at the initial stage of the anodization process. In contrary, the bottom part of the same PA sample consists of closely packed pore tips which are uniformly ordered in triangular

DL: T-1536-2009/ISBN: 978-84-692-4555-2

lattice. In conclusion, although the pores start to grow in a disordered way at the very beginning of the first anodization, at the end the pore tips are already somehow self-ordered at the bottom part of the oxide [2, 9]. Therefore, after the following oxide removal step, the rounded tips at the bottom leave an imprinted pattern on the Al surface (see Figure 18). This is a key point of the two step process, where the self-ordering phenomenon acts as a kind of "natural" lithography. During the second anodization step the pores directly grow from the pattern sites. As a result, the newly formed PA has a highly ordered distribution of the uniform pores on the top as well as the bottom surface of the oxide film.

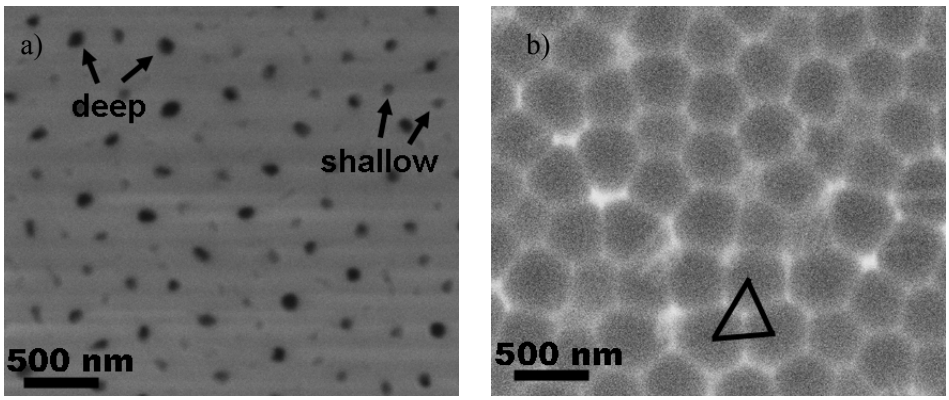


**Figure 20.** ESEM a) top and b) bottom surface images of the porous alumina anodized in one step using phosphoric acid solution.

### 2.3.3 Self-ordered Porous Alumina

In order to describe fundamental features and geometrical properties of the analysed PA structures, the following conception in the Figure 21 was established. The representing PA samples were fabricated using a) oxalic and b) phosphoric electrolytes with applied voltage of 50 V and 160 V, respectively. Figure 21(a) represents ESEM top surface image with a well-ordered matrix of hexagonal cells with central pores. As it is remarked, the interpore distance $D_{int}$ is defined as pore-to-pore length which is equal to cell size, and the pore diameter $d_p$ represents the size of air hole in each cell. Figure 21(b) refers to ESEM cross-sectional image of PA fracture with halved pores. The pore tips at the bottom are covered by a curved oxide layer commonly known as the barrier layer.

UNIVERSITAT ROVIRA I VIRGILI
DEVELOPMENT OF TECHNOLOGY AND APPLICATIONS BASED ON POROUS ALUMINA NANOSTRUCTURES
Lukas Vojkuvka
DL: T-1536-2009/ISBN: 978-84-692-4555-2


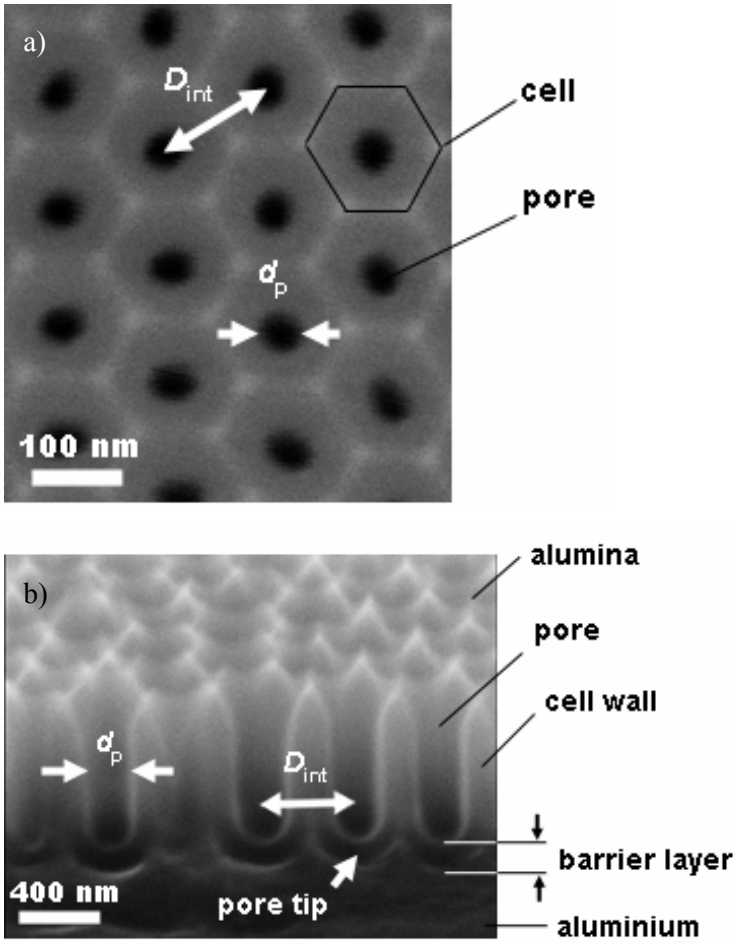


**Figure 21.** Description of morphology denoted for porous alumina using demonstrative a) top surface ESEM image (oxalic acid) and b) cross-section ESEM image (phosphoric acid).

The general overview of the resultant PA structures formed using three major sets of experimental conditions are summarized in the Figure 22: a) first set uses 10 wt.% $H_2SO_4$ as an electrolyte with temperature $T_e$ = 1 ºC and applied voltage $U_a$ = 20 V, b) second set uses 0.3 M oxalic acid at $T_e$ = 17 ºC under $U_a$ = 40 V and c) third set uses 3 wt.% $H_3PO_4$ at $T_e$ = 1 ºC and applied voltage $U_a$ = 170 V. In order to avoid a repetition of the long terms for sample names, the following denotation will be assigned for PA samples prepared in sulphuric (SPA), oxalic (OPA) and phosphoric (PPA) solution. Primary conclusion withdrawn from Figure 22 is that the pore diameter $d_p$ and interpore distance $D_{int}$ significantly

increase for SPA, OPA and PPA samples with corresponding $d_p$ = 20, 30 and 100 nm and $D_{int}$ = 60, 105 and 455 nm. This confirms well-known relationship between $D_{int}$ and applied voltage: $D_{int} = k_p U_a$, where $k_p$ is proportionality constant [2, 4, 29]. A detailed study of all the morphological properties of particular PA structure will be analysed and compared in the following section.

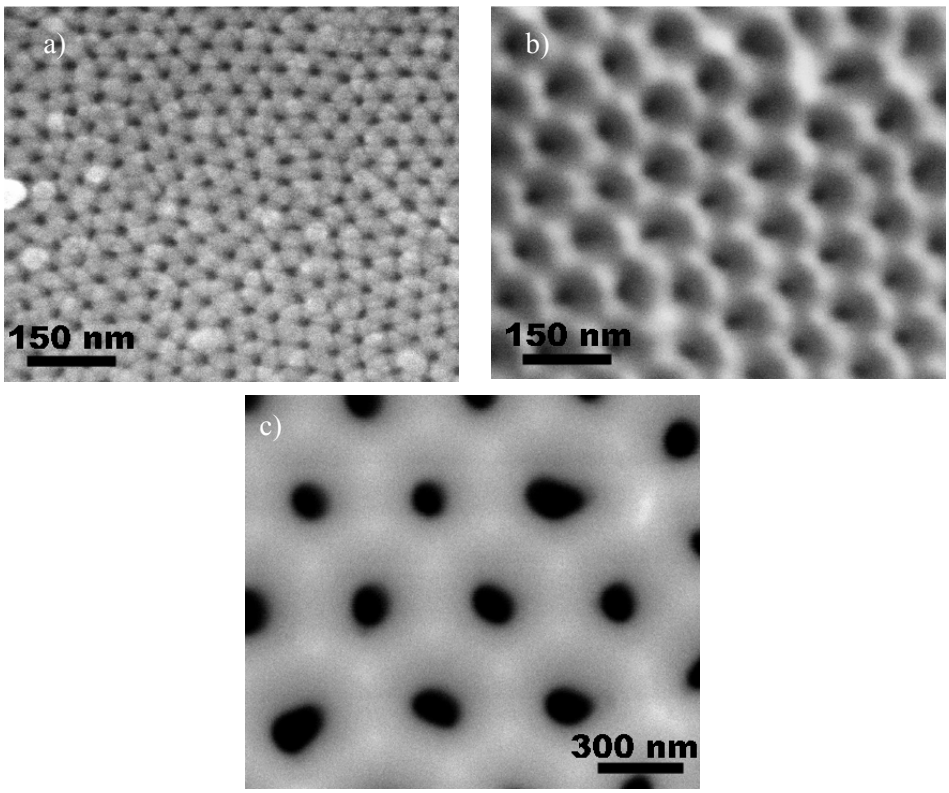


**Figure 22.** Top surface images of porous alumina produced in 2 step anodization using the following conditions: a) 10 wt.% $H_2SO_4$ at 20 V and 1 ºC, b) 0.3 M $(COOH)_2$ at 40 V and 17 ºC and c) 3 wt.% $H_3PO_4$ at 170 V and 1 ºC (a, b –SEM, c-ESEM).

In order to observe large areas on the porous alumina surface, Figure 23 represents SEM top surface images taken with less magnification on the a) SPA, b) OPA and c) PPA samples. In all the cases, the hexagonally ordered pores are arranged in the several domains with irregular shapes and areas. It is noticeable, that the domain frontiers are particularly defined by the white spots which are dislocations in the perfect triangular lattice. The insets of all the images (a-c) in Figure 23 represent the magnified areas of such dislocation points closely surrounded by the pores. It is interesting that the total number of dislocations

UNIVERSITAT ROVIRA I VIRGILI
DEVELOPMENT OF TECHNOLOGY AND APPLICATIONS BASED ON POROUS ALUMINA NANOSTRUCTURES
Lukas Vojkuvka
DL: T-1536-2009/ISBN: 978-84-692-4555-2


appear to be very similar for all the sample types with largely different surface areas. This could indicate that the origins of dislocations could become from anodizing process itself rather than from Al substrate properties such as purity or impact of the annealing and electro-polishing treatments [20, 103]. Moreover, a high brightness of these points could be attributed to the higher level of Al presented in the structure.

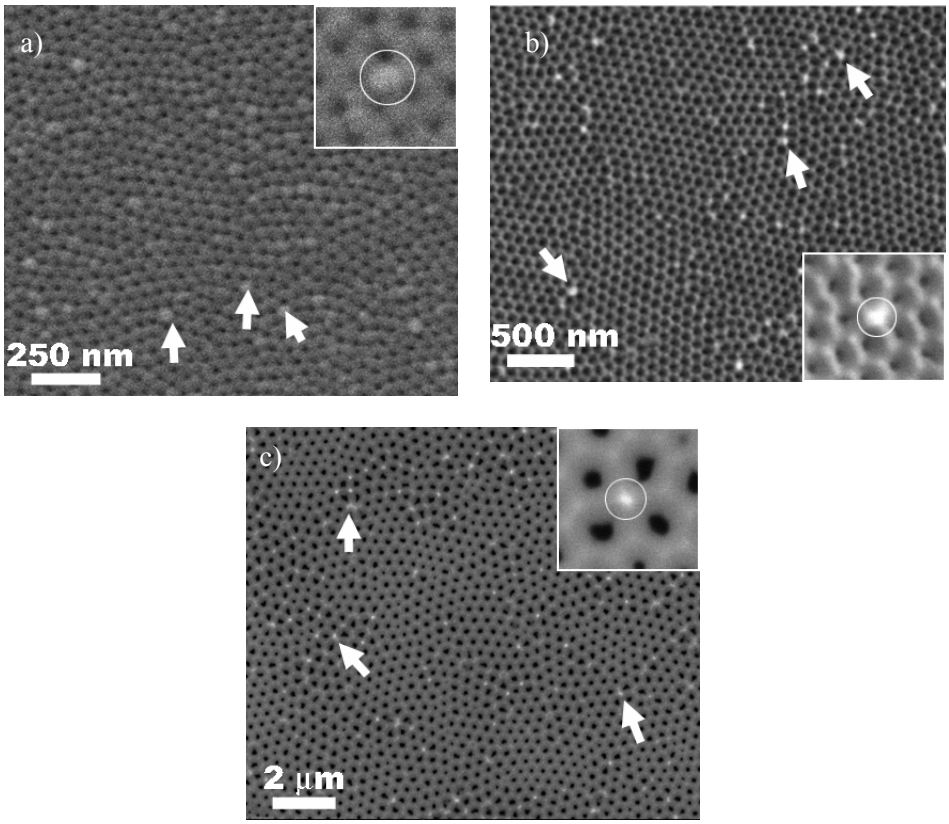


**Figure 23.** Large-area top surface images of porous alumina: a) $H_2SO_4$ sample, b) $(COOH)_2$ sample and c) $H_3PO_4$ sample fabricated with the same experimental conditions described in Figure 22. (a, b – SEM, c- ESEM)

The effect of the long-lasting anodization on the pore distribution is demonstrated in Figure 24, where a) top surface ESEM image of OPA sample anodized in first step for 1 hour and in the second step for 24 hours and b) the bottom surface image of the same sample showing the development of the porous domains during the long-lasting anodization. The pore domains at the bottom surface are significantly larger than on the top surface. The number of

DL: T-1536-2009/ISBN: 978-84-692-4555-2

dislocations is also suppressed by an expanding of the domain areas. Therefore, the duration of the first anodization step is an essential parameter to obtain Al patterning with large domains with perfect hexagonal periodicity [12, 17, 103]. In the subsequent second anodization, the pores will grow in the large domains following the Al patterning.

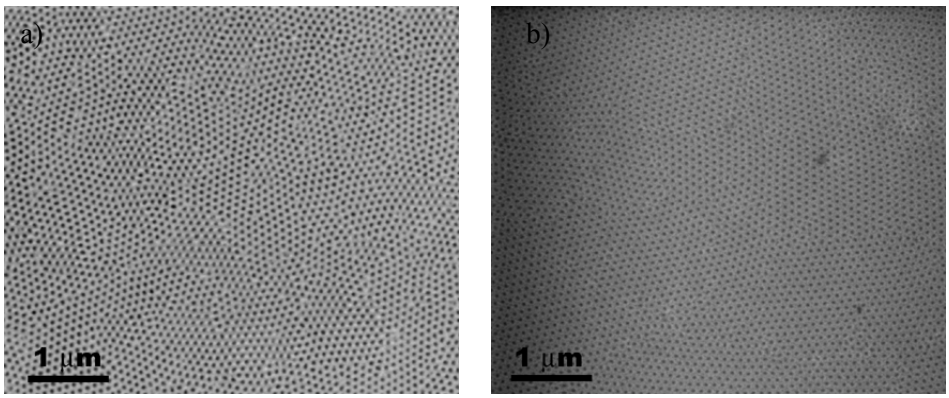


**Figure 24.** Large-area ESEM images from a) top and b) bottom surface of porous alumina sample anodized in oxalic acid for 24 hours.

AFM topographic images with the three-dimensional (3D) view are illustrated in the Figure 25. The analysed samples were a) SPA, b) OPA and c) PPA produced using the appropriate anodizing conditions as described previously. The surface profile analysis performed on ten consecutive pores is placed below each AFM graphic. It was showed out that the peak roughness is only few nanometers for SPA and OPA samples and it is slightly higher in order of few tens of nanometers for PPA sample [95, 97]. From these profiles, the mean value of interpore distance was estimated to be $D_{int}$ = 60 nm, 105 nm and 455 nm for SPA, OPA and PPA sample, respectively.

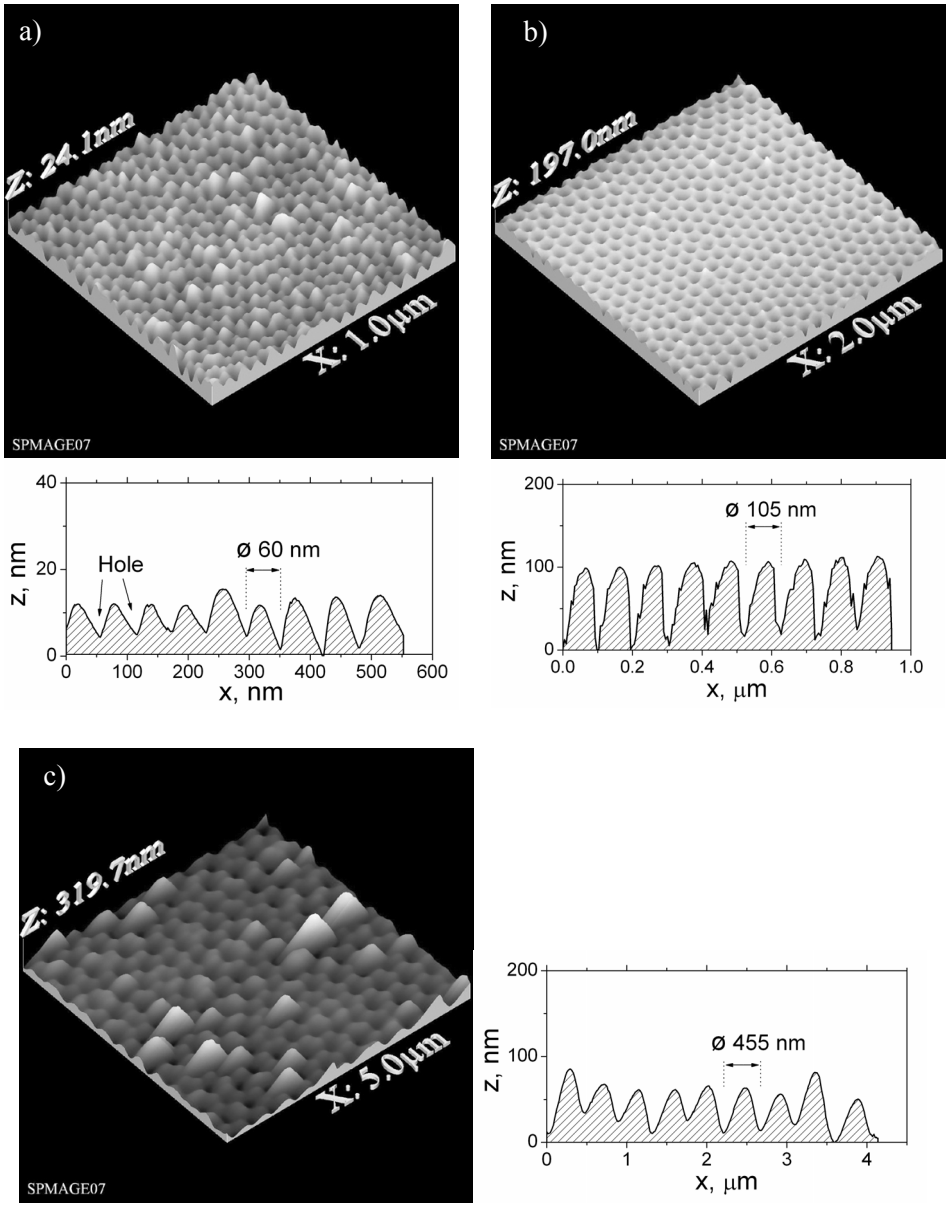


**Figure 25.** AFM 3D topographs from the top surface of porous alumina samples prepared using standard conditions. The corresponding surface profiles determined from each topograph of a) $H_2SO_4$, b) $(COOH)_2$ and c) $H_3PO_4$ sample are presented. The mean interpore distance $D_{int}$ = 60 nm, 105 nm and 455 nm were estimated from the total length of ten consecutive pores.

DL: T-1536-2009/ISBN: 978-84-692-4555-2

### 2.3.4 Pore Widening Process to Control the Porosity

In the previous section, the pore diameter of the as-made porous alumina was roughly estimated from the SEM images as $d_p$ = 20, 30 and 100 nm for SPA, OPA and PPA samples. However, it can be easily tuned to desired dimensions using a simple wet chemical etching, so-called pore widening, in 5 wt. % $H_3PO_4$ at 30 – 40 ºC [3, 21, 98, 104]. Figure 26 summarized the FEG-SEM results of the experimental set that was carried out in order to study the pore widening effect on the pore diameter. The as-made SPA, OPA and PPA samples were produced using standard conditions with the applied voltage $U_a$ = 20 V, 40 V and 170 V. The anodizing period in the second step for all the samples lasted 3 hours that gives the final alumina thickness of approximately 30 μm. After the primary FEG-SEM analysis of the as-made samples in order to study the pore morphology, the samples were etched in two successive pore widening steps using 5 wt. % $H_3PO_4$ at 35 ºC by applying different etching times $t_{pw}$ = 5, 10 and 20 min in this order corresponding to SPA, OPA and PPA sample. Between the etching steps FEG SEM analysis was carried out for all the samples in order to study the pore widening effect.

From the obtained high-resolution top surface images, the pore diameter and porosity of the OPA and PPA samples) were determined using a software application for image analysis [105]. It has to be mentioned that SPA images have insufficient resolution for digital analysis and the value of pore diameter was measured manually. Figure 27 shows a demonstration of image analysis for OPA and PPA samples, where first a high resolution image of each sample was processed with particle analysis. The calculated area distribution of the particle map gives the mean particle area ($S_m$). Considering that the particle has a perfect circular shape, the pore diameter $d_p$ can be solved using the formula for circle area as shown in Figure 27. Another value extracted from the particle analysis is sample porosity $P_a$ given by dividing the particle area ($S_p$) and total analysed area ($S_t$). Finally, the pore density $\delta_p$ was estimated as ratio $N/S_t$, where $N$ is particle count and $S_t$ is total analysed area. Besides the analysed porosity $P_a$, the ideal porosity $P_{10\%}$ was calculated following the 10% porosity rule reported previously in [30]. The $P_{10\%}$ takes into an account the hexagonal shape of the cells in the PA structure. It can be determined from this expression:

UNIVERSITAT ROVIRA I VIRGILI
DEVELOPMENT OF TECHNOLOGY AND APPLICATIONS BASED ON POROUS ALUMINA NANOSTRUCTURES
Lukas Vojkuvka
DL: T-1536-2009/ISBN: 978-84-692-4555-2


$$P_{10\%} = \frac{2\pi}{\sqrt{3}}\left(\frac{r_p}{D_{\text{int}}}\right)^2$$

, where $r_p$ is the pore radius ($d_p/2$) and $D_{\text{int}}$ is the interpore distance of corresponding SPA, OPA and PPA sample.

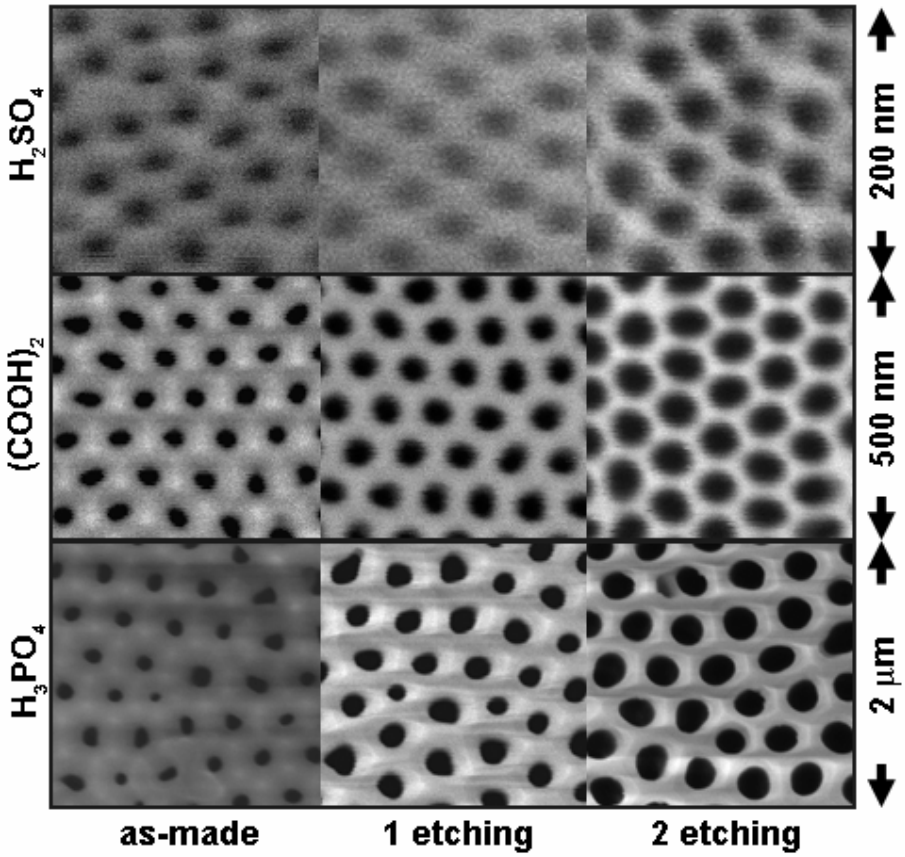


**Figure 26.** Pore widening effect represented by FEG-SEM top surface insets of porous alumina samples produced at $H_2SO_4$, $(COOH)_2$ and $H_3PO_4$ electrolyte (respective insets in rows). The as-made samples in the first column were etched in two consecutive cycles (1 and 2 etching) in 5 wt% $H_3PO_4$ at 30 ºC for 5 min ($H_2SO_4$), 10 min ($(COOH)_2$) and 20 min ($H_3PO_4$).

DL: T-1536-2009/ISBN: 978-84-692-4555-2

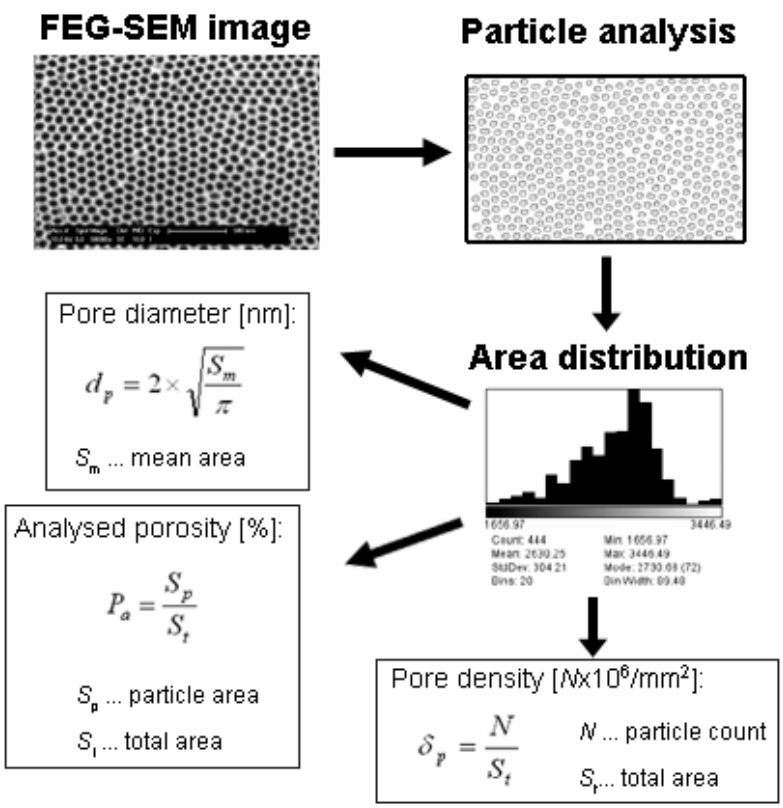


**Figure 27.** Schematic of the image processing with particle analysis. Pore diameter $d_p$, analysed porosity $P_a$ and pore density $\delta_p$ of the porous alumina samples were extracted from the particular analysis.

Table 1 gives the summary of the main experimental parameters used for the fabrication of SPA, OPA and PPA samples from the study of pore widening effect together with the obtained results from image analysis. The data from Table 1 are plotted in various graphs in Figure 28, where a) represents a general characteristic of the interpore distance that is linearly increasing between $D_{int}$ = 60 – 160 nm for applied voltage $U_a$ = 20 – 60 V, and between $D_{int}$ = 400 – 450 nm for $U_a$ = 160 – 175 V [98, 99]. Notice, that data in this graph were supported by more particular results of OPA and PPA samples produced using an extended range of applied voltage. The proportionality constant calculated from $D_{int}$ and $U_a$ relationship as $k_p = D_{int} \cdot U_a$ slightly varies between 2.6 - 3 nm/V for all the PA samples. This is in a good agreement with the results reported by other groups [2, 17, 28, 29]. Figure 28(b) shows the pore diameter widening in the function of etching time where the initial pore diameters of 18 nm, 35 nm

and 124 nm were enlarged up to 31 nm, 58 nm and 242 nm in two successive etching steps with total etching time $t_{pw2}$ = 10 min, 20 min and 40 min for SPA, OPA and PPA, respectively. Notice, that there is a certain maximum for pore diameter obtainable for each type of sample given by the cell size i.e. interpore distance. The corresponding increase of sample porosity due to the pore widening is compared in Figure 28(c), where analysed porosity $P_a$ (solid line) together with calculated ideal porosity $P_{10\%}$ (dashed line) are shown. Both porosities $P_a$ and $P_{10\%}$ are closely related to the reference results $P_r$ from the work carried out with similar experimental conditions [30]. A slight difference between $P_{10\%}$ and $P_a$ is caused by the dislocations in the periodical structure that are not considered in the perfect hexagonal model used in the $P_{10\%}$ formula. The porosity $P_a$ for sample S-PA is absent because of the low image resolution required for the image processing.

| | **10 wt.% $H_2SO_4$** | | | **0.3 M $(COOH)_2$** | | | **3 wt.% $H_3PO_4$** | | |
|---|---|---|---|---|---|---|---|---|---|
| **Applied voltage** $U_a$ [V] | 20 | | | 40 | | | 170 | | |
| **Interpore distance** $D_{int}$ [nm] | 60 | | | 105 | | | 455 | | |
| **Proportionality Constant** $k_p$ [nm/V] | 3 | | | 2.6 | | | 2.7 | | |
| **Pore density** $\delta_p$ [$N$x$10^6$/mm$^2$] | 450 | | | 110 | | | 7 | | |
| **Etching time** $t_{pw}$ [min] | $t_{pw0}$ | $t_{pw1}$ | $t_{pw2}$ | $t_{pw0}$ | $t_{pw1}$ | $t_{pw2}$ | $t_{pw0}$ | $t_{pw1}$ | $t_{pw2}$ |
| | 0 | 5 | 10 | 0 | 10 | 20 | 0 | 20 | 40 |
| **Pore diameter** $d_p$ [nm] | 18 | 24 | 31 | 35 | 49 | 58 | 124 | 191 | 242 |
| **Analysed porosity** $P_a$ [%] | - | - | - | 12 | 22 | 31 | 11 | 20 | 32 |
| **Ideal porosity** $P_{10\%}$ [%] | 8 | 15 | 25 | 10 | 20 | 27 | 7 | 16 | 27 |
| **Reference porosity** $P_r$ [%] | 12 | - | - | 8 | - | - | 9 | - | - |

**Table 1.** Summary of the major porous alumina types with their specific anodizing conditions and geometrical features. (Refernce porosity from [30])

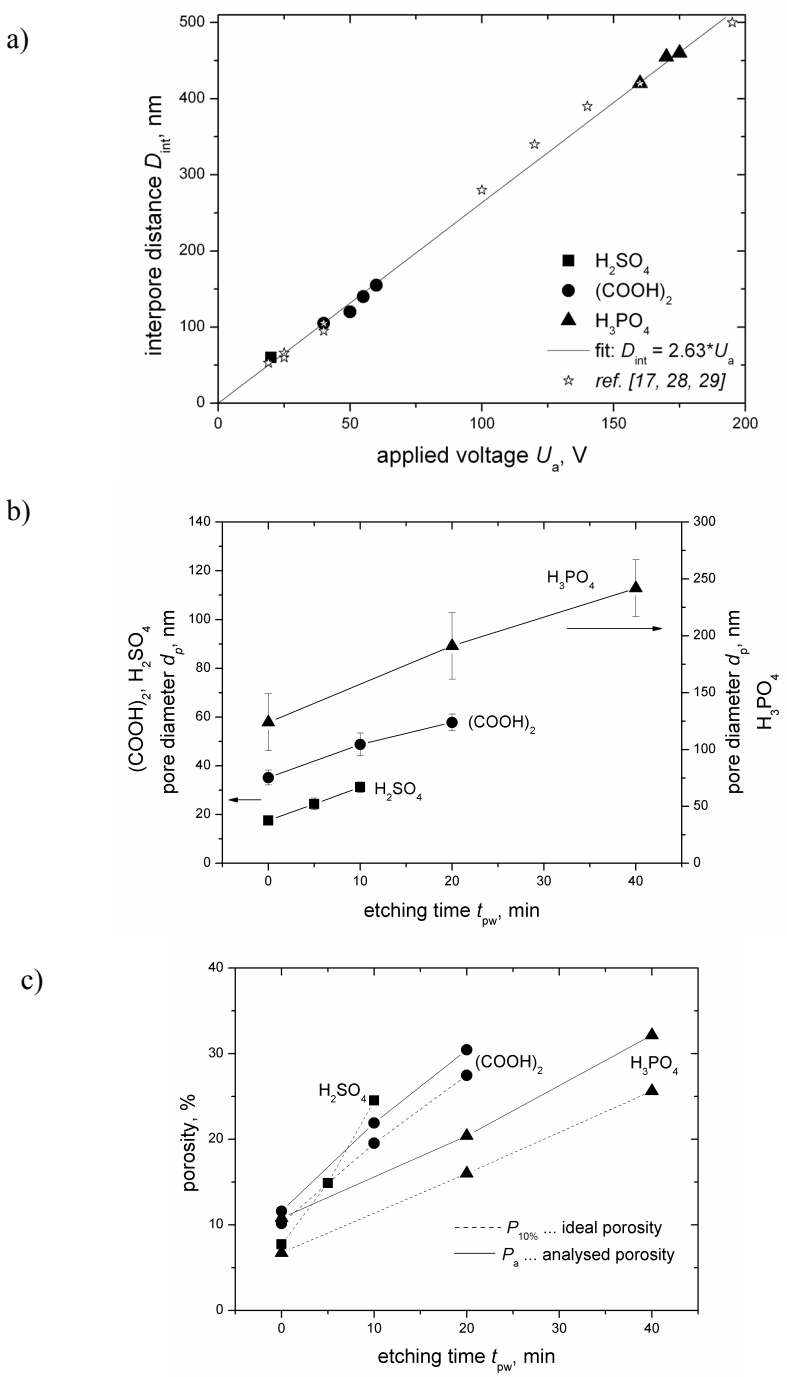


**Figure 28.** Graphics represent the experimental data from Table 1: a) interpore distance $D_{int}$ as a linear function of applied voltage $U_a$, b) pore diameter $d_p$ and c) porosity dependence on the etching time $t_{pw}$.

DL: T-1536-2009/ISBN: 978-84-692-4555-2

The desired film thickness of porous alumina can be obtained by adjusting the anodizing current and anodizing period. Since the current is also temperature-dependent factor, the thickness of the final porous alumina film can be estimated more precisely only with a proper control of temperature condition [106, 107]. In this work, the pore growth rate between 3 - 9 μm/h was determined for SPA, OPA and PPA produced under specific conditions. Generally, low anodizing temperatures lead to slower pore growth rates compared to ambient conditions. The steady current flow always starts to slightly decrease during a long anodizing period and therefore also a variance of pore growth rate should be expected. The porous alumina thickness is neither infinite, because after a certain limit, where the pore depth reaches maximum values, the electrolyte reconditioning at the pore bottoms becomes difficult [20]. Nevertheless, porous alumina structures with a broad range of aspect ratios (pore depth/pore diameter) varying from few hundreds to several thousands are feasible using corresponding anodizing parameters.

### 2.3.5 Model of Pore Development Based on Current Behaviour

Typical current curve from the aluminium anodizing has a specific profile with four regimes described in the previous chapter 1. This current behaviour can be applied to propose a model for the pore development at the early stage. Figure 29 summarizes current transients from the first (dashed line) and second (solid line) anodizing steps corresponding to a) SPA, b) OPA and c) PPA samples. Generally, for all the PA samples the current recorded from the long-time second step has a stable behaviour. Nevertheless, a detailed comparison of the current curves in the inset graphs from the first anodization performed on the smooth Al substrate and from the second anodization performed on the patterned Al substrate show out several differences which could be described with the following possible explanations.

First, in the initiation of the first step the immediate current drop to the minimum value Im1 is caused by the formation of insulating barrier layer (BL) on the Al surface [31, 101, 102]. The time $t_{BL}$ required for the complete growth of BL is noticeably shorter $t_{BL}$ = 8 s and 12 s for SPA and OPA compared to $t_{BL}$ = 85 s of PPA sample. This can be explained by the different BL thickness that is strongly voltage dependent [2, 108, 109] and it increases correspondingly

with applied voltage $U_a$ = 20 V, 40 V and 170 V for SPA, OPA and PPA sample. After the BL formation, the current rises from Im1 until it recovers a maximum at $I_{r1}$. This rise is owing to a gradual Al surface enlarging caused by a pore nucleation process which starts with the formation of curved pore bottoms. Once the current reaches the maximum, some of the minor pores cease growing due to the more dominant development of the neighbouring pores which is characterized by a current decrease. After that the current continues in a steady mode for the remaining anodization time.

After the removal of the oxide formed in the first step, the current transients recorded from the second step are clearly different. The BL formed on the pre-textured Al surface is non-uniform and it has evidently lower thickness compared to the BL thickness formed on the smooth surface in the first step. This conclusion can be made out from two facts: 1) the current minimum $I_{m2}$ is much higher due to the lower resistance i.e. thickness of the formed BL, 2) the formation time of BL in second step is faster $t_{BL}$ = 4 s, 9 s and 60 s for SPA, OPA and PPA sample. Based on the previous suggestion that after drop to the minimum the current rises due to the development of the curved pore bottoms, one could not expect any similar behaviour on the already curved surface of patterned Al. However, there is a short current recovery from the minimum $I_{m2}$ to the steady value $I_{r2}$ which can be produced by an inhomogeneous oxidation of the patterning pits during the BL formation. It is possible that the pit edges are preferentially oxidized faster than the pit shallows at the initial BL formation as it is schematically shown in Figure 30(b). This leads to a reduction of total Al surface area. Then the original shape of the pore bottoms must be recovered which is characterized by the current rise from $I_{m2}$ to $I_{r2}$ (see points A and B in Figure 30(a)). Notice also the absence of the pore dying in the second step because all the pores should only grow directly from the patterning pits.

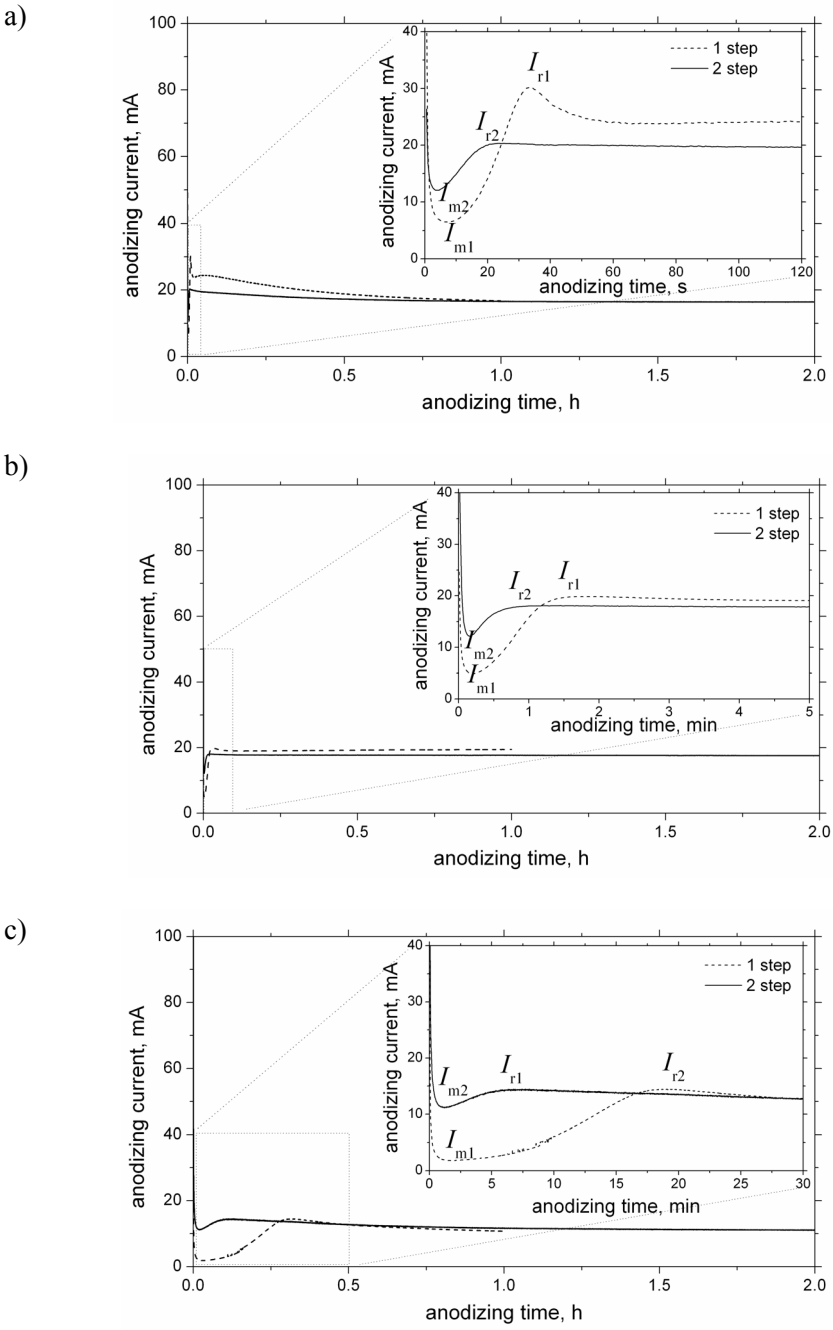


**Figure 29.** Typical current – time graphs from first (dashed line) and second (solid line) anodizing step of porous alumina samples prepared using: a) $H_2SO_4$, b) $(COOH)_2$ and c) $H_3PO_4$. For all the samples, the duration of the first and second step was 1 h and 3 h, respectively.

*Chapter 2*

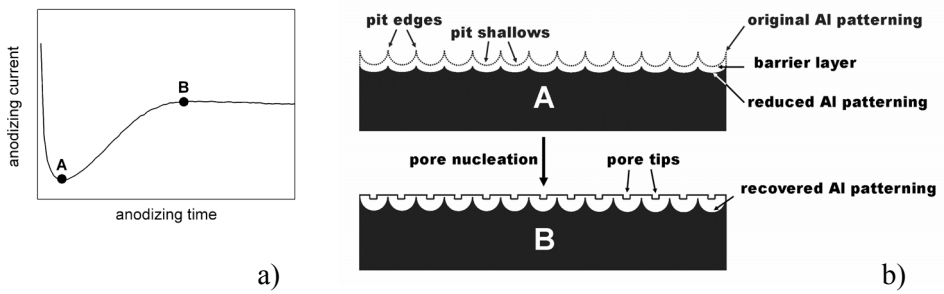


**Figure 30.** a) Demonstrative current – time curve from second anodizing step with indicated points that corresponds to the current minimum (A) and the current recovery (B); b) current-based model of pore development at the beginning of second anodizing step.

Typical current curve from the second anodizing step with the minimum (A) and recovery (B) current values are shown in the Figure 30(a). The absolute current required for the recovery from the minimum (A) to steady value (B) $I_{AB} = I_{r2} - I_{m2}$ at beginning of the second step has a tendency to decrease $I_{AB}$ = 8, 6 and 3.5 mA corresponding to SPA, OPA and PPA sample. This could be related to the size of the patterning pits i.e. cell sizes of 60 nm, 105 nm and 455 nm for SPA, OPA and PPA, respectively. Apparently, a larger amount of Al bulk is oxidized from the pit edges and consequently a larger area reduction is expected for SPA sample with a fine pattern of densely packed pits than for PPA pattern that consists of large-area pits with shorter total length of edge perimeter. Notice that one PPA pit covers approximately area of twenty OPA pits and around eighty SPA pits.

Generally, the current – time (I-t) characteristic recorded in the anodization process gives the direct information source about the sample state. Figure 31(a) shows two couples of current transients from OPA sample that was anodized at $U_a$ = 40 V and 60 V. In both voltage cases, there is a noticeable difference between the current minimums at the initial stage of the anodization. Later SEM analysis of OPA sample with lower current minimum at 60 V represented in Figure 31(b) showed out a disordered pore distribution on the top surface of the sample and in Figure 31(c) two distinct oxide structures are presented in the cross-section image of the same sample. The variance of current minimums in the Figure 31(a) turned out to be due to the insufficient removal of the oxide layer formed in the first step. Therefore, the remaining oxide act as an interfering element that permits neither the proper current drop nor the well

ordered pore growth from the patterned Al substrate. The Figure 31(c) clearly shows the transform between the part with unremoved oxide from the first step and newly formed oxide from the second step. By a closer checking of the current curve during the anodization, one can predict the possible consequences from the observed anomalies.

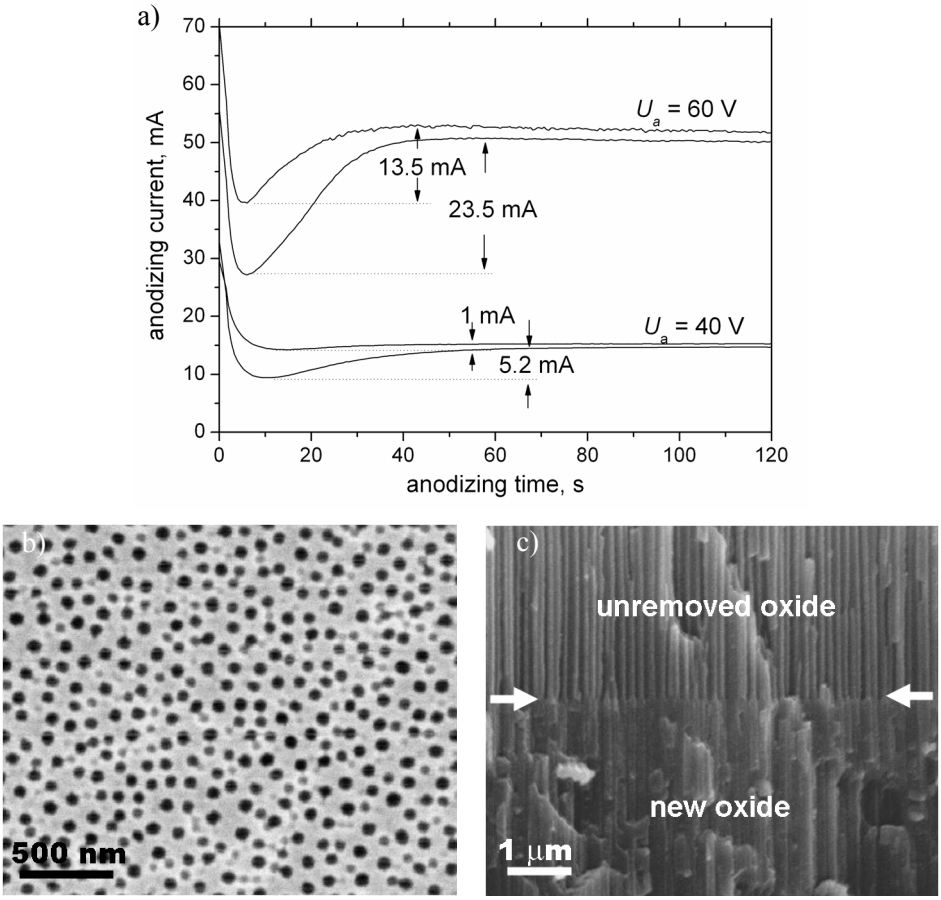


**Figure 31.** a) Comparison of the current-time curves from the second anodizing step in oxalic acid, b) top surface and c) cross-section SEM images of the sample after two step anodization with insufficient oxide removal in between of anodizing steps.

UNIVERSITAT ROVIRA I VIRGILI
DEVELOPMENT OF TECHNOLOGY AND APPLICATIONS BASED ON POROUS ALUMINA NANOSTRUCTURES
Lukas Vojkuvka
DL: T-1536-2009/ISBN: 978-84-692-4555-2


### 2.3.6 Detachment Techniques for Porous Alumina Films

In order to obtain a free-standing porous alumina film separated from Al substrate a few detachment techniques were carried out. First option is a simple selective etching of the whole as-produced PA sample in a mixture of $CuCl_2$ and HCl [110, 111]. Usually several minutes were enough to remove the entire Al layer leaving solely a porous film. Figure 32(b) shows the ESEM bottom surface image of O-PA after a complete substrate removal. Although this technique is very effective and reproducible, a contamination of heavy ions from the removal solution is present in the porous films. Later, if the contaminated film is exposed to a high temperature, excessive bending and cracking occurs on the sample.

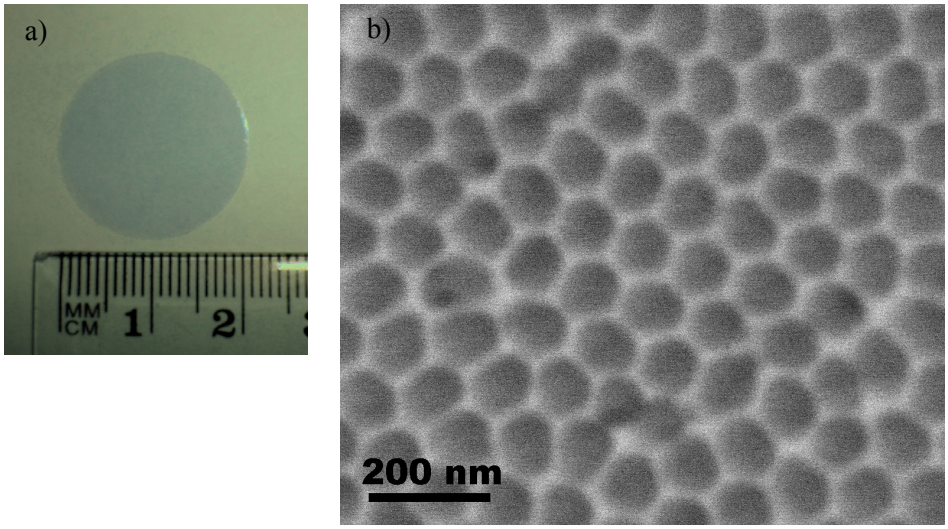


**Figure 32.** a) As-made free-standing porous alumina film, b) SEM bottom surface image of the porous alumina film after the wet chemical etching of Al substrate in a mixture of HCl and $CuCl_2$.

Another different approach for alumina detachment is based on the application of the voltage with reversed polarity [112]. When the second anodization is finished, the anode and cathode poles are switched and the voltage between 15 V and 25 V (for OPA) is applied to the system, meanwhile the rest of the anodizing parameters remain unchanged. In this case, the sample is employed as a cathode and therefore a reduction reaction is in progress on the Al surface producing hydrogen ($H_2$) bubbles. Since the entire exposed Al area is covered by PA layer, the tensile pressure of the $H_2$ gas accumulated at the metal/oxide

interface pushes up the alumina film. This technique turns out to be very fast and it can be easily performed on the same setup just after the anodization process. However, the SEM results in Figure 33(a) reveals the fact, that high stresses in the Al/alumina interface were in course during the separation process. These stresses often lead to alumina cracking and it is a challenging task to obtain a complete PA film. On the other hand, the bottom surface image of the detached piece of OPA in Figure 33(b) shows very compact crack-free structure. One of the important advantages of this technique is the possibility to recycle the remaining Al substrate. Only with the precisely adjusted conditions for each alumina type (SPA, OPA and PPA) and taking into account also the film thickness, one can assure the successfulness of this technique.

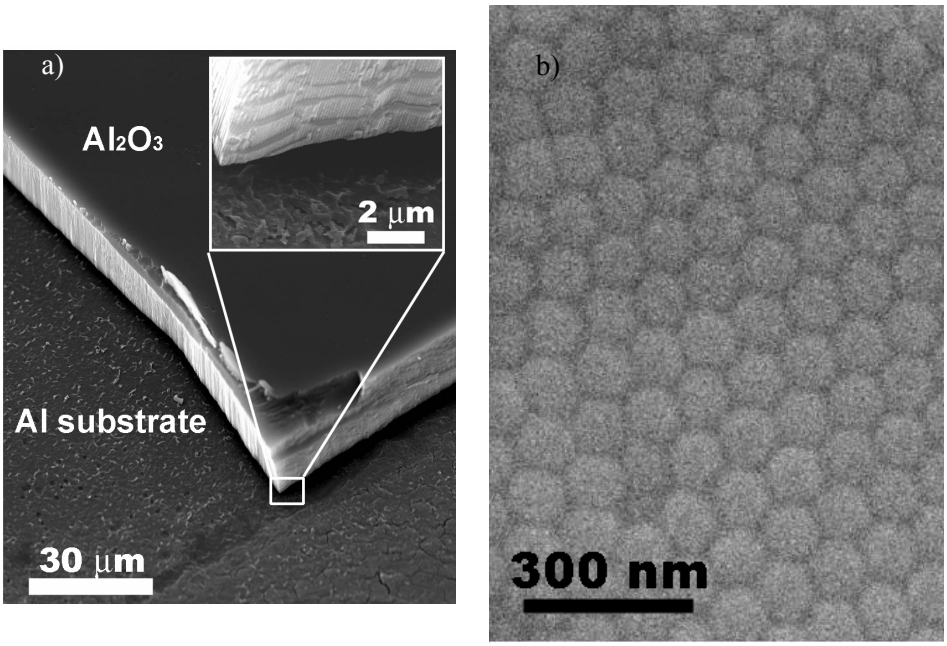


**Figure 33.** SEM images of a) the fractured porous alumina film on the Al substrate after detachment using the reversed polarity of applied voltage and b) bottom surface of the detached alumina film.

Finally, another direct lifting of alumina film from Al substrate is a via short voltage pulse (few seconds) using the electro-polishing mixture [113-115]. For the OPA sample, the voltage pulse of 15 V higher than anodizing voltage was applied for 2 - 3 seconds. Figure 34 compares the bottom surface images of as-detached OPA sample a) before and b) after pore widening etching. It is worth

UNIVERSITAT ROVIRA I VIRGILI
DEVELOPMENT OF TECHNOLOGY AND APPLICATIONS BASED ON POROUS ALUMINA NANOSTRUCTURES
Lukas Vojkuvka
DL: T-1536-2009/ISBN: 978-84-692-4555-2


to notice, that even before the pore widening process the pore bottoms were already half-opened. This could be a promising way to obtain alumina membranes opened on the both sides, which is an essential requirement for the synthesis of nanowires and nanotubes [116].

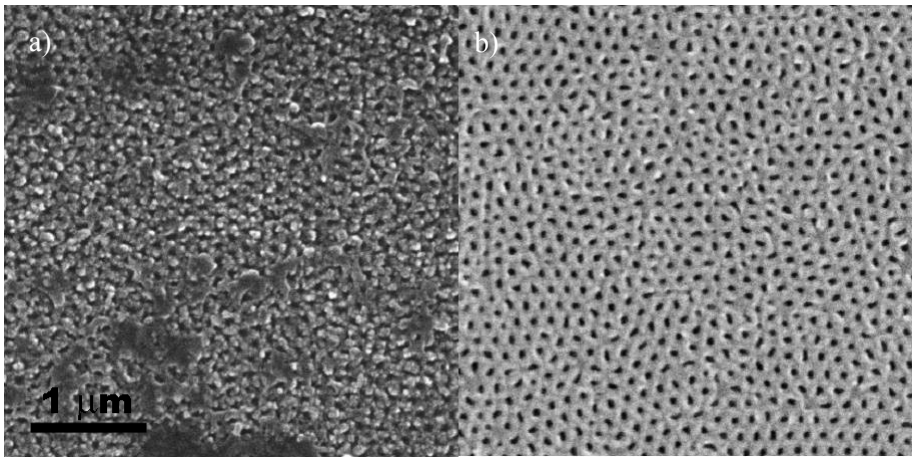


**Figure 34.** Comparison of SEM bottom surface images of the detached porous alumina films a) before and b) after the pore widening treatment.

UNIVERSITAT ROVIRA I VIRGILI
DEVELOPMENT OF TECHNOLOGY AND APPLICATIONS BASED ON POROUS ALUMINA NANOSTRUCTURES
Lukas Vojkuvka
DL: T-1536-2009/ISBN: 978-84-692-4555-2

## 2.4

## Summary

This chapter studies the fabrication process of self-ordered porous alumina using two-step anodization. For the electrochemical etching of aluminium, we used home-made anodizing cells equipped with elements for electronic and temperature control. The study of annealing and electropolishing treatments performed on the aluminium substrates before anodizing showed a large grain increase after heat treatment and a very smooth aluminium surface after polishing. Three major types of porous alumina samples were successfully produced by two-step anodization in various electrolytes based on sulphuric acid, oxalic and phosphoric acid. The examination of the morphology demonstrated that the porous alumina structures produced had highly diverse geometrical features: pore diameters between 20 nm and 250 nm, interpore distances of 50 nm, 100 nm and 450 nm, and aspect ratios (pore depth/pore diameter) as high as 5000. The pore widening process was investigated in order to control the porosity of the porous alumina samples. The current-based model of pore formation in the early stage of the anodization process was proposed for all three major types of porous alumina. It was observed that the different phases of pore development are directly reflected in the measured current characteristic. Several detachment techniques for obtaining free-standing porous alumina films were carried out.

UNIVERSITAT ROVIRA I VIRGILI
DEVELOPMENT OF TECHNOLOGY AND APPLICATIONS BASED ON POROUS ALUMINA NANOSTRUCTURES
Lukas Vojkuvka
DL: T-1536-2009/ISBN: 978-84-692-4555-2

UNIVERSITAT ROVIRA I VIRGILI
DEVELOPMENT OF TECHNOLOGY AND APPLICATIONS BASED ON POROUS ALUMINA NANOSTRUCTURES
Lukas Vojkuvka
DL: T-1536-2009/ISBN: 978-84-692-4555-2

# 3

# Hard Anodization Process

UNIVERSITAT ROVIRA I VIRGILI
DEVELOPMENT OF TECHNOLOGY AND APPLICATIONS BASED ON POROUS ALUMINA NANOSTRUCTURES
Lukas Vojkuvka
DL: T-1536-2009/ISBN: 978-84-692-4555-2

*Chapter 3*

**Beyond two-step anodization**

Many attempts been made recently to find novel anodizing techniques for fabricating porous alumina with arbitrary properties. The state-of-the-art focused in porous alumina fabrication has been described in the first chapter. Among others new trends, it is worth mentioning the preparation of monodomain alumina using aluminium pre-patterning, high-field anodization or hard anodization.This chapter deals with the fabrication of self-ordered porous alumina using hard anodization.

Special attention is paid to the formation of the porous layer at the different phases of the process. The dependence of the pore self-ordering effect on the voltage is discussed. A comparative study is made of hard anodization and two-step anodization, and the geometrical features of porous alumina structures from both anodizing techniques are discussed. At the end of this chapter several attempts at fabricating novel porous alumina structures based on the combination of hard and two-step anodization are reported.

UNIVERSITAT ROVIRA I VIRGILI
DEVELOPMENT OF TECHNOLOGY AND APPLICATIONS BASED ON POROUS ALUMINA NANOSTRUCTURES
Lukas Vojkuvka
DL: T-1536-2009/ISBN: 978-84-692-4555-2

## 3.1

## Experimental Preparation and Characterization of Hard Anodized Porous Alumina

### 3.1.1 Hard Anodization Process

In this section, the experimental procedure for fabrication of porous alumina (PA) using hard anodization (HA) process will be given. A detailed observation of the anodizing current curve was performed in order to understand the main stages of pore development during HA process. Also the key factors affecting the HA process are commented.

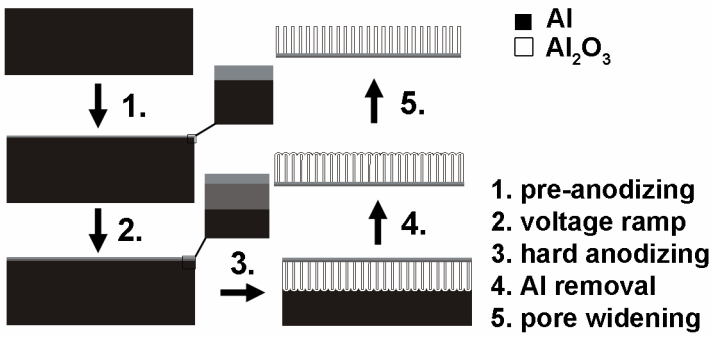


**Figure 35.** Scheme of the experimental preparation of porous alumina using hard anodization process.

Although the experimental setup for preparation of PA using HA process and conventional anodization (CA) 2 step process is identical, the anodizing conditions are significantly different. The same Al foils as in CA process were used as starting substrates with corresponding annealing and electro-polishing treatments. The electrolyte was prepared from 0.3 M oxalic acid with working temperature maintained at 1 ºC. In contrary to CA 2 step process, the fabrication of hard anodized porous alumina (HPA) sample only consist of one step anodization with specific profile of applied voltage ($U_a$). Figure 35 shows a scheme of fabrication stages in the HA process starting with electro-polished Al substrate. Then, a specific voltage profile with initial short CA pre-step (1) was applied followed by a voltage ramp (2) up to target voltage required for HA

($U_{HA}$) which usually varied between $U_{HA}$ = 100 – 150 V [52, 117]. Finally, once the HA stage was performed (3), the remaining Al substrate was chemically removed (4). The achieved HA film can be etched in a diluted mixture of phosphoric acid in order to remove the barrier layer (5). The fabrication steps (1) – (3) corresponding to the mentioned HA stages are always performed at once by applying a specific voltage profile, which will be described in detail in the following text.

### 3.1.2 Specific Current Characteristic

Representative current and voltage transients recorded from HA process are shown in Figure 36. Basically, the HA process consist of three fundamental stages starting with a short CA pre-step with applied voltage of $U_{CA}$ = 40 V. This step usually lasted from 5 to 10 min and the purpose of this pre-step is to create a kind of protective oxide layer in order to avoid a breakdown during the HA stage with high applied voltage [52, 117]. Figure 36(b) shows the CA current curve which follows the expected behaviour similarly observed in current curves from the previous chapter focused on 2 step CA process. In this case, the current reaches a recovered maximum after 5 minutes which corresponds to the formation of barrier layer (A) and nucleation of pore bottoms (B). Notice in Figure 36(b), that the current arrived at point (B) much slower (5 min) than in the CA 2 step process (1.5 min). This time difference is caused by a low working temperature (~1 ºC) that significantly affects the oxide growth rate [12].

Figure 36(c) shows the second stage of HA process characterized by a voltage ramp with a typical rate in the range of 0.5 – 0.8 V/s depending on the target voltage $U_{HA}$. In the presented example is $U_{HA}$ = 140 V with rate of 0.7 V/s. The ramp rate is one of the crucial factors of HA process because the breakdown or often called burning of the sample occurs if the applied rate is too high [57, 59]. Generally, slower ramp rates are used when a high target voltage is required. The current characteristic at logarithmic scale in the Figure 36(c) presents first a rapid step at the very beginning of the voltage ramp. Then the curve slowly increases up to 10 mA followed by a sharp rise when the ramp voltage ($U_R$) goes over 80 V. Finally, the current reaches a stable form at a corresponding $U_R$ = 100 V and it remains constant during the final phase of ramp until the target voltage $U_{HA}$ = 140 V is achieved.

UNIVERSITAT ROVIRA I VIRGILI
DEVELOPMENT OF TECHNOLOGY AND APPLICATIONS BASED ON POROUS ALUMINA NANOSTRUCTURES
Lukas Vojkuvka
DL: T-1536-2009/ISBN: 978-84-692-4555-2

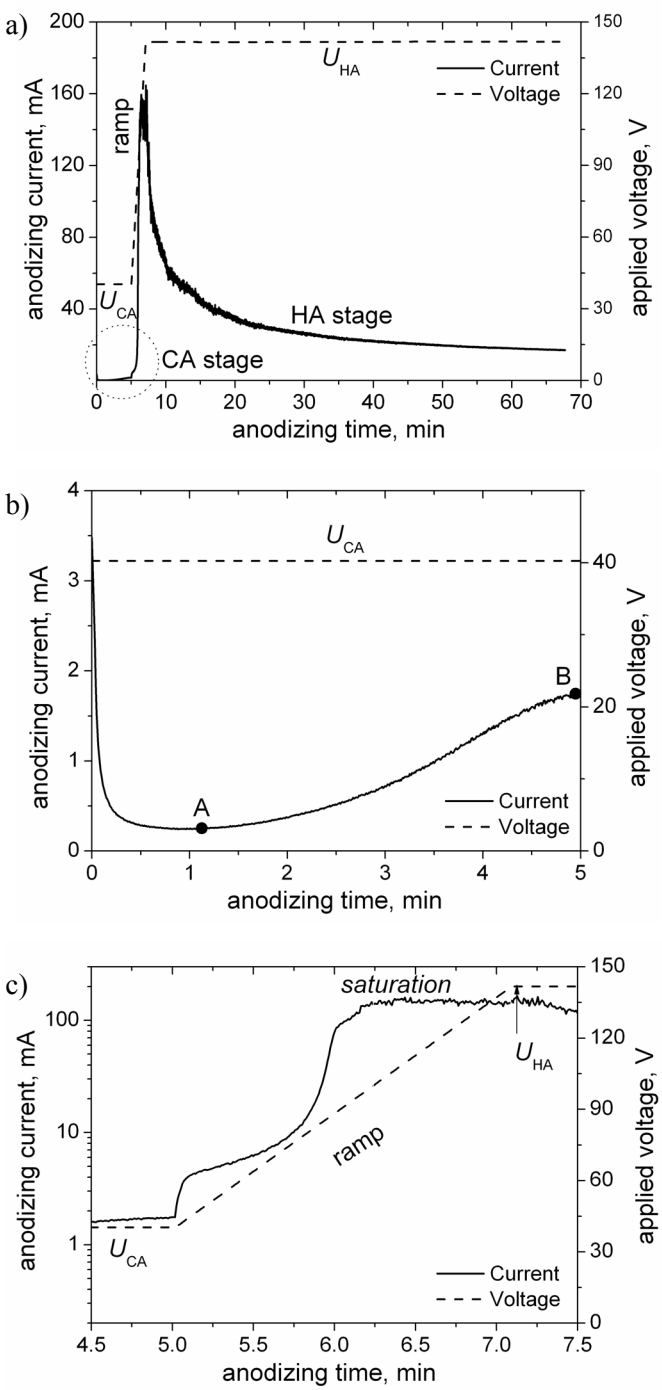


**Figure 36.** a) Typical current and voltage transients from hard anodization process with b) initial pre-step of conventional anodization (CA) at 40 V followed by c) voltage ramp to target voltage required for hard anodization (HA) stage.

In Figure 36(a) is illustrated the third and last stage of HA process, where a constant anodizing voltage $U_{HA}$ = 140 V is applied for anodizing period of 1 hour. Immediate current drop is observed during the first minutes of the anodization followed by an exponential current decrease until a steady flow is observed in the remaining time.

### 3.1.3 Morphology of Hard Anodized Alumina

The HPA samples produced using HA process were analysed using ESEM. The morphology difference of the top surface, bottom surface and cross-section of the HPA were examined with an objective to understand the pore development at corresponding HA stages.

Figure 37 shows ESEM top surface images (a, c, e) and bottom surface images (b, d, f) of the HPA film fabricated with $U_{HA}$ = 140 V and during one hour of anodizing period. The as-produced HPA sample (a, b) was subsequently etched in two consecutive cycles. First etching was performed in the mixture for oxide removal ($H_3PO_4$ + $H_2CrO_4$) at 60 ºC for 5 min (c, d) and the second etching in pore widening mixture using 5 wt% $H_3PO_4$ at 30 ºC for 30 min (e, f).

The surface of as-produced HPA sample in Figure 37(a) showed out a disordered pore distribution with various diameters. The mean interpore distance is less than 100 nm which corresponds to pore nucleation phase that takes place at the end of CA stage. At the bottom image in Figure 37(b) are shown large pore tips covered with barrier layer with uniformly rounded shape and perfectly ordered triangular lattice. Compared to top surface, the mean distance between pore tips at the bottom is constantly around 300 nm [52, 117]. A great difference between top and bottom surface is clearly given by experimental conditions such as applied voltage at the beginning ($U_{CA}$ = 40 V) and at the end ($U_{HA}$ = 140 V) of the HA process.

After first etching, the pores in Figure 37(c) appear to be larger and with different depth indicated by the hue intensity. This difference in the pore depth is caused by the voltage ramp in the second stage of HA process, where the ramp voltage ($U_R$) linearly increases with time from $U_R$ = 40 V up to target voltage $U_{HA}$ = 140 V. Since the interpore distance is strictly voltage dependent it is continuously extended in the course of the voltage ramp [2, 21]. This

causes an expanding of the dominant pores represented by a darker hue meanwhile the rest of the brighter and shallower pores cease growing. The bottom image of the same sample in Figure 37(d) shows the etched pore tips with a covering barrier layer that was significantly reduced during the first etching. The spacing between the pore tips have now a circular shape compared to the triangular shape in Figure 37(b). Each pore tip is surrounded by six tiny holes. Notice also, that the pores in the centre of each rounded tip start to be visible through the thinned barrier layer. The marked large hole was probably created in the aluminium (Al) removal step after HA process. During the fast growth of the pores at high applied voltages, the bulk Al is often pushed upwards forming short needles in between of the growing pores [60]. Afterwards these Al needles are etched away in the substrate removal step leaving large holes in the HPA film.

In Figure 37(e), the second wet chemical etching leaves the top surface of the HPA sample with a high porosity formed by big non-uniform pores with large distance over 250 nm. The entire thin oxide layer with minor pores as it is noticeable in Figure 37(a, c) was etched away. The porous layer in Figure 37(e) probably grows at the end of the ramp stage when the voltage $U_R$ pass over 100 V and the measured current is saturated as it was commented value in Figure 36(c). In this steady current phase, the oxide layer is supposed to grow linearly with increasing $U_R$ = 100 – 140 V. On the other side of the HPA sample in Figure 37(f), the pore tips are completely opened leaving an ideal distribution of uniform pores with measured diameter $d_p$ = 160 nm and interpore distance $D_{int}$ = 310 nm.

The cross-section ESEM image of the fractured HPA sample is shown in Figure 38. The captured area corresponds to the porous oxide formed in the third stage of HA process, where already constant voltage $U_{HA}$ = 140 V is applied. The channels are very uniform and straight reflecting a stabilized growth in the third HA stage compared to disordered growth in the second HA stage with voltage ramp.

UNIVERSITAT ROVIRA I VIRGILI
DEVELOPMENT OF TECHNOLOGY AND APPLICATIONS BASED ON POROUS ALUMINA NANOSTRUCTURES
Lukas Vojkuvka
DL: T-1536-2009/ISBN: 978-84-692-4555-2


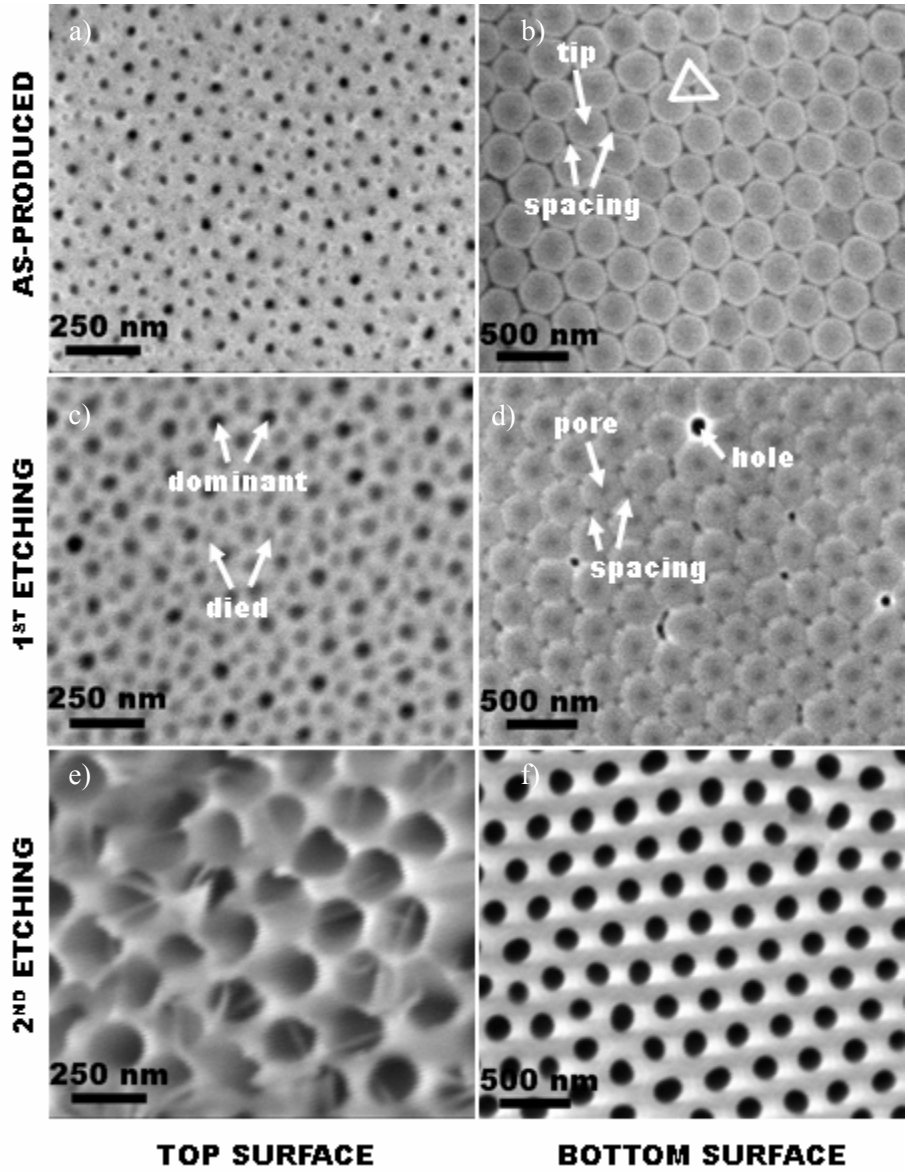


**Figure 37.** ESEM top (a, c, e) and bottom (b, d, f) surface images of the porous alumina sample prepared with hard anodization process at 140 V for 1 hour with 5 min of CA pre-step at 40 V and with the voltage ramp of 0.8V/s. The anodized sample (a, b) was etched in the mixture for oxide removal (c, d) and then in the pore widening solution (e, f).

DL: T-1536-2009/ISBN: 978-84-692-4555-2

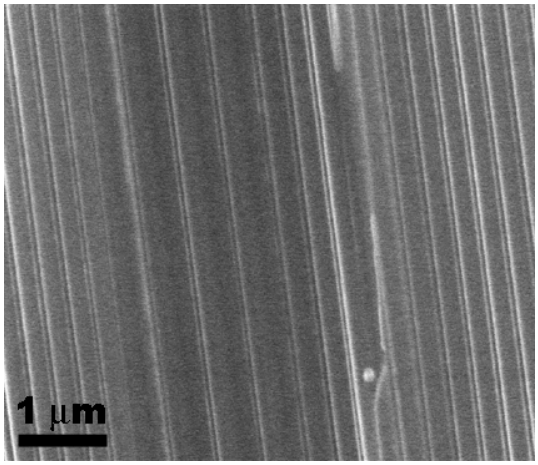


**Figure 38.** Cross-section ESEM image from the fractured porous alumina sample produced by hard anodization at 140 V for 1 hour.

### 3.1.4 Pore Development during Hard Anodization Process

From the previous experimental results of ESEM analysis in Figure 37 and according to the linear dependence of interpore distance on the applied voltage [2, 21], it is clear that the pore distribution varies significantly at the different fabrication stages of the HA process. Particularly, in the second HA stage with ramp, when the voltage rapidly increases with time, the pore developing is rather doubtful and it needs to be clarified. Therefore, the following set of experiments focused on pore state at different stages of HA process were carried out.

AFM topology micrographs in the Figure 39 represents Al surface on the samples prepared in the HA process with only two stages of CA pre-step and the voltage ramp stopped at target voltages $U_R$ = 105 V (a) and $U_R$ = 140 V (b). The oxide layer formed on the Al was selectively removed in order to study the patterns of pore bottoms imprinted on the Al substrate. The complete HA process with all three stages including CA pre-step, voltage ramp and hard anodization was performed in order to compare the pore state. Figure 39(c) shows AFM scan of bottom surface on the HPA sample anodized at $U_{HA}$ = 140 V for 1 hour. In contrary to samples in Figure 39(a, b) the remaining Al substrate was dissolved to observe directly the pore tips on the bottom part of HPA sample.

The corresponding surface profiles for each AFM topographic (a-c) are plotted below in the collective graph in Figure 39(d). The size of the imprinted pits on the Al sample with $U_R$ = 105 V are noticeably smaller and shallower than for Al sample with $U_R$ = 140 V, where the pits are larger and deeper. This means, that during the voltage ramp in the range of $U_R$ = 100 – 140 V the pores are continuously expanded meanwhile the total Al area remains unchanged. Based on this suggestion that the sample area do not alter significantly, the current saturation in the voltage range $U_R$ = 100 – 140 V (see Figure 36(c)) indicates a fact that the sample resistance given by the entire oxide thickness also linearly increases with ramp voltage.

Notice, that due to the high current value during the saturation (~150 mA), the resistance enhance i.e. the oxide growth rate is expected to be very fast. This fast growth is accompanied with high heat evolution at the oxide/metal interface and therefore a proper temperature control is an essential part of experimental setup for the HA process. In contrary, the breakdown and burning of the sample often occurs as a consequence to the extremely high current [52, 57]. The fast oxide expansion due to the high electrical field also causes the formation of Al pyramids on the Al surface as shown in Figure 39(a, b). This is a typical phenomenon of the high voltage anodization previously observed also in the 2 step process using phosphoric electrolyte and applied voltage over 160 V [60].

The bottom of the HPA sample after one hour of HA at $U_{HA}$ = 140 V in Figure 39(c) showed out an array of half-sphere pore tips with regular size and similar depth. The intertip distance as well as depth is even much higher (310 nm) than the interpit distance (190 nm and 245 nm) measured on the patterned Al surface at the end of ramps with $U_R$ = 105 V and 140 V. Apparently, the pores continues developing also in the initial phase of the HA stage. Generally, when the voltage ramp reaches the target value $U_{HA}$ and it continues in the constant mode, the immediate current drop is observed (see Figure 36(a)). This drop supports the explanation for the saturated current during the final phase of the voltage ramp, where although the oxide thickness i.e. sample resistance increases very fast, the current instead of decrease is balanced by rising voltage ramp. Once the applied voltage passes to constant mode, the fast oxide growth continues and the current decreases exponentially with anodizing time.

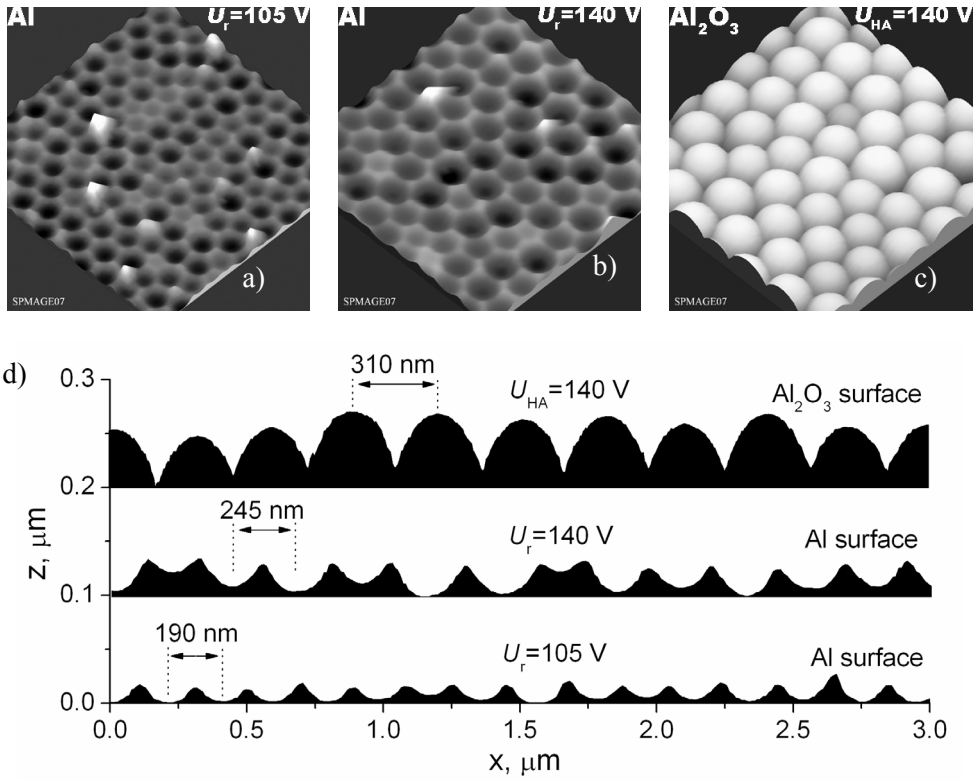


**Figure 39.** AFM topographs of a) Al surface after voltage ramp to target voltage $U_r$ = 105 V and b) $U_r$ = 140 V. In both Al samples (a, b) the formed oxide layer was selectively removed; c) bottom surface of porous alumina sample produced by hard anodization at $U_{HA}$ = 140 V for 1 hour. In this case, the Al substrate was selectively removed; d) surface profiles measured on the studied topographs (a-c).

UNIVERSITAT ROVIRA I VIRGILI
DEVELOPMENT OF TECHNOLOGY AND APPLICATIONS BASED ON POROUS ALUMINA NANOSTRUCTURES
Lukas Vojkuvka
DL: T-1536-2009/ISBN: 978-84-692-4555-2


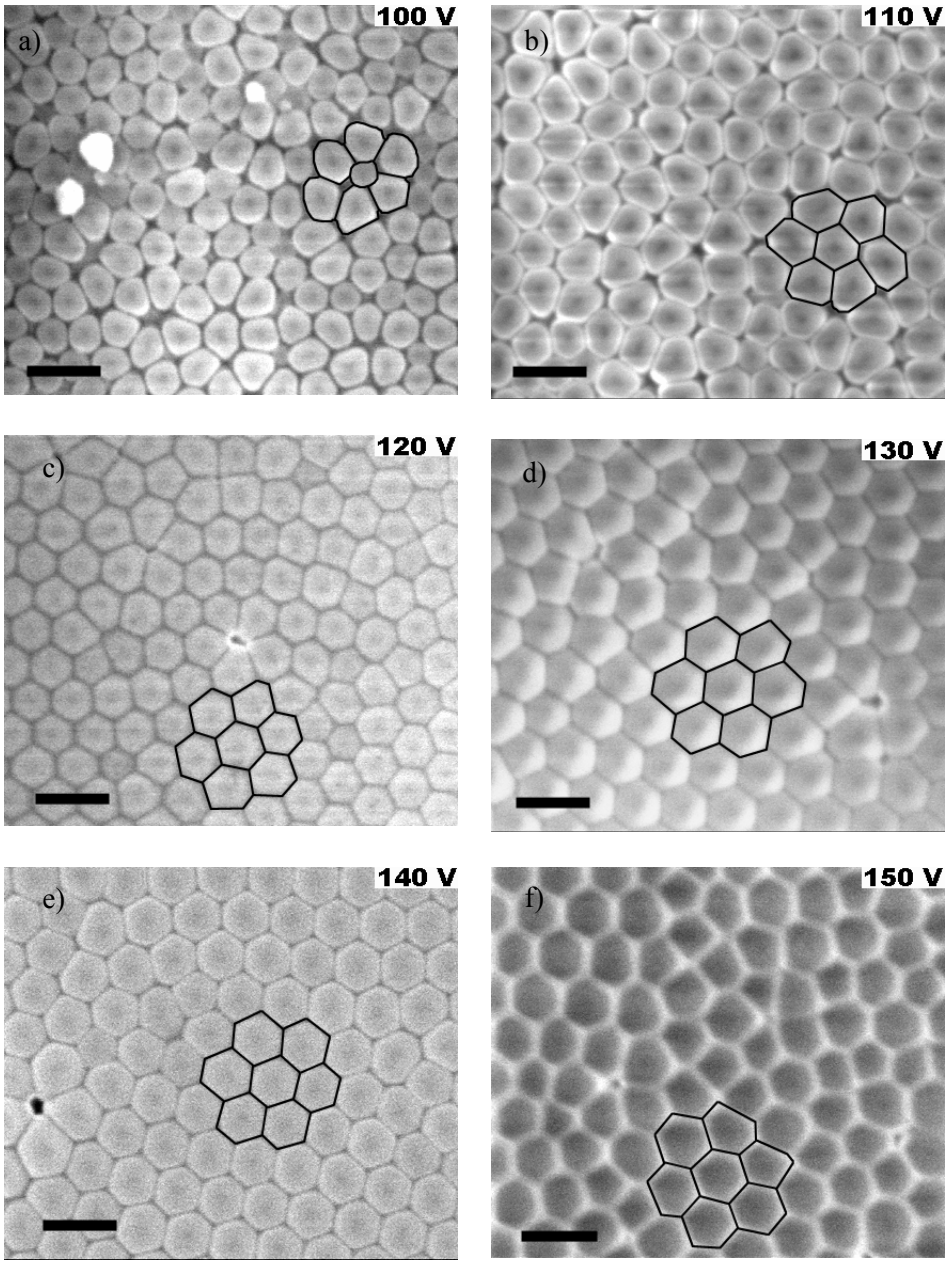


**Figure 40.** Bottom surface ESEM images of porous alumina samples fabricated using hard anodization at various applied voltage $U_{HA}$ = 100 – 150 V for anodizing period of 1hour in 0.3 M oxalic acid.

DL: T-1536-2009/ISBN: 978-84-692-4555-2

### 3.1.5 Self-ordering Dependence on Applied Voltage

The voltage interval of 100 V to 140 V seems to be crucial for the self-ordering formation of the pores in the HA process. Therefore a series of the experiments focused on the pore ordering at different HA voltages $U_{HA}$ = 100 V, 110 V, 120 V, 130 V, 140 V and 150 V was investigated. The results of the analysed HPA samples after one hour of HA at corresponding applied voltage $U_{HA}$ are summarized in Figure 40 composed with ESEM bottom surface images. The HPA samples in Figure 40 with $U_{HA}$ = 100 V and 110 V are characterized by a random distribution of pores with non-uniform shapes and large spacing between the pore tips. The pore uniformity and triangular lattice noticeably improve from $U_{HA}$ = 120 V and further up to $U_{HA}$ = 140 V, where the pore tips are well ordered over the surface with hexagonal shape of the cells. For $U_{HA}$ = 150 V the ordering degree and hexagonal cell uniformity seems to get worse significantly. There must be an ideal range of applied voltage $U_{HA}$ that assures a sufficient but not excessive electric field required for the self-ordered formation of the pores.

The mean intertip distance measured for each sample and showed out a linear increase from 240 nm to 320 nm according to applied voltage $U_{HA}$ = 100 V – 150 V. It is worth to notice, that the distance for the HPA samples produced at 100 V and 110 V are significantly larger (240-260 nm) compared to the mean interpit value observed on the patterned Al surface (190 nm) after ramp with target voltage $U_r$ = 105 V ( see Figure 39(d)). This confirms the suggestion that the final intertip distance is definitely adjusted in the last HA stage with constant applied voltage.

## 3.2

## Novel Porous Alumina from Hard and Conventional Anodizing Processes

### 3.2.1 Overview of the Feasible Porous Alumina

The self-ordered porous alumina (PA) can be obtained via 2 step anodization process that was described in the second chapter. Basically, three major types of PA with diverse geometrical properties can be produced using three common electrolytes prepared from sulphuric, oxalic or phosphoric acid. In this chapter, a new technique so-called hard anodization in oxalic electrolyte was introduced and the fourth type of hard anodized PA (HPA) was successfully fabricated using this technique. The first part of the following section will be focused on comparative analysis of PA structures from conventional 2 step anodization (CA) and HPA from hard anodization (HA) process. In the second part of this section, it will be taken an advantage of managing two anodizing techniques in order to attempt the fabrication of novel porous alumina structures. Three approaches based on conventional and hard anodization are proposed: i) pre-patterning of Al using HA process, ii) combined CA-HA anodizing process and iii) multi-step HA process.

Figure 41 shows ESEM surface images in a comparison of PA and HPA samples produced at CA and HA process using the following electrolytes and applied voltage: a) sulphuric acid and 20 V, b) oxalic acid and 40 V, c) phosphoric acid and 170 V, and d) oxalic acid and 140 V. Notice, that (a-c) are top surface images whereas (d) is bottom surface image. The scanned sample areas of each Figure 41(a-d) were chosen intentionally to be multiples of each other. In other words, sample area (a) is four times smaller than (b) and similarly (b) is sixteen times and nine times smaller than (c) and (d) respectively, (d) is only 0.75 times smaller than (c). The corresponding area proportions are shown in the insets of each figure. At first sight in Figure 41, the PA sample (c) and HPA sample (d) have a very resembling pore distribution and diameters. However, the HPA sample demonstrates a better ordering in triangular lattice and also more circular pores.

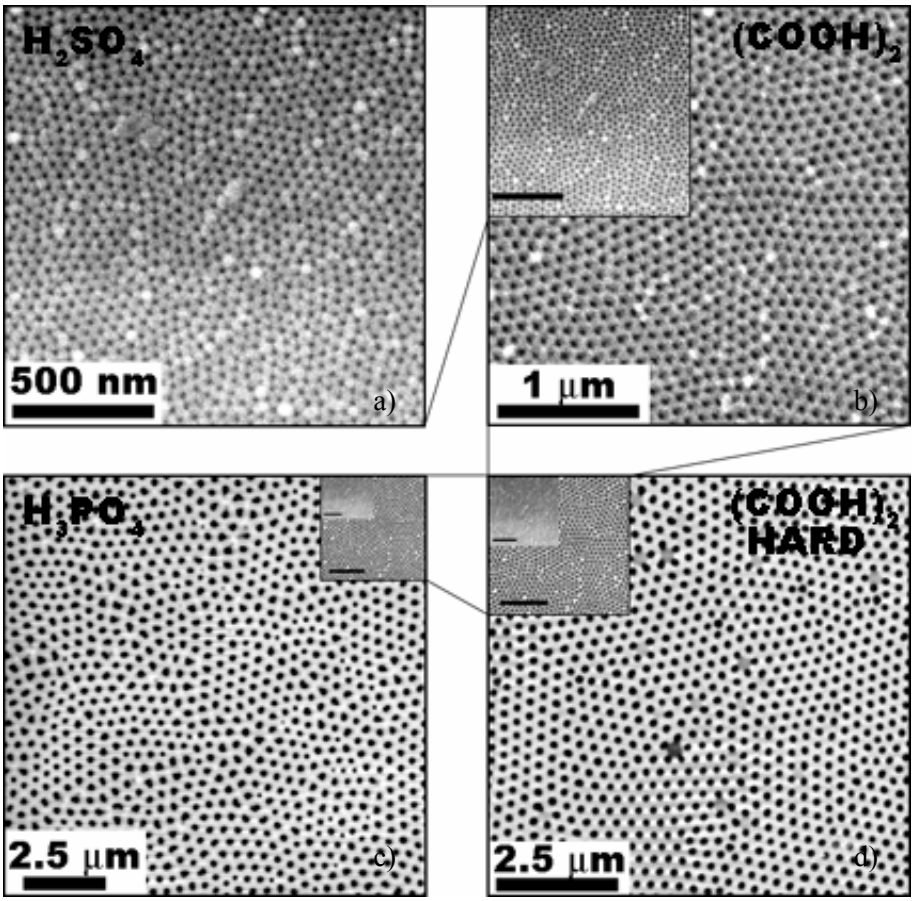


**Figure 41.** Comparison of SEM and ESEM images of porous alumina produced using conventional anodization with a) 10% wt. sulphuric acid at 20 V, b) 0.3M oxalic acid at 40 V, c) 3% wt. phosphoric acid at 170 V, and d) using hard anodization at 140 V in 0.3M oxalic acid. The insets in b), c) and d) were placed in order to remark the area proportion between each sample.

The feasibility of various PA types represented in the Figure 41 offers porous films that consist of well ordered nano-pores with diverse geometrical properties. The desired dimension of the pore diameter can be obtained with the appropriate anodizing conditions followed by pore widening process. The pore diameter in the range of 20 nm up to 300 nm with corresponding interpore distance of 60, 105, 310 and 450 nm can be achieved.

UNIVERSITAT ROVIRA I VIRGILI
DEVELOPMENT OF TECHNOLOGY AND APPLICATIONS BASED ON POROUS ALUMINA NANOSTRUCTURES
Lukas Vojkuvka
DL: T-1536-2009/ISBN: 978-84-692-4555-2


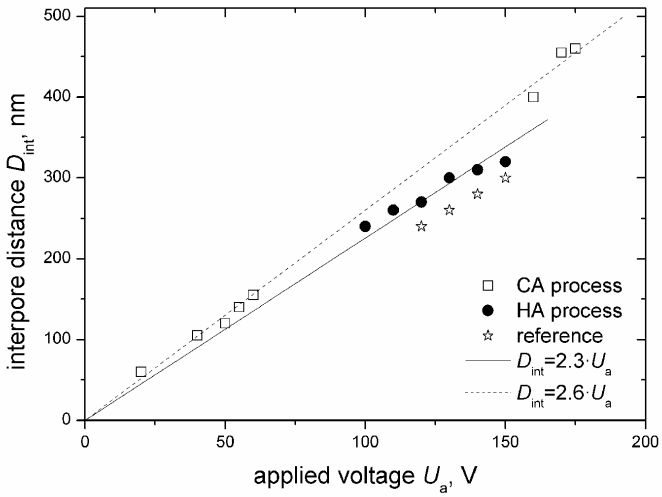


**Figure 42.** Interpore distance with linear dependence on the applied voltage. The experimental data were measured on the porous alumina samples produced with conventional 2 step anodization (CA) and hard anodization (HA) process. (ref. - [52])

The interpore distance and applied voltage relationship established in the Figure 42 summarizes the examination of PA samples from CA (squares) and HA (circles) processes. The linear fit performed on the HA data (solid line) deviates slightly from the fit of CA data (dashed line). The proportionality constant is $k_p$ = 2.3 and 2.6 for HA and CA process respectively. Notice that the interpore distance for HA process is in a good agreement with the reference work [52].

The detailed comparison of conventional anodization (CA) and hard anodization (HA) techniques together with the main features and experimental parameters of the as-produced PA and HPA structures are given in Table 2. Generally from the technological point of view, the HA process requires a system with well-controlled temperature due to a high current which occurs during the anodizing at high applied voltages. On the other hand, CA process is quite time-consuming with a necessity of various anodizing steps with long-time durations. Although HA process is up to 10 times faster than CA process, the exponential current profile makes difficult the estimation of expected film thickness. The quality of the produced PA structures by means of pore uniformity is better for CA because HA process consists of inevitable voltage ramp that forms oxide layer with disordered pore distribution on the top surface

DL: T-1536-2009/ISBN: 978-84-692-4555-2

of the sample. Nevertheless, the preferable usage of CA or HA technique has to be decided depending on the particular application and its technological and quality requirements.

| Features | Conventional anodization | Hard anodization |
|---|---|---|
| Applied voltage $U_a$, [V] | 40 | 100 – 150 |
| Electrolyte temperature, [ºC] | 17 | 1 |
| Anodizing current, [mA] | Linear, < 5 | Exponential, 200 - 30 |
| Interpore distance $D_{int}$ [nm] | 105 | 240-320 |
| Pore diameter $d_p$, [nm] | 35 | 80 |
| $k_p$, [nm/V] | 2.6 | 2.1 – 2.4 |
| Porosity $P$, [%] | 10 | 6 |
| Growth rate, [μm/h] | Slow, 9 | Fast, 80 |
| Pore density , [Nx$10^6$/mm$^2$] | 110 | 17 |

**Table 2** Comparison of the main features of porous alumina from CA and HA process.

### 3.2.2 Pre-patterning using Hard Anodization Process

Figure 43(a) shows a scheme of the pre-patterning approach applied in the common 2 step anodization with 0.3 M oxalic acid, where instead of first anodization step with CA conditions, the HA process with voltage $U_{HA}$ = 140 V is performed. After the selective removal of the oxide formed in the HA step, the Al surface is patterned with ordered large pits. Then, the second anodization step is carried out on the patterned sample using CA conditions with applied voltage $U_{CA}$ = 40 V.

UNIVERSITAT ROVIRA I VIRGILI
DEVELOPMENT OF TECHNOLOGY AND APPLICATIONS BASED ON POROUS ALUMINA NANOSTRUCTURES
Lukas Vojkuvka
DL: T-1536-2009/ISBN: 978-84-692-4555-2


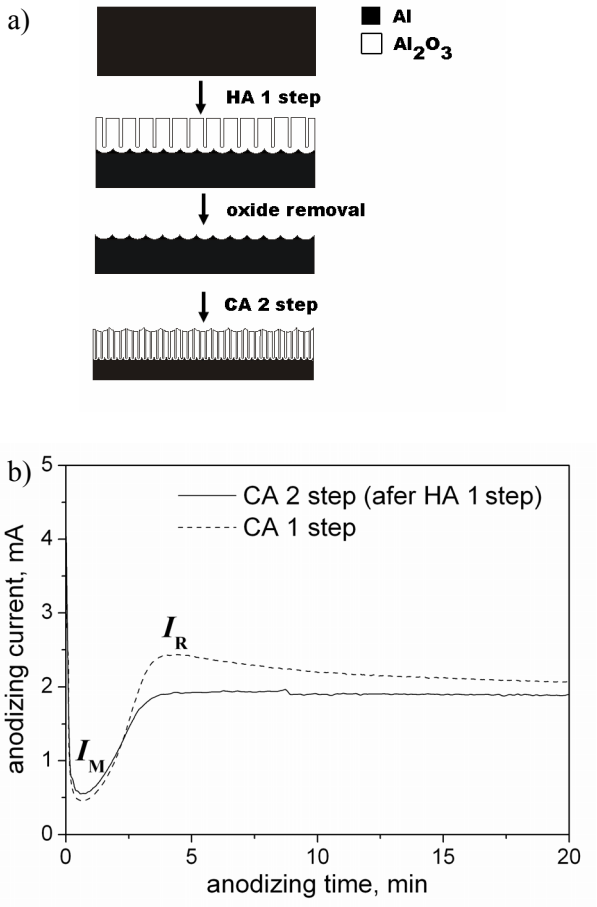


**Figure 43.** a) Scheme of the fabrication procedures for the combined anodization process where the first step is hard anodization (HA) and second step is conventional anodization (CA), b) current-time characteristics of the second step of combined anodization (solid line) compared to first (dashed) step of two step anodization.

Current-time characteristics in the Figure 43(b) represent the second step (solid line) from combined HA-CA 2 step process compared to the current curve of the first step (dashed line) from CA 2 step. Initially, the HA-CA current curve follows the same behaviour as CA first step curve. The same time needed to reach the current minimum $I_M$ and recovery current $I_R$ indicates that the initial formation of the barrier layer and subsequent pore nucleation on the flat (CA first step) and patterned Al surface (HA-CA second step) are very similar. Large pits on the patterned Al probably do not accelerate the formation of barrier layer which is significantly faster in the usual CA second step. Moreover, the missing

bump for $I_R$ in the HA-CA curve can be ascribed to the absence of pore dying process. Apparently, the patterning pits formed on the Al during HA first step contribute to avoid the pore dying phase and the current passes immediately to steady mode.

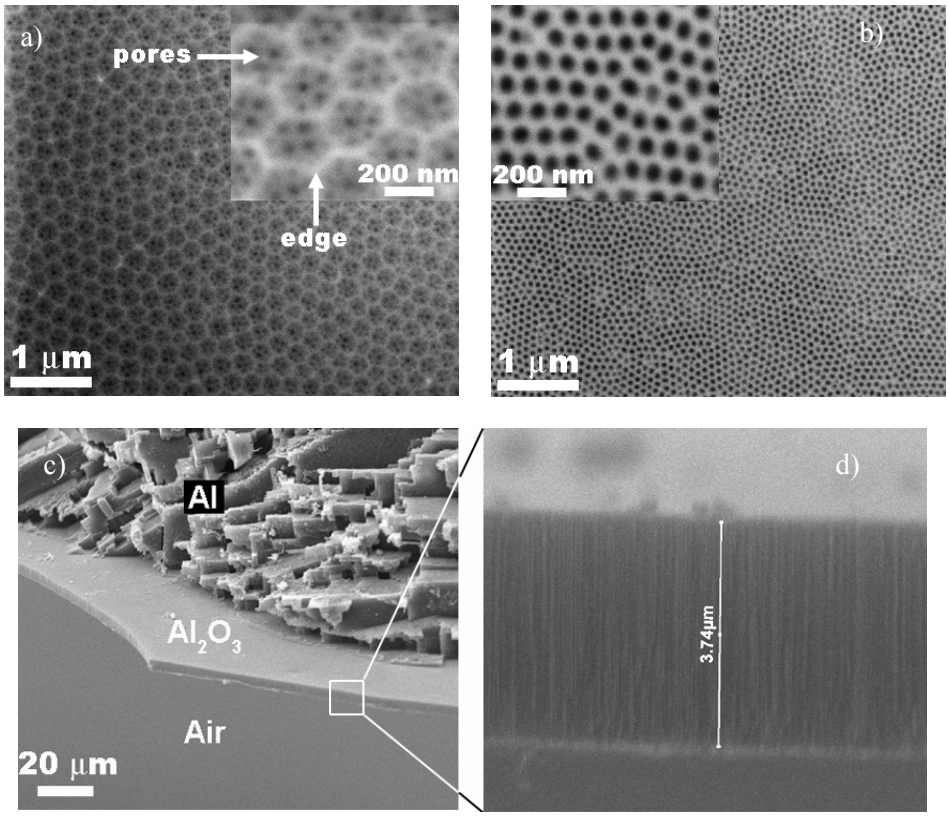


**Figure 44.** ESEM surface images from a) top and b) bottom part of the porous alumina sample produced using combined two step anodization and c-d) cross-section images of the same sample.

The ESEM images of Figure 44 show: a) top surface and b) bottom surface of the resultant PA structure produced in combined HA-CA two step process with first HA step at $U_{HA}$ = 140 V for 15 min and second CA step at $U_{CA}$ = 40 V for 1 hour. Notice, that for bottom surface observation, the remaining Al substrate was selectively etched away and the obtained PA film was consequently etched using pore widening process in 5 %wt. for about 20 min. Figure 44(a) demonstrates a regular roughness on the top surface of the PA sample that

consists of ordered pits with hexagonal shape. It seems that the pores preferentially grow in group inside these pits surrounded by pit edges. In this way, the individual groups of 4 up to 8 pores are formed over the PA top surface as it is shown in the detailed inset of Figure 44(a). This pore accumulations could be formed in the initial phase of the second CA step, when the forming process of the barrier layer completely oxides the tiny pit edges up to height at least 50 nm, which corresponds to the expected thickness of the barrier layer [2, 108]. Afterwards, the pores nucleate perpendicularly to the Al substrate preferentially at the pit bottoms leaving the oxidized pit edges intact. Figure 44(b) shows the result from the bottom surface of the PA sample, where the pores are arranged in expectable form with triangular periodicity. The mean interpore distance was estimated around 100 nm that fits well to the previous results from CA 2 step process.

The ESEM cross-section image in Figure 44(c) captures a fractured piece of PA sample with Al substrate. The detailed view on the oxide thickness in Figure 44(d) reveals the fact that only 3.7 μm of the oxide grew during the anodizing period of 1 hour. The slow growth rate is caused by very low temperature (1 ºC) of the electrolyte [12, 106, 107]. If the ambient temperature is used in common CA 2 step anodization, the growth rate is approximately 10 μm per hour.

### 3.2.3 Double-layered Porous Alumina

The particular PA films fabricated using CA or HA processes have significantly different geometrical properties such as pore diameter and interpore distance. Since both processes require the similar anodizing conditions except the applied voltage, they can be easily combined together in order to grow PA double-layered structure with distinct properties. One of such a possible combination of CA 2 step process and HA process is shown in the Figure 45(a). The illustration shows the fabrication of double-layer PA with first porous layer formed using CA process and the second layer grown using HA process. At the end of the CA second step the anodizing process is simply switched to HA process by applying a rapid voltage ramp meanwhile the rest of the anodizing conditions are kept unmodified.

Figure 45(b) shows the current in logarithmic scale measured during the combined CA-HA process with corresponding voltage profile that starts at $U_{CA}$

= 40 V followed by a voltage ramp with rate of 1 V/s up to target HA voltage $U_{HA}$ = 130 V. The complete CA-HA process consists of CA stage with duration of 3 hours, voltage ramp and final HA stage that lasted 15 minutes. It was observed that the current saturation in the final phase of the voltage ramp occurs already in lower current values (~40 mA) compared to common HA process (~110 mA). This current reduction is due to the relatively thick oxide layer formed in the previous CA stage. The insulating oxide with high pore density also forbids significantly a renewal of the electrolyte species at the pore bottoms. Therefore also the oxide growth that takes place at the metal/oxide interface is slowed down.

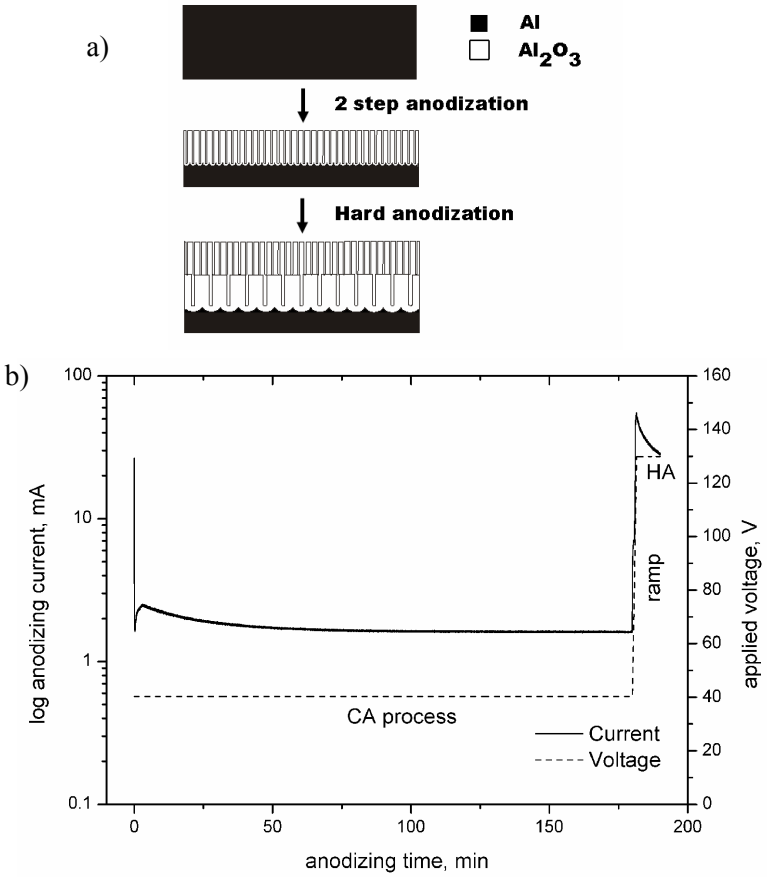


**Figure 45.** Scheme of the fabrication process of double-layer porous alumina produced using conventional two step anodization (CA) and hard anodization (HA), b) current and voltage transients from the CA-HA process.

The morphology analysis of the PA sample from the combined CA-HA process is shown in the Figure 46. The CA stage was conducted at $U_{CA}$ = 40 V for 3 hours and after a rapid voltage ramp to target voltage $U_{HA}$ = 130 V, the HA stage was performed for 15 min. The top surface ESEM image in Figure 46(a) corresponds to the CA stage, where the well ordered pores have distance around 100 nm and size of 40 nm. In comparison, the bottom surface in Figure 46(b) showed out ordered pore tips covered with barrier layer. The mean intertip distance of 240 nm corresponds to applied voltage of $U_{HA}$ = 130 V, however it is deviated from the ideal value (300 nm) obtained in the individual HA process with $U_{HA}$ = 130 V (see Figure 42). This difference of intertip distance is probably caused by the CA top layer that acts as an interfere element for the proper electrolyte removal at the pore bottoms. Notice also that the cell shapes are somehow worse than quite perfect hexagons observed in the Figure 40(d).

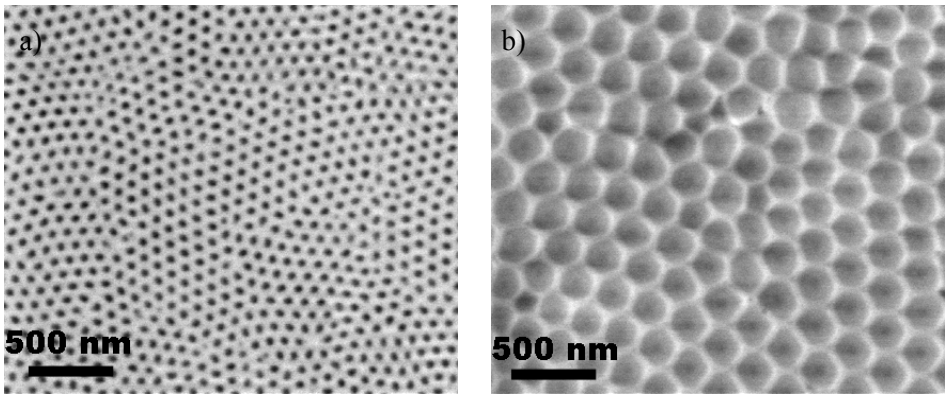


**Figure 46.** ESEM images from a) top and b) bottom surface of the double-layer porous alumina produced in CA-HA process.

The cross-section image of the fractured PA film in the Figure 47(a) was obtained with the optical microscope. As it is remarked in the image, the thickness of the upper CA layer is about 10 μm, whereas the bottom layer grown in HA stage has 15 μm. Note the difference of anodizing periods of 3 hours and 15 min and the calculated growth rate of 60 nm/min and 1000 nm/min for CA and HA stage including the ramp, respectively. The darker hue of CA layer and bright hue of the HA layer indicates the different properties of each porous layer. It was observed before that HA films have almost half porosity than films produced in CA process. The detailed ESEM image focused on the boundary between the CA layer and HA layer is shown in Figure 47(b).

In the upper part of the oxide fracture the pore density is obviously higher that in the bottom part corresponding to HA oxide. The difference of the pore density indicates that many pores most likely have stopped growing during the voltage ramp, where the CA process passed to HA process.

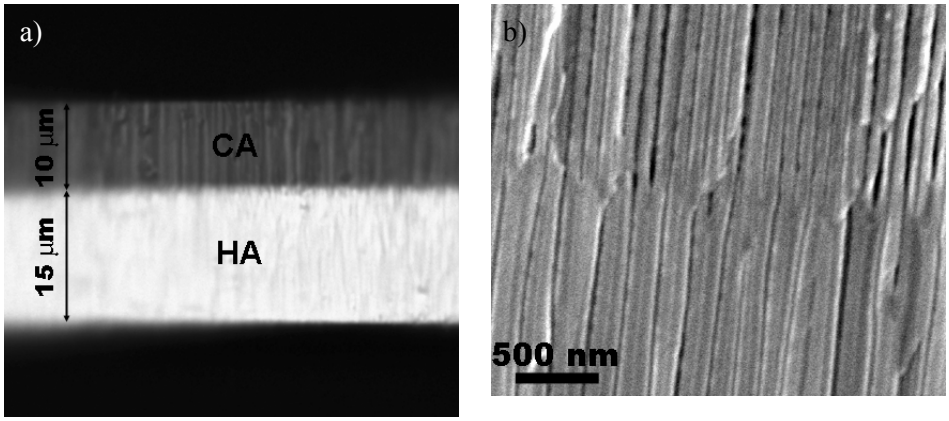


**Figure 47.** a) Cross – section image from the optical microscope showing two distinct porous layers grown in CA and HA process; b) ESEM cross-section image with a detailed view on the transition between CA and HA layer.

### 3.2.4 Multistep Hard Anodization

The fast oxide growth (~ 80 μm/h) during the HA process can be employed for a quick fabrication of multi-layered PA. Figure 48 shows current transient from the multi-step HA process with voltage profile, where the applied voltage varies between $U_{HA}$ = 130 V – 150 V with a period of 20 min for each step. As expected the current decreases exponentially in the first HA period with $U_{HA}$ = 130 V. Then the voltage is switched to $U_{HA}$ = 140 V for the next 20 min period, which is characterized be a rapid current peak at the beginning of the voltage step followed by a slow current decrease until the next voltage step with $U_{HA}$ = 150 V is applied. This step is also accompanied with the initial current peak with following current stabilization. When the next voltage step passes down from 150 V to 140 V and then to 130 V, the current is significantly reduced and also the absence of the initial peak is observed in every step. The final two voltage steps with $U_{HA}$ = 140 V and 150 V are similarly presented with current peaks followed by constant flow. The presence of the current peak after each step up to higher voltage can be explained by a momentary state of the barrier layer. As stated before, the barrier layer thickness is proportional to

applied voltage. Once the voltage is for some reason increased, the barrier layer has to grow up to the corresponding thickness. The current peak at the very beginning of each voltage step is an immediate response to the resistance drop due to the barrier layer recovery. When the proper thickness barrier layer is reached, the current peak is promptly followed by stable mode.
The optical microscope image from the cross-section of PA sample produced with mentioned voltage profile is inserted in Figure 48. The total PA thickness grown in seven steps (140 min) was measured to be 200 μm. All the porous layers formed at corresponding voltage $U_{HA}$ are clearly distinguishable across the sample fracture. The thickness of each layer is dependent on anodizing current since the thickest layer (3) and the thinnest layer (5) were formed correspondingly at $U_{HA}$ = 150 V and 130 V.

Finally, the Figure 49 shows the detailed investigation of the fractured multi-layered PA analysed by ESEM. The image from optical microscope is placed in (e) to facilitate the orientation of magnified ESEM images. Figure 49(a) focuses on the detailed view of the first layer in the multi-layered PA structure. It can be observed that the oxide structure begins to be significantly different at the pore depth of 5 μm from the top surface. The pore distribution seems to be more uniform at the upper part represented by the compact form of the PA fracture, whereas at the certain depth, the oxide fracture consist of many dashes instead of uniform channels. This structural difference is possibly caused in the early phase of the first HA step, where the pre-step CA stage and particularly voltage ramp play an important role. The formed oxide has non-ordered pore distribution due to the constantly increasing voltage and this causes the different forms of fracturing when the sample is mechanically broken. From the depth of approximately 20 μm the oxide fracture is represented by uniformly distributed channels which have grown after the voltage ramp reaches the constant voltage mode. The hypothesis for explaining the fracture anomalies is supported by two facts: i) the non-uniform fracture was observed only in the first oxide layer that is formed during the complete HA process including the pre-step and voltage ramp and ii) the disordered oxide part has the same thickness that was measured at different points along the sample fracture.

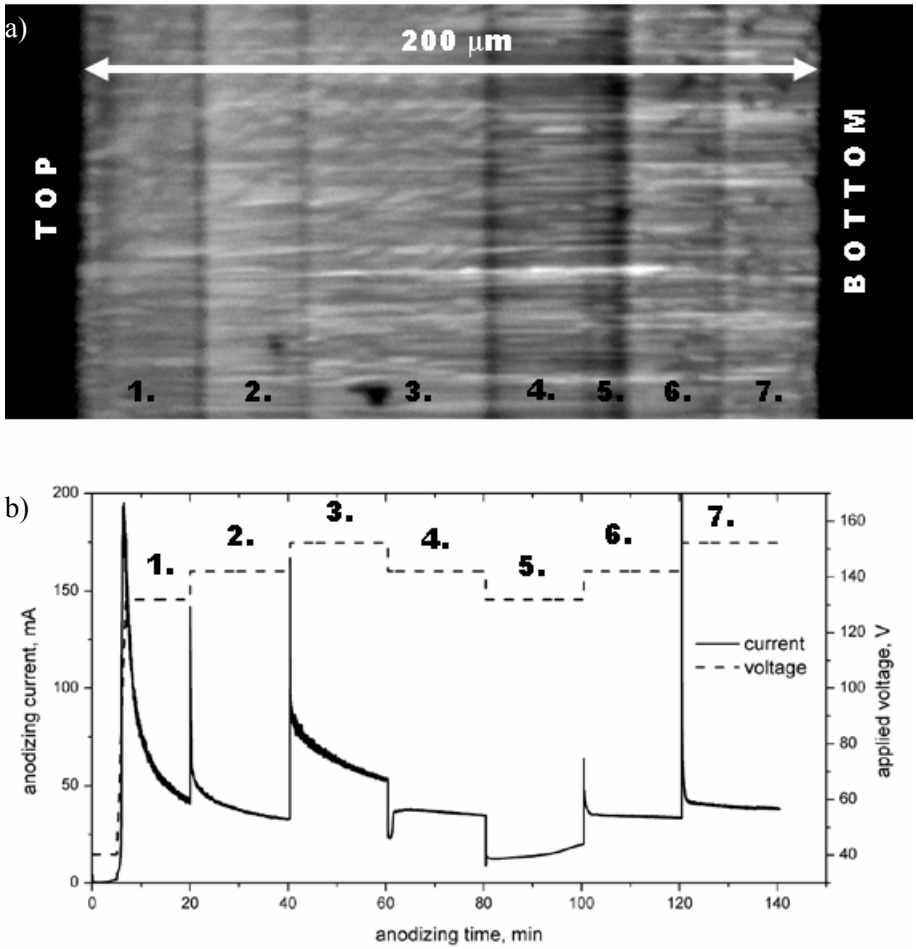


**Figure 48.** a) ESEM image from the fractured porous alumina sample produced in multi-step hard anodization process and b) corresponding current transient with stepped voltage profile.

The pore state at the bottom part of the last layer in the multi-layered PA structure is reflected in the Figure 49(b). The straight pores are evidently closed by a curved barrier layer. Although the total thickness of the multi-layered PA structure is 200 μm, there is still sufficient supply of electrolyte species to ensure the uniform pore growth.

Figures 49(c, d) represent the detailed views on the transition between two distinct porous layers. The both cases correspond to the step up lower to higher applied voltage that was always accompanied by the rapid current peak due to

UNIVERSITAT ROVIRA I VIRGILI
DEVELOPMENT OF TECHNOLOGY AND APPLICATIONS BASED ON POROUS ALUMINA NANOSTRUCTURES
Lukas Vojkuvka
DL: T-1536-2009/ISBN: 978-84-692-4555-2


the barrier layer recovery. In Figure 49(c) some of the pores are branched which is a typical phenomenon occurring in the anodizing with non-constant applied voltage. Figure 49(d) captures the pores that contain a node-like intersection in between left and right porous layer formed at different applied voltages. This pore enlargement could be attributed to the high current peak that was observed during the voltage step from $U_{HA}$ = 140 V to 150 V (see Figure 48). The instant current boost is accompanied with temporal temperature enhancement at the pore bottoms which can cause the local pore dissolution. Afterwards, the current continues in stable mode and the temperature increase is immediately dissipated due to the working temperature maintained close to 1 ºC.

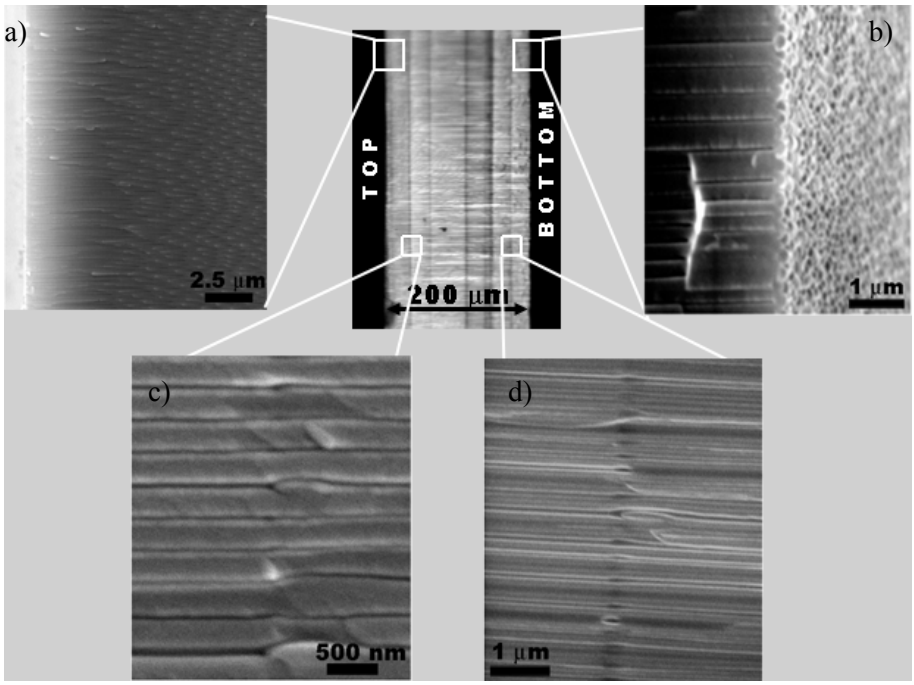


**Figure 49.** Detailed ESEM analysis from the a) top, b) bottom part of the fractured porous alumina sample obtained after multi-step hard anodization. The detailed views on the transition c) between first and second layer and d) between last two layers.

UNIVERSITAT ROVIRA I VIRGILI
DEVELOPMENT OF TECHNOLOGY AND APPLICATIONS BASED ON POROUS ALUMINA NANOSTRUCTURES
Lukas Vojkuvka
DL: T-1536-2009/ISBN: 978-84-692-4555-2

## 3.3

## Summary

This chapter describes the fabrication of self-ordered porous alumina by hard anodization using an oxalic acid electrolyte. The results showed that the formation of the porous layer depends on the specific profile of the voltage applied at different phases of the anodization process. The self-ordering of the pores was best for the voltage between 130 V and 140 V. The interpore distances of the porous alumina produced by hard anodization vary between 240 nm and 320 nm. These values can be used to make up for the values that cannot be obtained between 100 nm and 450 nm in the porous alumina produced by two-step anodization. The biggest advantages of hard anodization over two-step anodization were the effectiveness of the single anodization step and the fast oxide growth. On the other hand, hard anodization produces porous alumina structures with significantly worse pore uniformity because of the variation in the applied voltage. At the end of this chapter new attempts at fabricating novel porous alumina structures are proposed by combining hard anodization and two-step anodization. Ordered pore accumulations were formed on the porous alumina surface by a hybrid two-step anodization in which hard anodization was used as the first anodizing step. Double-layered porous alumina was prepared by a combined process of two-step and hard anodization.

UNIVERSITAT ROVIRA I VIRGILI
DEVELOPMENT OF TECHNOLOGY AND APPLICATIONS BASED ON POROUS ALUMINA NANOSTRUCTURES
Lukas Vojkuvka
DL: T-1536-2009/ISBN: 978-84-692-4555-2

UNIVERSITAT ROVIRA I VIRGILI
DEVELOPMENT OF TECHNOLOGY AND APPLICATIONS BASED ON POROUS ALUMINA NANOSTRUCTURES
Lukas Vojkuvka
DL: T-1536-2009/ISBN: 978-84-692-4555-2

# 4

# Characterization of Porous Alumina

UNIVERSITAT ROVIRA I VIRGILI
DEVELOPMENT OF TECHNOLOGY AND APPLICATIONS BASED ON POROUS ALUMINA NANOSTRUCTURES
Lukas Vojkuvka
DL: T-1536-2009/ISBN: 978-84-692-4555-2

*Chapter 4*

**Understanding the properties of alumina**

Recently, a great deal of research has been made on porous alumina to extend knowledge of its physical properties and to determine a suitable field of application. This chapter, then, uses various analysis techniques to characterize porous alumina structures. The structural properties of porous alumina are determined by X-ray diffraction (XRD). A large section of this chapter studies the optical properties of porous alumina films using such spectroscopy techniques as optical spectroscopy (UV-Vis), Fourier transform infrared spectroscopy (FT-IR) and photoluminescence spectroscopy (PL). At the end of the chapter, the results of studying the mechanical properties using nanoindentation and friction tests are given.

UNIVERSITAT ROVIRA I VIRGILI
DEVELOPMENT OF TECHNOLOGY AND APPLICATIONS BASED ON POROUS ALUMINA NANOSTRUCTURES
Lukas Vojkuvka
DL: T-1536-2009/ISBN: 978-84-692-4555-2

## 4.1

## Crystallization Process of Porous Alumina

The crystallography of porous alumina (PA) structure during the annealing process can be determined by X-ray diffraction (XRD) technique. Basically, the XRD analysis consists of collecting the diffraction patterns that emerge from a rotary sample which is targeted by X-ray beam [118].

The use of porous alumina in many applications such as gas sensors requires a good stability at high working temperatures [119, 120]. The relatively thin PA films (< 100 μm) should sustain large stresses caused by working temperatures of few hundreds centigrade. In this work, several as-produced PA films were annealed at different temperatures from 600 ºC to 1000 ºC in order to study the mechanical stability. It was observed that very thin PA films (< 10 μm) tend to bend due to a large temperature stress. Moreover, the annealed PA film has changed the colour from yellowish to white after annealing over 800 ºC. This indicates significant structural changes that have taken place within the material.

The structural properties of PA films produced at oxalic acid were analysed using X-ray diffractometer Siemens D5000. During the XRD analysis the pulverized PA sample was gradually heated up from the room temperature to the top value of 1200 ºC with various ramp rates of 10º/min, 5ºC/min and 2ºC/min. The XRD spectra were continuously collected at different temperatures of annealing process. The selected spectra with corresponding temperatures are plotted in Figure 50. First, it has to be taken into account the fact, that the three peaks observable at 25 ºC and 700 ºC were detected to have the origin from the platinum sample holder. These peaks are also inevitably present in all of the presented spectra. Considering this point, it can be concluded that analyzed PA sample has amorphous structure up to 700 ºC. At temperature in between of 850 ºC – 1050 ºC initiates the crystallization process demonstrated by several minor peaks which are attributed to the phase mixtures of gamma (γ-) alumina. Notice that also some of the γ- alumina peaks at 2θ = 46 º and 67 ºare overlapped with platinum which can be perceived from the peak width. The major phase transition of alumina takes place at 1100 ºC where the first diffraction peaks of alpha (α-) alumina showed up in the collected spectra.

UNIVERSITAT ROVIRA I VIRGILI
DEVELOPMENT OF TECHNOLOGY AND APPLICATIONS BASED ON POROUS ALUMINA NANOSTRUCTURES
Lukas Vojkuvka
DL: T-1536-2009/ISBN: 978-84-692-4555-2


Finally, at 1200 ºC the crystallization process of alumina is finished by forming almost pure α-alumina, commonly known as corundum, which is represented by nine diffraction peaks in the spectra at 1200 ºC. The similar results were reported also by other groups [110, 121-124]. Based on these experimental data together with the theoretical models, the proportion of the γ- and α-alumina phase was extracted with respect to total crystal content at different temperatures. The results revealed the fact that up to 1000 ºC only γ-alumina phases (~97 %) is present in the crystallized alumina structure. The α-alumina phase is initially formed at temperature above 1000 ºC with a corresponding proportion of 36 % at 1100 ºC and of 93 % at 1200 ºC. Consequently, γ-alumina phase content is reduced to 60 % and 7 % at 1100 ºC and 1200 ºC, respectively.

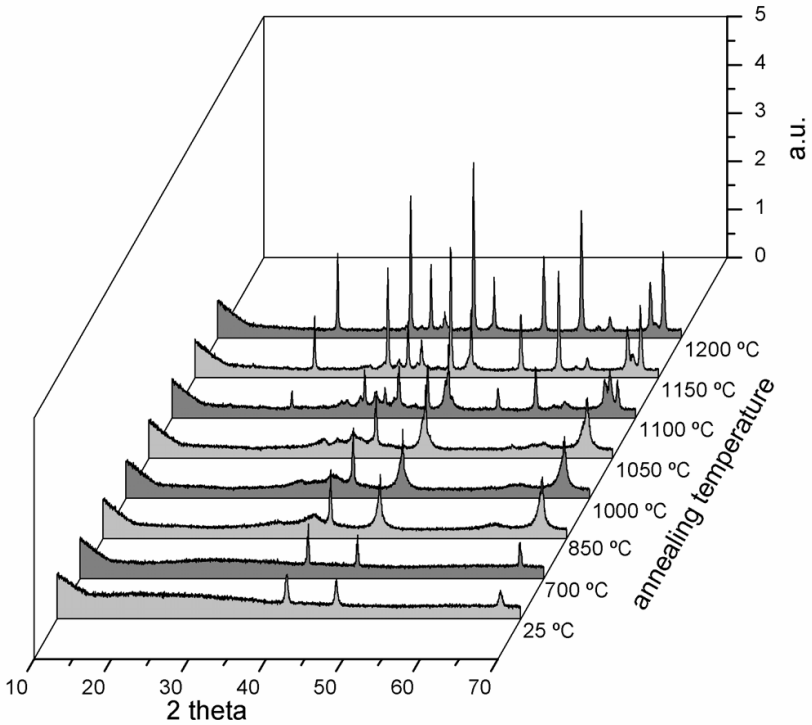


**Figure 50.** Crystallization process during the high-temperature treatment of porous alumina. X-ray diffraction spectra were collected at different temperatures that were gradually increased from ambient temperature up to final temperature of 1200 ºC.

DL: T-1536-2009/ISBN: 978-84-692-4555-2

## 4.2

## Optical Properties of Porous Alumina Films

In last few decades many efforts to study optical materials have been done by the scientific community. The goal is to control the optical properties of novel materials fabricated using ultimate technological advances. A wide range of potential applications are at stake for those materials that could respond to light waves with desired range of frequencies by perfectly reflecting them, or allowing them to pass through only in certain direction or confining them into a specified volume. Already, the discovery of fibre-optic cables which simply guide the light, have caused a revolution in telecommunication industry.

Porous alumina is considered to be interesting optical material due to the periodical structure in nanometric scale. Besides, the relatively facile fabrication process and especially low-cost production makes porous alumina a promising candidate for applications in the field of optical devices such as photonic crystals [41, 44, 82, 87, 125-131].

### 4.2.1 Photonic Band Gap in UV Range

One of the common techniques to study the optical properties of the substances is ultraviolet-visible spectroscopy (UV-Vis). The measuring element in this technique is the source of light with the wavelengths in UV and visible range, where the molecules experience electronic transition. Basically, the optical analysis consists of measuring the intensity of light before ($I_0$) and after ($I$) it passes through the sample. The ratio $I/I_0$ is called transmittance and it is usually expressed as a percentage (%). The obtained results can be interpreted from transmittance spectra as a function of wavelength.

The experimental setup for optical characterization used in this work is shown in Figure 51. The basic components are a light source, a monochromator unit and a detector. A tungsten filament was used as the light source (350 nm – 2500 nm) for the optical analysis of porous alumina. The monochromator with different diffraction gratings was employed to separate the incident light into a single wavelength. The detector of is typically a photodiode or a charge-coupled

UNIVERSITAT ROVIRA I VIRGILI
DEVELOPMENT OF TECHNOLOGY AND APPLICATIONS BASED ON POROUS ALUMINA NANOSTRUCTURES
Lukas Vojkuvka
DL: T-1536-2009/ISBN: 978-84-692-4555-2


device (CCD). The measured sample is fixed with holder placed in the chamber between the monochromator and detector.

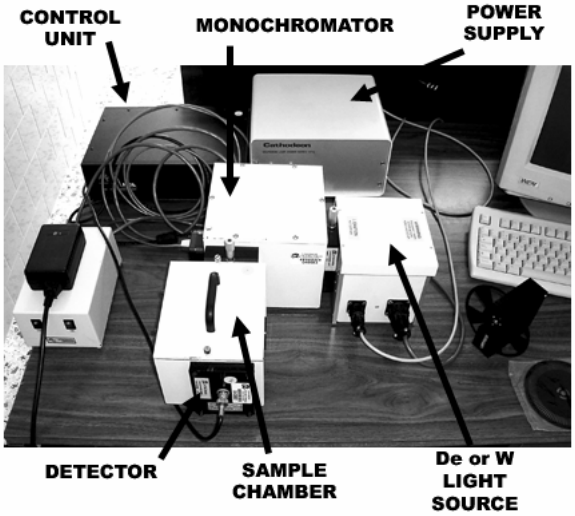


**Figure 51.** Experimental setup for optical characterization in the visible range of electromagnetic spectrum.

The samples for optical characterization were prepared via 2 step anodization process that was already described in the previous chapter. Briefly, after cleaning, annealing and electropolishing treatments of aluminium foils, the ready Al samples were anodized at 40 V in 0.3 M oxalic acid at ambient temperature for 30 min. After oxide removal, the second step was performed with different anodizing times of 1 h, 3 h and 5 h in order to grow the oxides with different thicknesses. Finally, the voltage pulse technique was applied to obtain free-standing PA films. Each PA sample was thoroughly cleaned and divided into four pieces which were consequently annealed at 600 ºC, 800 ºC and 1000 ºC. After the SEM examination of the as-produced PA samples, the complete set of 12 samples consisted of: 3 as-produced PA samples with thicknesses of 9 μm, 24 μm and 45 μm, 3x3 PA samples with the same thicknesses annealed at 600 ºC, 800 ºC and 1000 ºC, respectively.

The PA samples with different thicknesses of 9 μm, 24 μm and 45 μm and annealed at different temperatures: as produced, 600 ºC, 800 ºC and 1000 ºC

DL: T-1536-2009/ISBN: 978-84-692-4555-2

were analyzed by UV-Vis spectroscopy. The transmittance spectra of each sample were measured using a spectrophotometer (SpectraPro-150 monochromator from ARC Inc.) in the wavelength range from 300 nm to 1000 nm. The incident beam from the spectrophotometer was naturally polarized and its direction was perpendicular to the sample surface.

The measured data were analyzed using a standard method for optical characterization [132]. The transmittance spectra were least–squares fitted to simulated spectra that assume a given model for the sample. This model consisted of a free-standing membrane made of a material with the same thickness determined by SEM for as-produced samples. The specific optical properties of the modelled material follow the model of the Lorentz Oscillators with two oscillators. To this end, the simulated spectra for the three thicknesses (9 μm, 24 μm and 45 μm) and with the same annealing temperatures (as-produced, 600 ºC, 800 ºC and 1000 ºC) are analyzed simultaneously using the method described in [132]. With this, the simulation considers that all the samples are made of the same material with the same optical properties. Finally, the goal is to determine the evolution of the optical constants such as refractive index ($n$) and absorption coefficient ($\kappa$) as a function of the annealing temperature.

a)

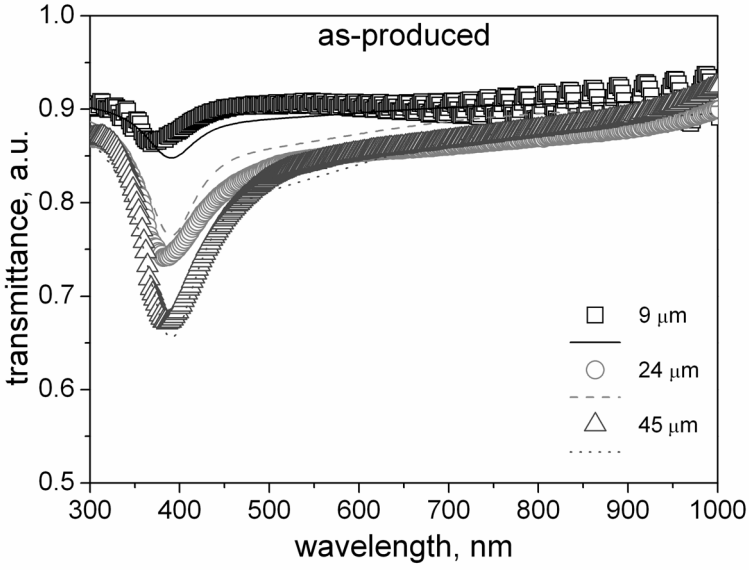
as-produced
transmittance, a.u.
wavelength, nm
9 μm
24 μm
45 μm

b)

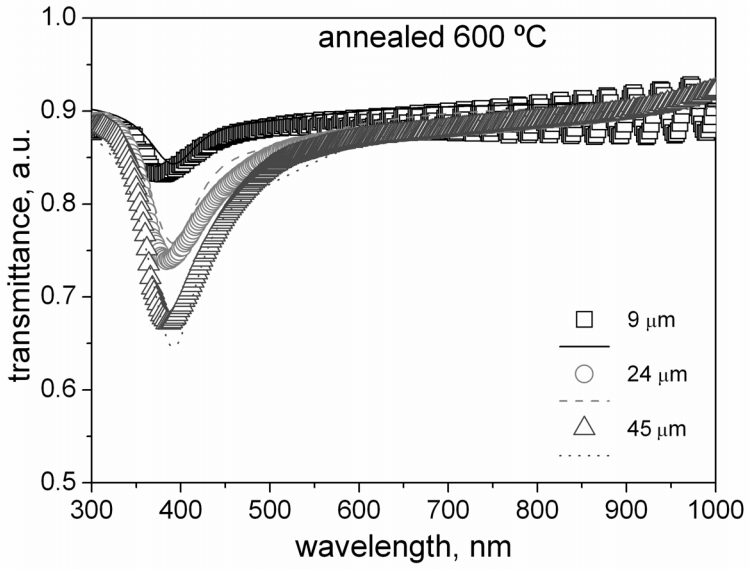
annealed 600 ºC
transmittance, a.u.
wavelength, nm
9 μm
24 μm
45 μm

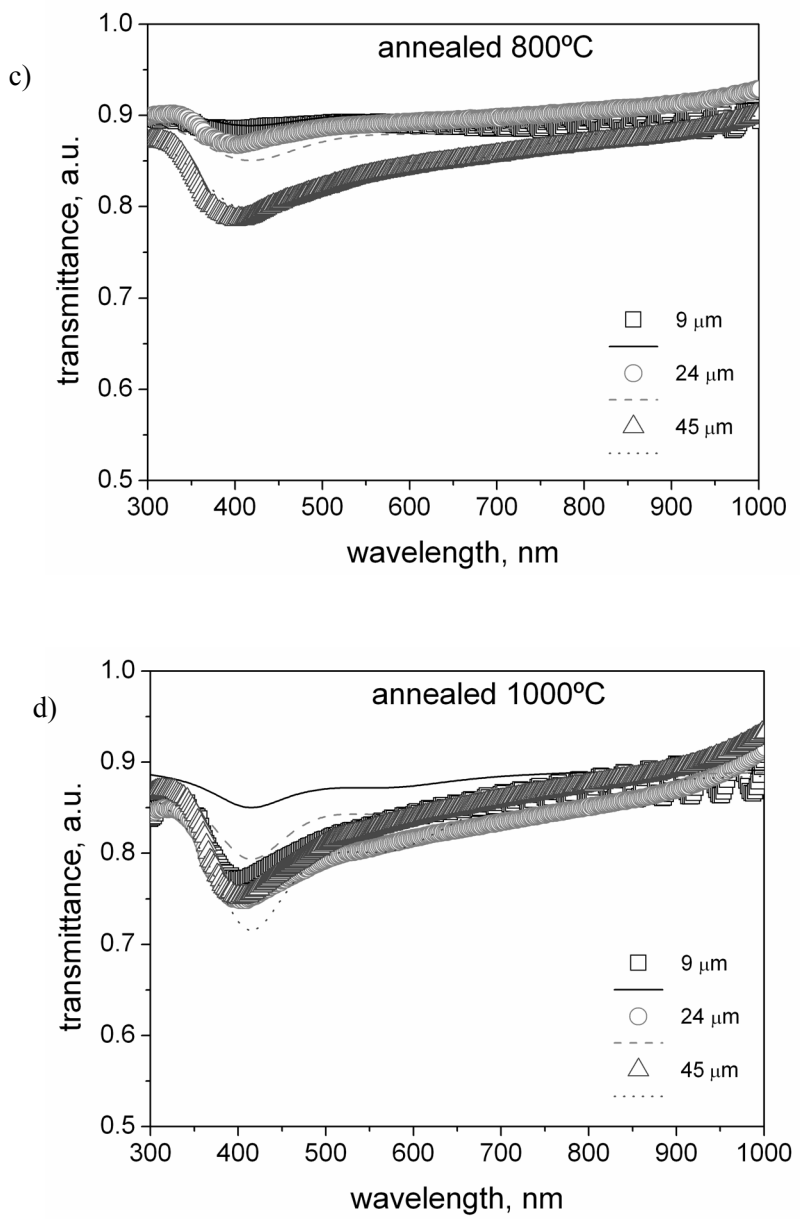


**Figure 52.** Transmittance spectra measured in the UV-Vis range from 300 nm to 1000 nm for porous alumina films with different thicknesses of 9 μm, 24 μm and 45 μm and annealed at temperatures: a) as-produced, b) 600 ºC, c) 800 ºC and d)1000 ºC.

UNIVERSITAT ROVIRA I VIRGILI
DEVELOPMENT OF TECHNOLOGY AND APPLICATIONS BASED ON POROUS ALUMINA NANOSTRUCTURES
Lukas Vojkuvka
DL: T-1536-2009/ISBN: 978-84-692-4555-2


Figure 52 shows the experimentally measured transmittance together with simulated results for PA films with different thickness and annealing temperature. Each plot in Figure 52 corresponds to different annealing treatment: a) as-produced, b) 600 ºC, c) 800 ºC and d) 1000 ºC. The best fits of experimental data were obtained with two oscillators centred at 389 nm and 507 nm. In all the spectra there is an absorption peak with a minimum placed in between of ultra-violet and violet spectrum corresponding approximately to wavelength of 380 nm. The samples thermally treated at 800 ºC and 1000 ºC have this minimum peak slightly blue-shifted and much broader which can be related to changing of structural properties in the annealing process. The as-produced and 600 ºC films recovers the transparency at green spectrum of visible light at 550 nm, whereas the transmittance of 800 ºC and 1000 ºC films after the absorption linearly increase in the remaining wavelength. The thinnest PA sample showed out periodical oscillation of transmittance starting at 600 nm with amplitude that gradually increases with higher wavelengths in the near-infrared region. This is caused by the resonance effect of the Fabry-Pérot interferometer, where the incident light is reflected between two interfaces corresponding in this case to the top and bottom surface of PA film [104, 133].

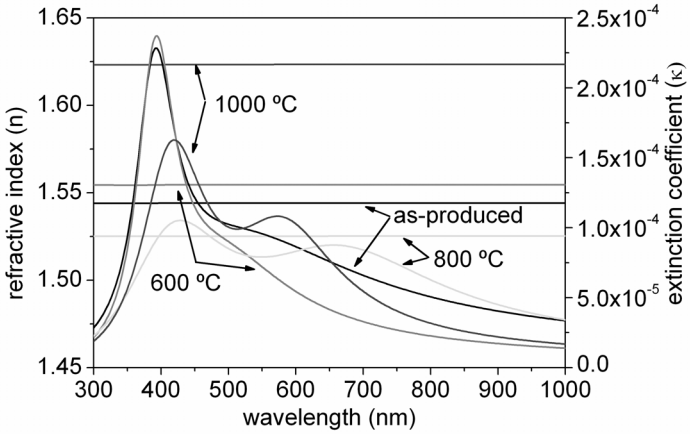


**Figure 53.** Refractive index *n* and extinction coefficient κ obtained for porous alumina with different annealing treatments.

DL: T-1536-2009/ISBN: 978-84-692-4555-2

The obtained optical constants of refractive index (n) and extinction coefficient (κ) for different annealing temperatures are represented in the Figure 53. The refractive index is constant in the measured wavelength range with values of 1.52, 1.54, 1.55 and 1.62 corresponding to as-produced, 600 ºC, 800 ºC and 1000 ºC, respectively. The obtained refractive index values are in a good agreement with those results determined by others groups [17, 104, 134-137]. The extinction coefficient for the as-produced and the 600 ºC annealed samples show one single absorption peak close to 400 nm. In contrast, for the annealing temperatures of 800 ºC and 1000 ºC the extinction coefficient shows two absorption peaks: i) first peak appears near 400 nm and it is blue-shifted with reference to the absorption peaks of the as-produced and 600 ºC annealed samples and ii) second peak that is much broader and centered at a higher wavelength than the first peak. Furthermore, for 800 ºC annealed sample this second peak appears farther and with lower maximum compared to 1000 ºC. The existence of these two peaks and its dependence on the annealing temperature are in good agreement with the photoluminescence observations reported by Xu et al. [121]. The two absorption peaks point to a presence of impurity centres.

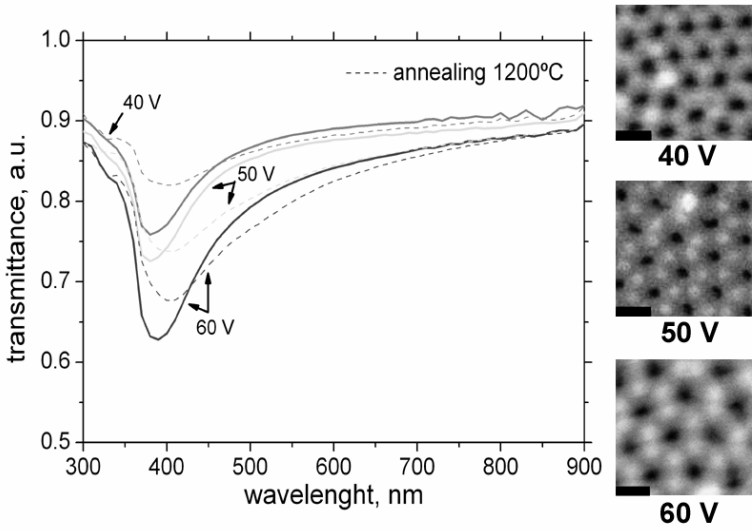


**Figure 54.** Transmittance spectra in the UV – Vis range for porous alumina films anodized at 40 V (red), 50 V (green) and 60 V (blue) and annealed at 1200 ºC. SEM micrographs represent the top surface of the porous film produced at corresponding applied voltage. (Scale bar = 100 nm)

UNIVERSITAT ROVIRA I VIRGILI
DEVELOPMENT OF TECHNOLOGY AND APPLICATIONS BASED ON POROUS ALUMINA NANOSTRUCTURES
Lukas Vojkuvka
DL: T-1536-2009/ISBN: 978-84-692-4555-2


For the additional optical characterization, various PA samples were prepared using distinct anodizing techniques and conditions. In Figure 54 are transmittance spectra experimentally measured for PA samples with the same film thickness of 25 μm produced at oxalic acid with different applied voltages of 40 V, 50 V and 60 V. The as-produced PA films (solid line) are compared with PA films annealed at 1200 ºC (dashed line). Similarly to the previous results, the same absorption peak was observed for all the PA samples and for all the annealed PA samples this peak is blue-shifted and much broader. The difference in absorption intensity can be related to different pore distribution and porosity of each PA sample. The insets with SEM top surface images are placed in Figure 54. The PA sample produced at 40 V has higher porosity than the PA samples produced at 50 V and 60V, and therefore it is more transparent for incident light.

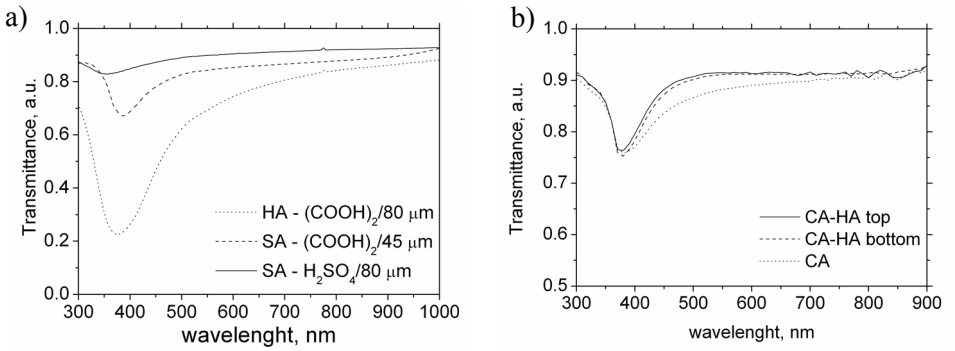


**Figure 55.** a) Transmittance spectra of hard anodized (HA) and conventionally anodized (SA) porous alumina films, and b) spectra for the porous sample prepared using a combination of hard and conventional process.

The results from Figure 55(a) represent transmittance spectra obtained for PA samples fabricated using conventional two step anodization (CA) and hard anodization (HA). The CA-PA sample (solid) was anodized in sulphuric acid and it is almost completely transparent in the measured wavelength range. In comparison, the HA-PA sample (dotted) with same film thickness has a very deep absorption at 380 nm. The adsorption intensity can be partly explained by the film colour, which is dark yellow for HA-PA and practically colourless for CA-PA sample, which indicates different level of impurities in the PA films. The PA sample porosity plays an important role in the material transparency. The porosity of PA samples prepared by hard anodization was previously

DL: T-1536-2009/ISBN: 978-84-692-4555-2

determined to be almost half of the porosity for PA samples from two step anodization.

Figure 55(b) shows the transmittance spectra of the double-layer PA sample prepared by a combination of CA and HA process using different anodizing parameters. The PA sample was measured in two modes with the incident light entering through i) the top sample surface with CA layer (solid line) and ii) the bottom sample surface with HA layer (dashed). The results reveal the absorption peak at 380 nm as compared with previously measured single-layer CA sample (dotted).

### 4.2.2 Impurities Detected in Porous Alumina

Another spectroscopic technique that works with infrared region of the electromagnetic spectrum is infrared (IR) spectroscopy. In this case, the IR spectrum is collected by passing a beam of infrared light through the analysed sample. The IR range of the electromagnetic spectrum is commonly divided into three regions named for their relation to the visible spectrum: the near-IR (NIR), mid-IR (MIR) and far-IR (FIR), covering the wavelength ranges of 1.4 μm - 800 nm, 30 – 1.4 μm and 1000 – 30 μm, respectively. During the measuring process, the wavelength of light can be gradually varied with a monochromator or by using an interferometer based on Fourier transform to achieve simultaneously all the wavelengths at once. The transmittance or absorption characteristics together with IR spectroscopy correlation tables can reveal the detailed information about the molecular composition of the sample. Nowadays, all the modern infrared spectrometers imply Fast Fourier infrared (FT-IR) spectroscopy technique because is cheaper, faster and more precise.

The same type of PA samples from UV-Vis spectroscopy were used for FT-IR analysis. The as-produced and annealed PA films were anodized in oxalic acid at 40 V up to film thickness of 9 μm and 24 μm. All the PA samples were measured in the NIR (1.4 μm - 800 nm) spectrum. The transmittance spectra of PA samples with thickness of a) 9 μm and b) 24 μm are shown in Figure 56. Notice that for IR spectrum is typically used the reverse wavenumber scale in $cm^{-1}$, where the energy decreases with wavenumber. Similarly as it was observed in UV-Vis optical analysis (Figure 52(a)), the thinner sample showed out a typical oscillation due to the Fabry-Pérot effect. A broad absorption peak

appears at 3500 $cm^{-1}$ in the all the spectra for 9 μm and 25 μm. This band is typically observed in the spectra of carboxylic acids, i.e. oxalic acid, water and alcohols caused by the presence of the hydroxyl-containing (OH) compounds [121, 138-141]. Generally, the OH absorption is one the most distinct and recognizable peak in an IR spectrum. However, usually this peak is broadened due the large number of individual molecules that can be bonded to hydrogen and each of the molecules has slightly different adsorption at corresponding wavenumber. Therefore the final OH peak is assumed as an average of all these variations in the absorption. A small peak noticeable at 3000 $cm^{-1}$ for 9 μm - 800 ºC and for 24 μm – as-produced and 600 ºC samples is assigned to CH stretch which occurs specifically in IR spectrum of alcohols such as ethanol. Finally, a large peak placed at 2400 $cm^{-1}$ is due to the presence of carbon dioxide ($CO_2$) and normally it is excluded from the spectra interpretation. In both spectra of 9 μm and 24 μm samples, the largest OH band corresponds to samples annealed at 800 ºC. It is interesting that the same kind of samples showed out the lowest absorption in the optical characterization UV-Vis range, which can be related to the highest level of OH compounds in the measured PA sample. Apparently, the porous alumina is contaminated by OH and CH groups from the electrolyte used for the anodization or from the ethanol in the cleaning procedure.

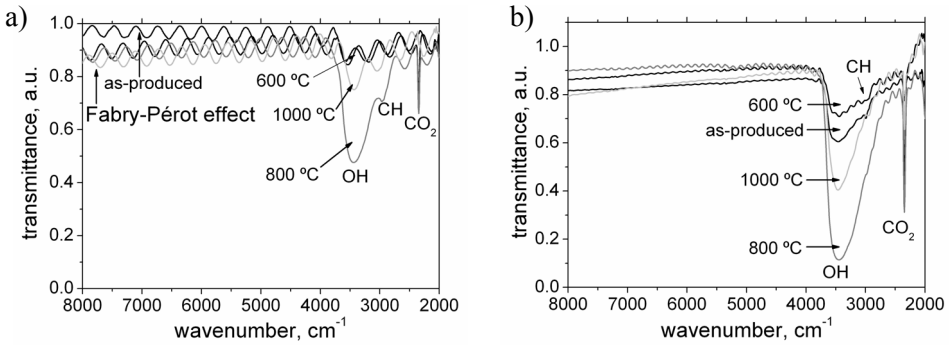


**Figure 56.** FT-IR transmittance spectra measured for porous alumina with different annealing temperatures and thicknesses of a) 9 μm and b) 24 μm.

UNIVERSITAT ROVIRA I VIRGILI
DEVELOPMENT OF TECHNOLOGY AND APPLICATIONS BASED ON POROUS ALUMINA NANOSTRUCTURES
Lukas Vojkuvka
DL: T-1536-2009/ISBN: 978-84-692-4555-2

### 4.2.3 Photoluminescence of Porous Alumina

Photoluminescence (PL) spectroscopy is a non-contact and non-destructive method of probing the electronic state of materials, where a substance is irradiated with the incident light source, which can cause the photo-excitation process within the substance. In other words, PL is an excitation of the substance to a higher energy state and then a return to lower energy state is accompanied by the release of energy in the form of photons. The PL emission spectrum contains specific peaks related to the corresponding energy levels which are used to determination of structural properties.

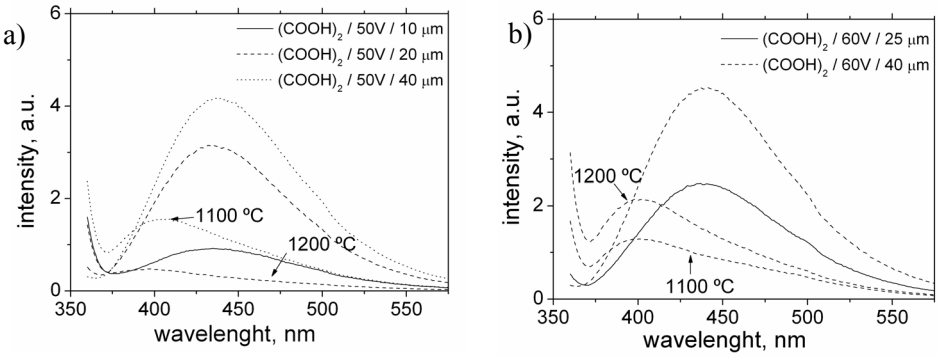


**Figure 57.** PL spectra of porous alumina anodized at a) 50 V and b) 60 V with annealing treatment. The samples were excited at 350 nm.

In this work, the PL spectra of PA samples were measured with a luminescence fluorimeter (Aminco-Bowman Series 2) equipped with source xenon lamp. The PA samples were excited by the light source (350 nm) at monitoring wavelength of 450 nm. The PL spectra were collected at wavelength between 350 nm and 600 nm at room temperature. Figure 57 shows PL spectra of PA samples prepared using oxalic acid at a) 50 V and b) 60 V and annealed at high temperature of 1100 ºC and 1200 ºC. All the as-produced PA samples without annealing treatment present a large blue PL peak centred at 440 nm. The intensity of this PL peak is reduced with the film thickness due to volume of the bulk material. In both cases of 50 V and 60 V, the annealed samples are blue-shifted and the observed PL peak is also significantly reduced. Accordingly, all the PL peaks are placed at wavelength of 400 nm. Recently, the blue PL in PA structures was ascribed to the $F^+$ and F centres from the oxygen vacancies, oxalic impurities and surface hydroxyl groups [142-148]. The blueshift of the PL peak caused by the heat treatment of the PA samples can be attributed to the

change of structural states and impurity concentrations within the material [121, 123, 139, 140, 149]. This observation can be confronted with FT-IR results, where the hydroxyl groups and other impurities cause a broad temperature dependent band.

UNIVERSITAT ROVIRA I VIRGILI
DEVELOPMENT OF TECHNOLOGY AND APPLICATIONS BASED ON POROUS ALUMINA NANOSTRUCTURES
Lukas Vojkuvka
DL: T-1536-2009/ISBN: 978-84-692-4555-2

## 4.3

## Mechanical Characterization Using Nanoindentation and Friction Test

A good knowledge of mechanical properties of porous alumina is required for the possible application in nanodevices, where the mechanical interaction with other objects is expected. Indentation tests are perhaps the most commonly applied techniques for determination of mechanical properties [150]. Recently, the concept of nanoindentation was also established and very small volumes of materials can be investigated in nanometric scale. Basically, the nanoindentation test uses a tip that is pressed on the sample surface under precisely controlled load. The tip, also called indenter, is made of hard material such as diamond with specific shape. The frequently used indenter for nanoindentation testing is a Berkovich tip which has three-sided pyramid geometry. During the course of indenting cycle, the depth of tip penetration vs. applied load is simultaneously monitored. From this relationship and with the exact indenter dimensions, the mechanical properties of the tested material such as indentation hardness and indentation modulus can be extracted by using a referenced method [151].

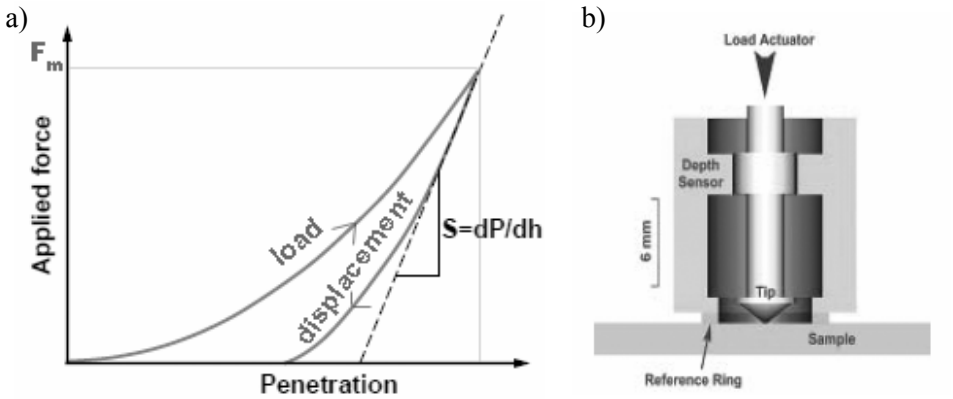


**Figure 58.** a) Typical load-displacement curve from indentation test and b) scheme of measuring system for indetations.

A typical load-displacement curve in the Figure 58 is usually plotted as function of applied force and tip penetration depth. The indentation hardness $H_{IT}$ of the tested material can be calculated as follows:

$$H_{IT} = \frac{F_m}{A_p}$$

, where $F_m$ is maximum applied force at the end of the loading process and $A_p$ is projected area at the same maximum force. The indentation modulus $E_{IT}$ is defined using the slope of the tangent of displacement curve and the tip properties:

$$E_{IT} = \frac{1-\nu_s^2}{\frac{1}{E_r} - \frac{1-\nu_i^2}{E_i}}$$

, where $E_i$ is the elastic modulus of the tip (1141 GPa for diamond), $\nu_i$ is the Poisson's ratio of the tip (0.07 for diamond) and $\nu_s$ is Poisson's ratio of the tested material (0.23 for alumina). The reduced modulus $E_r$ is calculated from experimental data as follows:

$$E_r = \frac{\sqrt{\pi} \cdot S}{2 \cdot \beta \cdot \sqrt{A_r}}$$

, where β is a geometrical constant, $S$ is a stiffness given by slope of the displacement curve d$F$/d$h$ and $A_r$ is projected area of the residual indentation after complete tip displacement. Notice, that $A_p$ and $A_r$ are calculated considering the penetration depth and perfect geometry of the Berkovich tip.

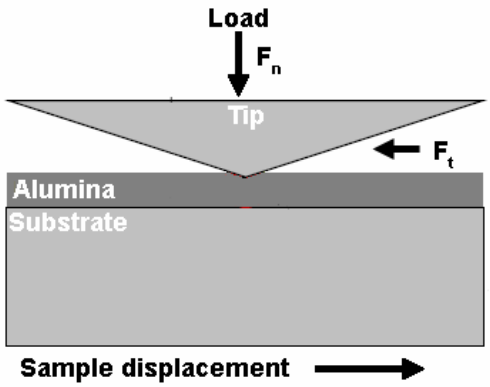


**Figure 59.** Scheme of scratch test, where a tip is pressed on the sample surface meanwhile the sample is displaced.

DL: T-1536-2009/ISBN: 978-84-692-4555-2

Scratch testing of materials is other well-established technique dedicated to characterization of the surface mechanical properties of thin films and coatings, e.g. adhesion, fracture or deformation. As it is shown in Figure 59, the scratch test involves generating of a controlled scratch by pressing a tip onto the material surface which is being displaced. During the test, the applied normal force $F_n$ and the tangential force $F_t$ are measured in order to quantify the friction coefficient of the tested material:

$$\mu = \frac{F_t}{F_n}$$

Three major types of porous alumina samples with different geometrical properties were prepared for mechanical testing using nanoindentation and scratch test. The fabrication was realized via two step anodization process using: i) electrolytes of 10 wt.% sulphuric acid, 0.3 M oxalic acid and 3 wt.% phosphoric acid and ii) applied voltages of 20 V, 40 V and 170 V, respectively. The duration of second anodization step was properly adjusted to obtain film thickness about 25 μm. In order to increase the sample porosity, the PA samples were etched in 5 wt.% $H_3PO_4$ at 35 ºC for various duration depending on sample type. More detailed description of the fabrication process, pore widening process, porosity calculation or SEM analysis can be found in the second chapter. To avoid a repetition of long sample labels, in the following text each PA sample produced at sulphuric acid, oxalic acid or phosphoric acid is denoted as SPA, OPA and PPA, respectively.

### 4.3.1 Dependence of Hardness and Young's Modulus on the Porosity

In this work, the PA samples were mechanically examined using nanoindentation tester (CSM instruments) with employed Berkovich tip. Two measurement modes were applied on the samples during the analysis: single indentation (SI) mode and multicycled indentation (MI) mode. In the SI mode the loading force is applied in wide range of 1 mN to 250 mN starting at $F_0$ = 1 mN in the first indentation and in every next indentation step the force is increased according to the following equation: $F_n = F_{(n-1)} + n$ [mN], where $n$ = 1 - 24. Each indentation with corresponding loading force $F_n$ was repeated five times in a row. In summary, one complete SI matrix has 5 per 25 indentations.

The MI mode is based on applying the loading force that is separated to ten cycles. In every cycle, the loading force is gradually increased with step of 25 mN starting at $F_1$ = 25 mN and finishing at $F_{10}$ = 250 mN. In this way, one complete MI measurement has finally ten loading-unloading cycles and each MI measurement was repeated five times in a row.

Representative load-unload curves in the Figure 60 were measured in the SI mode at maximum applied force $F_{max}$ = 250 mN for PA samples with different porosities: a) SPA sample with porosity of 9 % (solid), 18 % (dashed) and 29 % (dotted), b) OPA sample with 12 %, 24 % and 34 % and c) PPA sample with 8 %, 20 % and 32 %. In the following text, the corresponding sample porosities will be referred as low (9 %, 12 % and 8 %), medium (18 %, 24 % and 20 %) and high (29 %, 34 % and 32 %). First conclusion from all the unloading curves is that the studied porous alumina behaves rather as a plastic material considering very low applied force (250 mN). However there is a slight elastic behaviour observable for the PPA, especially for the sample with the high porosity. The penetration depth increases with the sample porosity, which can be also seen from the insets of the SEM analysis placed next to each graph. The size of indents for SPA and PPA samples are comparable, whereas the PPA sample has all the indents much smaller. The shape of loading curve of the SPA and OPA with highest porosity is significantly more bended than the shape of loading curves from the samples with lower porosity. This indicates that the more porous SPA and OPA samples behave distinctly under applied force. On the other hand, the PPA sample with high porosity has the loading curve represented by almost straight line which means very linear penetration of the tip.

In comparison, the Figure 61 represents the load-unload curves of the PA samples with medium porosity (after first etching). The MI mode with ten cycles (solid) is compared with results form SI mode (dashed). It can be seen that the results from the both modes have a good fit. In all the cases, the depth increment is higher for the first few cycles with low loads compared the last cycles at higher loads. This can be explained by the material compressing after each load-unload cycle. From the extracted mechanical properties, it was actually observed that the hardness increases after each indentation cycle.

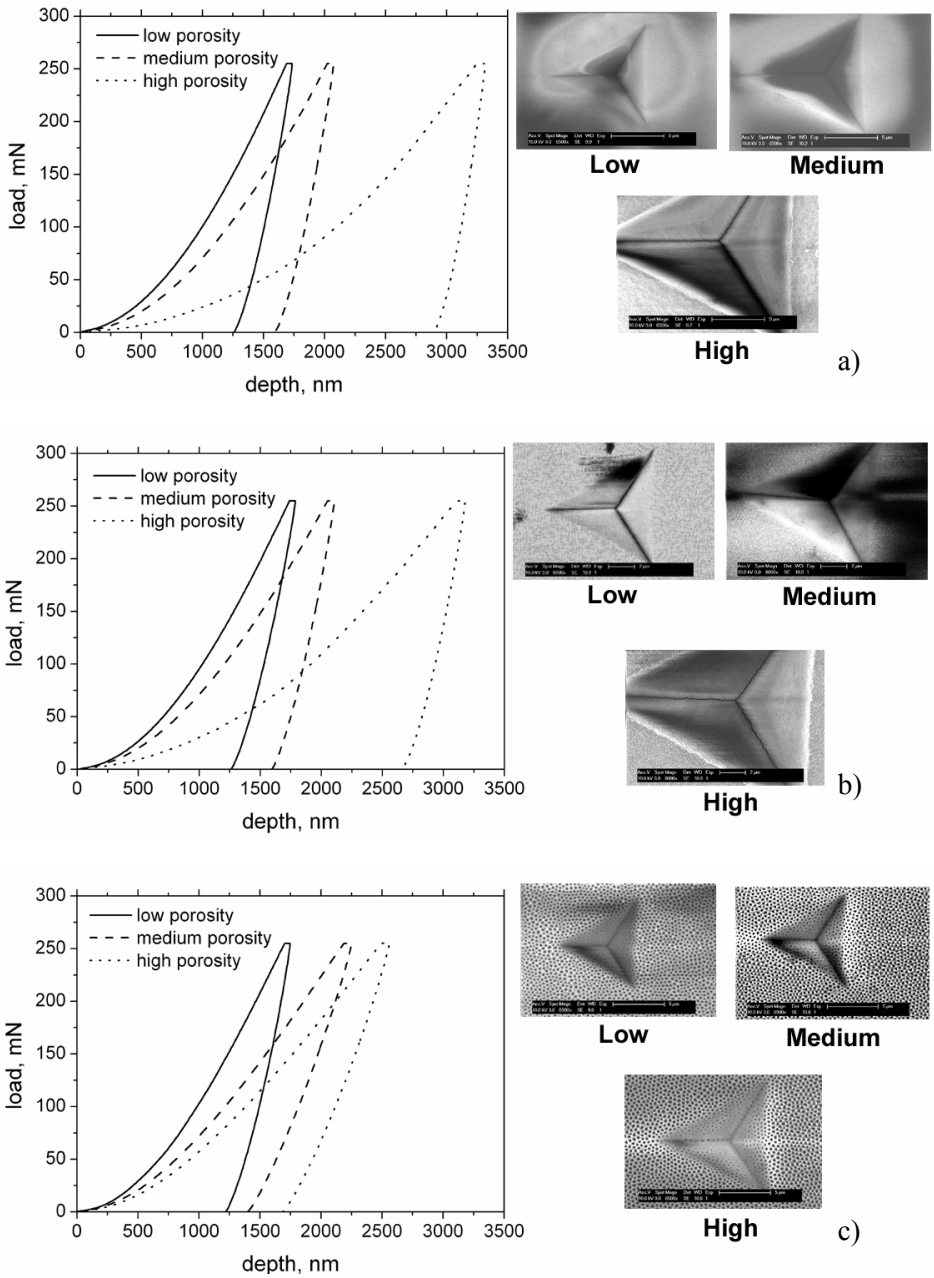


**Figure 60.** Load-unload curves from the single nanoindentation (SI) testing at applied force of 250 mN. The tested samples were porous alumina with different porosities and anodized at different electrolytes of: a) sulphuric acid, b) oxalic acid and c) phosphoric acid. FEG-SEM images represent the selected indents formed after the corresponding test.

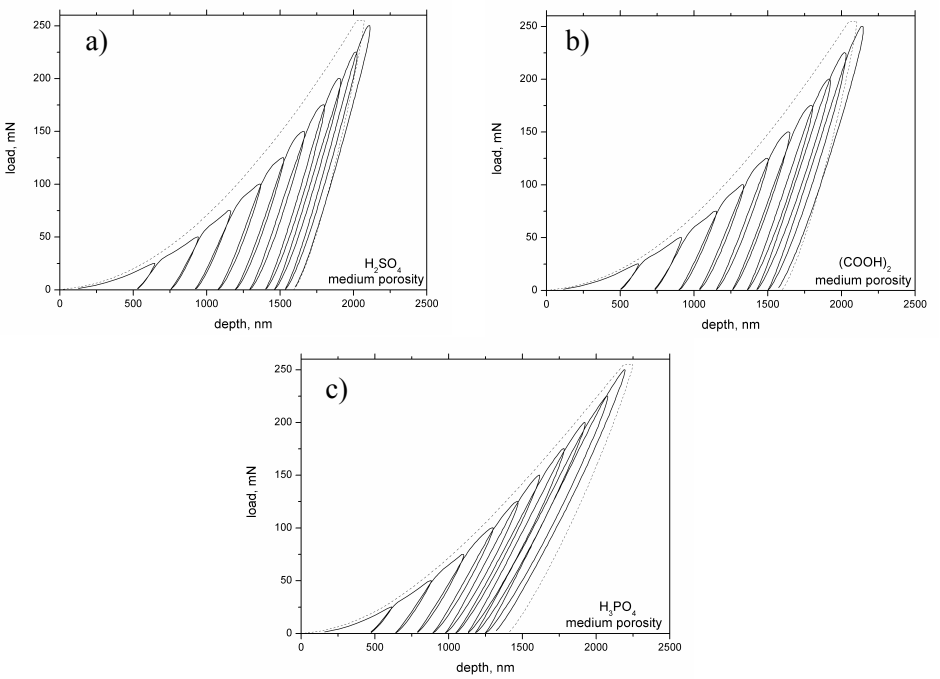


**Figure 61.** Load-unload curves from multi-cycled nanoindentation (MI) testing at 250 mN applied to porous alumina anodized at electrolytes of: a) sulphuric acid, b) oxalic acid and c) phosphoric acid. The dashed line represents the single indentation (SI) curve.

From the experimental data obtained during the indentation tests, the mechanical constants such as hardness *H* and Young's modulus *E* were extracted using Oliver and Pharr method described at the beginning of this chapter [151]. The calculation of the *H* and *E* values was processed via software developed by the nanoindenter provider. The results for SPA, OPA and PPA with low, medium and high porosity are summarized in Table 3. Notice that for SI mode the mean value of *H* and *E* calculated for all the performed indentations (5 x 25 = 125 values) are presented. In the same way for MI mode, the mean values of H and E were calculated always from all ten cycles and five repetitions (10 x 5 = 50 values). The results show that the *H* and *E* from SI mode and MI mode are closely comparable. The comparative Table 4 gives the results from the reported works with similar conditions [137, 152-162]. The difference between the values of *H* and *E* from this work and from the references is affected by the applied model for correlation of as-measured data.

| Sample | Pore etching [min] | Porosity [%] | *H* [GPa] | | *E* [GPa] | |
|---|---|---|---|---|---|---|
| | | | SI mode | MI mode | SI mode | MI mode |
| SPA | 0 | 8 | 5.1 | 5.3 | 109 | 93 |
| | 5 | 15 | 3.5 | 3.1 | 77 | 68 |
| | 10 | 25 | 1 | 1 | 50 | 46 |
| OPA | 0 | 10 | 5.9 | 5.4 | 105 | 92 |
| | 10 | 20 | 3.6 | 3.3 | 78 | 65 |
| | 20 | 28 | 1.5 | 1.2 | 49 | 44 |
| PPA | 0 | 7 | 6.5 | 5.1 | 135 | 85 |
| | 20 | 16 | 5.3 | 3.9 | 83 | 49 |
| | 40 | 26 | 3 | 2.8 | 50 | 39 |

**Table 3.** Hardness and Young's modulus of tested porous alumina samples.

| Alumina type | Porosity [%] | *H* [GPa] | *E* [GPa] | Reference |
|---|---|---|---|---|
| OPA | 8 - 58 | 13 - 4 | 130 - 60 | [157, 158] |
| OPA | 10 - 30 | 6 - 5 | 120 - 80 | [155] |
| OPA | 10 - 30 | 11 - 4 | 130 - 60 | [160, 161] |
| PPA | 10 - 50 | - | 105 - 30 | [160, 161] |
| Barrier-type | Non-porous | 7 | 122 | [153] |
| Fine-grained | Non-porous | 20 | 409 | [156] |

**Table 4.** Results obtained in previous works with similar experimental conditions.

UNIVERSITAT ROVIRA I VIRGILI
DEVELOPMENT OF TECHNOLOGY AND APPLICATIONS BASED ON POROUS ALUMINA NANOSTRUCTURES
Lukas Vojkuvka
DL: T-1536-2009/ISBN: 978-84-692-4555-2


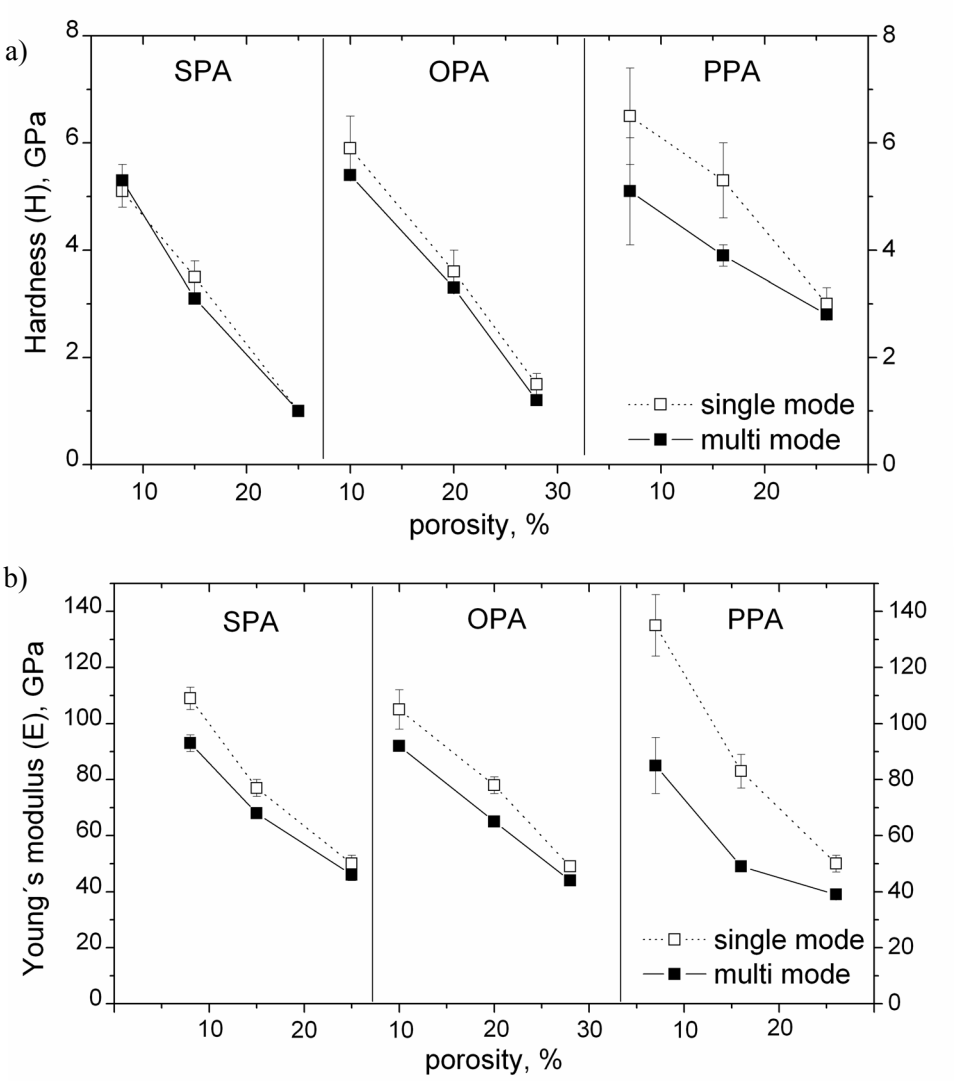


**Figure 62.** a) Hardness *H* and b) Young's modulus *E* dependence on the sample porosity of the porous alumina produced using $H_2SO_4$ - SPA, $(COOH)_2$ - OPA and $H_3PO_4$ - PPA electrolytes.

The data from Table 3 are plotted altogether in Figure 62, where is a) hardness *H* dependence on porosity and b) Young's modulus *E* dependence on porosity for all the three samples SPA, OPA and PPA. Notice that SI mode values are represented by solid line and MI mode values are in dotted line. The hardness linearly decrease from approximately 5 to 1 GPa, from 6 to 1.5 GPa and from 6.5 to 3 GPa, for SPA, OPA and PPA with low, medium and high porosities,

DL: T-1536-2009/ISBN: 978-84-692-4555-2

respectively. Notice, that *H* for SI mode is fairly superior to MI mode, which can be caused by the fact, that in the MI mode the material is allowed to relax in between the cycles, whereas during the SI mode it is continuously under loading force. Young's modulus also drops for SPA, OPA and PPA from 109 to 50 GPa, from 105 to 49 GPa and from 135 GPa to 50 GPa, respectively. Notice that for PPA sample the *E* values obtained from SI mode are highly different from those collected from MI mode. Moreover, with porosity increase of the PAA sample the E difference between both SI and MI modes is smaller. This means that: i) the tested PAA sample showed out a higher elasticity at single indentation, and ii) the low porosity causes that the mean elasticity in MI mode is much lower, because the material can disperse the stress accumulated in each loading cycle.

### 4.3.2 Friction Properties of Porous Alumina

Besides the nanoindentation analysis, the scratch tests of the SPA, OPA and PPA samples with different porosities were performed on multi specimen test machine (MUST - Falex). Only few works focused on the study of fiction properties of porous alumina were reported up to date [159, 160, 163, 164]. Table 5 gives the summary of various scratching devices with different cantilevers and tips. Basically, a glass cantilever with mounted Berkovich tip was used for very low applied forces $F_n$ only up to 10 mN. Steel cantilevers $S_1$ and $S_2$ are much stiffer and the tested range of applied force was $F_n$ = 20 mN – 450 mN. The cone tip on steel cantilever $S_3$ was utilized for scratch measurement with high loads.

The results shown in the Figure 63 were obtained from the scratch tests performed on the SPA, OPA and PPA samples with a) low porosity, b) medium porosity and c) high porosity. The friction coefficient of porous alumina ($c_f$) is calculated by dividing of the recorded tangential force Ft by applied force $F_n$. For the soft glass cantilever $G_1$ with applied force $F_n$ = 1 – 10 mN, the $c_f$ vary between 0.1 – 0.2 for all the samples and porosities. The results for steel cantilevers $S_2$ and $S_1$ with applied force $F_n$ in the range of 20 mN to 100 mN and 50 mN to 400 mN, respectively, showed out increasing tendency of $c_f$ due to the higher penetration depth of the tip. The contact area of the sample and the tip that has very plane three-sided shape increases significantly with the applied force. The approximate value of the depth and contact area can be estimated

from the previous nanoindentation tests. Notice, the $c_f$ values measured at the applied forces of 50 mN to 100 mN, where the $S_1$ and $S_2$ are overlapped, are very similar. In higher forces over 150 mN for PA samples with medium porosities, the $c_f$ is more stabilized in between 0.17 – 0.2 and for SPA and OPA and 0.15 – 0.17 for PPA sample. Notice, that the measured range for PA sample with low porosity was shorter. The $c_f$ of the SPA and OPA samples with high porosity is almost constant in the range of 20 – 400 mN with values in between 0.23 – 0. 26. The PPA sample with high porosity slightly increase the $c_f$ from 0.12 – 0.22. Finally, the results from the scratching with cone tip mounted on the steel cantilever $S_3$ are rather distinct from those obtained with Berkovich tip. This is due to the shape, dimension and material property of the cone tip, which has round shape with radius around 200 μm. The penetration depth of cone tip into the PA sample is much lower. Except for the low porosity PA samples, the $c_f$ obtained from scratches with $S_3$ are lower than from all the scratches performed with Berkovich tip.

| Label | Cantilever | Tip | $k_t$ [mN/μm] | $k_n$ [mN/μm] | $F_n$ (max) [mN] |
|---|---|---|---|---|---|
| $G_1$ | glass | berk. | 0.013 | 0.053 | 10 |
| $S_1$ | steel | berk. | 5.685 | 1.878 | 600 |
| $S_2$ | steel | berk. | 1.137 | 0.556 | 140 |
| $S_3$ | steel | cone | 4.729 | 1.748 | 430 |

**Table 5.** Cantilevers used for scratch tests and their mechanical properties.

The scratch width vs. applied force dependence shown in the Figure 64 was measured after friction tests with a) steel cantilever $S_2$ and b) $S_1$ for the applied forces in the range of 20 mN to 100 mN and from 50 mN to 400 mN (for low porosity samples only to 250 mN), respectively. The measured width of the scratches is linearly increased with the applied forces. With higher sample porosity, also the scratch width increases as the penetration of the tip into PA sample is deeper. One could expected, that for the PA samples with medium and high porosity and with the $c_f$ relatively constant in the applied force range of 150 – 400 mN, the scratch width should be also constant. However, the scratch width linearly increases in this force range. This means that the penetration depth of the tip during the course of scratching do not affect importantly the $c_f$.

DL: T-1536-2009/ISBN: 978-84-692-4555-2

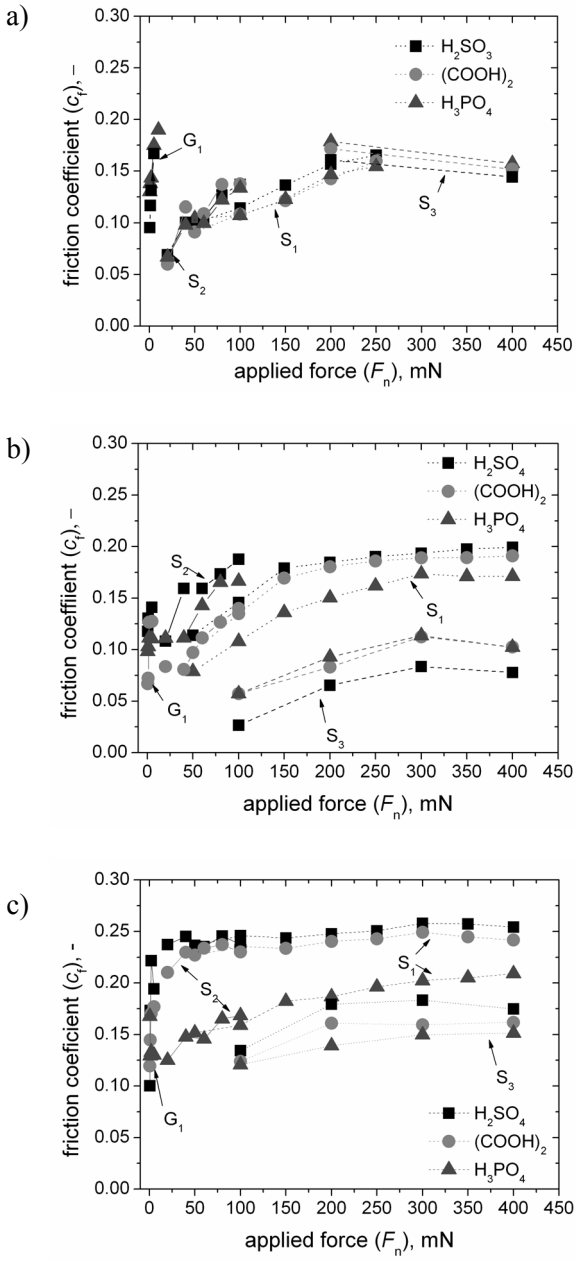


**Figure 63.** Friction coefficient of porous alumina in the function of the applied force. The data were obtained from scratch measurements using different type of scratching devices summarized in Table 2.

UNIVERSITAT ROVIRA I VIRGILI
DEVELOPMENT OF TECHNOLOGY AND APPLICATIONS BASED ON POROUS ALUMINA NANOSTRUCTURES
Lukas Vojkuvka
DL: T-1536-2009/ISBN: 978-84-692-4555-2


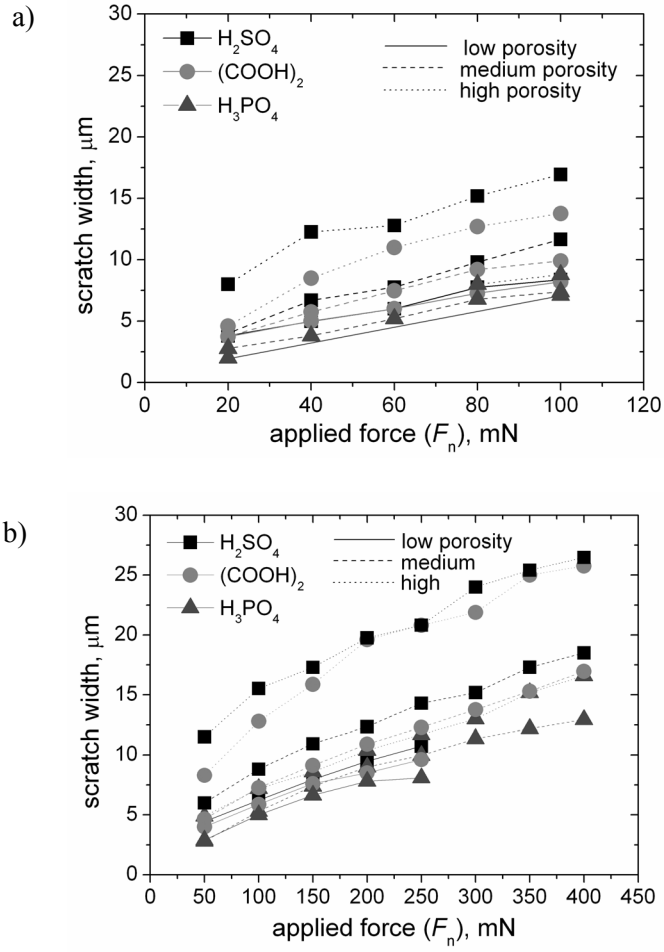


**Figure 64.** Scratch width vs. applied force in the linear dependence measured after the mechanical testing of porous alumina with different porosities.

### 4.3.3 Examination of Indents and Scratches

All the mechanically analysed PA samples (SPA, OPA and PPA) with low, medium and high porosity were inspected by FEG-SEM in order to study the indented areas after nanoindentation tests. Figure 65 collects FEG-SEM top surface images of the indents on the OPA sample with a) low, b) medium and c) high porosity. The indent depth increases with the sample porosity from 1.3 μm, to 1.6 μm and 2.7 μm corresponding to the low, medium and high sample

porosity, respectively. All the indents in Figure 65 were formed under the applied force of 250 mN. Similar results were also obtained for SPA and PPA samples. In all the cases, any superficial cracks were observed on the indent edges or indent sides. However, there was found a cleavage inside the indents of the SPA and OPA samples. The cleavage width is increasingly larger for samples with higher porosity. This cleavage is probably formed during the loading cycle of the indentation process, where the tip is penetrating inside the sample. The shear forces between the tip and the material are concentrated rather on the tip edges than on the tip sides. Therefore, the formed cleavages are also very uniform matching with pyramidal geometry of the tip.

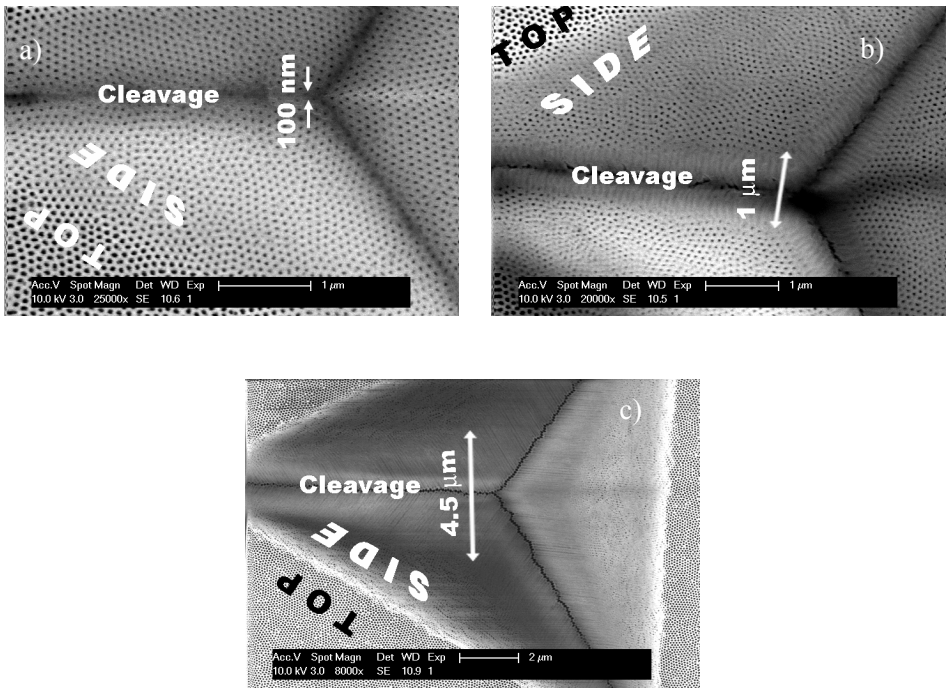


**Figure 65.** FEG-SEM top surface images of the indents on the OPA samples with a) low, b) medium and c) high porosity. The applied loading force was 250 mN.

UNIVERSITAT ROVIRA I VIRGILI
DEVELOPMENT OF TECHNOLOGY AND APPLICATIONS BASED ON POROUS ALUMINA NANOSTRUCTURES
Lukas Vojkuvka
DL: T-1536-2009/ISBN: 978-84-692-4555-2


a)

b)

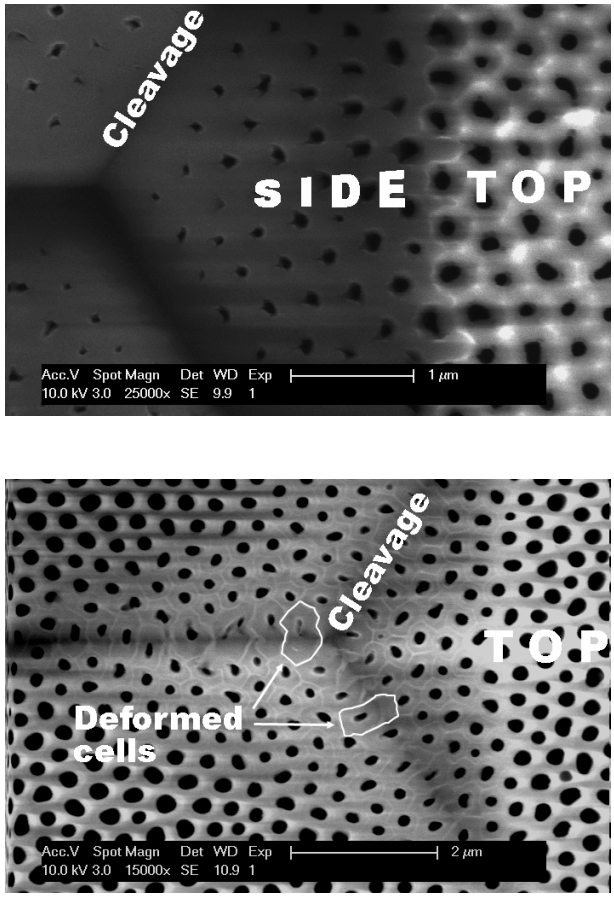


**Figure 66.** FEG-SEM top surface images of indents performed at the applied force of 250 mN on a) PPA sample with low porosity and b) the same indent after wet chemical etching in the phosphoric acid solution.

The indents in Figure 66 were performed under applied force of 250 mN on the PPA sample with low porosity. Figure 66(a) illustrates the indent side with compressed and deformed pores with irregular shapes compared to the original pores on the top surface of the sample. In Figure 66(b) is the same indent after wet chemical etching in phosphoric acid solution used for pore widening. It is noticeable that the deformed pore cells inside the indent are clearly distinguished by the white borders. These white borders of the deformed pore cells can be explained by a large stress that is accumulated between the compressed pore cells after the indentation process. In the course of wet

DL: T-1536-2009/ISBN: 978-84-692-4555-2

chemical etching, the borders of the compressed cells are dissolved in a different manner than the cell walls. The cell deformation is much higher on the indent cleavages than on the indent sides. This also supports the previous suggestion that the shear forces are concentrated on the tip edges during the loading cycle.

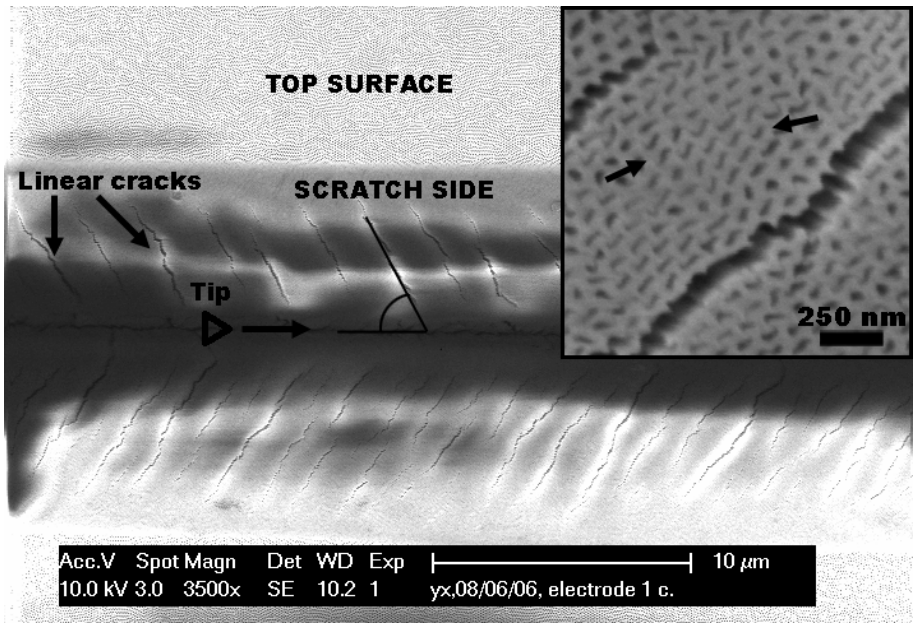


**Figure 67.** FEG-SEM top surface image of the scratch on the OPA sample with medium porosity. The applied load was 400 mN. The inset illustrates a detailed view of the crack.

Although the porous alumina is generally very brittle and stiff material, the absence of the visible cracks and the pore cell deformation on the indented SPA, OPA and especially PPA surfaces indicates surprisingly a plastic behaviour at micrometer scale. This plasticity could be attributed to a high contamination of the studied PA samples by the impurities from anodization and etching processes. It would be interesting to carry out the same set of indentation tests on the annealed PA samples. It was previously reported that during the anodization with high applied voltage, the presence of the aluminium between the cell walls of the porous oxide layer was observed [60]. Particularly for PPA sample anodized at 170 V, the possible existence of metal in the indented

volume could play an important role. Therefore, further analysis focused on the PPA composition is required in order to verify the proposed hypothesis.

After the scratch tests with different applied loads, the SPA, OPA and PPA samples with low, medium and high porosity were closely examined by FEG-SEM. In previous section, it was observed that the scratch width linearly increases with applied load (see Figure 64). FEG-SEM analysis showed out that the SPA, OPA and PPA samples with low porosity did not present any cracks in the scratched area. In contrary, Figure 67 shows FEG-SEM top surface image of the scratch on the OPA sample with medium porosity. Apparent linear cracks were formed along the scratch side as the tip moved forward during the test. The tip orientation and movement direction are indicated in Figure 67. All the cracks have the same angle with respect to the scratch bottom. This angle corresponds to the specific geometry of the pyramidal tip, where the half angle of the tip edges is 65 º. It means that in the course of scratching, the cracks are simultaneously formed on the both sides along the tip edges. Upon a closer observation of the crack area shown in the inset, the cells are collapsed together in rows parallel to the crack. The scratches observed on the SPA sample showed out the same results. Similar pore collapsing behaviour in the nanoindentation of the OPA samples was already reported by Xia et al. [155]. The collapsing mode and the shape of the deformed cells are also similar to shear band formation observed in the stress simulations of large-scale porous metals and polymers which have comparable hexagonal geometry [165, 166].

The FEG-SEM image in the Figure 68 is a part of the scratch performed on the OPA sample with high porosity. Besides the linear cracks presented on the scratch sides, there are also large circular cracks on the scratch bottom. The possible explanation of the appearance of the cracks with circular form can be due to the excessively high load (400 mN). It is generally recommended that during the mechanical testing of materials using nanoidentation, the penetration depth of the tip should be less than 10 % of the total material thickness in order to avoid substrate influence. In other words, for the studied OPA sample with the expected oxide thickness about 30 μm the tip penetration can only go up to 3 μm. Notice that the same OPA sample with high porosity had the indent depth close to 3 μm under applied force of 250 mN. Therefore, the depth limitation was probably exceeded by applying the force of 400 mN during the scratch test and the Al substrate affected the stress distribution and release within PA

DL: T-1536-2009/ISBN: 978-84-692-4555-2

sample. As the tip is moved forward in the curse of scratching, the compressed material is released behind the tip forming circular cracks. A closer inspection of the scratch bottom in the inset shows out that beneath the crushed non-porous alumina is still preserved original porous structure. The identical forming of the linear and circular cracks was observed as well on the SPA samples with high porosity.

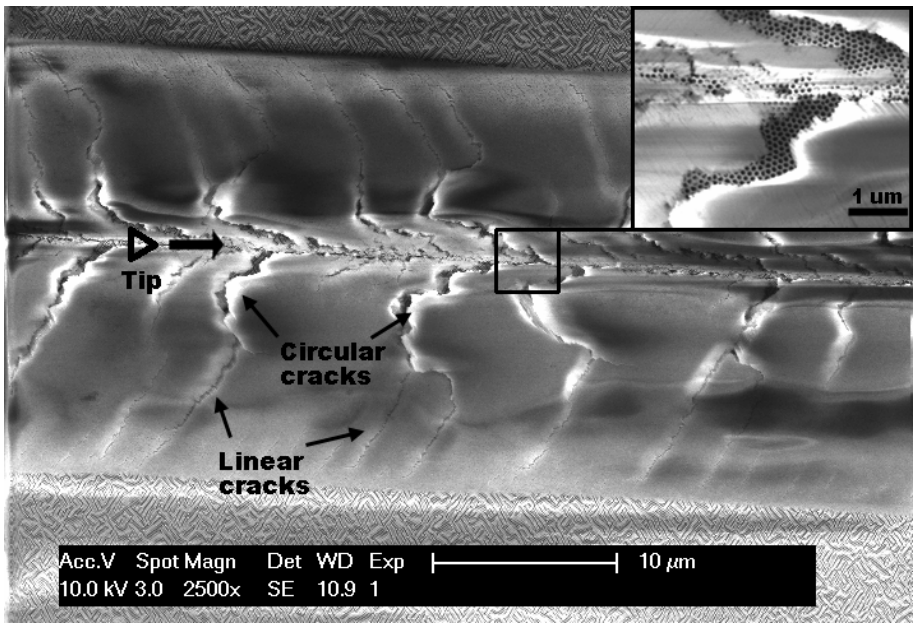


**Figure 68.** FEG-SEM top surface image of the scratch performed with load of 400 mN on the OPA sample with high porosity.

The mechanical behaving of the PPA sample during the scratch test is rather different compared to SPA and OPA samples. First, the absence of crack formation was noticed for low and medium sample porosities inclusively with the applied force of 400 mN. Figure 69 compares FEG-SEM images taken from the scratch sides of a) the PPA sample with medium porosity and b) the same scratch side after wet chemical etching. The scratch side structure in Figure 69(a) appears to be almost completely non-porous with the deformed pore cells arranged in rows. However, Figure 69(b) with the etched scratch side reveals an interesting fact that the material structure is significantly distinct beneath the covering thin layer. Once the non-porous superficial layer from Figure 69(a) is

UNIVERSITAT ROVIRA I VIRGILI
DEVELOPMENT OF TECHNOLOGY AND APPLICATIONS BASED ON POROUS ALUMINA NANOSTRUCTURES
Lukas Vojkuvka
DL: T-1536-2009/ISBN: 978-84-692-4555-2


removed, it can be seen that some of the cells are collapsed and compacted altogether in rows with the deformation direction corresponding to the tip movement (from left to right). The cell borders are clearly remarked due to the different etching behaviour of the sites with accumulated stress. This was already observed in the etched indents in Figure 66. The formation of thin layer of crushed material which is spread over the sample surface during the scratch process refers to plastic behaving of the PPA sample. A high level of impurities or metal presence within the porous structure could be responsible for such a high material plasticity.

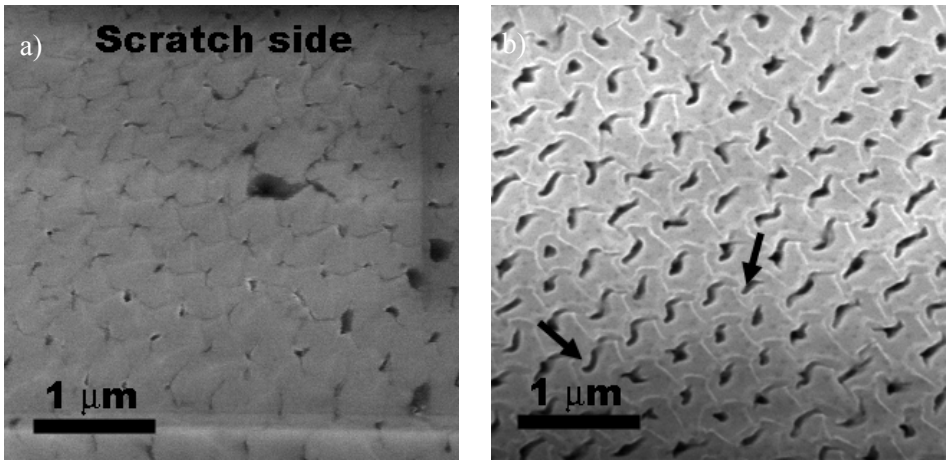


**Figure 69.** FEG-SEM images from the scratch side of a) PPA sample with medium porosity and b) the same scratched area after wet chemical etching.

The scratch in the Figure 70 was formed under the applied load of 400 mN on the PPA sample with high porosity. There are present some linear cracks on the scratch side, which were formed along the tip edges during the scratch process. Notice that the angle of the crack with respect to the crack bottom is the same as it was observed in the scratches of SPA and OPA samples. The penetration depth of the tip is much lower and therefore any radial cracks at the scratch bottom are expected. A large cleavage is formed on the scratch bottom caused by a high shear force between the top of the tip and the loaded material.

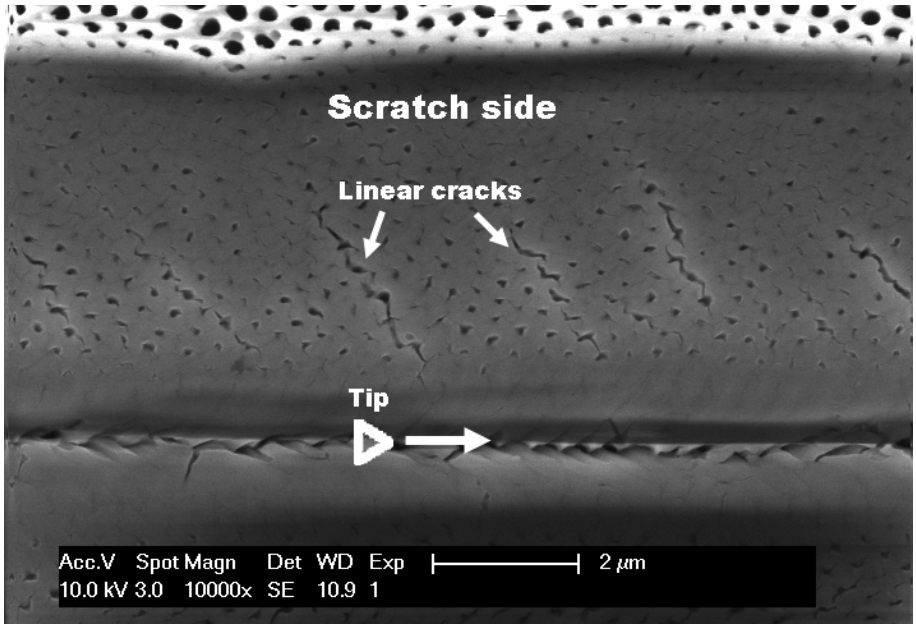


**Figure 70.** FEG-SEM image from the upper part of the scratch formed under applied load of 400 mN on the PPA sample with high porosity.

## 4.4

## Summary

This chapter summarizes the results of the structural, optical and mechanical characterization of porous alumina. The crystallization process of porous alumina was studied in-situ by X-ray diffraction measured between 25 ºC and 1200 ºC. The results showed that the amorphous phase was present up to 700 ºC. At temperatures between 850 ºC and 1000 ºC the phase mixture of gamma alumina was observed followed by final transition into alpha alumina at 1200 ºC. The transmission spectra from the optical characterization using UV-Vis spectroscopy show an absorption peak centred at a wavelength of 380 nm. For the porous alumina samples annealed at high temperatures of 800 ºC and 1000 ºC, this peak was blue-shifted in the wavelength scale. The refractive index and extinction coefficient were simulated using the model for porous alumina. The refractive index obtained was constant in the wavelength range studied with values between 1.52 – 1.62 for as-produced and annealed samples. The extinction coefficient showed an absorption peak close to 400 nm for the as-produced sample and the same sample annealed at 600 ºC. For the samples annealed at higher temperatures of 800 ºC and 1000 ºC, the extinction coefficient presented two absorption peaks: 1) one close to 400 nm, which was slightly blue-shifted with respect to absorption peaks of as-produced and 600 ºC samples and ii) the other at higher wavelengths of 600 nm and 700 nm for annealing temperatures of 1000 ºC and 800 ºC, respectively.

The spectra from FT-IR measurements showed one broad and one stretch absorption peak centred at 3500 cm-1 and 3000 cm-1, respectively. These peaks were attributed to the hydroxyl (OH) and alcohol (CH) impurities formed during anodization and cleaning. Interestingly, the largest OH peak was observed for the sample annealed at 800 ºC, which showed the lowest peak in the spectra of UV-Vis measurements. This peak coincidence indicates that the optical properties depend on the impurity state within the porous alumina. Also the peaks in the PL spectra of the annealed porous alumina samples were shifted and reduced with respect to the as-produced samples. This may be due to the structural changes and different impurity concentrations in the annealed and as-produced samples. The mechanical properties expressed by hardness, Young's modulus and the friction coefficient were extracted from the nanoindentation and friction measurements of the three major types of porous alumina samples

with different porosities. It was observed that hardness and Young's modulus decreased for more porous samples from 5 GPa to 1 GPa and 130 GPa to 40 GPa, respectively. Friction coefficients estimated from the scratch tests were found in the range between 0.7 – 0.25 depending on sample type and porosity. Closer examination by SEM of the indents and scratches revealed that the porous alumina samples studied behaved plastically under the applied load. This may be due to high water contamination and the presence of aluminium within the porous alumina structure.

UNIVERSITAT ROVIRA I VIRGILI
DEVELOPMENT OF TECHNOLOGY AND APPLICATIONS BASED ON POROUS ALUMINA NANOSTRUCTURES
Lukas Vojkuvka
DL: T-1536-2009/ISBN: 978-84-692-4555-2

UNIVERSITAT ROVIRA I VIRGILI
DEVELOPMENT OF TECHNOLOGY AND APPLICATIONS BASED ON POROUS ALUMINA NANOSTRUCTURES
Lukas Vojkuvka
DL: T-1536-2009/ISBN: 978-84-692-4555-2

# 5

# Applications and Promising Future Work

UNIVERSITAT ROVIRA I VIRGILI
DEVELOPMENT OF TECHNOLOGY AND APPLICATIONS BASED ON POROUS ALUMINA NANOSTRUCTURES
Lukas Vojkuvka
DL: T-1536-2009/ISBN: 978-84-692-4555-2

*Chapter 5*

## Template-based applications and a new approach to pore dimensioning

The following chapter discusses the applications derived from porous alumina and the promising novel technique of anodization that makes it possible to modulate pores. One category of applications is the fabrication of nanostructures with porous alumina templates. At the beginning of this chapter the synthesis of metal nanowire arrays and polymer nanopillar arrays is described. Another group of applications focuses on the optical properties of porous alumina. The periodical distribution of the pores in the alumina structure is very similar to that of photonic crystals. For this reason, this chapter also reports the results of simulating the ideal photonic crystal with the geometrical properties of porous alumina prepared in laboratory. The last part of the chapter gives the preliminary results of a new anodizing technique known as discontinuous anodization, which makes it possible to fabricate three-dimensional porous alumina structures.

DL: T-1536-2009/ISBN: 978-84-692-4555-2

## 5.1

## Metal Nanowire Arrays

In last years, nanowires have increasingly attracted a great attention due to their possible application in fabrication of nanodevices. Porous alumina with tuneable geometrical properties and low-cost production is one of the ideal templates for nanowire synthesis. Metal or semiconductor nanoscale structures can be used in many applications such as high-density magnetic storages [167, 168], single electron devices [169], nanoelectrodes [170] or optical devices [171]. Among different deposition techniques, the electrodeposition has been widely used for filling of alumina templates with nickel (Ni) [108], silver (Ag) [172], cuprous oxide ($CuO_2$) [173], antimony (Sb) [174] or cadmium sulphide (CdS) [175]. Basically, the electrodeposition technique is based on electrochemical process where the porous alumina template is employed as a working electrode and an electrolyte is made of chemicals containing desired substance for deposition. By applying a specific voltage (dc) or current (ac) profile, the pores in the template are filled up in the course of electrochemical deposition.

In some cases, the main problem of using porous alumina templates directly after the anodization process is the insulating compact barrier layer that covers the pore tips. Since the electrical contact at the pore bottoms is required for the electrodeposition process, the barrier layer acts as an interfering element. To overcome this limitation several techniques have been proposed such as thinning of the barrier layer [108] or a selective removal of the barrier layer after detachment from Al substrate.

In this work, the thinning process of the barrier layer was developed for the porous alumina samples produced by the hard anodization process. The successful barrier layer removal was realized using re-anodization technique based on the applying of current profile with decreasing steps. The obtained porous alumina templates were employed in the synthesis of nickel and cobalt nanowires by electrodeposition process.

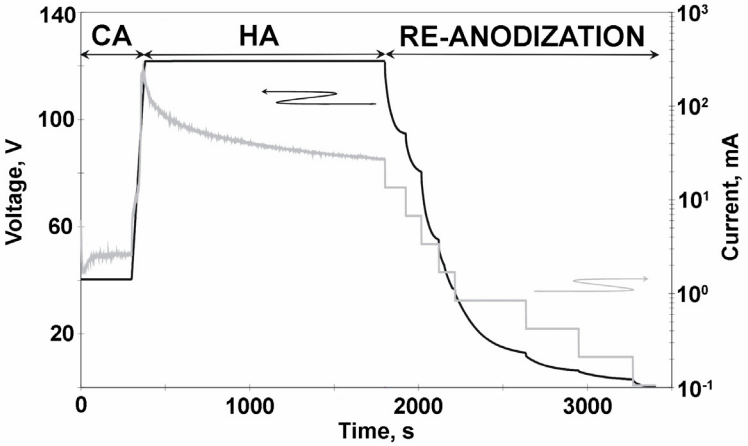


**Figure 71.** Typical votage-current transient from the preparation of porous alumina template on the aluminium substrate using re-anodization technique.

Typical voltage-current transients from the hard anodization and re-anodization process are illustrated in Figure 71. After the hard anodization, the potenciostatic (voltage-controlled) mode is switched to galvanostatic (current-controlled) mode used in the re-anodization process. The applied current profile consists of stepwise decreasing from the actual value to minimum. Each current step is accompanied with corresponding voltage drop. In this way, the voltage is gradually reduced close to zero. Since the barrier layer thickness is strongly voltage-dependent, it is continuously thinned during the course of re-anodizing process. In fact, this technique is more complex and it involves many important factors. The further and detailed explanation will be given elsewhere [176].

The fabricated porous alumina templates were analysed with environmental scanning electron microscope (ESEM). Figure 72 shows the cross-sectional ESEM images of the fractured porous template on the Al substrate. As can be seen in Figure 72(a) the straight vertical pores are clearly opened at the bottom part. This means that the barrier layer was completely removed leaving the alumina template attached to the Al substrate with alumina stems which were formed probably during the re-anodizing process. From the Figure 72(b) is possible to observe the triangular shape of these stems. The inset in Figure 72(b) demonstrates the difference of the alumina template with curved barrier layer covering the pore tips.

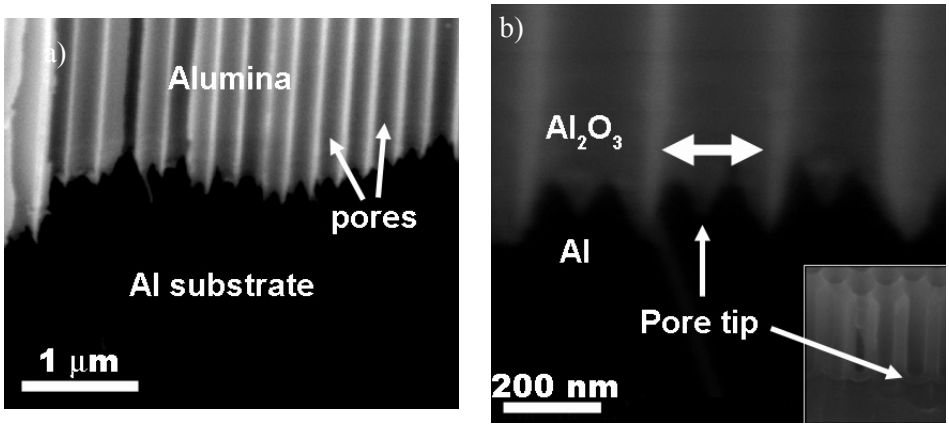


**Figure 72.** ESEM cross-sectional images of a) fractured part of the porous alumina template attached to aluminium substrate with b) detailed view on the opened pore tips. The inset shows the pore tips without applying re-anodization technique.

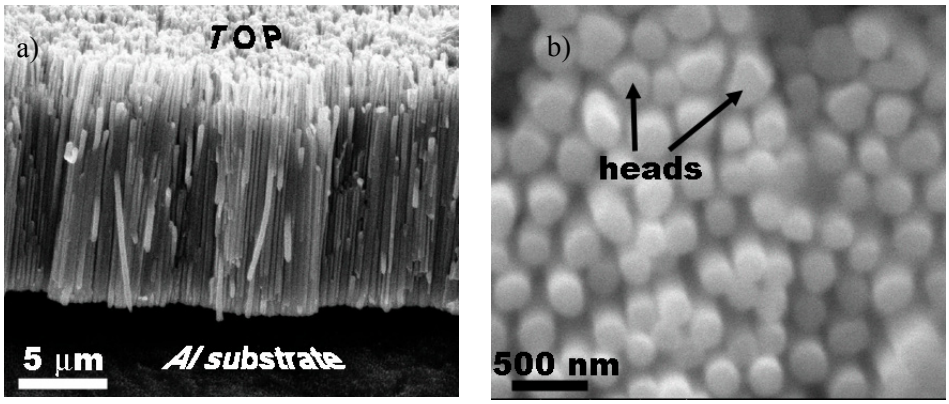


**Figure 73.** a) ESEM lateral view on the array of nickel nanowires and b) top view on the nanowire heads.

The synthesized array of nickel nanowires is shown in the cross-sectional ESEM image in Figure 73(a). The densely-packed uniform nanowires array is fixed to the Al substrate which indicates the mechanical stability and easy manoeuvrability. Figure 73(b) shows the top ESEM surface of the nanowire array with regular distribution of wire diameters.

## 5.2

## Polymer Nanopillar Arrays

Recently, polymer nanopillar arrays with periodical ordering are intensively studied nanoscale structures due to their wide range of possible applications such as microfluidics [177], stamps for imprinting [178], separation beds [179] or porous replicas [180, 181]. Several approaches for synthesis of nanopillar arrays were proposed on the basis of sol-gel, self-assembly or replication process [178, 182-184]. Particularly, template-based replication approaches are cost-effective and allow for high-throughput fabrication of various materials. Porous alumina templates (PAT) with well-ordered nanometric holes are one of the suitable host materials for synthesis of periodical pillar arrays.

In this work, the as-produced PATs were employed for fabrication of free-standing polymer nanopillar arrays (NPA). The replication process is based on the vacuum infiltration of the polymeric solution based on poly(methyl methacrylate) (PMMA) directly to into the PAT.

The porous alumina structures were prepared using two-step anodization process which was described in the second chapter. The desired dimensions of PAT for the PMMA nanopillars can be easily adjusted by choosing the proper anodizing conditions with a combination of the pore widening treatment. In this way, the nanopillars can have various aspect ratios (height vs. diameter).
The detailed description of the polymer infiltration is given elsewhere [185]. Briefly, after the complete PAT preparation including two-step anodizing process and pore widening treatment, the as-produced PAT was placed in a vacuum chamber. Afterwards, the infiltration of the polymer substance was realized by putting a drop of PMMA solution on the top surface of PAT. Then the sample was annealed at 110 ºC for a few hours in order to indurate the infiltrated polymer substance. Finally, the remaining aluminium substrate and PAT were selectively removed in the appropriate etching solutions. The free-standing PMMA nanopillar arrays (PMMA - NPA) were analysed using ESEM equipment.

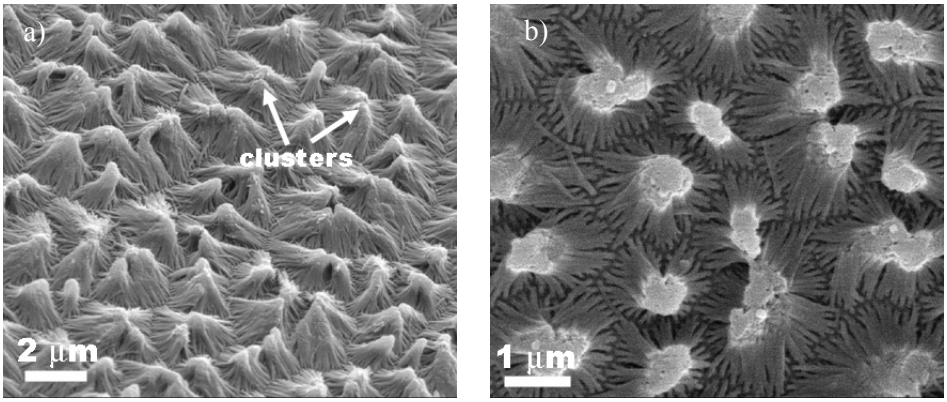


**Figure 74.** a) ESEM image of the PMMA nanopillar array with aspect ratio 25 and b) detailed view on the formed nanopillar clusters.

The ESEM images in the Figure 74 corresponds to the as-produced PMMA-NPA with aspect ratio = 25 (1.3 μm / 50 nm). Original PAT was fabricated using oxalic acid solution with applied voltage of 50 V. From the view of inclined PMMA-NPA surface in Figure 74(a) it can be seen that the very thin and high nanopillars are closely packed together forming pyramidal clusters. Figure 74(b) corresponds to the top view of PMMA-NPA, where the pyramidal clusters of collapsed polymer pillars have approximately the size of 1 – 2 μm. Each cluster is composed of hundreds of pillars which are bunched altogether on the top. The reason of the pillar instability is very high aspect ratio, in other words pillars are too long and too thin to withstand erectly.

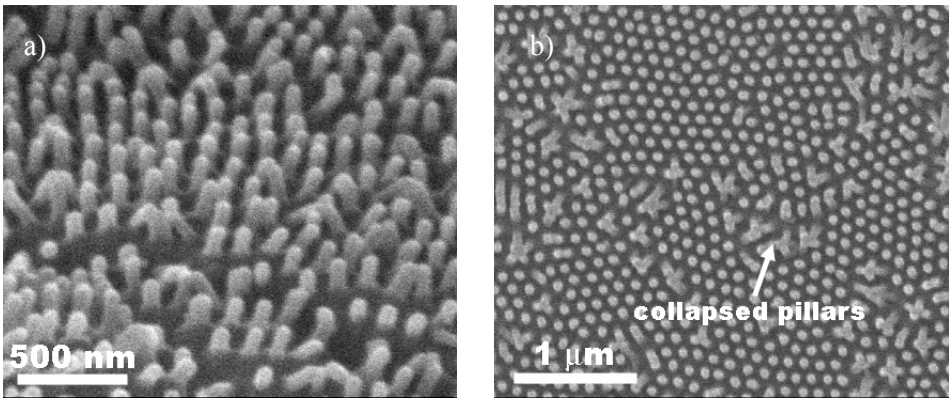


**Figure 75.** a) ESEM image of the PMMA nanopillar array with low aspect ratio of 3.6 and b) top view on the surface of nanopillar array

The Figure 75 shows ESEM images of the PMMA-NPA samples fabricated using suitable PAT to obtain final aspect ratio of 3.6 (200 nm / 55 nm). Figure 75(a) illustrates the array of erected pillars with uniform diameter and height over PMMA-NPA sample. Top view on the PMMA-NPA surface in Figure 75(b) reflects the ordered distribution of the pillars with the distance between them around 110 nm and mean pillar diameter of 55 nm, which corresponds to geometry of the host PAT. Some of the pillars are also collapsed causing the imperfections in the PMMA-NPA distribution. It is important to notice, that some of the distribution imperfections can be particularly caused by the pore dislocations that are already present in the original PAT. In order to obtain perfectly ordered PMMA-NPA samples, the mono-domain PAT is required. The fabricated free-standing PMMA-NPA has a potential use in the preparation of advanced porous structures made of various materials such as $TiO_2$ [180] or $WO_3$ [181].

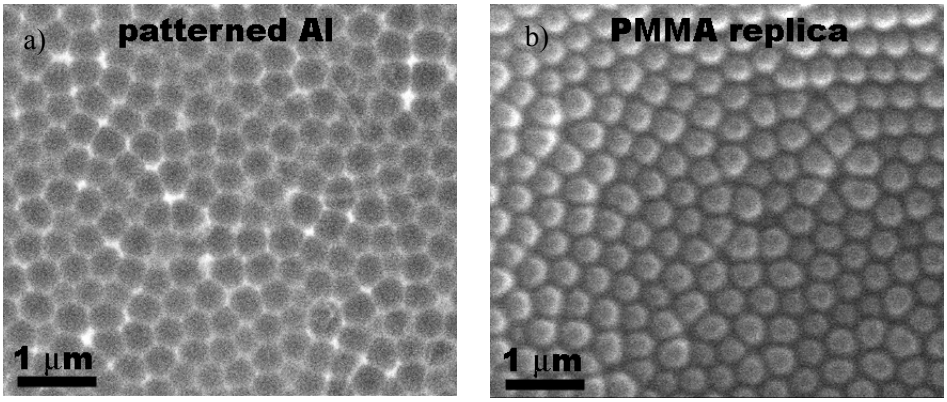


**Figure 76.** ESEM top surface images of a) patterned aluminium substrate used as a template and b) formed PMMA nanodot array replicated from Al template.

Besides PAT for synthesis of PMMA-NPA, a different approach for nanostructure production based on the employing a patterned aluminium (Al) substrate as a template was developed. The patterned Al templates were obtained after the anodization using phosphoric acid solution and applied voltage of 170 V. The formed oxide layer was selectively removed leaving the Al substrate with ordered pattern of pits. Afterwards, PMMA replica of Al template was realized following the same procedures as for PMMA-NPA described above. Figure 76 compares ESEM top surface images of a) Al template and b) PMMA replica of the Al template. The produced replica

consists of the ordered array of PMMA nanodots with dot diameter around 350 nm and dot height less than half of dot diameter. These highly ordered PMMA replicas could be used as the imprinting stamps for surface patterning.

In conclusion, it was shown that PMMA nanopillar arrays can be successfully fabricated using home-made porous alumina template. Although the aspects ratio of the resultant polymer nanoarrays is limited to 3.6 due to the collapsing of pillars higher than 1 μm, the desired dimensions of the pillars could be achieved by a proper design of the original porous alumina template. Moreover, highly ordered PMMA nanodot arrays with dot diameter of 350 nm were also produced using patterned Al substrate as a template. Both type of PMMA nanoarrays have their possible use in further applications such as porous replicas or contact imprinting methods.

## 5.3

## Photonic Crystals based on Porous Alumina

Photonic crystal (PC) is a low-loss periodic dielectric medium that allows optical control and manipulation [125]. In other words, PC is an optical analogue of a conducting crystal, in which periodically distributed atoms or molecules are replaced by macroscopic media with different refractive indexes. The particular behaviour of photons inside these PCs with the existence of photonic bands and gaps makes them potential candidate for a great variety of applications such as PC fibres [186], low-threshold lasers [187] or photonic circuits [188]. PCs can be classified as one-(1D), two-(2D) or three-dimensional (3D) depending on their dielectric distribution. Particularly, the fabrication of 2D PCs can be realized with a combination of lithography and consequent etching [189-191].

Porous alumina (PA) with periodically ordered nano-holes represents one of the potential materials for 2D PCs. Although the perfect ordering of the holes in PA is limited to the domain size of a few microns, it has still several benefits for optical applications: i) the geometrical properties of PA can be easily tuned for applications in the visible range [52], i) it is transparent in this range [129] and iii) it has also luminescent properties [121]. The poly-domain distribution of naturally grown PA can overcome the use of advanced fabrication techniques such as substrate pre-patterning [34].

Several methods for the characterization of materials with photonic band gap have been proposed [192, 193]. One of the common techniques is also the angular-dependent reflectance spectroscopy (ADRS) [194]. The ADRS technique is based on the identification of resonant features in the reflectivity spectra at different incident angles. It has been already applied to the characterization of macro-porous silicon structures [195, 196].

In this work, the possibility of using ADRS technique for characterization of 2D PC based on PA is proposed. The study consists of the numerical simulation of the interaction between the incident light and PA. The simulation method is based on the scattering matrix treatment proposed by Whittaker et al. [197], which follows the same approach as the plane-wave expansion (PWE) method

including additional features to calculate the angular-dependent reflectance (ADR) spectra. The detailed description of the numerical method can be found elsewhere [198].

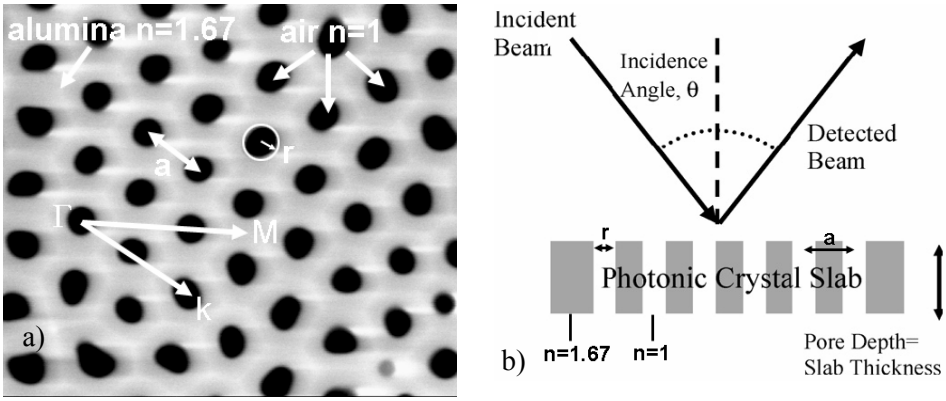


**Figure 77.** a) Illustrative ESEM image of home-made porous alumina with indicated high-symmetry directions and basic geometrical features used in simulation, b) schematic diagram of model for the photonic crystal based on the porous alumina.

The representative ESEM top surface image of as-produced PA is placed in the Figure 77(a) with the indicated high-symmetry directions (ΓM, Γk) and the respective geometrical features (lattice constant a, hole radius r). In contrast to poly-domain hole ordering in the experimentally prepared PA, the model for the simulations requires that the sample have ideally periodical hole distribution. For this reason, a perfect triangular arrangement of the holes is assumed in the simulations. More concisely, Figure 77(b) shows a schematic diagram of the model for PC sample consisting of a slab of alumina (n = 1.67) [99, 100], surrounded by air (n = 1), with a periodic triangular lattice (a) of circular holes (r). The thickness of the slab is equal to the pore depth and the angle of incident light is θ.

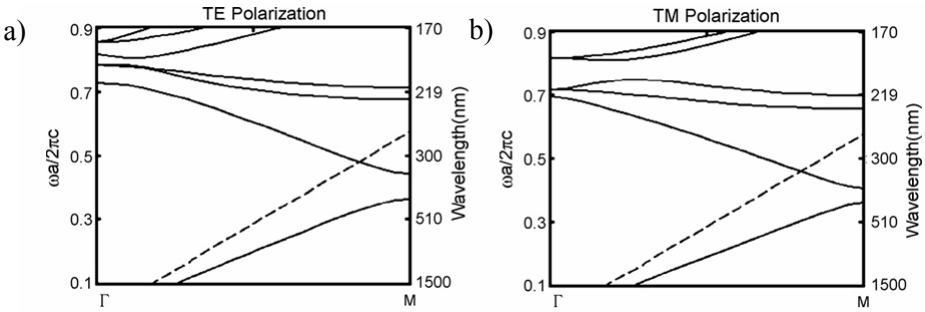


**Figure 78.** Photonic band structures (calculated by PWE method) for the ΓM direction of an ideal photonic crystal based on the porous alumina; a) shows the bands for TE polarization and b) for TM polarization. The dashed lines correspond to incident light.

The photonic bands of an ideal PA 2D-PC from the Figure 78 were calculated with PWE method. The values of *a* and *r* used in the simulation were extracted from the ESEM analysis of the PA sample prepared in laboratory. The present bands for both a) TE (electric field perpendicular to the pores) and b) TM (magnetic field perpendicular to the pores) in Figure 78 correspond to the lattice direction ΓM. The dashed line represents the light line. The results show that some of the photonic bands and band gaps lie in the UV-vis region of the electromagnetic spectrum, which is in a good agreement with the transmittance measurements of the PA films described previously in Chapter 4 [99, 100].

The Figure 79 shows ADR spectra for PA PC slab with thickness i.e. pore depth of 300 nm and with the same geometry (*a*, *r*) of PA model as it was used for the band calculation in previous section (Figure 78). Figures 79 represents the reflection coefficient versus the frequency of the incident light (ω) and incident angle (θ). The simulation was performed for incident light along the ΓM direction and for TE polarization of the incident and detected light. The second, third and fourth TE photonic bands taken from Figure 78 are overlapped in Figure 79. There exist several resonant features in the ADR spectra for the second and third TE bands with ω = 0.66 and 0.74 $2\pi c/a$ at θ = 20º respectively. Such features are due to the coupling of the incident light to the photonic modes that propagate inside the structure at different angles with respect to the surface. Another noticeable characteristic in the ADR spectra are oscillations in the reflectance spectra (the dark and light stripes in the 2D plot). This could be

DL: T-1536-2009/ISBN: 978-84-692-4555-2

ascribed to Fabry-Pérot interferences observed also in the experimentally measured transmittance spectra of very thin PA film (see Chapter 4).

In conclusion, it was shown that the results from the simulations of photonic bands and ADR spectra for an ideal porous alumina photonic crystal are closely related to the results obtained form the optical spectroscopy performed on the porous alumina films.

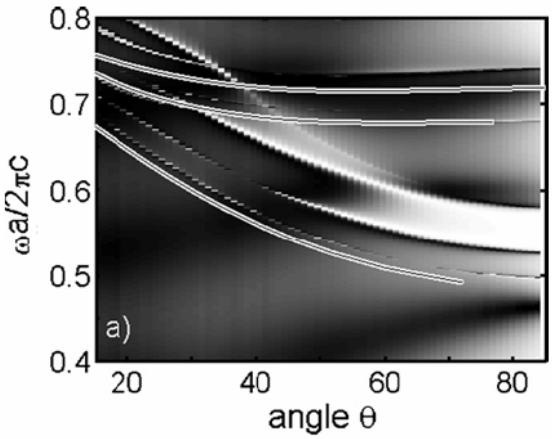


**Figure 79.** Angular-dependent reflectance spectra of photonic crystal slabs with thicknesses of 300 nm. The spectra is represented as a grey map of the reflectivity with respect to the angle of incidence and the normalized frequency. The reflectance spectra are for the light incident in the ΓM direction and the bands correspond to the TE polarization and the ΓM direction.

UNIVERSITAT ROVIRA I VIRGILI
DEVELOPMENT OF TECHNOLOGY AND APPLICATIONS BASED ON POROUS ALUMINA NANOSTRUCTURES
Lukas Vojkuvka
DL: T-1536-2009/ISBN: 978-84-692-4555-2


## 5.4

## Discontinuous Anodizing: Pore Modulation

The ordinary self-ordered porous alumina consists of uniform tubular pores with constant diameter all over the pore length. However, it is also highly desirable to manage with the fabrication of PA structures with modulated pore diameter. Such a three-dimensional (3D) porous material could broaden the application field especially in optics and nano-structuring.

Recently, a few approaches for the fabrication of 3D PA have been proposed by several groups. The detailed overview of this techniques is given in chapter one. Among others, the remarkable progress in pore modulation of PA was done by Lee et al [52, 55]. Their first work has described the fabrication of PA with periodically modulated pore diameters achieved by repetitive anodizing cycles with conventional and hard anodizing conditions [52]. Although this process is well controllable, it is technologically complex and time-consuming. The second work has reported on a novel technique, designated by authors as pulsed anodization that is based on the conventional anodizing with a sequence of hard anodization pulses using a sulphuric acid electrolyte [55].

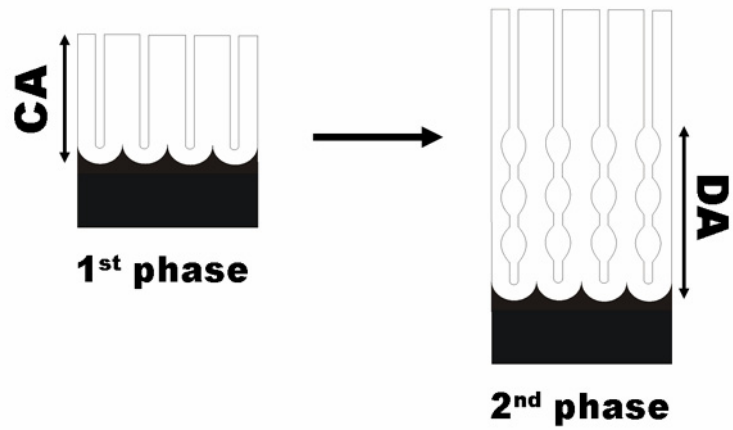


**Figure 80.** Scheme of fabrication steps for porous alumina with modulated pore diameter. The process has two consecutive phases of conventional anodization (CA) and discontinous anodization (DA).

UNIVERSITAT ROVIRA I VIRGILI
DEVELOPMENT OF TECHNOLOGY AND APPLICATIONS BASED ON POROUS ALUMINA NANOSTRUCTURES
Lukas Vojkuvka
DL: T-1536-2009/ISBN: 978-84-692-4555-2

The following section will be dedicated to a newly proposed attempt for the fabrication of novel PA with modulated pores based on the discontinuous anodizing in the heated phosphoric acid solution. Figure 80 shows the scheme of the complete experimental procedure that basically consists of two anodizing phases: i) conventional 2 step anodization (CA) that was described in chapter two, and ii) discontinuous anodizing (DA) where some unusual conditions such as heated electrolyte and specific voltage profile are employed in order to modulate the pores.

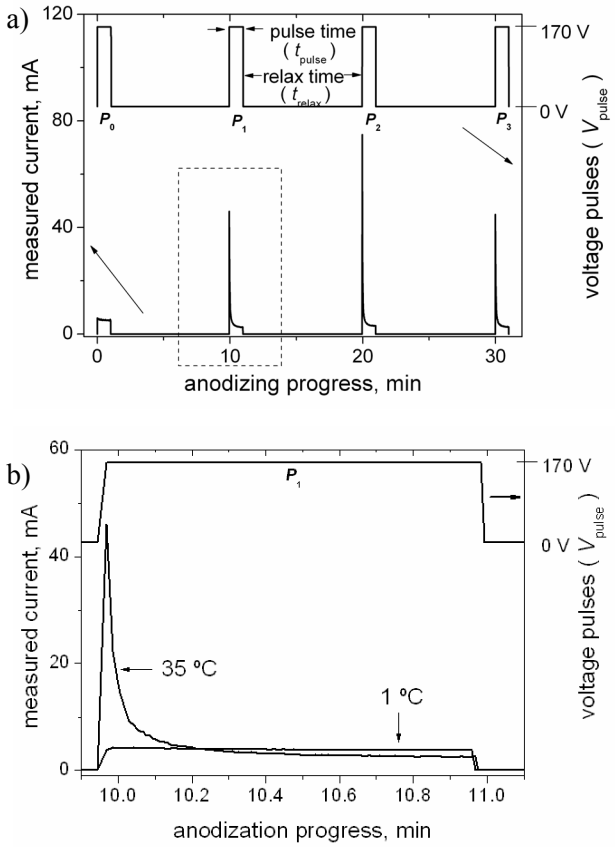


**Figure 81.** a) Typical current-voltage transient from discontinuous anodizing with a specific voltage profile of short pulses and b) comparison of the current responses to the voltage pulse in cold (1 ºC) and heated (35 ºC) electrolyte.

The first CA phase was performed using 3 wt.% phosphoric acid at 1 ºC with applied constant voltage of 170 V. After the second step of CA process, the

electrolyte temperature was immediately increased to 35 ºC and second DA phase was carried out using a specific voltage profile with several voltage pulses of 170 V with duration $t_{pulse}$ = 1 min and each pulse was followed by open-circuit period ($t_{relax}$). Figure 81(a) shows a typical current and voltage transients from the second DA phase. In this case, the applied DA profile consist of four pulses $P_0$ – $P_3$ with $U_p$ = 170 V and $t_{pulse}$ = 1 min. The open-circuit intervals between pulses lasted $t_{relax}$ = 9 min. There are noticeable high current peaks for every pulse $P_1$ - $P_3$ at the very beginning of each pulse, whereas first pulse $P_0$ is without peak. Figure 81(b) compares the current curves recorded during the pulse $P_1$ with heated (35 ºC) and cold (1 ºC) electrolyte. It can be seen that the additional experiment with the DA process performed at 1 ºC did not exhibit any current peak.

The detailed morphological examination of the samples fabricated using DA process was performed on an environmental scanning electron microscope (ESEM). Figure 82 shows cross-sectional views of the resultant PA structure with modulated pores. The inset in Figure 82(a) shows ESEM image of approximately one $\mu m^2$ on the PA top surface. The hexagonally ordered pores have 80 nm in diameter and interpore distance of 450 nm, which correspond to the previous results observed for the PA samples from two-step CA process. The upper part of the cross-section in Figure 82(a) labelled as "1 phase" that is two-step CA process, consists of straight parallel pores produced during the second anodizing step. In contrast, the lower part with label "2 phase" demonstrates the resultant PA structure after the DA process. It can be seen that the pores are not straight any more but show a variation in the diameter. A closer observation of the marked cross-section in Figure 82(b) shows the number of diameter variations in each pore that corresponds to the three voltage pulses $P_1$, $P_2$ and $P_3$ with the high current peaks observed previously in Figure 81(a). After each modulation the pore becomes again uniform.

From these experimental data it can be deduced several points. The first is that the current peaks during the pulses $P_1$ and subsequent indicate that the overall resistance of the electrochemical system has dropped. Furthermore, the number of these pulses corresponds with the pore diameter variations. This could be explained in terms of the very thin oxide layer between the metal and the electrolyte at the pore bottoms, called the barrier layer BL (see Figure 82(b)). During the two-step anodizing process the BL thickness is always constant and

it is strictly given by the constant anodizing voltage. In contrary, in the DA process during the relax time a thinning of the BL takes place at the pore bottoms due to the local temperature-enhanced dissolution. This local temperature enhancement is due the fact that the current density is accompanied by a relatively high Joule heating and it is concentrated at the pore bottoms. After each voltage pulse the BL dissolution continues as long as the temperature is increased. Therefore, high temperature of the electrolyte is an essential parameter for the BL dissolution. The higher temperature results in: i) a higher chemical dissolution rate and ii) the local heating is dissipated more slowly than if the cold electrolyte is used. This also explains the absence of the current peaks in the DA process where cold electrolyte was employed (see Figure 81(b)). When a new voltage pulse is applied after the relax time, the thinner BL has a lower resistance which could be an origin of the current peaks.

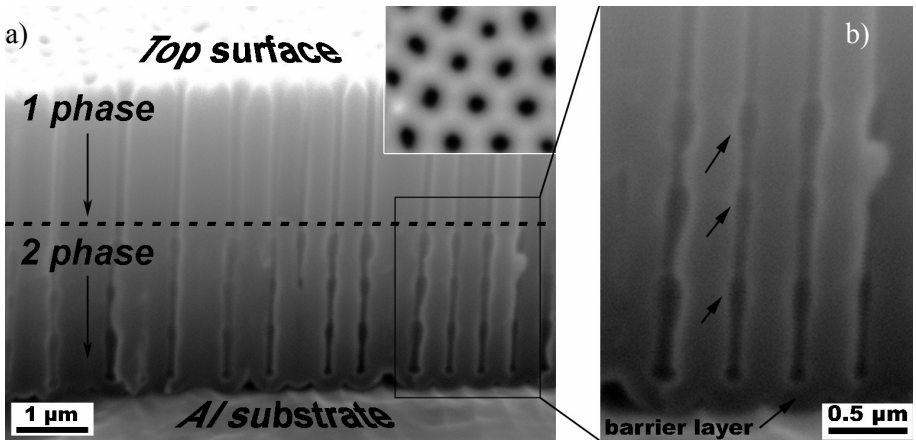


**Figure 82.** ESEM images of a) fractured porous alumina sample with modulated pores formed during discontinuous anodizing and b) a detailed view on the pore modulations.

This modulation process has a schematic drawing in Figure 83. As it is outlined, when the circuit is open during the relax time ($U$ = 0 V), the heated electrolyte causes the local dissolution of the BL oxide at the pore base. Afterwards, when the voltage pulse of 170 V is applied to the system, the current peak is observed due to the reduced BL thickness. Then the anodizing process promptly continues in the steady-state form characterized by the uniform pore growth. In this instant, the BL fully recovers its original thickness corresponding to the applied voltage.

UNIVERSITAT ROVIRA I VIRGILI
DEVELOPMENT OF TECHNOLOGY AND APPLICATIONS BASED ON POROUS ALUMINA NANOSTRUCTURES
Lukas Vojkuvka
DL: T-1536-2009/ISBN: 978-84-692-4555-2


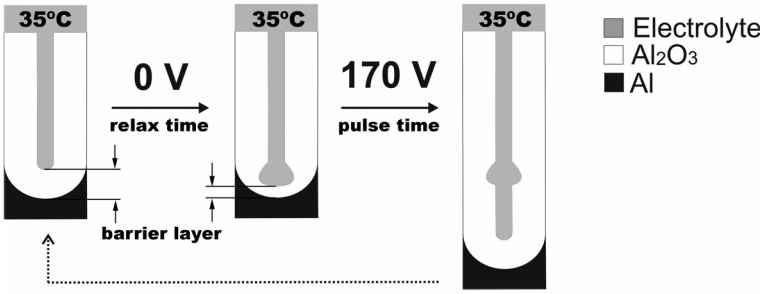


**Figure 83.** Scheme of pore modulation cycle during the discontinuous anodizing.

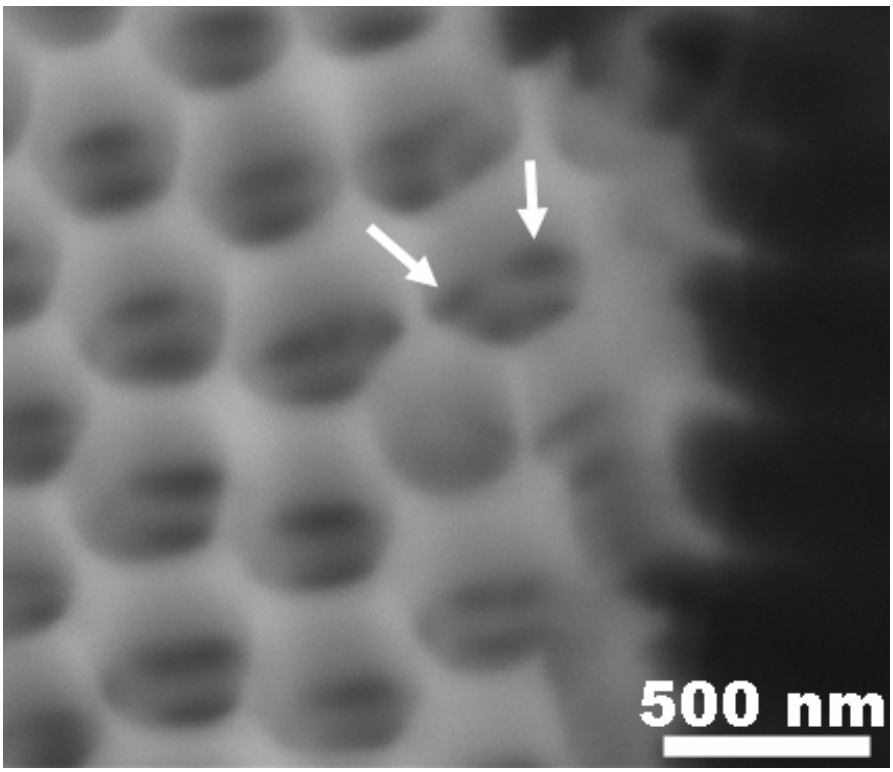


**Figure 84.** Novel 3D porous alumina structure obtained by the discontinuous anodization process combined with wet chemical etching.

The advantage of the DA technique to create a novel 3D PA structures is demonstrated in the Figure 84 with ESEM image of the sample produced by DA

DL: T-1536-2009/ISBN: 978-84-692-4555-2

process combined with a subsequent wet chemical etching in diluted phosphoric acid. The pores are periodically perforated at different points which correspond to the pore variations formed during DA process. The wet chemical etching causes uniform dissolution of the pore wall until the neighbouring pores are interconnected. These 3D PA structures with a new horizontal dimension could have a great potential as template for nano-structuring or as material with unique optical properties.

## 5.5

## Summary

In conclusion, this chapter describes the applications of porous alumina in the fields of nanostructures and optics. Porous alumina templates were successfully used to synthesize metal and polymer nanostructured arrays. The re-anodization technique was directly applied after the hard anodization process in order to open the pore bottoms. The porous template was attached to the aluminium substrate that serves as a conducting base for the electrodeposition of metal, and Ni and Co nanowire arrays were produced using the re-anodized porous templates. PMMA nanopillar arrays were fabricated by directly infiltrating the polymer into the porous alumina templates. The desired geometry of the nanopillars and nanowires was controlled using the appropriate porous alumina template. The numerical simulation of the optical properties of ideal photonic crystal, which was intentionally modelled with the same geometrical properties as the porous alumina prepared in the laboratory, showed the results that are very similar to the results from the optical spectroscopy measurements performed on the porous alumina. Novel porous alumina with modulated pores was fabricated by the discontinuous anodization process, which consists of applying a pulsed voltage profile. The electrolyte temperature was shown to be a crucial parameter for successful pore modulation. The experimental data indicate that the pore modification has its origin in a thinning of the barrier layer caused by temperature-enhanced chemical dissolution at the pore tips. These preliminary results present a challenge for future investigation.

UNIVERSITAT ROVIRA I VIRGILI
DEVELOPMENT OF TECHNOLOGY AND APPLICATIONS BASED ON POROUS ALUMINA NANOSTRUCTURES
Lukas Vojkuvka
DL: T-1536-2009/ISBN: 978-84-692-4555-2

# 6

# Conclusions

DL: T-1536-2009/ISBN: 978-84-692-4555-2

## *Conclusions*

The first chapter of this thesis presented a general overview of self-ordered porous alumina starting with some basic concepts of aluminium anodizing. It is generally accepted that the pores are self-organized in the triangular lattice only if specific anodizing parameters—so called self-ordering regimes—are maintained throughout the anodizing process. Several mechanisms have been suggested to explain the self-organizing phenomenon: i) cracking and self-healing of the oxide layer; ii) local corrosion at the pore bottoms; or iii) mechanical stress. However, there is still no clear evidence of the real origin of the self-organized formation of pores. In 1995 a two-step anodization process was reported that fabricates three major types of self-ordered porous alumina with ideally formed pore distribution. Besides these well-known porous alumina structures, a great deal of research and development has recently focused on fabricating novel alumina structures. In particular, anodizing techniques based on aluminium pre-patterning enable perfectly ordered porous alumina with large areas to be fabricated. These studies on novel anodizing approaches are summarized in the tables in the Appendix.

The second chapter describes the process of fabricating self-ordered porous alumina using two-step anodization. For the electrochemical etching of aluminium, we used a home-made anodizing cell equipped with elements for electronic and temperature control. The study of annealing and electropolishing treatments performed on the aluminium substrates before anodizing showed a large grain increase after heat treatment and a very smooth aluminium surface after polishing. Three major types of porous alumina samples were successfully produced by two-step anodziation using various electrolytes based on sulphuric acid, oxalic and phosphoric acid. The examination of the morphology demonstrated that the porous alumina structures produced had highly diverse geometrical features: pore diameters between 20 nm and 250 nm, interpore distances of 50 nm, 100 nm and 450 nm, and high aspect ratios (pore depth/pore diameter) as high as 5000. The pore widening process was investigated in order to control the porosity of the porous alumina samples. The current-based model of pore formation in the early stage of the anodization process was proposed for all three major types of porous alumina. It was observed that the different phases of pore development are directly reflected in the measured current characteristic. Several detachment techniques for obtaining free-standing porous alumina films were carried out. The porous alumina films detached after wet

chemical etching were highly contaminated which caused film cracking later in the annealing process.

Chapter three deals with the fabrication of self-ordered porous alumina by hard anodization using an oxalic acid electrolyte. The results showed that the formation of the porous layer depends on the specific profile of the voltage applied at different phases of the anodization process. The self-ordering of the pores was best for the voltage between 130 V and 140 V. The interpore distances of the porous alumina produced by hard anodization vary between 240 nm and 320 nm. These values can be used to make up for the values that cannot be obtained between 100 nm and 450 nm in the porous alumina produced by two-step anodization. The main advantage of hard anodization over two-step anodization was the effectiveness of the single anodization step and the fast oxide growth. On the other hand, hard anodization produces porous alumina structures with significantly worse pore uniformity because of the variation in the applied voltage. At the end of this chapter new attempts at fabricating novel porous alumina structures are proposed by combining hard anodization and two-step anodization. Ordered pore accumulations were formed on the porous alumina surface by a hybrid two-step anodization, in which hard anodization was used as the first anodizing step. Double-layered porous alumina was prepared by a combined process of two-step and hard anodization.

The fourth chapter summarizes the results from the structural, optical and mechanical characterization of porous alumina. The crystallization process of porous alumina was studied in-situ by X-ray diffraction measured between 25 ºC and 1200 ºC. The results showed that the amorphous phase was present up to 700 ºC. At temperatures between 850 ºC and 1000 ºC the phase mixture of gamma alumina was observed followed by the final transition into alpha alumina at 1200 ºC. The transmission spectra from the optical characterization using UV-Vis spectroscopy show an absorption peak centred at a wavelength of 380 nm. For the porous alumina samples annealed at high temperatures of 800 ºC and 1000 ºC, this peak was blue-shifted in the wavelength scale The refractive index and extinction coefficient were simulated using the model for porous alumina. The refractive index obtained was constant in the wavelength range studied with values between 1.52 – 1.62 for as-produced and annealed samples. The extinction coefficient showed an absorption peak close to 400 nm for the as-produced sample and the same sample annealed at 600 ºC. For the

samples annealed at higher temperatures of 800 ºC and 1000 ºC, the extinction coefficient presented two absorption peaks: 1) one close to 400 nm, which was slightly blue-shifted with respect to absorption peaks of as-produced and 600 ºC samples and ii) the other at higher wavelengths of 600 nm and 700 nm for samples annealed at temperatures of 1000 ºC and 800 ºC, respectively. The spectra from FT-IR measurements showed one broad and one stretch absorption peak centred at 3500 $cm^{-1}$ and 3000 $cm^{-1}$, respectively. These peaks were attributed to the hydroxyl (OH) and alcohol (CH) impurities formed during anodization and cleaning. Interestingly, the largest OH peak was observed for the sample annealed at 800 ºC, which showed the lowest peak in the spectra of UV-Vis measurements. This peak coincidence indicates that the optical properties depend on the impurity state within the porous alumina. Also the peaks in the PL spectra of the annealed porous alumina samples were shifted and reduced with respect to the as-produced samples. This may be due to the structural changes and different impurity concentrations in the annealed and as-produced samples. The mechanical properties expressed by hardness, Young's modulus and the friction coefficient were extracted from the nanoindentation and friction measurements of the three major types of porous alumina samples with different porosities. It was observed that hardness and Young's modulus decreased for more porous samples from 5 GPa to 1 GPa and 130 GPa to 40 GPa, respectively. Friction coefficients calculated from the scratch tests were found in the range between 0.7 – 0.25 depending on sample type and porosity. Closer examination by SEM of the indents and scratches revealed that the porous alumina samples studied behaved plastically under the applied load. This may be due to high water contamination and the presence of aluminium within the porous alumina structure.

The last chapter describes the applications of porous alumina in the fields of nanostructures and optics. The porous alumina templates were successfully used to synthesize metal and polymer nanostructured arrays. The re-anodization technique was directly applied after the hard anodization process in order to open the pore bottoms. The porous template was attached to the aluminium substrate that serves as a conducting base for the electrodeposition process. Ni and Co nanowire arrays were produced using the re-anodized porous templates. PMMA nanopillar arrays were fabricated by directly infiltrating the polymer into the porous alumina templates. The desired geometry of the nanopillars and nanowires was controlled using the appropriate porous alumina template. The

DL: T-1536-2009/ISBN: 978-84-692-4555-2

numerical simulation of the optical properties of ideal photonic crystal, which was intentionally modelled with the same geometrical properties as the porous alumina prepared in the laboratory, showed the results that are very similar to the results from the optical spectroscopy measurements performed on the porous alumina. Novel porous alumina with modulated pores was fabricated by discontinuous anodization process. This process consists of applying a pulsed voltage profile. The electrolyte temperature was shown to be a crucial parameter for successful pore modulation. The experimental data indicate that the pore modification has its origin in a thinning of the barrier layer caused by the temperature-enhanced chemical dissolution at the pore tips. These preliminary results present a challenge for future investigation.

DL: T-1536-2009/ISBN: 978-84-692-4555-2

## Journal Articles

1. **Vojkuvka**, L., Marsal, L. F., Ferre-Borrull, J., Formentin, P., Pallares, J., *Self-ordered porous alumina membranes with large lattice constant fabricated by hard anodization.* Superlattices and Microstructures, 2008. **44**(4-5): p. 577-582.

2. Kral, Z., **Vojkuvka**, L., Garcia-Caurel, E., Ferre-Borrull, J., Marsal, L. F., Pallares, J.,, *Calculation of Angular-Dependent Reflectance and Polarimetry Spectra of Nanoporous Anodic Alumina-Based Photonic Crystal Slabs.* Photonics and Nanostructures: Fundamental Applications, 2008.Accepted, doi:10.1016/j.photonics.2008.11.005

3. Marsal, L.F., **Vojkuvka**, L., Formentin, P., Pallares, J., Ferre-Borrull, J., *Fabrication and optical characterization of nanoporous alumina films annealed at different temperatures.* Optical Materials, 2008. Accepted, doi:10.1016/j.optmat.2008.09.008

4. Santos, A., **Vojkuvka**, L., Pallares, J., Ferre-Borrull, J., Marsal, L. F.,, *In-situ electrochemical dissolution of the oxide barrier layer of porous anodic alumina fabricated by hard anodization.* Journal of Electroanalytical Chemistry, 2008. Accepted

5. Marsal, L.F., **Vojkuvka**, L., Ferre-Borrull, J., Trifonov, T., Pallares, J., *Optical characterization of self-ordered porous alumina membranes of various thicknesses.* Physica Status Solidi C - Current Topics in Solid State Physics, 2007. **4**(6): p. 1918-1922.

DL: T-1536-2009/ISBN: 978-84-692-4555-2

## Selected Conference Contributions

1. **Vojkuvka, L.**, Santos, A., Marsal, L. F., Ferre-Borrull, J., Pallares, J. *Novel 3-D porous alumina structures fabricated by pulsed anodization*. in *Spanish Conference on Nanophotonics (CEN)*. 2008. Tarragona, Spain.

2. Marsal, L.F., Formentin, P., Palacios, R., **Vojkuvka**, L., Trifonov, T., Rodriguez, A., Ferre-Borrull, J., Pallares, J., Alcubilla, R. *Micro and nanostructures based on silicon and alumina templates for photonic and optoelectronic application*. in *214th ECS Meeting*. 2008. Honolulu, Hawai.

3. **Vojkuvka**, L., Marsal, L. F., Ferré-Borull, J., Formentin and P., Pallarés, J. *Morphological study of self-ordered porous alumina with large lattice constant fabricated by high voltage anodization*. in *The European materials research society (E-MRS)*. May, 2007. Strasbourg, France.

4. **Vojkuvka**, L., Marsal, L. F., Pallares, J. *Study of Porous Alumina Porosity after Pore Widening Process*. in *Conference on Electronic Devices (CDE)*. January, 2007. Madrid, Spain.

5. Marsal, L.F., **Vojkuvka**, L., Ferré-Borrull, J., Trifonov T., Pallarés, J. *Annealing effect on optical properties of porous alumina membranes*. in *Porous Semiconductor Science and Technology (PSST)*. March, 2006. Sitges, Spain.

6. Marsal, L.F., **Vojkuvka**, L., Ferré-Borrull, J., Trifonov, T., Pallarés, J. *Optical characterization of self-ordered porous alumina membranes of various thicknesses*. in *The European materials research society (E-MRS)*. May, 2006. Nice, France.

7. **Vojkuvka**, L., Marsal, L.F., Ferré-Borrull, J., Pallarés, J. *Fabrication and characterization of porous alumina membranes*. in *Workshop on Nanoelectronics and Photonics Systems*. July, 2006. Tarragona, Spain.

8. **Vojkuvka**, L., Marsal, L. F., Ferré-Borrull, J., Trifonov, T., Pallarés, J. *Fabrication of self-ordered porous alumina*. in *XXII Trobades científiques de la Mediterrània*. October, 2006. Mao, Menorca.

UNIVERSITAT ROVIRA I VIRGILI
DEVELOPMENT OF TECHNOLOGY AND APPLICATIONS BASED ON POROUS ALUMINA NANOSTRUCTURES
Lukas Vojkuvka
DL: T-1536-2009/ISBN: 978-84-692-4555-2

UNIVERSITAT ROVIRA I VIRGILI
DEVELOPMENT OF TECHNOLOGY AND APPLICATIONS BASED ON POROUS ALUMINA NANOSTRUCTURES
Lukas Vojkuvka
DL: T-1536-2009/ISBN: 978-84-692-4555-2

# Appendix

UNIVERSITAT ROVIRA I VIRGILI
DEVELOPMENT OF TECHNOLOGY AND APPLICATIONS BASED ON POROUS ALUMINA NANOSTRUCTURES
Lukas Vojkuvka
DL: T-1536-2009/ISBN: 978-84-692-4555-2

*Table I-a: Anodization of pre-patterned aluminium: Monodomain alumina*

| Substrate | Alumina Features | Experimental Details | Fabrication |
|---|---|---|---|
| Al | Monodomain | • Al pre-patterning with SiC mold<br>• Anodizing: 0.3 $H_2SO_4$, 0.3 M $(COOH)_2$, 0.5 M $H_3PO_4$/25 V, 60 – 80 V/17 ºC/6 – 20 min | 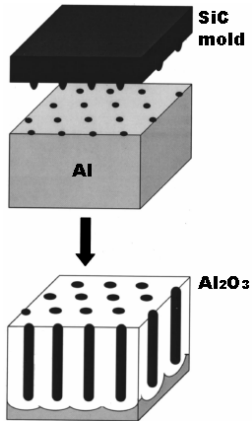 |
| Al | Monodomain | • Al pre-patterning with imprint stamp of $Si_3N_4$ pyramids<br>• Anodizing: 1.7 wt% $H_3PO_4$/100-120 V/2 ºC/60 min | 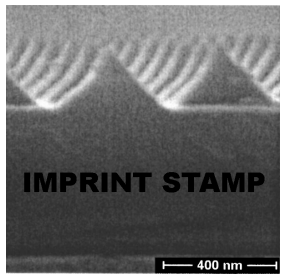 |
| Al | Monodomain | • Al pre-patterning with conventional e-beam or focus-ion-beam lithography<br>• Anodizing: 0.04 M or 0.3 M $(COOH)_2$/40 V, 85V/3-5 ºC/hours | 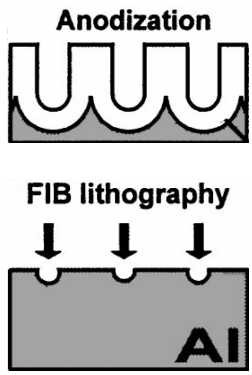 |

*Table I-a: Anodization of pre-patterned aluminium: Monodomain alumina*

| Results | Time | Cost | Reference |
|---|---|---|---|
| 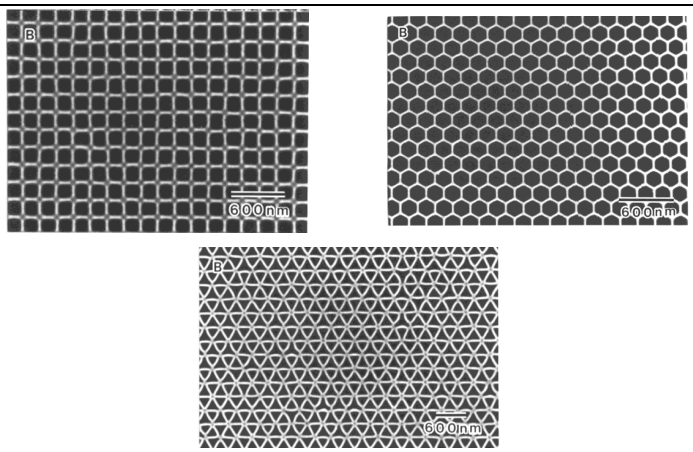  | Medium | Medium | [34, 35, 37] |
| 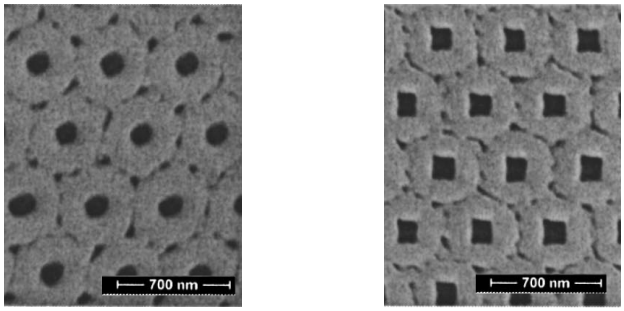  | Fast | Medium | [40, 41] |
| 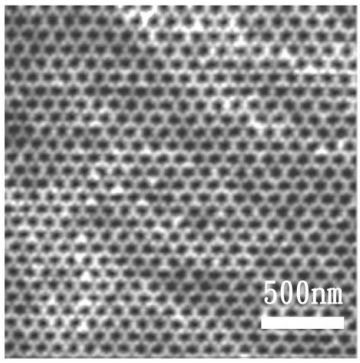  | Medium | Slow | [29, 45, 46] |

DL: T-1536-2009/ISBN: 978-84-692-4555-2

*Table I-b: Anodization of pre-patterned aluminium: Monodomain alumina*

| | | | |
|---|---|---|---|
| Al/Si | Monodomain | • Si pre-patterning with holographic lithography<br>• Al thermal evaporation<br>• Anodizing:<br>• 1:800 $H_3PO_4$:$H_2O$/140 V/20 ºC/40 min | 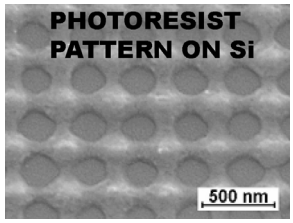 |
| Al/$SiO_2$/Si | Monodomain | • e-beam evaporation<br>• Spin-coating<br>• Interference lithography<br>• Combined anodizing:<br>5 %wt $H_3PO_4$/86 V/5 ºC<br>0.015 M $(COOH)_2$/86 V/ 5 ºC | 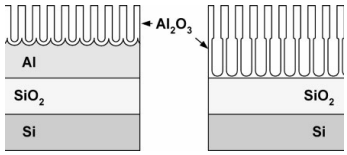 |
| Al/$Fe_2O_3$/Si | Monodomain | • Monodisperse array of $Fe_2O_3$ nanoparticles<br>• DC sputtering of Al<br>• Anodizing:<br>0.3 M $H_2SO_4$/3 V/16 ºC/15 min | 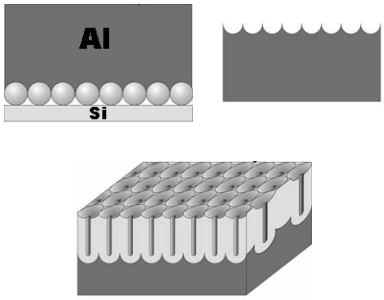 |
| Al | Monodomain | • Al pre-patterning with nanosphere arrays<br>• Anodizing:<br>0.3 M $H_3PO_4$/32 – 200 V/0 ºC | 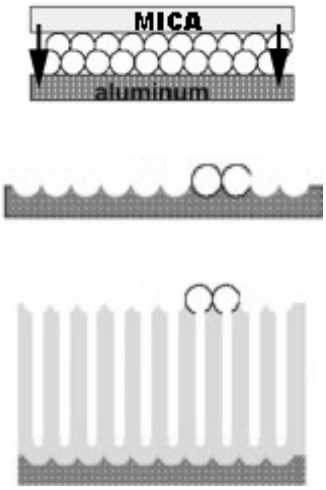 |

UNIVERSITAT ROVIRA I VIRGILI
DEVELOPMENT OF TECHNOLOGY AND APPLICATIONS BASED ON POROUS ALUMINA NANOSTRUCTURES
Lukas Vojkuvka
DL: T-1536-2009/ISBN: 978-84-692-4555-2

*Table I-b: Anodization of pre-patterned aluminium: Monodomain alumina*

| | | | | |
|---|---|---|---|---|
| 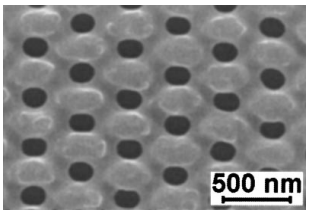 | 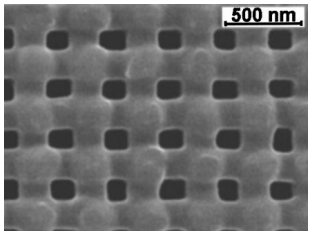 | Slow | High | [47] |
| 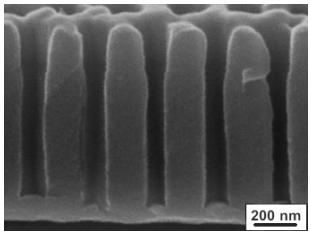 | 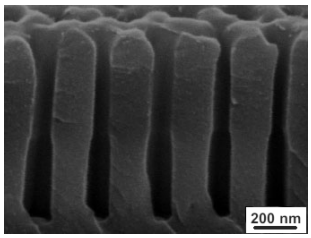 | Slow | High | [48] |
| 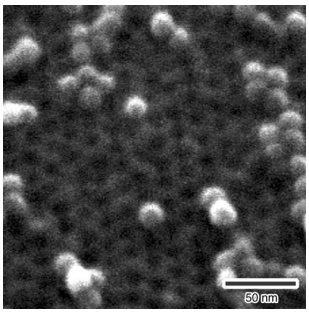 | 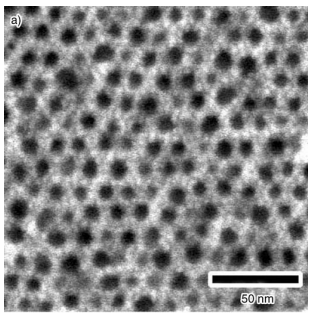 | Slow | Medium | [50] |
| 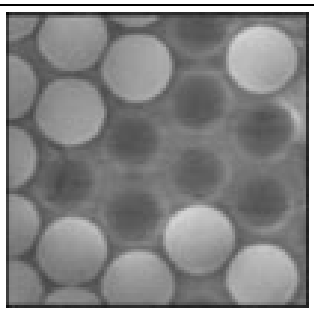 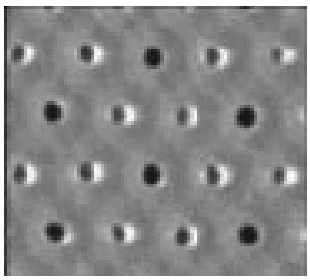 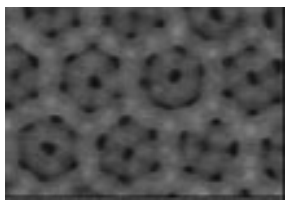 | | Medium | Medium | [49] |

*Table I-c: Anodization of pre-patterned aluminium: Monodomain alumina*

| | | | |
|---|---|---|---|
| Al | 2D/3D alumina composite | • Templating process with polystyrene beads<br>• Multistep anodizing: | 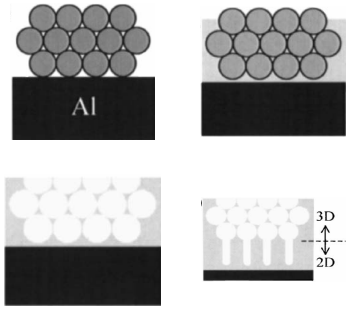 |
| Al | Monodomain | • Al patterning with optical diffraction grating<br>• Anodizing:<br>1:600 $H_3PO_4$:$H_2O$/200 V/3 h | 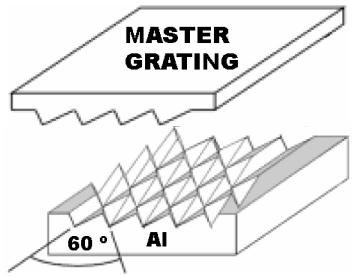 |
| Al/Glass | Monodomain | • Al evaporation or sputtering onto Ni mould<br>• Anodizing:<br>0.3 M $(COOH)_2$/40 V/17 ºC/210 s | 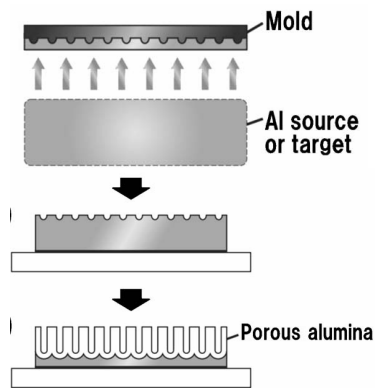 |

UNIVERSITAT ROVIRA I VIRGILI
DEVELOPMENT OF TECHNOLOGY AND APPLICATIONS BASED ON POROUS ALUMINA NANOSTRUCTURES
Lukas Vojkuvka
DL: T-1536-2009/ISBN: 978-84-692-4555-2

*Table I-c: Anodization of pre-patterned aluminium: Monodomain alumina*

| | | | |
|---|---|---|---|
| 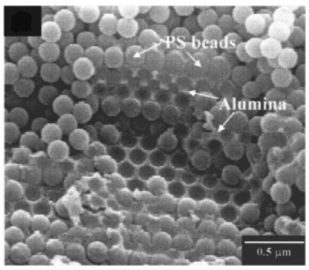 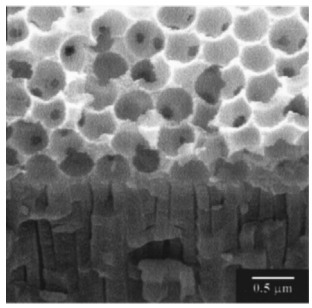 | Slow | Medium | [51] |
| 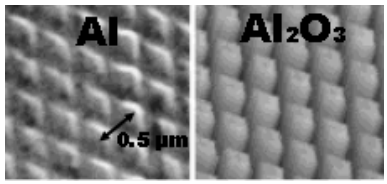 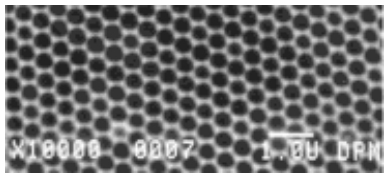 | Fast | Medium | [44] |
| 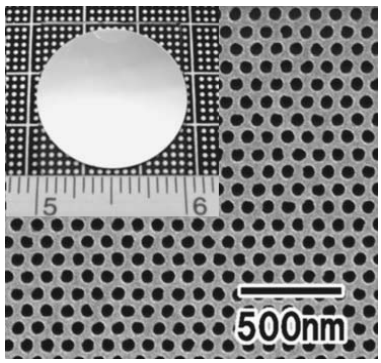 | Medium | Medium | [39] |

*Table II-a: Novel anodization techniques: New self-ordering regimes*

| Substrate | Alumina Features | Experimental Details | Fabrication |
|---|---|---|---|
| Al | 3D membranes | • Ni stamp imprinting<br>• Multicycled anodizing: 4 wt% $H_3PO_4$/110 V/10 ºC<br>0.015 M $(COOH)_2$/137 V/0.5 ºC | 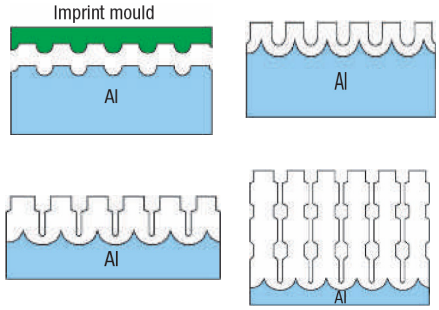 |
| Al | Hard-anodized | • Anodizing: 1.8 M $H_2SO_4$/25 – 1000 mA + 40 – 80 V/1 ºC<br>• Or: 0.3 and 0.03 M $H_2SO_4$/25 V + 40 – 80 V/0 ºC | 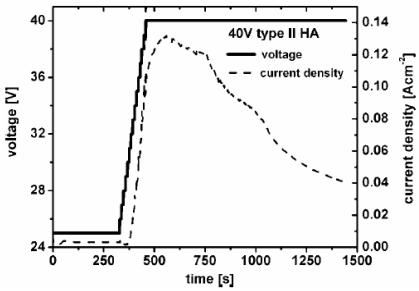 |
| Al | 3D Multi-layer membranes | • Pulse anodization: 0.3 M $H_2SO_4$/25 V – mild pulse (MA), 35 V – hard pulse (HA) | 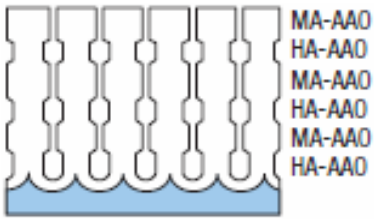 |
| Al | Organic acids | • One step anodizing: 5 mol/L malonic, 2 mol/L tartaric and 2 mol/L citric acid/120 V, 195 V and 240 V/5 ºC/hours | 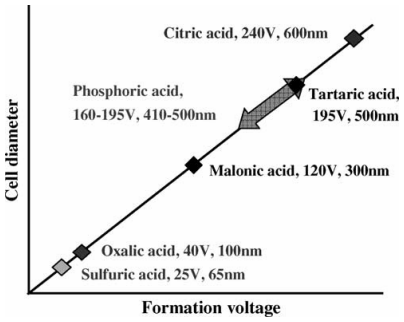 |

UNIVERSITAT ROVIRA I VIRGILI
DEVELOPMENT OF TECHNOLOGY AND APPLICATIONS BASED ON POROUS ALUMINA NANOSTRUCTURES
Lukas Vojkuvka
DL: T-1536-2009/ISBN: 978-84-692-4555-2

*Table II-a: Novel anodization techniques: New self-ordering regimes*

| Results | Time | Cost | Reference |
|---|---|---|---|
| 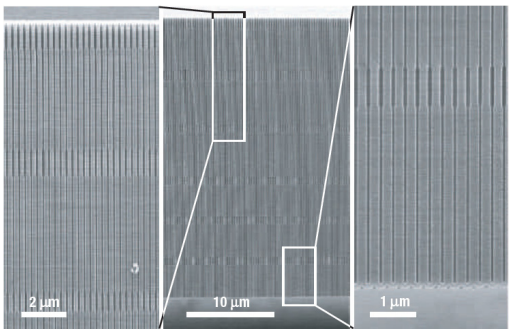  | Slow | Medium | [52] |
| 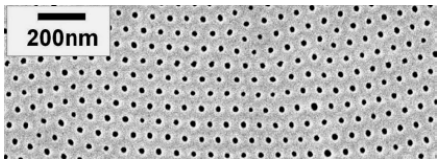  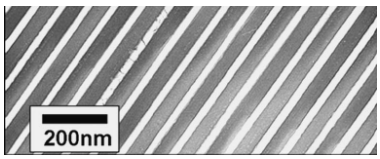  | Fast | Low | [54] |
| 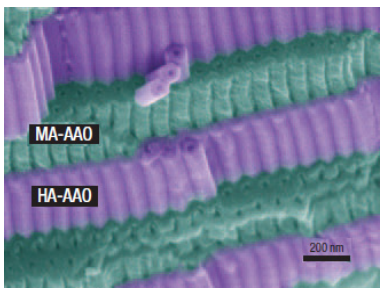  | Fast | Low | [55] |
| 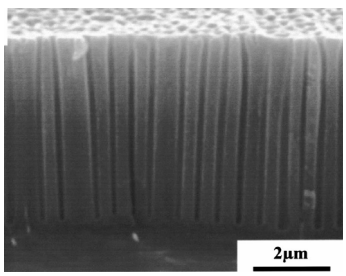  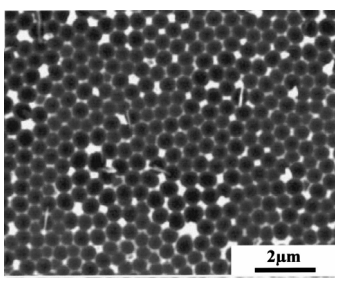  | Fast | Low | [57-59] |

DL: T-1536-2009/ISBN: 978-84-692-4555-2

*Table II-b: Novel anodization techniques: New self-ordering regimes*

| | | | |
|---|---|---|---|
| Al/ITO/Glass | 3D with extra large cell size | • Multi-cycled sputtering<br>• Anodizing: $(COOH)_2$, $H_3PO_4$, Citric acid/140 – 280 V/10 ºC | 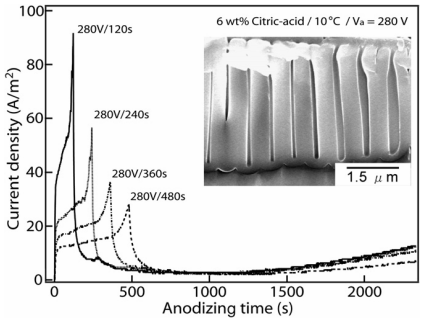 |
| Al | Combined interpore distance | • Anodizing in acid mixture: 0.3 M $(COOH)_2$ + 0.3 M $H_2SO_4$/20 – 50 V/3 ºC | 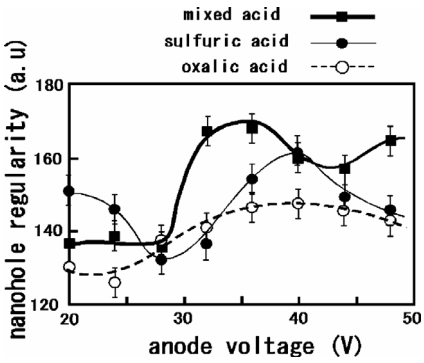 |
| Al, Al/ITO/Glass, Al/FTO/Glass | Arbitrary pore intervals | • Sputtering<br>• Critical-potential anodization: $H_2SO_4$, $(COOH)_2$, $H_3PO_4$, glycolic, tartaric, malic and citric acids/8 – 450 V/ various concentrations and temperatures | 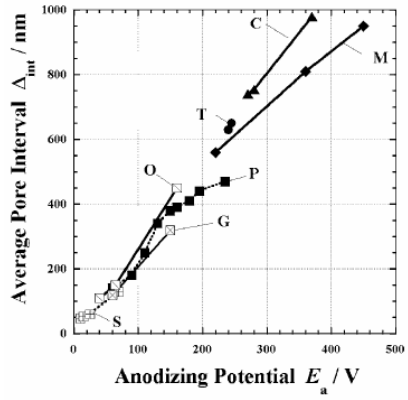 |
| Al | Extra short interpore distance | • Anodizing: 1. step 6-8 M $H_2SO_4$/10-18 V/20 – 60 ºC 2. step 0.3 M $H_2SO_4$/10 – 18 V/0 ºC | 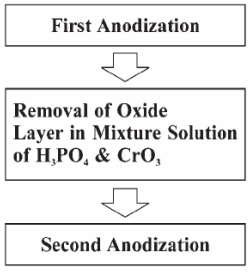 |

UNIVERSITAT ROVIRA I VIRGILI
DEVELOPMENT OF TECHNOLOGY AND APPLICATIONS BASED ON POROUS ALUMINA NANOSTRUCTURES
Lukas Vojkuvka
DL: T-1536-2009/ISBN: 978-84-692-4555-2

*Table II-b: Novel anodization techniques: New self-ordering regimes*

| | | | |
|---|---|---|---|
| 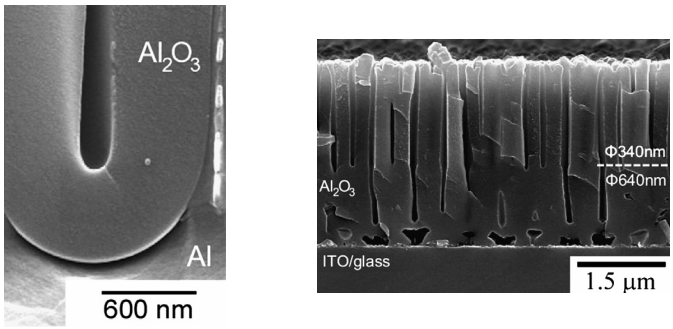 | Slow | Medium | [61] |
| 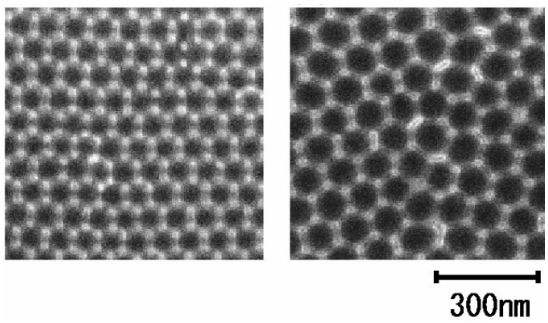 | Fast | Low | [23] |
| 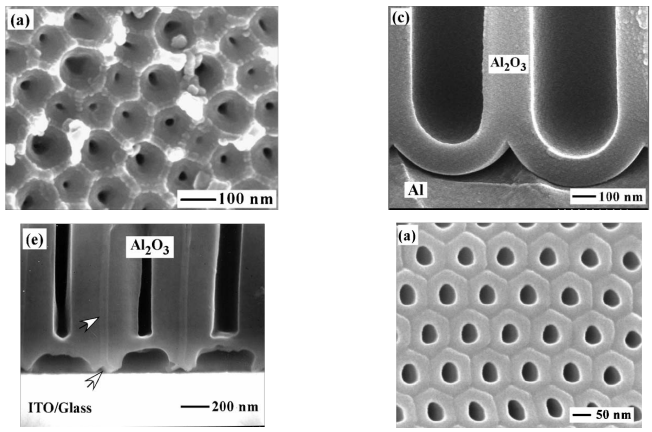 | Medium | Medium | [62, 63] |
| 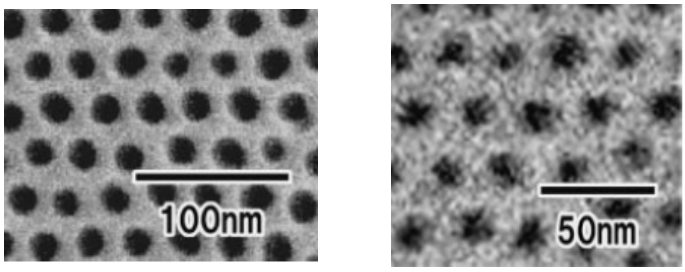 | Fast | Low | [64, 65] |

*Table II-c: Novel anodization techniques: New self-ordering regimes*

| | | | |
|---|---|---|---|
| A1 | Diverse pore intervals | • High-field anodization: Acid/ethanol/water solutions $H_2SO_4$, $(COOH)_2$, $H_3PO_4$/30 – 180 V/-10 – 0 ºC | 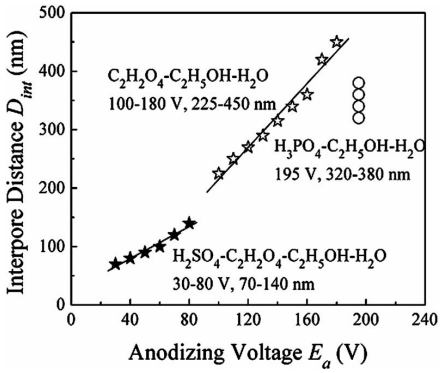 |

*Table II-c: Novel anodization techniques: New self-ordering regimes*

| | | | |
|---|---|---|---|
| 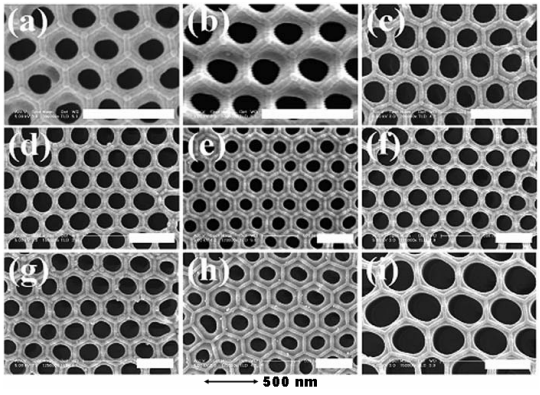 | Fast | Low | [66, 67] |

UNIVERSITAT ROVIRA I VIRGILI
DEVELOPMENT OF TECHNOLOGY AND APPLICATIONS BASED ON POROUS ALUMINA NANOSTRUCTURES
Lukas Vojkuvka
DL: T-1536-2009/ISBN: 978-84-692-4555-2

*Table III-a: Miscellaneous and complex-shaped porous alumina*

| Substrate | Alumina Features | Experimental Details | Fabrication |
|---|---|---|---|
| $SiO_2$/Al/$SiO_2$/Si | Horizontal | • DC sputtering of Al<br>• e-beam evaporation of $SiO_2$<br>• Anodizing:<br>0.2 M $(COOH)_2$/40 V/20 ºC | 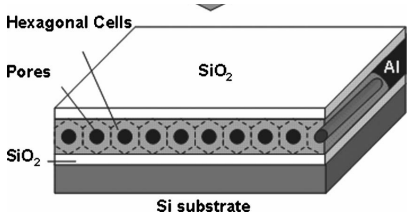 |
| $SiO_2$/Al/$SiO_2$/Si | Horizontal | • Thermal evaporation of Al<br>• Optical photolithography<br>• PEVCD<br>• Anodizing:<br>$H_2SO_4$, $(COOH)_2$, $H_3PO_4$/10 – 130 V/0 ºC | 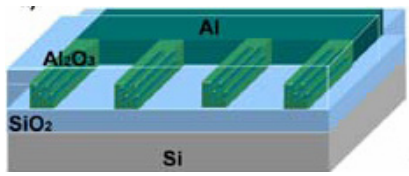 |
| Al | Nonlinear pores | • Complex-shaped Al substrates<br>• Anodizing:<br>0.4 M $(COOH)_2$/60V/0 ºC/12 – 24 h | 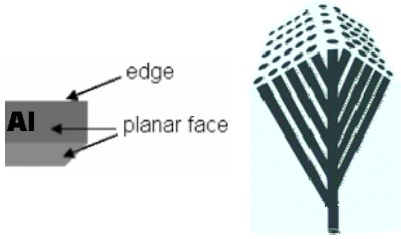 |
| Al | Cylindrical | • Al wire substrate<br>• Anodizing:<br>0.3 $(COOH)_2$/40 V/5 ºC<br>10 wt% $H_2SO_4$/25 V/3 ºC | 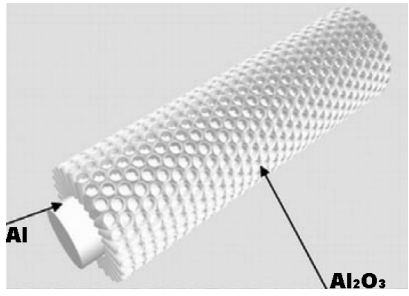 |

*Table III-a: Miscellaneous and complex-shaped porous alumina*

| Results | Time | Cost | Reference |
|---|---|---|---|
| 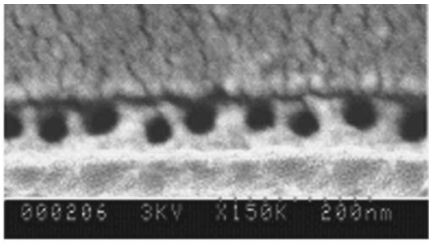  | Slow | High | [75] |
| 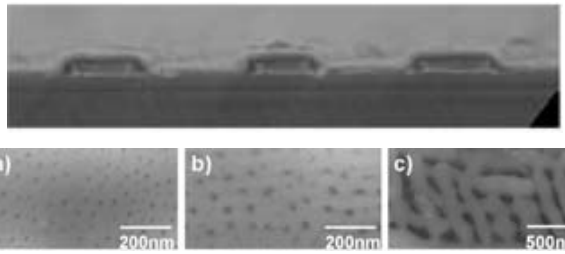  | Slow | High | [76] |
| 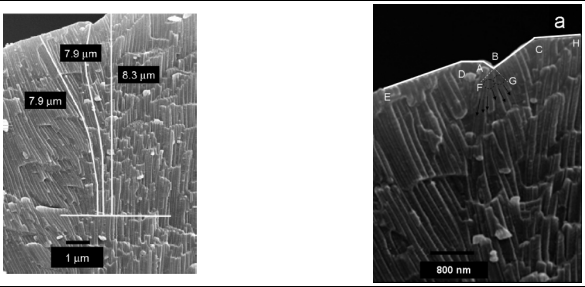  | Fast | Low | [78] |
| 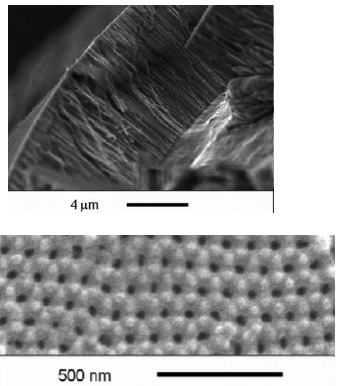  | Fast | Low | [79] |

UNIVERSITAT ROVIRA I VIRGILI
DEVELOPMENT OF TECHNOLOGY AND APPLICATIONS BASED ON POROUS ALUMINA NANOSTRUCTURES
Lukas Vojkuvka
DL: T-1536-2009/ISBN: 978-84-692-4555-2

*Table III-b: Miscellaneous and complex-shaped porous alumina*

| | | | |
|---|---|---|---|
| Al | Netlike mesoporous | • Anodizing:<br>Saw-like voltage profile<br> 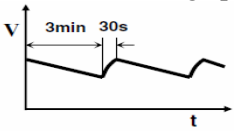 <br>0.3 M $(COOH)_2$ | 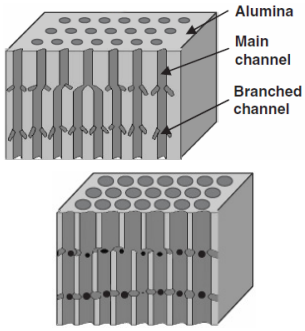 |
| Al | Tree-like | • Non-steady-state anod.:<br>0.3 M $(COOH)_2$/exponential profile from 40 V to 5 V/4 ºC | 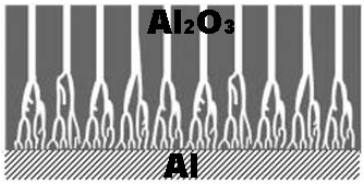 |
| Al, Al/Si | Multi-tiered | • e-beam evaporation<br>• Combined anodizing:<br>0.3 M $H_3PO_4$/130 V/25 ºC/50 min<br>0.15 M $(COOH)_2$/80-100 V/0 ºC/3 min<br>• Pore widening | 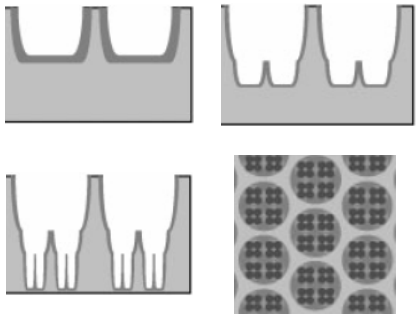 |
| Al | Stepped pores | • Anodizing:<br>0.3 M $(COOH)_2$/40-45 V/10-17 ºC<br>• Pore widening | 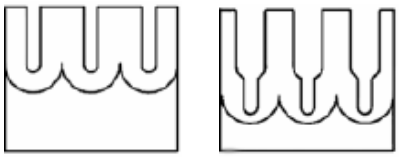 |
| Al | Tapered pores | • Anodizing:<br>0.3 M $(COOH)_2$/40 V/17 ºC or<br>2 vol.% $H_3PO_4$/120 V/10 ºC/40 – 590 s<br>• Pore widening | 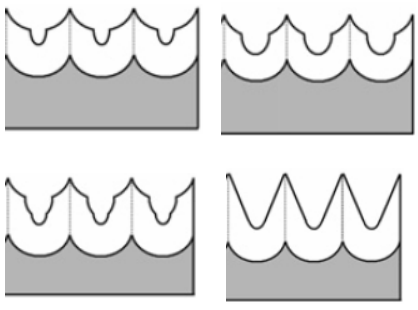 |

*Table III-b: Miscellaneous and complex-shaped porous alumina*

| | | | |
|---|---|---|---|
| 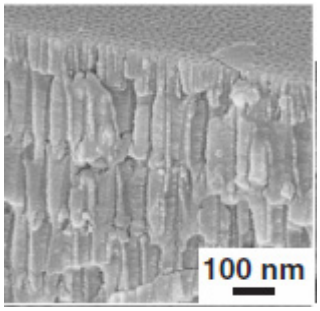 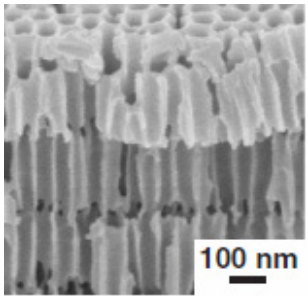 | Fast | Low | [81, 82] |
| 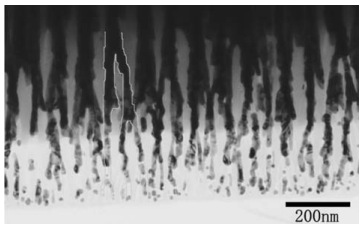 | Fast | Low | [83] |
| 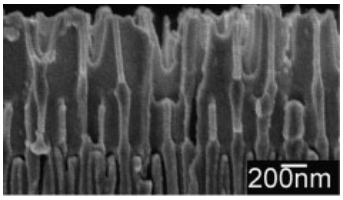 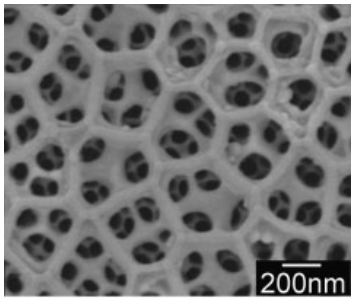 | Slow | Medium | [84] |
| 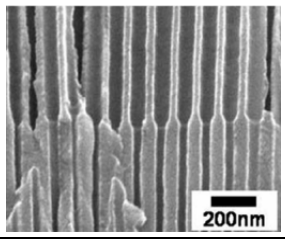 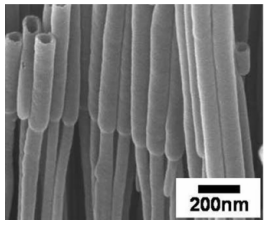 | Medium | Low | [85, 86] |
| 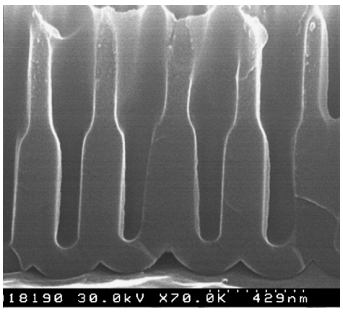 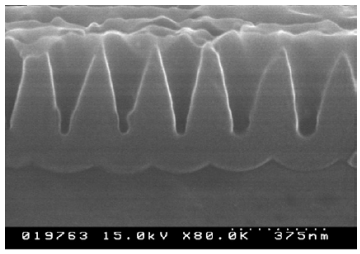 | Medium | Low | [87, 91] |

DL: T-1536-2009/ISBN: 978-84-692-4555-2

*Table III-c: Miscellaneous and complex-shaped porous alumina*

| | | | |
|---|---|---|---|
| Al | Ring pore ordering | • High-current anodization: 0.8 M $H_2SO_4$ + 0.1 M $Al_2(SO_4)_3$/160 mA/1 ºC<br>• HCl/$CuCl_2$ wet etching | 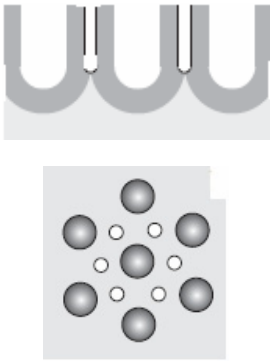 |
| Al | Tip-like | • Anodizing: $H_3PO_4$ + citric + ethanol + Al ions/180 V/20 ºC/25 – 50 min | 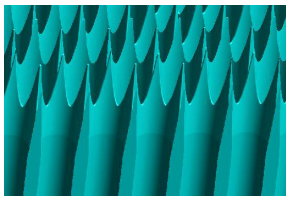 |
| Al | Ultrathick barrier layer | • Anodizing: 1. ethylene glycol sol. of 6 wt% $H_3PO_4$/5 mA/298 K 2. eth. glyc. sol. of 5 wt% ammonium sebacate/7 mA/323 K | 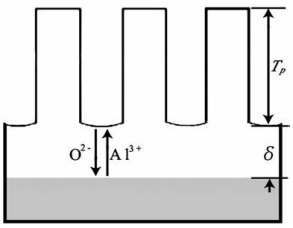 |

*Table III-c: Miscellaneous and complex-shaped porous alumina*

| | | | | |
|---|---|---|---|---|
| 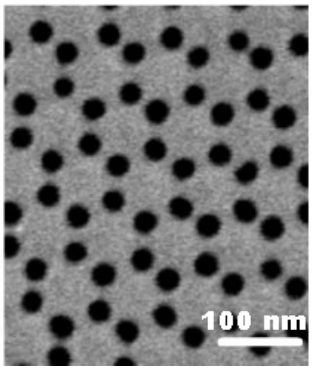 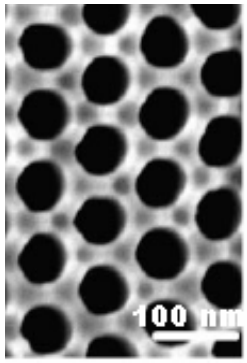 | Fast | Low | [92] |
| 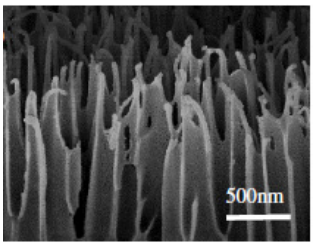 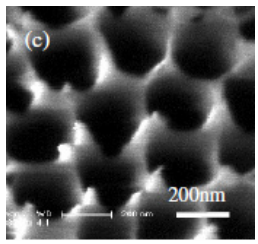 | Fast | Low | [93] |
| 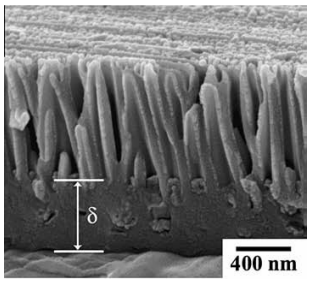 | Fast | Low | [94] |

UNIVERSITAT ROVIRA I VIRGILI
DEVELOPMENT OF TECHNOLOGY AND APPLICATIONS BASED ON POROUS ALUMINA NANOSTRUCTURES
Lukas Vojkuvka
DL: T-1536-2009/ISBN: 978-84-692-4555-2

UNIVERSITAT ROVIRA I VIRGILI
DEVELOPMENT OF TECHNOLOGY AND APPLICATIONS BASED ON POROUS ALUMINA NANOSTRUCTURES
Lukas Vojkuvka
DL: T-1536-2009/ISBN: 978-84-692-4555-2

# Bibliography

DL: T-1536-2009/ISBN: 978-84-692-4555-2

1. Sheasby, P.G. and W.E. Cook, *The electrolytic colouring of anodized aluminum.* Transaction of the Institute of Metal Finishing, 1974. **52**: p. 103-106.

2. Keller, F., M.S. Hunter, and D.L. Robinson, *Structural Features of Oxide Coatings on Aluminum.* Journal of the Electrochemical Society, 1953. **100**(9): p. 411-419.

3. Diggle, J.W., T.C. Downie, and C.W. Goulding, *Anodic oxide films on aluminum.* Chemical Reviews, 1969. **69**(3): p. 365-&.

4. Thompson, G.E. and G.C. Wood, *Porous anodic film formation on aluminum.* Nature, 1981. **290**(5803): p. 230-232.

5. Skeldon, P., et al., *Evidence of oxygen bubbles formed within anodic films on aluminium-copper alloys.* Philosophical Magazine a-Physics of Condensed Matter Structure Defects and Mechanical Properties, 1997. **76**(4): p. 729-741.

6. Thompson, G.E., *Porous anodic alumina: Fabrication, characterization and applications.* Thin Solid Films, 1997. **297**(1-2): p. 192-201.

7. Itaya, K., et al., *Properties of porous anodic aluminum-oxide films as membranes.* Journal of Chemical Engineering of Japan, 1984. **17**(5): p. 514-520.

8. Furneaux, R.C., W.R. Rigby, and A.P. Davidson, *The formation of controlled-porosity membranes from anodically oxidized aluminum.* Nature, 1989. **337**(6203): p. 147-149.

9. Masuda, H. and K. Fukuda, *Ordered metal nanohole arrays made by a 2-step replication of honeycomb structures of anodic alumina.* Science, 1995. **268**(5216): p. 1466-1468.

10. Lei, Y., W.P. Cai, and G. Wilde, *Highly ordered nanostructures with tunable size, shape and properties: A new way to surface nano-patterning using ultra-thin alumina masks.* Progress in Materials Science, 2007. **52**: p. 465-539.

11. Masuda, H., *Highly ordered nanohole arrays in anodic porous alumina*, in *Ordered Porous Nanostructures and Applications*, R.B. Wehrspohn, Editor. 2005, Springer.

12. Li, F.Y., L. Zhang, and R.M. Metzger, *On the growth of highly ordered pores in anodized aluminum oxide.* Chemistry of Materials, 1998. **10**(9): p. 2470-2480.

13. Dekker, M., *Encyclopedia of electrochemistry of the elements*. 1973: New York and Basel.

14. Jessensky, O., F. Muller, and U. Gosele, *Self-organized formation of hexagonal pore arrays in anodic alumina.* Applied Physics Letters, 1998. **72**(10): p. 1173-1175.

15. Wu, Z., C. Richter, and L. Menon, *A study of anodization process during pore formation in nanoporous alumina templates.* Journal of the Electrochemical Society, 2007. **154**(1): p. E8-E12.

16. Friedman, A.L., D. Brittain, and L. Menon, *Roles of pH and acid type in the anodic growth of porous alumina.* Journal of Chemical Physics, 2007. **127**.

17. Choi, J., *Fabrication of monodomain porous alumina using nanoimprint lithography and its application*, in *Mathematisch Naturwissenschaftlich Technischen Fakultät*. 2004, Martin Luther Universität: Halle.

18. Parkhutik, V.P. and V.I. Shershulsky, *Theoretical modeling of porous oxide - growth on aluminium.* Journal of Physics D-Applied Physics, 1992. **25**(8): p. 1258-1263.

19. Yuzhakov, V.V., H.C. Chang, and A.E. Miller, *Pattern formation during electropolishing.* Physical Review B, 1997. **56**(19): p. 12608-12624.

20. Jessensky, O., F. Muller, and U. Gosele, *Self-organized formation of hexagonal pore structures in anodic alumina.* Journal of the Electrochemical Society, 1998. **145**(11): p. 3735-3740.

21. Li, A.P., et al., *Hexagonal pore arrays with a 50-420 nm interpore distance formed by self-organization in anodic alumina.* Journal of Applied Physics, 1998. **84**(11): p. 6023-6026.

22. Sulka, G.D., et al., *Effect of tensile stress on growth of self-organized nanostructures on anodized aluminum.* Journal of the Electrochemical Society, 2004. **151**(5): p. B260-B264.

23. Shingubara, S., et al., *Self-organization of a porous alumina nanohole array using a sulfuric/oxalic acid mixture as electrolyte.* Electrochemical and Solid State Letters, 2004. **7**(3): p. E15-E17.

24. Ebihara, K., Takahashi, H., Nagayama, M., J. Met. Finish. Soc. Jpn., 1982. **33**: p. 4.

25. Sui, Y.C., et al., *Pore structure, barrier layer topography and matrix alumina structure of porous anodic alumina film.* Thin Solid Films, 2002. **406**(1-2): p. 64-69.

26. Masuda, H., F. Hasegwa and S. Ono, *Self-ordering of cell arrangement of anodic porous alumina formed in sulfuric acid solution.* Journal of the Electrochemical Society, 1997. **144**: p. L 127 - L 130.

27. Masuda, H., K. Yada and A. Osaka, *Self-ordering of cell configuration of anodic porous alumina with large-size pores in phosphoric acid solution.* Japanese Journal of Applied Physics Part 2-Letters & Express Letters, 1998. **37**: p. L1340-L1342.

28. Li, A.P., et al., *Polycrystalline nanopore arrays with hexagonal ordering on aluminum.* Journal of Vacuum Science & Technology a-Vacuum Surfaces and Films, 1999. **17**(4): p. 1428-1431.

29. Li, A.P., F. Muller, and U. Gosele, *Polycrystalline and monocrystalline pore arrays with large interpore distance in anodic alumina.* Electrochemical and Solid State Letters, 2000. **3**(3): p. 131-134.

DL: T-1536-2009/ISBN: 978-84-692-4555-2

30. Nielsch, K., et al., *Self-ordering regimes of porous alumina: The 10% porosity rule.* Nano Letters, 2002. **2**(7): p. 677-680.

31. Osulliva J. P. and G.C. Wood, *Morphology and mechanism of formation of porous anodic films on aluminium.* Proceedings of the Royal Society of London Series a-Mathematical and Physical Sciences, 1970. **317**(1531): p. 511-&.

32. Masuda, H., et al., *Highly ordered nanochannel-array architecture in anodic alumina.* Applied Physics Letters, 1997. **71**(19): p. 2770-2772.

33. Pang, S.W., et al., *Direct nano-printing on Al substrate using a SiC mold.* Journal of Vacuum Science & Technology B, 1998. **16**(3): p. 1145-1149.

34. Asoh, H., et al., *Conditions for fabrication of ideally ordered anodic porous alumina using pretextured Al.* Journal of the Electrochemical Society, 2001. **148**(4): p. B152-B156.

35. Asoh, H., et al., *Fabrication of ideally ordered anodic porous alumina with 63 nm hole periodicity using sulfuric acid.* Journal of Vacuum Science & Technology B, 2001. **19**(2): p. 569-572.

36. Masuda, H., et al., *Square and triangular nanohole array architectures in anodic alumina.* Advanced Materials, 2001. **13**(3): p. 189-192.

37. Asoh, H., et al., *Growth of anodic porous alumina with square cells.* Electrochimica Acta, 2003. **48**(20-22): p. 3171-3174.

38. Masuda, H., et al., *Self-repair of ordered pattern of nanometer dimensions based on self-compensation properties of anodic porous alumina.* Applied Physics Letters, 2001. **78**(6): p. 826-828.

39. Nishio, K., et al., *Fabrication of ideally ordered anodic porous alumina with large area by vacuum deposition of Al onto mold.* Journal of Vacuum Science & Technology B, 2008. **26**(1): p. L10-L12.

40. Choi, J., et al., *Fabrication of monodomain alumina pore arrays with an interpore distance smaller than the lattice constant of the imprint stamp.* Journal of Vacuum Science & Technology B, 2003. **21**(2): p. 763-766.

41. Choi, J., et al., *Large-area porous alumina photonic crystals via imprint method.* Materials and Devices for Optoelectronics and Microphotonics, 2002. **722**: p. 417-422.

42. Lee, W., et al., *Wafer-scale Ni imprint stamps for porous alumina membranes based on interference lithography.* Small, 2006. **2**(8-9): p. 978-982.

43. Yasui, K., et al., *Ideally ordered anodic porous alumina with Sub-50 nm hole intervals based on imprinting using metal molds.* Journal of Vacuum Science & Technology B, 2005. **23**(4): p. L9-L12.

44. Mikulskas, I., et al., *Aluminum oxide photonic crystals grown by a new hybrid method.* Advanced Materials, 2001. **13**(20): p. 1574-+.

45. Liu, C.Y., A. Datta, and Y.L. Wang, *Ordered anodic alumina nanochannels on focused-ion-beam-prepatterned aluminum surfaces.* Applied Physics Letters, 2001. **78**(1): p. 120-122.

46. Liu, C.Y., et al., *Enhanced growth of anodic alumina nanochannels on Ga-ion pre-irradiated aluminum.* Journal of Vacuum Science & Technology B, 2008. **26**(2): p. 651-654.

47. Sun, Z.J. and H.K. Kim, *Growth of ordered, single-domain, alumina nanopore arrays with holographically patterned aluminum films.* Applied Physics Letters, 2002. **81**(18): p. 3458-3460.

48. Krishnan, R. and C.V. Thompson, *Monodomain high-aspect-ratio 2D and 3D ordered porous alumina structures with independently controlled pore spacing and diameter.* Advanced Materials, 2007. **19**(7): p. 988-+.

49. Fournier-Bidoz, S., et al., *Highly ordered nanosphere imprinted nanochannel alumina (NINA).* Advanced Materials, 2004. **16**(23-24): p. 2193-+.

50. Matsui, Y., K. Nishio, and H. Masuda, *Highly ordered anodic porous alumina with 13-nm hole intervals using a 2D array of monodisperse nanoparticles as a template.* Small, 2006. **2**(4): p. 522-525.

51. Asoh, H. and S. Ono, *Design of two-dimensional/three-dimensional composite porous alumina by colloidal crystal templating and subsequent anodization.* Applied Physics Letters, 2005. **87**(10).

52. Lee, W., et al., *Fast fabrication of long-range ordered porous alumina membranes by hard anodization.* Nature Materials, 2006. **5**(9): p. 741-747.

53. Csokán, P., et al., *Hard anodizing: Studies of the relation between anodizing conditions and the growth and properties of hard anodic oxide coatings.* Electroplat. Metal Finish, 1962. **15**: p. 75-82.

54. Schwirn, K., et al., *Self-ordered anodic aluminum oxide formed by H2SO4 hard anodization.* Acs Nano, 2008. **2**(2): p. 302-310.

55. Lee, W., et al., *Structural engineering of nanoporous anodic aluminium oxide by pulse anodization of aluminium.* Nature Nanotechnology, 2008. **3**(4): p. 234-239.

56. Li, Y., et al., *Fabrication of novel porous anodic alumina membranes by two-step hard anodization.* Nanotechnology, 2008. **19**(22).

57. Ono, S., M. Saito, and H. Asoh, *Self-ordering of anodic porous alumina induced by local current concentration: Burning.* Electrochemical and Solid State Letters, 2004. **7**(7): p. B21-B24.

58. Ono, S., M. Saito, and H. Asoh, *Self-ordering of anodic porous alumina formed in organic acid electrolytes.* Electrochimica Acta, 2005. **51**(5): p. 827-833.

59. Ono, S., et al., *Controlling factor of self-ordering of anodic porous alumina.* Journal of the Electrochemical Society, 2004. **151**(8): p. B473-B478.

60. Lee, W., K. Nielsch, and U. Gosele, *Self-ordering behavior of nanoporous anodic aluminum oxide (AAO) in malonic acid anodization.* Nanotechnology, 2007. **18**(47).

61. Katsuta, Y., et al., *Three-dimensionally nanostructured alumina film on glass substrate: Anodization of glass surface.* Journal of Non-Crystalline Solids, 2008. **354**: p. 451-455.

62. Chu, S.Z., et al., *Large-scale fabrication of ordered nanoporous alumina films with arbitrary pore intervals by critical-potential anodization.* Journal of the Electrochemical Society, 2006. **153**(9): p. B384-B391.

63. Chu, S.Z., et al., *Fabrication of ideally ordered nanoporous alumina films and integrated alumina nanotubule arrays by high-field anodization.* Advanced Materials, 2005. **17**(17): p. 2115-+.

64. Masuda, H., et al., *Long-range-ordered anodic porous alumina with reduced hole interval formed in highly concentrated sulfuric acid solution.* Japanese Journal of Applied Physics Part 2-Letters & Express Letters, 2006. **45**(12-16): p. L406-L408.

65. Masuda, H., et al., *Long-range-ordered anodic porous alumina with less-than-30 nm hole interval.* Japanese Journal of Applied Physics Part 2-Letters & Express Letters, 2006. **45**(42-45): p. L1165-L1167.

66. Li, D.D., et al., *Investigation on highly ordered porous anodic alumina membranes formed by high electric field anodization.* Materials Chemistry and Physics, 2008. **111**(1): p. 168-171.

67. Li, Y.B., M.J. Zheng, and L. Ma, *High-speed growth and photoluminescence of porous anodic alumina films with controllable interpore distances over a large range.* Applied Physics Letters, 2007. **91**.

68. Li, Y.B., et al., *Fabrication of highly ordered nanoporous alumina films by stable high-field anodization.* Nanotechnology, 2006. **17**(20): p. 5101-5105.

69. Shingubara, S., *Fabrication of nanomaterials using porous alumina templates.* Journal of Nanoparticle Research, 2003. **5**(1-2): p. 17-30.

70. Prida, V.M., et al., *Self-organized magnetic nanowire arrays based on alumina and Titania templates.* Journal of Nanoscience and Nanotechnology, 2007. **7**(1): p. 272-285.

71. Xu, C.L., et al., *Electrodeposition and magnetic properties of Ni nanowire arrays on anodic aluminum oxide/Ti/Si substrate.* Applied Surface Science, 2006. **253**(3): p. 1399-1403.

72. Govyadinov, A.N. and S.A. Zakhvitcevich, *Field emitter arrays based on natural self-organized porous anodic alumina.* Journal of Vacuum Science & Technology B, 1998. **16**(3): p. 1222-1225.

73. Holland, E.R., et al., *Large area gridded field emitter arrays using anodised aluminium.* Displays, 2000. **21**(2-3): p. 99-104.

74. Hubalek, J., et al., *Pt-loaded Al2O3 catalytic filters for screen-printed WO3 sensors highly selective to benzene.* Sensors and Actuators B-Chemical, 2004. **101**(3): p. 277-283.

75. Chen, Z. and H.G. Zhang, *Mechanisms for formation of a one-dimensional horizontal anodic aluminum oxide nanopore array on a Si substrate.* Journal of the Electrochemical Society, 2005. **152**(12): p. D227-D231.

76. Xiang, Y., et al., *Microstructured horizontal alumina pore arrays as growth templates for large area few and single nanowire devices.* Physica Status Solidi-Rapid Research Letters, 2008. **2**(2): p. 59-61.

77. Gowtham, M., et al., *Controlled fabrication of patterned lateral porous alumina membranes.* Nanotechnology, 2008. **19**.

78. Zakeri, R., et al., *Synthesis and characterization of nonlinear nanopores in alumina films.* Chemistry of Materials, 2007. **19**: p. 1954-1963.

79. Sanz, R., et al., *Fabrication and magnetic functionatization of cylindrical porous anodic alumina.* Small, 2007. **3**(3): p. 434-437.

80. Li, J., C. Papadopoulos, and J. Xu, *Nanoelectronics - Growing Y-junction carbon nanotubes.* Nature, 1999. **402**(6759): p. 253-254.

81. Wang, B., et al., *Preparation of three-dimensional netlike mesoporous alumina membrane.* Chemistry Letters, 2006. **35**(12): p. 1336-1337.

82. Wang, B., et al., *Preparation of photonic crystals made of air pores in anodic alumina.* Nanotechnology, 2007. **18**.

83. Cheng, W.L., et al., *Tree-like alumina nanopores generated in a non-steady-state anodization.* Journal of Materials Chemistry, 2007. **17**(33): p. 3493-3495.

84. Ho, A.Y.Y., et al., *Controlled fabrication of multitiered three-dimensional nanostructures in porous alumina.* Advanced Functional Materials, 2008. **18**(14): p. 2057-2063.

85. Lee, J.S., et al., *Growth of carbon nanotubes on anodic aluminum oxide templates: Fabrication of a tube-in-tube and linearly joined tube.* Chemistry of Materials, 2001. **13**(7): p. 2387-2391.

86. Im, W.S., et al., *Stepped carbon nanotubes synthesized in anodic aluminum oxide templates.* Diamond and Related Materials, 2004. **13**(4-8): p. 1214-1217.

87. Yanagishita, T., K. Nishio, and H. Masuda, *Two-dimensional photonic crystal composed of ordered polymer nanopillar arrays with high aspect ratios using anodic porous alumina templates.* Applied Physics Express, 2008. **1**(1).

88. Yanagishita, T., et al., *Antireffection polymer surface using anodic porous alumina molds with tapered holes.* Chemistry Letters, 2007. **36**(4): p. 530-531.

89. Nagaura, T., F. Takeuchi, and S. Inoue, *Fabrication and structural control of anodic alumina films with inverted cone porous structure using multi-step anodizing.* Electrochimica Acta, 2008. **53**: p. 2109-2114.

DL: T-1536-2009/ISBN: 978-84-692-4555-2

90. Nagaura, T., et al., *Fabrication of ordered Ni nanocones using a porous anodic alumina template.* Electrochemistry Communications, 2008. **10**(5): p. 681-685.

91. Yamauchi, Y., et al., *Evolution of standing mesochannels on porous anodic alumina substrates with designed conical holes.* Journal of the American Chemical Society, 2008. **130**(31): p. 10165-10170.

92. Zhao, S.Y., et al., *Novel structure of AAO film fabricated by constant current anodization.* Advanced Materials, 2007. **19**: p. 3004-+.

93. Sun, Q.W., et al., *Tip-like anodic alumina.* Nanotechnology, 2007. **18**(21).

94. Li, D.D., et al., *Fabrication of porous anodic alumina membranes with ultrathick barrier layer.* Materials Letters, 2008. **62**(17-18): p. 3228-3231.

95. Rauf, A., et al., *The effects of electropolishing on the nanochannel ordering of the porous anodic alumina prepared in oxalic acid.* Journal of Solid State Electrochemistry, 2009. **13**(2): p. 321-332.

96. Caicedo-Martinez, C.E., G.E. Thompson, and E.V. Koroleva, *Nanoscale engineering of aluminium surfaces.* Surface Engineering, 2002. **18**(2): p. 145-150.

97. Montero-Moreno, J.M., M. Sarret, and C. Muller, *Influence of the aluminum surface on the final results of a two-step anodizing.* Surface & Coatings Technology, 2007. **201**(14): p. 6352-6357.

98. Vojkuvka, L., L.F. Marsal, and J. Pallares, *Study of porous alumina porosity after pore widening process.* 2007 Spanish Conference on Electron Devices, Proceedings, 2007: p. 41-43.

99. Marsal, L.F., Vojkuvka, L., Formentin, P., Pallares, J., Ferre-Borrull, J., *Fabrication and optical characterization of nanoporous alumina films annealed at different temperatures.* Optical Materials, 2008.

100. Marsal, L.F., Vojkuvka, L., Ferre-Borrull, J., Trifonov, T., Pallares, J., *Optical characterization of self-ordered porous alumina membranes of various thicknesses.* Physica Status Solidi C - Current Topics in Solid State Physics, 2007. **4**(6): p. 1918-1922.

101. Schwartz, G.C. and V. Platter, *ANODIC PROCESSING FOR MULTILEVEL LSI.* Journal of the Electrochemical Society, 1976. **123**(1): p. 34-37.

102. Schwartz, G.C. and V. Platter, *ANODIC PROCESS FOR FORMING PLANAR INTERCONNECTION METALLIZATION FOR MULTILEVEL LSI.* Journal of the Electrochemical Society, 1975. **122**(11): p. 1508-1516.

103. Matefi-Tempfli, S., M. Matefi-Tempfli, and L. Piraux, *Characterization of nanopores ordering in anodic alumina.* Thin Solid Films, 2008. **516**(12): p. 3735-3740.

104. Xu, W.L., et al., *Optical transmission spectra of ordered porous alumina membranes with different thicknesses and porosities.* Optical Materials, 2006. **28**(10): p. 1160-1165.

105. Abramoff, M.D., P.J. Magelhaes, and S.J. Ram, *Image processing with ImageJ.* Biophotonics International, 2004. **11**(7): p. 36-42.

106. Kashi, M.A. and A. Ramazani, *The effect of temperature and concentration on the self-organized pore formation in anodic alumina.* Journal of Physics D-Applied Physics, 2005. **38**(14): p. 2396-2399.

107. Sulka, G.D. and K.G. Parkola, *Temperature influence on well-ordered nanopore structures grown by anodization of aluminium in sulphuric acid.* Electrochimica Acta, 2007. **52**(5): p. 1880-1888.

108. Nielsch, K., et al., *Uniform nickel deposition into ordered alumina pores by pulsed electrodeposition.* Advanced Materials, 2000. **12**(8): p. 582-586.

109. Sulka, G.D., et al., *Electrochemical impedance spectroscopic study of barrier layer thinning in nanostructured aluminium.* Journal of Applied Electrochemistry, 2007. **37**(7): p. 789-797.

110. Mardilovich, P.P., et al., *New and modified anodic alumina membranes Part I. Thermotreatment of anodic alumina membranes.* Journal of Membrane Science, 1995. **98**(1-2): p. 131-142.

111. Xu, T.T., R.D. Piner, and R.S. Ruoff, *An improved method to strip aluminum from porous anodic alumina films.* Langmuir, 2003. **19**(4): p. 1443-1445.

112. Tian, M.L., et al., *Penetrating the oxide barrier in situ and separating freestanding porous anodic alumina films in one step.* Nano Letters, 2005. **5**(4): p. 697-703.

113. Yuan, J.H., et al., *Mechanism of one-step voltage pulse detachment of porous anodic alumina membranes.* Electrochimica Acta, 2006. **51**(22): p. 4589-4595.

114. Lira, H.D.L. and R. Paterson, *New and modified anodic alumina membranes - Part III. Preparation and characterisation by gas diffusion of 5 nm pore size anodic alumina membranes.* Journal of Membrane Science, 2002. **206**(1-2): p. 375-387.

115. Chen, W., et al., *An environment-friendly electrochemical detachment method for porous anodic alumina.* Journal of Electroanalytical Chemistry, 2007. **600**(2): p. 257-264.

116. Zhao, Y.C., et al., *A facile approach to formation of through-hole porous anodic aluminum oxide film.* Materials Letters, 2005. **59**(1): p. 40-43.

117. Vojkuvka, L., Marsal, L. F., Ferre-Borrull, J., Formentin, P., Pallares, J., *Self-ordered porous alumina membranes with large lattice constant fabricated by hard anodization.* Superlattices and Microstructures, 2008. **44**(4-5): p. 577-582.

118. Cullity, B.D., *Elements of X-ray diffraction*. 2nd ed. 1978, Massachusetts, USA: Addison Wesley.

119. Vallejos, S., et al., *Micro-machined WO3-based sensors selective to oxidizing gases.* Sensors and Actuators B-Chemical, 2008. **132**(1): p. 209-215.

120. Vallejos, S., et al., *Ozone monitoring by micro-machined sensors with WO3 sensing films.* Sensors and Actuators B-Chemical, 2007. **126**: p. 573-578.

121. Xu, W.L., et al., *Effects of high-temperature annealing on structural and optical properties of highly ordered porous alumina membranes.* Applied Physics Letters, 2004. **85**(19): p. 4364-4366.

122. Kirchner, A., et al., *Structural characterisation of heat-treated anodic alumina membranes prepared using a simplified fabrication process.* Journal of Membrane Science, 2007. **287**(2): p. 264-270.

123. Li, Y., et al., *Photoluminescence and optical absorption caused by the F+ centres in anodic alumina membranes.* Journal of Physics-Condensed Matter, 2001. **13**(11): p. 2691-2699.

124. Yakovleva, N.M., A.N. Yakovlev, and E.A. Chupakhina, *Structural analysis of alumina films produced by two-step electrochemical oxidation.* Thin Solid Films, 2000. **366**(1-2): p. 37-42.

125. Joannopoulos, J.D., et al., *Photonic crystals, Molding the flow of light*. 2nd ed. 2008, Woodstock, UK: Pricenton University Press.

126. Masuda, H., et al., *Lasing from two-dimensional photonic crystals using anodic porous alumina.* Advanced Materials, 2006. **18**(2): p. 213-+.

127. Mikulskas, I., Juodkazis, S., et al., *Aluminium oxide film for 2D photonic structure: room temperature formation.* Optical Materials, 2001. **17**(1-2): p. 343-346.

128. Choi, J., et al., *Perfect two-dimensional porous alumina photonic crystals with duplex oxide layers.* Journal of Applied Physics, 2003. **94**(8): p. 4757-4762.

129. Takayama, O. and M. Cada, *Two-dimensional metallo-dielectric photonic crystals embedded in anodic porous alumina for optical wavelengths.* Applied Physics Letters, 2004. **85**(8): p. 1311-1313.

130. Huang, J.Y., X.D. Wang, and Z.L. Wang, *Controlled replication of butterfly wings for achieving tunable photonic properties.* Nano Letters, 2006. **6**(10): p. 2325-2331.

131. Chen, H.M., et al., *Controlling optical properties of aluminum oxide using electrochemical deposition.* Journal of the Electrochemical Society, 2007. **154**(6): p. K11-K14.

132. Bosch, S., J. Ferre-Borrull, and J. Sancho-Parramon, *A general-purpose software for optical characterization of thin films: specific features for microelectronic applications.* Solid-State Electronics, 2001. **45**(5): p. 703-709.

133. Hohlbein, J., U. Rehn, and R.B. Wehrspohn, *In-situ optical characterisation of porous alumina.* Physica Status Solidi a-Applied Research, 2004. **201**(4): p. 803-807.

134. Huber, K., *PORE VOLUME OF ELECTROLYTICALLY PRODUCED PROTECTIVE COATINGS ON ALUMINUM.* Journal of Colloid Science, 1948. **3**(3): p. 197-206.

135. Hass, G., *ON THE PREPARATION OF HARD OXIDE FILMS WITH PRECISELY CONTROLLED THICKNESS ON EVAPORATED ALUMINUM MIRRORS.* Journal of the Optical Society of America, 1949. **39**(7): p. 532-540.

136. Nakamura, S., et al., *INFRARED OPTICAL-CONSTANTS OF ANODIC ALUMINA FILMS WITH MICROPORE ARRAYS.* Japanese Journal of Applied Physics Part 1-Regular Papers Short Notes & Review Papers, 1992. **31**(11): p. 3589-3593.

137. Wang, J.L., et al., *Tribological and optical properties of crystalline and amorphous alumina thin films grown by low-temperature reactive magnetron sputter-deposition.* Surface & Coatings Technology, 2001. **146**: p. 189-194.

138. Kimura, Y., et al., *In situ real-time infrared spectroscopy study of formation of porous anodic alumina on Si.* Journal of the Electrochemical Society, 2006. **153**(5): p. C296-C300.

139. Gao, T., G.M. Meng, and L.D. Zhang, *Blue luminescence in porous anodic alumina films: the role of the oxalic impurities.* Journal of Physics-Condensed Matter, 2003. **15**(12): p. 2071-2079.

140. Gao, T., G.W. Meng, and L.D. Zhang, *Origin of the blue luminescence in porous anodic alumina films formed in oxalic acid solutions.* Chinese Physics Letters, 2003. **20**(5): p. 713-716.

141. Fan, D.H., et al., *Anion impurities in porous alumina membranes: Existence and functionality.* Microporous and Mesoporous Materials, 2007. **100**(1-3): p. 154-159.

142. Huang, G.S., et al., *Strong blue emission from anodic alumina membranes with ordered nanopore array.* Journal of Applied Physics, 2003. **93**(1): p. 582-585.

143. Huang, G.S., et al., *On the origin of light emission from porous anodic alumina formed in sulfuric acid.* Solid State Communications, 2006. **137**(11): p. 621-624.

144. Huang, G.S., et al., *Photoluminescence from 8-hydroxy quinoline aluminum embedded in porous anodic alumina membrane.* Applied Physics Letters, 2005. **87**(15).

145. Huang, G.S., et al., *Light emission from silicon-based porous anodic alumina formed in 0.5 M oxalic acid.* Journal of Applied Physics, 2003. **94**(4): p. 2407-2410.

146. Huang, K., et al., *Photoluminescence oscillations in porous alumina films.* Applied Physics Letters, 2006. **89**(20).

147. Li, Z.J. and K.L. Huang, *Blue luminescence in porous anodic alumina films.* Journal of Physics-Condensed Matter, 2007. **19**(21).

148. Yang, M.D., et al., *Time-resolved photoluminescence in anodic aluminum oxide membranes.* Nanotechnology, 2007. **18**.

149. Du, Y., et al., *Preparation and photoluminescence of alumina membranes with ordered pore arrays.* Applied Physics Letters, 1999. **74**(20): p. 2951-2953.

DL: T-1536-2009/ISBN: 978-84-692-4555-2

150. Bueno, S. and C. Baudin, *Instrumented Vickers microindentation of alumina-based materials.* Journal of Materials Research, 2006. **21**(1): p. 161-173.

151. Oliver, W.C. and G.M. Pharr, *AN IMPROVED TECHNIQUE FOR DETERMINING HARDNESS AND ELASTIC-MODULUS USING LOAD AND DISPLACEMENT SENSING INDENTATION EXPERIMENTS.* Journal of Materials Research, 1992. **7**(6): p. 1564-1583.

152. Krell, A. and S. Schadlich, *Nanoindentation hardness of submicrometer alumina ceramics.* Materials Science and Engineering a-Structural Materials Properties Microstructure and Processing, 2001. **307**(1-2): p. 172-181.

153. Alcala, G., et al., *Mechanical properties of amorphous anodic alumina and tantala films using nanoindentation.* Nanotechnology, 2002. **13**(4): p. 451-455.

154. Bao, Y.W., W. Wang, and Y.C. Zhou, *Investigation of the relationship between elastic modulus and hardness based on depth-sensing indentation measurements.* Acta Materialia, 2004. **52**(18): p. 5397-5404.

155. Xia, Z., et al., *Mechanical properties of highly ordered nanoporous anodic alumina membranes.* Reviews on Advanced Materials Science, 2004. **6**(2): p. 131-139.

156. Gong, J.H., Z.J. Peng, and H.Z. Miao, *Analysis of the nanoindentation load-displacement curves measured on high-purity fine-grained alumina.* Journal of the European Ceramic Society, 2005. **25**(5): p. 649-654.

157. Ko, S., et al., *Mechanical properties and residual stress in porous anodic alumina structures.* Thin Solid Films, 2006. **515**(4): p. 1932-1937.

158. Ko, S.H., et al., *Mechanical properties and residual stress measurements in anodic aluminium oxide structures using nanoindentation.* Glass Physics and Chemistry, 2005. **31**(3): p. 356-363.

159. Choi, D., et al., *Structure-dependent adhesion and friction on highly ordered metallic nanopore membranes.* Nanotechnology, 2008. **19**(14).

160. Choi, D., et al., *Dependence of adhesion and friction on porosity in porous anodic alumina films.* Scripta Materialia, 2008. **58**(10): p. 870-873.

161. Choi, D., et al., *Dependence of the mechanical properties of nanohoneycomb structures on porosity.* Journal of Micromechanics and Microengineering, 2007. **17**(3): p. 501-508.

162. Fang, T.H., et al., *Physical behavior of nanoporous anodic alumina using nanoindentation and microhardness tests.* Nanoscale Research Letters, 2007. **2**(8): p. 410-415.

163. Latella, B.A., *Scratch damage in porous alumina ceramics.* Journal of Materials Science Letters, 2000. **19**(13): p. 1127-1130.

164. Bhushan, B. and S. Sundararajan, *Micro/nanoscale friction and wear mechanisms of thin films using atomic force and friction force microscopy.* Acta Materialia, 1998. **46**(11): p. 3793-3804.

165. Papka, S.D. and S. Kyriakides, *In-plane crushing of a polycarbonate honeycomb.* International Journal of Solids and Structures, 1998. **35**(3-4): p. 239-&.

166. Papka, S.D. and S. Kyriakides, *Experiments and full-scale numerical simulations of in-plane crushing of a honeycomb.* Acta Materialia, 1998. **46**(8): p. 2765-2776.

167. Almawlawi, D., N. Coombs, and M. Moskovits, *MAGNETIC-PROPERTIES OF FE DEPOSITED INTO ANODIC ALUMINUM-OXIDE PORES AS A FUNCTION OF PARTICLE-SIZE.* Journal of Applied Physics, 1991. **70**(8): p. 4421-4425.

168. Li, F.Y., R.M. Metzger, and W.D. Doyle, *Influence of particle size on the magnetic viscosity and activation volume of alpha-Fe nanowires in alumite films.* Ieee Transactions on Magnetics, 1997. **33**(5): p. 3715-3717.

169. Tager, A.A., J.M. Xu, and M. Moskovits, *Spontaneous charge polarization in single-electron tunneling through coupled nanowires.* Physical Review B, 1997. **55**(7): p. 4530-4538.

170. Kruis, F.E., et al., *Preparation of size-classified PbS nanoparticles in the gas phase.* Applied Physics Letters, 1998. **73**(4): p. 547-549.

171. Wackelgard, E., *A study of the optical properties of nickel-pigmented anodic alumina in the infrared region.* Journal of Physics-Condensed Matter, 1996. **8**(27): p. 5125-5138.

172. Sauer, G., et al., *Highly ordered monocrystalline silver nanowire arrays.* Journal of Applied Physics, 2002. **91**(5): p. 3243-3247.

173. Oh, J., Y. Tak, and Y. Lee, *Electrodeposition of Cu2O nanowires using nanoporous alumina template.* Electrochemical and Solid State Letters, 2004. **7**(3): p. C27-C30.

174. Zhang, Y., et al., *Antimony nanowire arrays fabricated by pulsed electrodeposition in anodic alumina membranes.* Advanced Materials, 2002. **14**(17): p. 1227-+.

175. Routkevitch, D., et al., *Electrochemical fabrication of CdS nanowire arrays in porous anodic aluminum oxide templates.* Journal of Physical Chemistry, 1996. **100**(33): p. 14037-14047.

176. Santos, A., Vojkuvka, L., Pallares, J., Ferre-Borrull, J., Marsal, L. F.,, *In-situ electrochemical dissolution of the oxide barrier layer of porous anodic alumina fabricated by hard anodization.* Journal of Electroanalytical Chemistry, 2008.

177. Chen, G., et al., *Integration of large-area polymer nanopillar arrays into microfluidic devices using in situ polymerization cast molding.* Lab on a Chip, 2007. **7**(11): p. 1424-1427.

178. Kuo, C.W., J.Y. Shiu, and P.L. Chen, *Size- and shape-controlled fabrication of large-area periodic nanopillar arrays.* Chemistry of Materials, 2003. **15**(15): p. 2917-2920.

179. Chen, G.F., et al., *Functional template-derived poly(methyl methacrylate) nanopillars for solid-phase biological reactions.* Chemistry of Materials, 2007. **19**: p. 3855-3857.

180. Masuda, H., K. Nishio, and N. Baba, *FABRICATION OF POROUS TIO2 FILMS USING 2-STEP REPLICATION OF MICROSTRUCTURE OF ANODIC ALUMINA.* Japanese Journal of Applied Physics Part 2-Letters, 1992. **31**(12B): p. L1775-L1777.

181. Nishio, K., K. Iwata, and H. Masuda, *Fabrication of nanoporous WO3 membranes and their electrochromic properties.* Electrochemical and Solid State Letters, 2003. **6**(10): p. H21-H23.

182. Chen, G., S.A. Soper, and R.L. McCarley, *Free-standing, erect ultrahigh-aspect-ratio polymer nanopillar and nanotube ensembles.* Langmuir, 2007. **23**(23): p. 11777-11781.

183. Steinhart, M., et al., *Polymer nanotubes by wetting of ordered porous templates.* Science, 2002. **296**(5575): p. 1997-1997.

184. Lee, S.B., et al., *Self-assembly of biocidal nanotubes from a single-chain diacetylene amine salt.* Journal of the American Chemical Society, 2004. **126**(41): p. 13400-13405.

185. Palacios, R., et al., *Polymer nanopillars using self-ordered nanoporous alumina templates.* Physica Status Solidi C - Current Topics in Solid State Physics, 2008.

186. Russell, P., *Photonic crystal fibers.* Science, 2003. **299**(5605): p. 358-362.

187. Park, H.G., et al., *Electrically driven single-cell photonic crystal laser.* Science, 2004. **305**(5689): p. 1444-1447.

188. Akmansoy, E., et al., *Graded photonic crystals curve the flow of light: An experimental demonstration by the mirage effect.* Applied Physics Letters, 2008. **92**(13).

189. Mertens, G., et al., *Tunable defect mode in a three-dimensional photonic crystal.* Applied Physics Letters, 2005. **87**(24).

190. Martinez, L.J., A. Garcia-Martin, and P.A. Postigo, *Photonic band gaps in a two-dimensional hybrid triangular-graphite lattice.* Optics Express, 2004. **12**(23): p. 5684-5689.

191. Sugitatsu, A., T. Asano, and S. Noda, *Line-defect-waveguide laser integrated with a point defect in a two-dimensional photonic crystal slab.* Applied Physics Letters, 2005. **86**(17).

192. Yablonovitch, E. and T.J. Gmitter, *PHOTONIC BAND-STRUCTURE - THE FACE-CENTERED-CUBIC CASE.* Physical Review Letters, 1989. **63**(18): p. 1950-1953.

193. Labilloy, D., et al., *Quantitative measurement of transmission, reflection, and diffraction of two-dimensional photonic band gap structures at near-infrared wavelengths.* Physical Review Letters, 1997. **79**(21): p. 4147-4150.

194. Astratov, V.N., et al., *Heavy photon dispersions in photonic crystal waveguides.* Applied Physics Letters, 2000. **77**(2): p. 178-180.

195. Kral, Z., et al. *Characterization of 2D macroporous silicon photonic crystals: Improving the photonic band identification in angular-dependent reflection spectroscopy in the mid-IR*. in *Symposium on Semiconductor Nanostructures towards Electronic and Optoelectronic Device Applications held at the 2007 EMRS Spring Meeting*. 2007. Strasbourg, FRANCE.

196. Kral, Z., et al., *Mid-IR characterization of photonic bands in 2D photonic crystals on silicon.* Thin Solid Films, 2008. **516**(22): p. 8059-8063.

197. Whittaker, D.M. and I.S. Culshaw, *Scattering-matrix treatment of patterned multilayer photonic structures.* Physical Review B, 1999. **60**(4): p. 2610-2618.

198. Kral, Z., Vojkuvka, L., Garcia-Caurel, E., Ferre-Borrull, J., Marsal, L. F., Pallares, J.,, *Calculation of Angular-Dependent Reflectance and Polarimetry Spectra of Nanoporous Anodic Alumina-Based Photonic Crystal Slabs.* Photonics and Nanostructures: Fundamental Applications, 2008.